University of Ioannina
School of Sciences
Department of Physics

Coherent Ultrashort Extreme Ultraviolet Sources and Quantum Control of their Characteristics with Applications to Multispectral Diffraction Microscopy

Stylianos Petrakis

PhD Dissertation

Ioannina 2024

Πανεπιστήμιο Ιωαννίνων
Σχολή Θετικών Επιστημών
Τμήμα Φυσικής

Σύμφωνες Υπερβραχείς Πηγές Ακραίου Υπεριώδους και Κβαντικός Έλεγχος των Χαρακτηριστικών τους με Εφαρμογές στην Πολυφασματική Περιθλαστική Μικροσκοπία

Στυλιανός Πετράκης

Διδακτορική Διατριβή

Ιωάννινα 2024

PhD Advisory Committee

1. Emmanouil Benis (advisor) - Associate Professor, University of Ioannina
2. Nektarios Papadogiannis - Professor, Hellenic Mediterranean University
3. Michael Tatarakis - Professor, Hellenic Mediterranean University

PhD Examination Committee

1. Emmanouil P. Benis (advisor) - Associate Professor, University of Ioannina
2. Nektarios Papadogiannis - Professor, Hellenic Mediterranean University
3. Michael Tatarakis - Professor, Hellenic Mediterranean University
4. Constantinos Kosmidis - Professor, University of Ioannina
5. Samuel Cohen - Professor, University of Ioannina
6. Spiridon Kaziannis - Assistant Professor, University of Ioannina
7. Dimitrios Sofikitis - Assistant Professor, University of Ioannina

Acknowledgements

My PhD research took place at the Institute of Plasma Physics & Lasers (IPPL) of the University Centre of Research & Innovation of the Hellenic Mediterranean University which funded me throughout the entire period of my studies. Completing this PhD thesis has been a culmination of not just my own efforts, but a collective endeavor involving the support, guidance, and encouragement of individuals and institutions.

I would like to express my deepest gratitude to my advisor, Manolis Benis, for his unwavering support, mentorship, and invaluable guidance throughout my PhD journey. His expertise and encouragement have been instrumental in shaping the direction and outcomes of this research, closely followed by the significant contribution of Nektarios Papadogiannis, whose guidance, mentorship, and unwavering support have been akin to that of my advisor. Nektarios Papadogiannis also served as the scientific responsible for the project *T1EDK-04549* that funded this research, for which I am deeply grateful.

I am also immensely thankful to the IPPL Director Michael Tatarakis for his support as a member of my Advisory and Examination Committee.

My sincere appreciation goes to Makis Bakarezos for his support, his contribution in this research and for his trials to teaching me how to be more organized...

I would like to acknowledge the University of Ioannina and the Institute of Plasma Physics and Laser (IPPL) for providing the academic framework and resources essential for this endeavor. Special thanks to the staff at IPPL, including Vasilios Dimitriou, Evaggelos Kaselouris, and all PhD and Master students, for creating a conducive working environment.

Special thanks to Yannis Orphanos for his support and for the implementation of LabView code, which significantly enhanced the efficiency and accuracy of the experiments conducted in this study.

A special thanks to Ioannis Fitilis for his cooperation, especially with the laser system "babysitting". His collaboration has been invaluable in ensuring the smooth operation and maintenance of the laser system throughout the duration of this

research.

I would like to express my appreciation to the cooperators on project T1EDK-04549, including Alekos Skoulakis, Tassos Grigoriadis, Georgia Adrianaki, Dimitrios Louloudakis, Nathanail Kortsalioudakis, Athanasios Tsapras, Costas Balas, Dimitrios Zouridis, and Efthymios Pachos, for their contributions to the project.

I extend my gratitude to Aleka Manousaki at FORTH-IESL for providing us with the SEM images crucial to our research.

Additionally, I extend my thanks to Eugene Clark for his support and for the enlightening discussions we had on physics and biology, enriching my understanding and perspective in both fields.

I am also deeply grateful to have witnessed and contributed, according to my abilities, to the creation and operation of the IPPL. Living through these unique moments has been a privilege, and I am thankful for the opportunity to be a part of its inception.

Last but not least, I am deeply grateful to my wife and my daughters for their unwavering support and patience throughout this journey. Their love and encouragement have been my source of strength, and I am truly blessed to have them by my side.

Dedication

Dedicated to my wife Pelagia and my daughters Vasiliki and Iliana, who graciously provide their love and imbue my life with meaning...

Funding

02/2020 - 05/2023

This research has been co-financed by the European Regional Development Fund of the European Union and Greek national funds through the Operational Program Competitiveness, Entrepreneurship and Innovation, under the call RESEARCH—CREATE—INNOVATE (project code: T1EDK-04549, project title: Development of a coherent X-ray multispectral microscopy system).

Χρηματοδότηση

02/2020 - 05/2023

Η παρούσα ερευνητική εργασία χρηματοδοτήθηκε από το έργο με τίτλο "Ανάπτυξη συστήματος πολυφασματικής μικροσκοπίας σύμφωνων ακτίνων-Χ "(κωδικός έργου: Τ1ΕΔΚ-04549) (Κ.Ε.80721), που υλοποιήθηκε στο πλαίσιο της Ενιαίας Δράσης Κρατικών Ενισχύσεων Έρευνας, Τεχνολογικής Ανάπτυξης & Καινοτομίας «ΕΡΕΥΝΩ - ΔΗΜΙΟΥΡΓΩ - ΚΑΙΝΟΤΟΜΩ» του Ε.Π. «Ανταγωνιστικότητα, Επιχειρηματικότητα και Καινοτομία» (ΕΠΑνΕΚ) 2014-2020 και συγχρηματοδοτείται από το Ευρωπαϊκό Ταμείο Περιφερειακής Ανάπτυξης (ΕΤΠΑ).

Με τη συγχρηματοδότηση της Ελλάδας και της Ευρωπαϊκής Ένωσης

List of Publications

PhD Articles

1. **Petrakis, S.**, Bakarezos, M., Tatarakis, M., Benis, E. P., & Papadogiannis, N. A., "Electron quantum path control in high harmonic generation via chirp variation of strong laser pulses," *Scientific Reports*, *11*(1), 23882, 2021. https://doi.org/10.1038/s41598-021-03424-3

2. **Petrakis, S.**, Bakarezos, M., Tatarakis, M., Benis, E. P., & Papadogiannis, N. A., "Spectral and Divergence Characteristics of Plateau High-Order Harmonics Generated by Femtosecond Chirped Laser Pulses in a Semi-Infinite Gas Cell," *Atoms*, *10*(2), 2022. https://doi.org/10.3390/atoms10020053

3. **Petrakis, S.**, Skoulakis, A., Orphanos, Y., Grigoriadis, A., Andrianaki, G., Louloudakis, D., Kortsalioudakis, N., Tsapras, A., Balas, C., Zouridis, D., Pachos, E., Bakarezos, M., Dimitriou, V., Tatarakis, M., Benis, E. P., & Papadogiannis, N. A., "Coherent XUV Multispectral Diffraction Imaging in the Microscale," *Applied Sciences (Switzerland)*, *12*(20),2022. https://doi.org/10.3390/app122010592

PhD-related Articles

1. Clark, E. L., Grigoriadis, A., **Petrakis, S.**, Tazes, I., Andrianaki, G., Skoulakis, A., Orphanos, Y., Kaselouris, E., Fitilis, I., Chatzakis, J., Bakarezos, E., Dimitriou, V., Benis, E. P., Papadogiannis, N. A., & Tatarakis, M., "High-intensity laser-driven secondary radiation sources using the ZEUS 45 TW laser system at the Institute of Plasma Physics and Lasers of the Hellenic Mediterranean University Research Centre," *High Power Laser Science and Engineering*, *9*, 53, 2021. https://doi.org/10.1017/hpl.2021.38

2. Fitilis, I., Grigoriadis, A., Tazes, I., **Petrakis, S.**, Andrianaki, G., Dimitriou, V., Bakarezos, E., Benis, E. P., Tsiapa, I., Boursianis, T., Kalaitzakis, G., Bontzos, G., Liakopoulos, D. A., Pappas, E., Detorakis, E. T., Clark, E. L.,

Maris, T. G., Papadogiannis, N. A., & Tatarakis, M., "Polymer-Gel Radiation Dosimetry of Laser-Based Relativistic Electron Sources for Biomedical Applications: First Qualitative Results and Experimental Challenges," *Frontiers in Physics*, *10*, 2022. https://doi.org/10.3389/fphy.2022.727511

PhD Poster Presentations

1. **S. Petrakis**, Y. Orphanos, I. Fitilis, E.L. Clark, V. Dimitriou, M. Bakarezos, M.Tatarakis, E. P. B. and N. A. P., "High harmonics generation and characterization using the Zeus laser at CPPL," *35th European Conference on Laser Interaction with Matter*, 2018.

2. E.L. Clark, A. Grigoriadis, I. Tazes, G. Andrianaki, I. Fitilis, **S. Petrakis**, A. Skoulakis, E. Kaselouris, T.G. Maris, I. Tsiapa, M. Bakarezos, I.K. Nikolos, V. Dimitriou, E.P. Benis, N. A. Papadogiannis, and M. Tatarakis, "Secondary sources generated with the ZEUS 45TW laser system at CPPL," *International Conference on Applications of Nuclear Techniques*, 2019.

3. **S. Petrakis**, E.P. Benis, A. Skoulakis, Y. Orphanos, V. Dimitriou, M. Bakarezos, M. Tatarakis, N. Kortsalioudakis, A. Tsapras, P. Tsopelas, C. Balas, D. Zouridis, E. Pachos, and N. A. Papadogiannis, "Coherent femtosecond x-ray multi-spectral microscopy system: The XMMaS project," *18th International Conference on Nanosciences & Nanotechnologies (NN21)*, 2021.

4. N.A. Papadogiannis, **S. Petrakis**, A. Grigoriadis, G. Andrianaki, I. Tazes, A. Skoulakis, Y. Orphanos, M. Bakarezos, V. Dimitriou, E.P. Benis, M. Tatarakis, "Laser-generated ultrafast and coherent x-ray sources and their applications in nanoscopy," *18th International Conference on Dynamics of systems on the Nanoscale* (Dyson), Santa Margherita, Ligure, Italy, 18-22 October 2021.

5. E. Kaniolakis-Kaloudis, **S. Petrakis**, G. Andrianaki, A. Grigoriadis, A. Skoulakis, M. Bakarezos, M. Tatarakis, E.P. Benis, N.A. Papadogiannis, "Preliminary results on the divergence of Ar-gas generated high harmonic beam using chirped femtosecond laser pulses,", *TUMIEE, COST action 17126 meeting*, Prague, Check Republic, 28-29 April, 2022.

6. **S. Petrakis**, A. Skoulakis, V. Dimitriou, M. Bakarezos, M. Tatarakis, E.P. Benis, N.A. Papadogiannis, "Ultrafast and coherent multispectral diffraction imaging in the Extreme Ultraviolet Stereodynamics," *2022 conference*, 30 October – 4 November, Rethymnon, Crete, Greece 2022.

7. **S. Petrakis**, A. Skoulakis, V. Dimitriou, M. Bakarezos, M. Tatarakis, E.P. Benis and N.A. Papadogiannis, "Ultrafast Nanoscale Coherent XUV Diffraction Imaging," *37th Panhellenic Conference on Solid State Physics & Materials Science*, Thessaloniki, Greece,17-20 September 2023.

Contents

List of Figures

List of Tables

Abstract

The objective of this thesis is to explore the dynamics of the high order harmonic generation (HHG) during the interaction of ultra-short intense laser pulses with gas targets, control the HHG characteristics and use the HHG as an optimized secondary coherent source in the extreme ultra-violet (XUV) for applications in diffraction microscopy. The investigation is based upon the systematic study of the effects of the experimental parameters, such as gas species, gas pressure, focusing conditions and chirp of the laser pulse, in the HHG process. The novelty of the study relies upon the fact that HHG takes place at the leading edge of the laser pulse, conditions that depart from the typical HHG conditions reported in the literature. Thus, highly non-linear phenomena, such as self-phase modulation, that largely affect the HHG process come into play. These effects can be controlled by the laser characteristics and consequently the HHG quality characteristics can also be controlled. Thus, a complete parametrization of the HHG spectral and spatial characteristics (line broadening, spectral shifting, angular divergence and tunability) was performed as a function of the experimental parameters of gas species, gas pressure and laser chirp, showcasing the optimum conditions for HHG in these intense laser pulses conditions. The study highlighted that control over the electron trajectories (quantum paths) can be achieved by varying the chirp of laser pulse. The suppression of the long trajectory was evident in the HHG image spectra for low positive laser chirp values, and this was further supported by model calculations. Finally, this thesis explores the capability for extending the technique of XUV coherent diffraction imaging (CDI) to multispectral XUV CDI in a proof-of-principle experimental realization. This multispectral XUV CDI approach has potential applications in nanoscale microscopy in many areas, such as material science, biology, medical sciences as well as in real time dynamic behavior of chemical systems on surfaces and in spatiotemporal imaging of the evolution of the critical plasma density front.

Περίληψη

Ο στόχος αυτής της διατριβής είναι να διερευνήσει τη δυναμική της παραγωγής των υψηλής τάξης αρμονικών (HHG) κατά την αλληλεπίδραση ισχυρών παλμών λέιζερ με αέριους στόχους, να ελέγξει τα χαρακτηριστικά των αρμονικών και να χρησιμοποιήσει τις αρμονικές ως βελτιστοποιημένη δευτερεύουσα σύμφωνη πηγή ακτινοβολίας ακραίου υπεριώδους (XUV) για εφαρμογές σε περιθλαστική μικροσκοπία. Η διερεύνηση βασίζεται στη συστηματική μελέτη των επιδράσεων των πειραματικών παραμέτρων, όπως τα είδη αερίων, η πίεση αερίου, οι συνθήκες εστίασης και το chirp του παλμού λέιζερ, στη διαδικασία HHG. Η καινοτομία της μελέτης βασίζεται στο γεγονός ότι η HHG λαμβάνει χώρα στο προπορευόμενο χρονικά άκρο του παλμού λέιζερ, συνθήκη που διαφέρει από τις τυπικές συνθήκες παραγωγής αρμονικών που αναφέρονται στη βιβλιογραφία. Έτσι, μη γραμμικά φαινόμενα, όπως η αυτοδιαμόρφωση φάσης, που επηρεάζουν σε μεγάλο βαθμό τη διαδικασία HHG, εμφανίζονται ως ρυθμιστές. Αυτές οι επιδράσεις μπορούν να ελεγχθούν από τα χαρακτηριστικά του παλμού λέιζερ και έτσι τα ποιοτικά χαρακτηριστικά HHG μπορούν επίσης δευτερογενώς να ελεγχθούν. Με αυτόν τον τρόπο, πραγματοποιήθηκε μια πλήρης παραμετροποίηση των φασματικών και χωρικών χαρακτηριστικών των αρμονικών (διεύρυνση γραμμής, φασματική μετατόπιση, και γωνιακή απόκλιση) ως συνάρτηση των πειραματικών παραμέτρων του είδους του αερίου, της πίεσης του αερίου και του chirp του παλμού λέιζερ, αναδεικνύοντας τις βέλτιστες συνθήκες για το HHG σε συνθήκες ισχυρών παλμών λέιζερ. Η μελέτη έδειξε ότι μπορεί να επιτευχθεί ο έλεγχος των τροχιών των ηλεκτρονίων (κβαντικά μονοπάτια) μεταβάλλοντας το chirp του παλμού λέιζερ. Η καταστολή της μακράς ηλεκτρονικής τροχιάς ήταν εμφανής στα φάσματα εικόνας HHG για χαμηλές θετικές τιμές του chirp του παλμού λέιζερ, και αυτό υποστηρίχθηκε περαιτέρω από κβαντομηχανικούς υπολογισμούς. Τέλος, η παρούσα διατριβή διερευνά την ικανότητα επέκτασης της τεχνικής της σύμφωνης περιθλαστικής απεικόνισης στο ακραίο υπεριώδες (XUV CDI) σε πολυφασματική XUV CDI μέσω της πειραματικής της πραγματοποίησης και της απόδειξης αρχής λειτουργίας. Η πολυφασματική XUV CDI έχει εφαρμογές στη μικροσκοπία νανοκλίμακας σε πολλούς τομείς, όπως η επιστήμη των υλικών, η βιολογία, οι ιατρικές επιστήμες, η δυναμική συμπεριφορά χημικών συστημάτων σε

πραγματικό χρόνο σε επιφάνειες, καθώς και η χωροχρονική απεικόνιση της εξέλιξης του μετώπου κρίσιμης πυκνότητας πλάσματος.

Chapter 1

Introduction

The Nobel Prize in Physics in 2023 was awarded to Pierre Agostini, Ferenc Krausz, and Anne L'Huillier for their seminal experiments, which unveiled a groundbreaking method for generating pulses of light of unprecedented duration [1]. This method, based on the process of high harmonic generation (HHG) through the interaction of intense ultrafast laser pulses with atomic gases, yielded pulses with duration in the attosecond regime (1 as = 10^{-18} s). These ultrashort pulses enabled the precise measurement of swift electron dynamics and energy transitions within atoms and molecules, thus revolutionizing the understanding of fundamental processes at the quantum level. This pioneering work not only provided scientists with new tools for exploring the intricate world of electrons but also laid the foundation for advancements in attosecond physics as well as in the nanoscale imaging technology such as the Coherent Diffraction Imaging (CDI).

The advancements in HHG were triggered by the rapid evolution in the technology of intense and coherent electromagnetic fields, i.e. in femtosecond laser pulses (1 fs = 10^{-15} s), over the last three decades. With the development of techniques like CPA by Donna Strickland and Gérard Mourou, femtosecond laser pulses have become indispensable tools in various fields of research, from ultrafast spectroscopy to high energy physics. These intense fs pulses enabled researchers to probe and control matter with unprecedented precision, opening new avenues for understanding fundamental processes in physics, chemistry, and biology. The culmination of these efforts was recognized with the awarding of the Nobel Prize in Physics in 2018 to Donna Strickland and Gérard Mourou for their groundbreaking work on CPA, highlighting the transformative impact of femtosecond laser technology on scientific exploration and innovation [2, 3]. Laser pulse peak intensities of the orders of $10^{13} - 10^{16}$ W/cm^2 are currently routinely available in laboratories worldwide.

The interaction of intense fs laser pulses with atoms has unveiled a plethora of new strong-field phenomena that have significantly expanded our understanding of atomic and molecular physics. These phenomena include above threshold ionization [4, 5], tunneling ionization [6], over-the-barrier ionization [7, 8], and HHG [9]. HHG, in particular, has emerged as a remarkable process that enables the generation of coherent spectral sources in the eXtreme UltraViolet (XUV) region. These developments have paved the way for the development of powerful tools for investigating ultrafast processes in matter, with implications ranging from attosecond science to advanced spectroscopic techniques. The bandwidth required for generating extremely short pulses was proposed to be facilitated by the plateau [10–12]. In such intense electromagnetic fields, the interaction between the laser field and the atom is governed primarily by the laser pulse characteristics (peak intensity, temporal frequency and phase) as well as the depth of the atomic Coulombic well. Consequently, semiclassical theories have been developed to describe such interactions, the most renowned being the three-step model for the HHG process [9, 13–15].

Since the dawn of HHG studies, attosecond metrology has emerged as a pivotal tool in investigating ultrafast processes in matter, facilitating the exploration of electronic dynamics with unprecedented temporal resolution. Papadogiannis *et al.* conducted experiments where they observed how higher-order harmonics, generated in argon gas by two short laser pulses, overlap and interact [16, 17]. They were the first to discovered features in the data that lasted less than 100 attoseconds, indicating the production of pulses in the attosecond range. This work laid the foundation for further studies into attosecond physics. Hentschel *et al.* achieved attosecond time resolution by combining soft x-ray pulses with very short visible light pulses, allowing them to observe electronic dynamics with a resolution of 150 attoseconds [18]. Their findings showed how atoms respond on this incredibly short timescale, opening up new possibilities for studying electrons in detail. Paul *et al.* proposed a method for measuring the relative phases of high harmonics, revealing a series of attosecond pulses in the time domain [19]. This discovery suggested that harmonic generation could be a useful tool for making attosecond measurements, further advancing attosecond metrology. Tzallas *et al.* [20] established the first direct measurement of harmonic pulse temporal properties in the subfemtosecond regime. They analyzed the second-order autocorrelation trace of an attosecond pulse train, observing evidence of attosecond light bunching in harmonics 7 to 15 emitted from a xenon gas jet [21–25]. The impact of attosecond metrology goes beyond fundamental research. Goulielmakis *et al.* highlighted its importance in understanding how electrons move in atoms, which has implications for biology, x-ray technology, and electronics [26]. They emphasized the role of

precise laser pulses and synchronized attosecond pulses in this research. In the effort to characterize pulses lasting less than 100 attoseconds, Gagnon *et al.* developed a specialized algorithm for analyzing electron spectra [27]. Their work addressed the challenges of accurately measuring these extremely short pulses, contributing to the improvement of attosecond measurement techniques.

Many modern laboratories are currently equipped with fs laser systems, which routinely deliver mJ pulses with repetition rates ranging from Hz to MHz. The coherent XUV radiation produced from the interaction of strong field pulses with atomic gaseous targets serves as a secondary source for applications related to ultrafast microscopy techniques based on CDI [28–31]. The necessity for development of such secondary coherent XUV sources, with high quality geometrical and spectral characteristics, has been recently emphasized [32]. CDI is an imaging technique that utilizes coherent light sources, such as x-rays or electrons, to probe the structure of samples at the nanoscale level. Unlike conventional imaging methods that rely on lenses to focus light and form an image, CDI reconstructs the sample's structure directly from the diffraction pattern produced by the interaction of the coherent light with the sample. This diffraction pattern contains information about the amplitude of the scattered light, which can be analyzed using computational algorithms to reconstruct a high-resolution image of the sample. Reconstruction algorithms iteratively refine an initial approximation of the object's structure until it aligns with constrictions related either with the diffraction pattern or the object [33]. CDI as a lensless microscopy technique holds considerable significance due to absence of x-ray optics [34].

It should be emphasized that multispectral CDI in the visible part of the EM spectrum and longer wavelengths up to thermal infrared is a well-established technique. Wavelength filtering is done using special filters, combined with suitable detectors, that are sensitive to particular wavelengths. The visible part of the EM spectrum is used for imaging of atmospheric pollutants, water, vegetation, soil, and biological tissues. The IR part is used for imaging of forest fires, geological features, clays, mapping terrain, and night studies [35–38]. However, multispectral XUV CDI is still a field of intense research, as it probes the way to the nanoscale imaging, seeking for an establishment similar to the visible and IR CDI .

Aim of the Study

The objective of this thesis is twofold. First, it seeks to investigate the dynamics of HHG at the leading edge of the laser pulse using ultra-short intense laser pulses. The study systematically investigates the impact of experimental parameters

such as gas species, pressure, focusing conditions, and laser pulse chirp on the production and coherent addition (phase matching) of the generated XUV radiation. Intense laser pulses are utilized to induce highly nonlinear phenomena, including self-phase modulation (SPM), which influence the HHG process. The study aims to understand quantum mechanical behavior under non-typical HHG conditions and to control HHG characteristics accordingly. Additionally, this thesis explores the application of the studied coherent HHG source in performing multispectral XUV CDI measurements and subsequent object reconstruction in the nanoscale.

Thesis Overview

In this thesis, we embark on a journey into the realm of ultrafast optics, exploring the generation and manipulation of HHG for applications in nanoscale imaging and spectroscopy. Beginning with a comprehensive overview of the theoretical foundations of ultra-short laser pulses and high harmonic generation, we delve into the experimental realization of HHG and multispectral imaging systems, highlighting key advancements and challenges in the field.

Chapter 2 provides the theoretical foundation necessary for understanding the principles underlying HHG. The fundamentals of ultra-short and intense laser pulses, essential for initiating the HHG process, are elucidated. The role of the optical Kerr effect and SPM in laser pulses is also presented. Subsequently, the intricate process governing HHG, exploring both classical and quantum mechanical pictures, are delved into. Additionally, the importance of propagation and phase matching in achieving efficient HHG is elucidated.

Chapter 3 details the experimental setup for HHG and CDI including the laser system, vacuum chambers manifold, HHG generation apparatus, diagnostics for HHG and XUV, wavelength selection, as well as provisions for CDI.

Chapters 4 deals with optimizing the HHG source. Optimization processes for the solid laser beam are discussed, covering aspects such as beam diameter, focus position, pressure, and the composition of gases and gas mixtures utilized in the generation process. Additionally, the chirp of laser pulses is examined for its impact on HHG efficiency. Similar optimization efforts are extended to the annular laser beam configuration, focusing on parameters such as pulse energy, beam diameter, and gas pressure. By fine-tuning these parameters, we aim to enhance the coherence and intensity of the generated XUV radiation.

Chapter 5 introduces a novel method for coherent control of two quantum paths in plateau harmonics generated in a noble gas, leveraging the chirp of the laser

pulse. By manipulating the chirp of high-intensity laser pulses, control over various parameters such as ionization degree, SPM, and trajectory evolution is achieved. Detailed studies highlight the efficiency of HHG and trajectory separation with chirped laser pulses. Experimental findings demonstrate accurate control over HHG efficiency and trajectory resolution, supported by a developed phenomenological model.

Chapter 6 presents a systematic study on the spectral and divergence characteristics of plateau harmonics within an Ar-filled semi-infinite gas cell. Gas pressures, laser beam focal conditions, and chirp imposed on laser pulses are systematically explored. The evolution of plateau HHG spectra from positive to negative chirp values with increasing gas pressures is monitored. High-intensity conditions favor negatively chirped pulses, leading to maximum HHG signal even at low pressures. Additionally, broader lines resembling a quasi-continuum spectrum emerge at higher pressures. The contribution of long and short trajectories to HHG spectra is tracked, providing insights into HHG dynamics. Experimental findings are supported by calculations based on a phenomenological model.

Chapter 7 presents the culmination of our research journey in the form of coherent XUV multispectral XUV CDI, offering insights into the future of nanoscale imaging and spectroscopy. This chapter details the development and proof-of-principle operation of a multispectral XUV CDI experimental setup. The system extends the multispectral paradigm to the XUV region, enabling comprehensive analyses in transmission and reflection modes. The efficacy of XUV CDI applications in various experimental scenarios is demonstrated, with a discussion on the implications for future discoveries concluding the chapter.

Finally, Chapter 8 presents the conclusion of this thesis along with future perspectives of this work.

Chapter 2

Theory

2.1 Fundamentals of Ultra-short Laser Pulses

2.1.1 Gaussian Laser Pulses

The temporal envelope and the transverse spatial profile of a laser beam are described by Gaussian functions [39].

2.1.1.1 Spatial Profile of Gaussian Laser Beams

Using Maxwell's equations in an isotropic charge-free medium, one can derive the complete expression for the electric field of a Gaussian TEM_{00} mode [39].

$$\begin{aligned} E(x,y,z) = & \quad \text{The electric field} \\ E_0 & \quad \text{Amplitude at z = 0} \\ \times & \\ \frac{w_0}{w(z)} \exp\left[-\frac{r^2}{w^2(z)}\right] & \quad \text{Variation of the amplitude with r and z} \\ \times & \\ \exp\left[-i\left(kz - \phi(z)\right)\right] & \quad \text{Longitudinal phase factor} \\ \times & \\ \exp\left[-i\frac{kr^2}{2R(z)}\right] & \quad \text{Radial phase factor} \end{aligned} \tag{2.1}$$

The first term is the electric field maximum amplitude. The second term describes the variation of the electric field amplitude as a function of the distance from the optical axis (radial coordinate r). The third term describes the phase change of the wave in the direction of the propagation axis z, with k being the wave number for

a corresponding plane wave.

In Eq.(2.1), $w(z)$ is the radial distance at which the field amplitude drops to $1/e$ of its maximum value, and correspondingly the intensity to $1/e^2$, defined as

$$w(z) = w_0\sqrt{1+\left(\frac{z}{z_R}\right)^2}. \tag{2.2}$$

w_0 is the beam waist, i.e. the minimum radial distance at the focus $z = 0$, as shown in Fig.2.1, and z_R is the Rayleigh length defined as

$$z_R = \frac{\pi w_0^2}{\lambda}, \tag{2.3}$$

with λ being the wavelength. The confocal length, or depth of focus, is defined twice the Rayleigh length, i.e. $b = 2z_R$. $R(z)$ is the radius of curvature defined as

$$R(z) = z\left(1+\left(\frac{z_R}{z}\right)^2\right), \tag{2.4}$$

while $\phi(z)$ is the Gouy phase, which corresponds to the phase difference between a Gaussian beam and the corresponding plane wave, defines as

$$\phi(z) = \tan^{-1}\left(\frac{z}{z_R}\right). \tag{2.5}$$

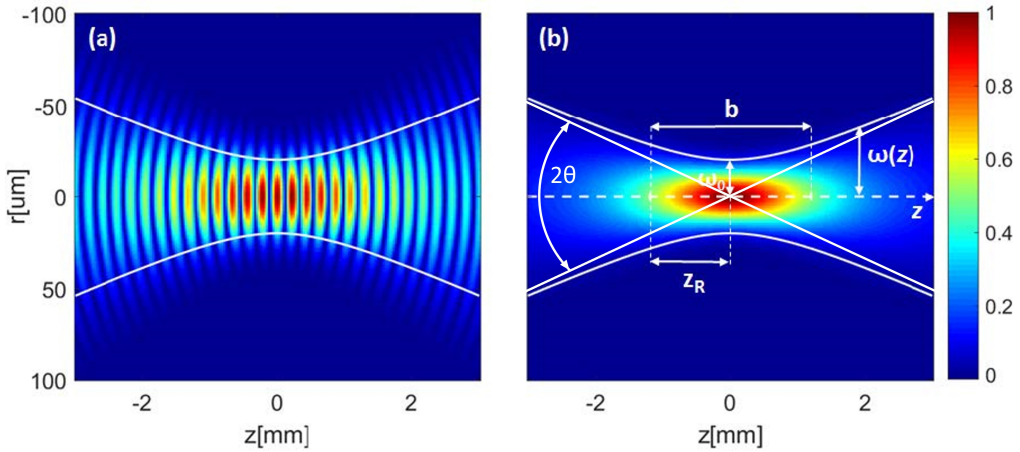

Figure 2.1
Gaussian Beam: (a) Distribution of the electric field around the focus ($z = 0$). (b) Distribution of the intensity around the focus with notation of the basic characteristic distances.

Based on the geometry shown in Fig.2.1 the divergence angle of a Gaussian

beam can be defined as

$$\theta = \lim_{z\to\infty} \frac{w(z)}{z} = \frac{w_0}{z_R} = \frac{\lambda}{\pi w_0}. \tag{2.6}$$

Gaussian beam intensity at the focus

The intensity distribution $I(z, r)$ of a Gaussian beam is described by the equation

$$I(z,r) = I_0 \left(\frac{w_0}{w(z)}\right)^2 \exp\left(-2\frac{r^2}{w(z)^2}\right) = I(z)\exp\left(-2\frac{r^2}{w(z)^2}\right), \tag{2.7}$$

where the peak intensity I_0 is related to the electric field amplitude by the following equation

$$I_0 = \frac{1}{2}\epsilon_0 c E_0^2. \tag{2.8}$$

The total power P carried by the Gaussian beam is determined by integrating the intensity over the entire radial plane as

$$\mathrm{P} = \int_0^\infty I(z,r)2\pi r dr = I(z)\frac{\pi w(z)^2}{2}. \tag{2.9}$$

Expressing the intensity $I(z)$ in terms of power and beam waist, we obtain

$$I(z) = \frac{2P}{\pi w(z)^2}. \tag{2.10}$$

This equation establishes the intensity as a function of axial distance z, total power P, and beam waist $w(z)$. Furthermore, the peak intensity at the beam waist ($z = 0$) is written as

$$I_0 = I(z=0) = \frac{2P}{\pi w_0^2}. \tag{2.11}$$

This equation provides the intensity at the beam waist in terms of the initial total power P and the beam waist size w_0.

From Eqs.(2.1) and (2.2), under the approximation $z \gg z_R$, $w(z)$ becomes

$$w(z) \approx \frac{w_0 z}{z_R} = \frac{\lambda z}{\pi w_0} \qquad (z \gg z_R). \tag{2.12}$$

Thus, for a lens with focal lens f the above equation becomes

$$w(z) = \frac{\lambda f}{\pi w_0}. \tag{2.13}$$

To define the Gaussian laser beam diameter D, various criteria have been adopted in the literature [40].

- Conservative criterion: The beam diameter is defined at the 99% of the total power, i.e., $D = \pi w(z)$. Then, the relationship between D and the beam waist w_0 results as $w_0 = \frac{f\lambda}{D}$. Accordingly, the peak intensity results

$$I_0 = \frac{2P}{\pi \left(\frac{f\lambda}{D}\right)^2}. \tag{2.14}$$

- $1/e^2$ criterion: The beam diameter is defined at the $1/e^2$ (or 86%) of the total power, i.e., $D = 2w(z)$. Then, the relationship between D and the beam waist w_0 results as $w_0 = \frac{2}{\pi}\frac{f\lambda}{D}$. Accordingly, the peak intensity results

$$I_0 = \frac{2P}{\pi \left(\frac{2f\lambda}{\pi D}\right)^2}. \tag{2.15}$$

2.1.1.2 Temporal Profile of Gaussian Laser Beams

The temporal part of the electric field of a Gaussian pulse can be expressed as

$$E(t) = E_0 e^{-2\ln 2\left(\frac{t}{\tau_e}\right)^2} e^{i\Phi}, \tag{2.16}$$

where τ_e is the full width at half maximum (FWHM) of the pulse. A laser pulse is termed "chirped" when its instantaneous frequency varies with time so that the pulse phase has time-dependent components causing a frequency variation across the pulse duration. The phase Φ can then be written as the oscillatory part of the central frequency $\omega_0 = 2\pi/T_0$ plus the remaining variation $\varphi(t)$ as:

$$\Phi(t) = \omega_0 t + \varphi(t). \tag{2.17}$$

The instantaneous frequency is derived from the phase Φ as

$$\omega(t) = \frac{d\Phi(t)}{dt} = \omega_0 + \frac{d\varphi(t)}{dt}. \tag{2.18}$$

In case $\varphi(t)$ is a quadratic function of time, i.e. $\varphi(t) = bt^2$, the instantaneous frequency becomes

$$\omega(t) = \frac{d}{dt}\left[\omega_0 t + \varphi(t)\right] = \omega_0 + 2bt, \tag{2.19}$$

where b is the chirp parameter. In this case the chirp is termed as linear.

In Fig.2.2, three cases of Gaussian pulses with central wavelength of 800 nm and duration of 7 fs are presented. In Fig.2.2(a), the pulse has negative chirp of $-0.13\,\mathrm{fs}^{-2}$, while in Fig.2.2(b), it has a positive chirp of $0.13\,\mathrm{fs}^{-2}$. As can be seen, for the positively chirped pulses the field oscillation increases with time, while for

the negatively chirped pulses it decreases. In Fig.2.2(c), an unchirped pulse, or Fourier-transform Limited (FTL) is shown for comparison. From equations (2.16)

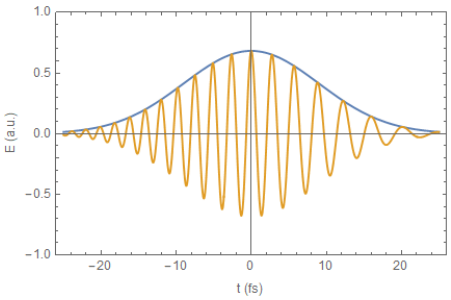

(a) Negatively chirped pulse with $b = -0.023\,\mathrm{fs}^{-2}$

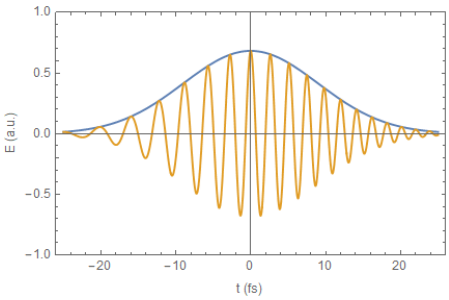

(b) Positively chirped pulse with $b = 0.023\,\mathrm{fs}^{-2}$

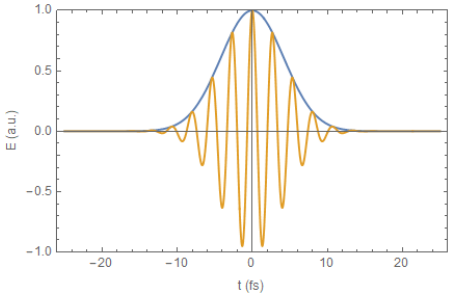

(c) Unchirped or FTL pulse.

Figure 2.2
The effect of chirping on a Gaussian pulse with a central wavelength of 800 nm and a duration of 7 fs.

and (2.17) it follows that the Gaussian pulse can be written as:

$$E(t) = E_0 e^{-2\ln 2\left(\frac{t}{\tau_e}\right)^2} e^{i(\omega_0 t + bt^2)}. \tag{2.20}$$

The temporal distribution of the intensity of an FTL laser pulse results from Eq.(2.16) as

$$I(t) = I_0 \exp\left(-4\ln 2 \frac{t^2}{\tau_{FTL}^2}\right) \tag{2.21}$$

where τ_{FTL} is the pulse duration measured at the FWHM of the pulse envelope. For a chirped laser pulse the temporal distribution of the intensity is described as

$$I(t) = I_0(\tau) \exp\left(-4\ln 2 \frac{t^2}{\tau^2}\right). \tag{2.22}$$

In this case, the peak intensity $I_0(\tau)$ depends on the laser pulse duration as [41]

$$I_0(\tau) = I_0 \frac{\tau_{FTL}}{\tau}. \tag{2.23}$$

Chirp parameter b determination

Eq.(2.20) can be written in the following form

$$E(t) = E_0 e^{-\Gamma t^2} e^{i\omega_0 t}, \tag{2.24}$$

with $\Gamma = a - ib$ and $a = 2\ln 2 \frac{1}{\tau^2}$. By applying a Fourier transform and taking the power spectrum FWHM we obtain

$$\Delta\omega = \frac{4\ln 2}{\tau}\sqrt{1 + \left(\frac{b}{a}\right)^2}. \tag{2.25}$$

Then, the chirp parameter b is obtained as a function of the pulse duration of the chirped pulse and the corresponding FTL pulse as:

$$b(\tau) = \pm\frac{4\ln 2}{\tau^2}\sqrt{\frac{\tau^2}{\tau_{FTL}^2} - 1}. \tag{2.26}$$

2.1.2 Optical Kerr Effect and Self-phase Modulation

SPM is a nonlinear optical phenomenon where the intensity of a laser pulse affects its own phase. This effect arises due to the Kerr nonlinearity, where the refractive index of the medium changes in response to the instantaneous intensity of the light passing through it. As the intensity increases, the refractive index changes, leading to a modification of the optical phase of the pulse.

SPM refers to a phenomenon where the intensity-dependent refractive index of a medium (see Eq. (2.27)) causes a change in the pulse's phase during propagation. In the Kerr-induced SPM, the Kerr nonlinear index induces phase modulation due to the intensity-dependent refractive index of the material. Additionally, plasma-induced SPM, involves changes in phase induced by varying plasma density. Both mechanisms contribute to the chirp, representing frequency variations within ultrashort laser pulses during propagation. Then, the index of refraction is written as

$$n(I) = n_0 + n_2 I(t), \tag{2.27}$$

where n_0 and n_2 are the field-free and non-linear refractive index, respectively.

The laser pulse frequency corresponding to the SPM effects is written as

$$\omega_{SPM}(t) = -\frac{n_2\omega_{L0}}{c} z_g \frac{dI(t)}{dt} + \frac{\omega_{L0}}{2n_0 c\rho_c} z_p \frac{d\rho(t)}{dt}, \tag{2.28}$$

where z_g is the propagation length of the laser beam in the Kerr medium within the Rayleigh length, excluding the plasma length, and z_p is the plasma length. $\rho(t)$

is the density of free electrons in the plasma depending on the gas pressure and ρ_c is the critical plasma density, with $\rho_c = 1.7 \times 10^{21}/\text{cm}^3$ at 800 nm. The first term describes the Kerr-induced SPM, while the second one the plasma-induced SPM [42, 43] In Fig.2.3 an example of the SPM effects is shown.

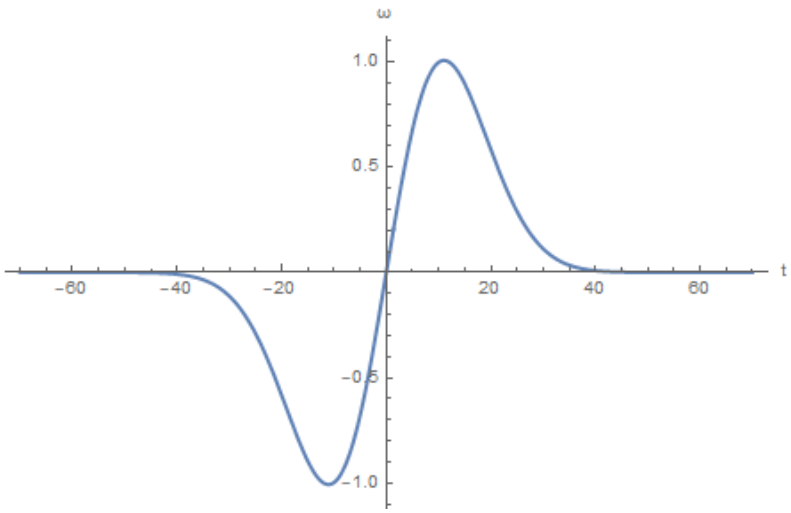

Figure 2.3
Example of the Self-phase Modulation effect, where the laser pulse frequency caused by SPM ω_{SPM} modulates from negative to positive values.

The instantaneous laser frequency including all the SPM effects in the atoms and the plasma is written as

$$\omega_L(t) = \omega_0 + \omega_{SPM}(t) + b(\tau)t, \tag{2.29}$$

where ω_0 is the central laser frequency and $b(\tau)$ the chirp parameter from Eq.(2.26).

2.2 Fundamentals of High Harmonic Generation

HHG is a nonlinear optical process that occurs when intense femtosecond laser pulses interact with a medium, typically a gas or solid. In the traditional gas-phase HHG, the laser ionizes atoms in a noble gas, and the emitted electrons, driven by the laser field, recombine with their parent ions, emitting photons at harmonics of the laser frequency as illustrated in Fig.2.4.

HHG coexists with ionization mechanisms determined by the laser intensity, i.e. multiphoton ionization, tunneling ionization, and over the barrier ionization. These mechanisms appear at increasing laser peak intensities determined by the Keldysh parameter which is defined as

$$\gamma \equiv \sqrt{\frac{I_p}{2U_p}}, \tag{2.30}$$

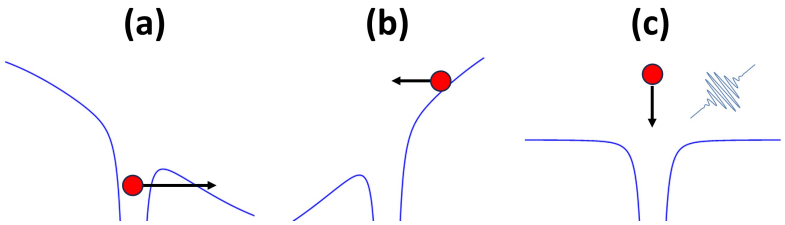

Figure 2.4
The basic steps in the HHG three-step model: (a) ionization, (b) acceleration, and (c) recombination.

where I_p is the ionization potential of the atom, and U_p is the ponderomotive potential calculated as

$$U_p = \frac{e^2 E_0^2}{4m\omega_0^2}, \tag{2.31}$$

where m is the electron mass. U_p quantifies the average kinetic energy gained by an electron in the oscillating laser field. Typically for $\gamma > 1$ multiphoton ionization dominates while for $\gamma << 1$ over the barrier ionization becomes dominant. For $\gamma < 1$ but closer to 1 tunneling ionization comes into play, as shown in Fig.2.5 These emphasize the importance of the Keldysh parameter in characterizing the transition between ionization mechanisms. Adjusting laser parameters enables precise control over ionization processes, influencing subsequent HHG and facilitating investigations in ultrafast laser physics.

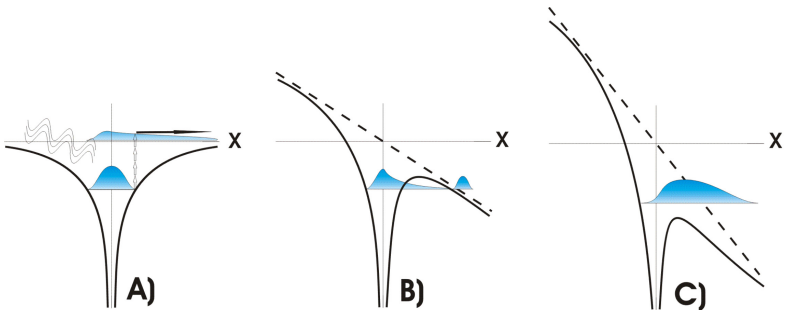

Figure 2.5
Ionization mechanisms of atoms under interaction with strong laser fields: (a) Multiphoton ionization, $\gamma > 1$. (b) Tunneling ionization, $\gamma < 1$. (c) Over the barrier ionization, $\gamma << 1$.

Tunneling ionization is described by the ADK model which calculates the probability of an electron tunneling out of an atom or molecule under the influence of an intense laser field. The formula for the ionization rate is [5, 44]

$$W_{ADK}(t) = |C_{l^* n^*}|^2 \, G_{lm} I_P \left(\frac{2F_0}{F(t)}\right)^{2n^* - |m| - 1} \exp\left(-\frac{2F_0}{3F(t)}\right), \tag{2.32}$$

where, l is the orbital quantum number, m is the magnetic quantum number, n^* is effective principal quantum number, $l^* = n^* - 1$ is the effective orbital quantum

number, I_P is the ionization potential of the atom, $F_0 = (2I_P)^{3/2}$, $F(t)[a.u.] = \sqrt{I(t)[W/cm^2]/(3.55 \times 10^{16})}$ the time dependent laser field strength, while $C_{l^*n^*}$ and G_{lm} are parameters depending on the quantum numbers. For the argon gas, in use here, the values of the parameters are as follows: $I_P = 15.76$ eV, $F_0 = 1.24665$ a.u., $l = 1$, $m = 0$, $n^* = 0.92915$, $l^* = -0.07085$, $G_{lm} = 3$ and $|C_{l^*n^*}|^2 = 4.11564$. The ionization probability $p(t)$ is obtained from Eq.(2.32) as

$$p(t) = 1 - \exp\left(-\int_{-\infty}^{t} W_{ADK}\left(t'\right) dt'\right), \tag{2.33}$$

2.2.1 Three-step Model: The Classical Picture

In the tunneling regime, the freed electron interacts with a strong laser electric field, causing it to accelerate. At first, the electron moves away from the atomic nucleus, then decelerates and reverses its direction when the electric field changes direction, and finally, it speeds back toward the nucleus.

Next, we will consider the motion of the electron after atom ionization using classical mechanics. The potential of the ion core is neglected, and only the electric field of the laser $E_L(t)$ is taken into account. In the one-dimensional case, it is assumed that the laser is a monochromatic light linearly polarized in the x direction, i.e.

$$E_L(t) = E_0 \cos(\omega_0 t). \tag{2.34}$$

The differential equation that describes the motion is

$$\frac{d^2x}{dt^2} = -\frac{eE_0}{m_e} \cos(\omega_0 t). \tag{2.35}$$

When the electron is emitted, both its starting position (x_0) and initial velocity (v_0) are set to 0. Then, the solution for the velocity results from the integration of Eq.2.35 as

$$v(t) = \frac{dx}{dt} = -\frac{eE_0}{m_e\omega_0} \left[\sin(\omega_0 t') - \sin(\omega_0 t)\right], \tag{2.36}$$

where t' is the ionization time. The electron position results from the integration of Eq.2.36 as

$$x(t) = \frac{eE_0}{m_e\omega_0^2} \left\{\left[\cos\left(\omega_0 t\right) - \cos\left(\omega_0 t'\right)\right] + \omega_0 \sin\left(\omega_0 t'\right)\left(t - t'\right)\right\}. \tag{2.37}$$

The electron kinetic energy can be calculateed from the equations (2.36) and (2.31) as

$$K = \frac{1}{2} m_e v^2(t) = 2U_p \left[\sin(\omega_0 t) - \sin(\omega_0 t')\right]^2 . \tag{2.38}$$

From Eq.(2.38) it follows that the maximum kinetic energy is $3.17U_p$. Thus, the maximum emission energy (cutoff) is

$$\hbar\omega_{\text{cutoff}} = I_p + 3.17U_p. \tag{2.39}$$

Equation ((2.38)) shows that the kinetic energy reaches its peak when t' has a value of 0.05 of the laser period. As a result, an electron released prior to t' will have the same energy as one released after t', albeit with a shorter trajectory. Electrons released before t' exhibit long trajectories, while those released after t' demonstrate shorter ones, as depicted in Fig.2.6. Over time, the energy of the short trajectories increases, leading to a positive chirp, while for the long trajectories, the opposite occurs.

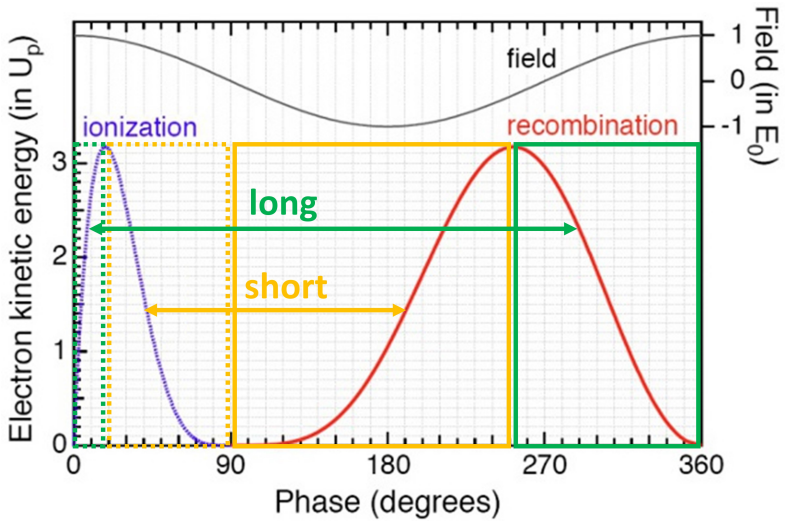

Figure 2.6
Ionization (dashed boxes) and recombination (solid boxes) phases influence the energy dependence of HHG photons. Long electron trajectories appear in green, while short trajectories appear in yellow.

2.2.2 Three-step Model: Quantum Mechanical Picture

In the quantum mechanical description, known as Lewenstein model, the following assumptions are made: [9]

(a) The impact of all bound states is not considered, except for the ground state, on the system's evolution.

(b) The depletion of the ground state is not considered.

(c) The electron in the continuum is treated as a free particle moving in the electric

field, with no influence from the parent potential.

Expressed in atomic units, the Schrödinger equation under the electric dipole approximation is formulated as follows

$$i\frac{\partial}{\partial t}|\Psi(\mathbf{x},t)\rangle = \left[-\frac{1}{2}\nabla^2 + V(\mathbf{x}) - \mathbf{E}(t)\cdot\mathbf{x}\right]|\Psi(\mathbf{x},t)\rangle, \tag{2.40}$$

where the time-dependent system wave function is denoted as $|\Psi(\mathbf{x},t)\rangle$, the atomic potential energy function is represented by $V(\mathbf{x})$, and the laser electric field is given by $\mathbf{E}(t)$.

The ionization occurs in the first step from the ground state $|0\rangle$ to continuum states $|u\rangle$, identified by the kinetic momentum of the outgoing electron

$$\boldsymbol{d}(\boldsymbol{v}) = \langle \boldsymbol{v}|\boldsymbol{x}|0\rangle. \tag{2.41}$$

The recombination, considered as the inverse process, is given by the complex conjugate, denoted as

$$\boldsymbol{d}^*(\boldsymbol{v}) = \langle 0|\boldsymbol{x}|\boldsymbol{v}\rangle. \tag{2.42}$$

In the continuum, the electron is treated as a free particle under the strong-field approximation (SFA). With a Keldysh parameter less than one, representing the tunneling regime, the time-dependent wave function is expanded as

$$|\Psi(t)\rangle = e^{iI_p t}\left(a(t)|0\rangle + \int d^3\boldsymbol{v}\, b(\boldsymbol{v},t)|\boldsymbol{v}\rangle\right), \tag{2.43}$$

where I_p is the ionization potential. $a(t)$ describes the ground-state $|0\rangle$ amplitude (or population) and is calculated using Eq.(2.32). $b(\boldsymbol{v},t)$ represents the amplitude of the continuum states $|\boldsymbol{v}\rangle$, i.e. the freed electron wave function in momentum space, given by the following equation

$$b(\boldsymbol{v},t) = i\int_0^t dt' a\left(t'\right)\boldsymbol{E}\left(t'\right)\cdot\boldsymbol{d}\left[\boldsymbol{v}+\boldsymbol{A}(t)-\boldsymbol{A}\left(t'\right)\right]e^{iS(\mathbf{p},t,t')}. \tag{2.44}$$

After solving the Schrödinger equation, the time-dependent dipole moment is calculated as

$$\boldsymbol{\mu}(t) = \langle\Psi(t)|\boldsymbol{x}|\Psi(t)\rangle. \tag{2.45}$$

By neglecting contributions from continuum-continuum transitions and setting $a(t) = 1$, the final expression for the dipole moment along an arbitrary direction n

is obtained as

$$\boldsymbol{\mu}_n(t) = i\int_0^t dt' \int d^3\boldsymbol{p}\times \\ \times \underbrace{[\boldsymbol{n}\cdot\boldsymbol{d}^*(\boldsymbol{p}-A(t))]}_{\text{recombination}} \times \underbrace{[\boldsymbol{E}(t')\cdot\boldsymbol{d}(\boldsymbol{p}-\boldsymbol{A}(t'))]}_{\text{ionization}} \times \underbrace{\exp\left[-iS(\mathbf{p},t,t')\right]}_{\text{propagation}} + \text{c.c.} \tag{2.46}$$

where the action S is described as:

$$S(\mathbf{p},t,t') = \int_{t'}^{t} dt'' \left(\frac{1}{2}\left[\mathbf{p}-\mathbf{A}(t'')\right]^2 + I_p\right), \tag{2.47}$$

with the canonical momentum $\mathbf{p} = \mathbf{v} + \mathbf{A}(t)$, and $\mathbf{A}(t)$ the vector potential corresponding to the laser electric field.

For the HHG production process the three steps are shown in Eq.(2.46): (1) The ionization of the atom by the laser field, where the transition from the ground state to the continuum occurs at time t'. (2) The electron propagation into the continuum where it acquires the phase factor up to the recombination time t. (3) The recombination of the electron at time t with the parent ion at ground state.

In this quantum mechanical picture, the cut-off energy of the harmonic spectra is determined by the following equation

$$\hbar\omega_{\text{cut off}} = 3.17U_p + I_p \cdot f\left(\frac{I_p}{U_p}\right), \tag{2.48}$$

which gives slightly higher value than that in the classical three-step model. The factor $f\left(\frac{I_p}{U_p}\right)$ is equal to 1.3 for $I_p \ll U_p$ and approaches unity for larger I_P.

The concept of short and long trajectories is justified by the quantum mechanical treatment. Indeed, it can be proven there is an infinite number of quantum paths that the recolliding electron can follow. However, for the same electron return energy, there are only two surviving quantum paths that result in a recollision with the parent ion during the first laser cycle. For these two paths, both ionization and recombination time instants are different. One of the paths lasts shorter time than the other and the paths are consequently termed short and long trajectories, respectively, as firstly treated in the classical treatment.

In the three-step model picture, the electron recollision process is repeated every half-cycle of the laser electric field. This periodicity is manifested in the frequency spectrum of the emitted photons as a comb of odd order harmonics. Specifically, as the harmonic order increases, there is initially a region in the frequency spectrum where the harmonics signal exhibits a decrease (lower order harmonics), followed by an extended region of harmonics with approximately the same efficiency (plateau),

and finally a region where the harmonics signal rapidly decreases (cutoff). This behavior can be obtained after taking the Fourier transform of Eq.(2.46), as shown in Fig.2.7.

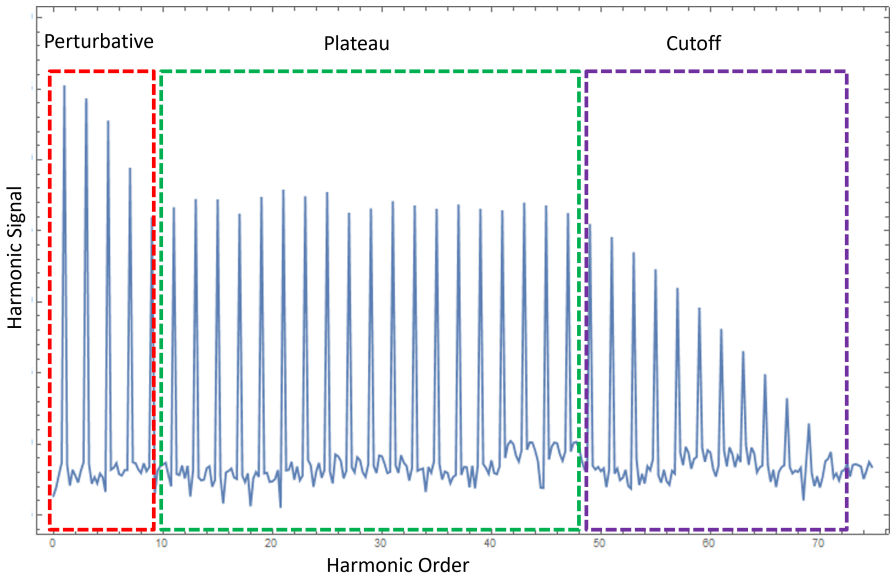

Figure 2.7
A typical harmonic spectrum, showcasing three distinct regions. The perturbative region is highlighted in red, the plateau region in green, and the cutoff region in blue.

As shown in Fig.2.7, in the initial perturbative region (red-boxed), low-intensity laser pulses ($<10\times10^{12}\,\mathrm{W/cm^2}$) interactions result in harmonic generation through multiphoton ionization. The harmonics intensity follows a linear decrease with increasing their order. As the laser intensity increases, entering the plateau region (green-boxed), the HHG process becomes more intricate. Intensified ionization of the medium leads to a plateau of high-energy harmonics, showcasing the complex interplay between the laser field and ionized electrons. Beyond a certain intensity in the cutoff region (blue-boxed), the gas medium becomes fully ionized. In this regime, the harmonic generation process deviates from the plateau behavior, displaying a cutoff that limits the maximum energy of the generated harmonics. This cutoff signifies the depletion of ground-state electrons and establishes the upper boundary for achievable harmonic energies.

2.2.3 Propagation and Phase Matching

The propagation of the q^{th} harmonic field, E_q, is described by the wave equation Eq.(2.49), derived assuming the slowly varying envelope and the paraxial approximations [45]

$$\nabla_{\perp}^2 E_q - 2\mathrm{i}k_q\frac{\partial E_q}{\partial z} = -\mu_0 q^2\omega_0^2 P_q \mathrm{e}^{-\mathrm{i}(qk_0-k_q)z} \tag{2.49}$$

with,

- $\nabla_{\perp}^{2} E_q$: The Laplacian of the transverse electric field E_q, representing the spatial variation of the electric field in the transverse direction.
- $2\mathrm{i}k_q \frac{\partial E_q}{\partial z}$: The rate of change of the electric field E_q with respect to the longitudinal coordinate z, related to the wave's propagation in the z-direction.
- $-\mu_0 q^2 \omega^2 P_q$: This term relates the following physical constants and parameters: μ_0, Permeability of free space, q: Harmonic order, ω_0: The fundamental laser angular frequency and, P_q: Polarization of the q^{th} harmonic.
- $\mathrm{e}^{-\mathrm{i}(qk_0 - k_q)z}$: Phase term, where k_0 is the wave number of the fundamental laser frequency, and k_q is the wave number of the q^{th} harmonic.

The coherent length is the distance over which the generated harmonics maintain a consistent phase relationship, exhibiting constructive interference. It is a measure of the spatial extent along the propagation direction where the high harmonics remain coherent. The coherent length is inversely proportional to the phase mismatch, Δk, the latter defined as

$$\Delta k \equiv q k_L - k_q \tag{2.50}$$

for the q^{th} harmonic order and for collinear generation geometry. The formula for coherent length L_{coh} is given by

$$L_{coh} = \frac{\pi}{\Delta k}. \tag{2.51}$$

In this expression, L_{coh} is a measure of the distance over which the harmonics generated maintain a coherent relationship.

Phase matching refers to the synchronization of the phases between the driving laser field and the emitted harmonic radiation. When the phases are appropriately aligned, the harmonics generated by the nonlinear interaction of the laser field with a medium add up coherently, leading to constructive interference. Phase matching conditions are affected by the following factors:

Geometry Effect (Δk_G)

As presented in Section 2.1.1, when a laser beam passes through the focus, the phase varies according to Eq.(2.5). The Gouy phase results in an increase in the fundamental phase velocity. The corresponding phase mismatch is given by [46]

$$\Delta k_{\mathrm{G}} = q\phi(z) = -\frac{qz_{\mathrm{R}}}{z^2 + z_{\mathrm{R}}^2} < 0. \tag{2.52}$$

Plasma Contribution (Δk_{plasma})

The presence of plasma introduces an additional factor to the phase matching condition. The index of refraction of plasma is

$$n_p\left(\omega_q\right) = \sqrt{1 - \left(\frac{\omega_p}{\omega_q}\right)^2} = \sqrt{1 - \left(\frac{N_e}{N_c(\omega_q)}\right)}, \tag{2.53}$$

where ω_p is is the plasma angular frequency given by

$$\omega_p^2 = \frac{N_e e^2}{\epsilon_0 m}. \tag{2.54}$$

N_e is the free electron density and N_c corresponds to the critical plasma density, indicating the point at which the plasma becomes fully absorbent to electromagnetic radiation with a frequency ω, given by

$$N_c = \frac{\varepsilon_0 m\omega^2}{e^2}. \tag{2.55}$$

If the plasma density is significantly smaller than the critical density ($N_c = 1.75 \times 10^{21}$ cm^{-3} for 800 nm laser radiation) we can use a linear approximation for the refractive index, resulting in

$$n_{\mathrm{plasma}}\left(\omega_0\right) \approx 1 - \frac{1}{2}\left(\frac{\omega_p}{\omega_0}\right)^2. \tag{2.56}$$

The contribution of the plasma to the wave vector can then be expressed as

$$k_{\mathrm{plasma}}\left(\omega_0\right) = \left(n_{\mathrm{plasma}}\left(\omega_0\right) - 1\right)\frac{\omega_0}{c} = -\frac{\omega_p^2}{2c\omega_0}. \tag{2.57}$$

For the wave vector mismatch, this results in [47]

$$\Delta k_{\mathrm{plasma}} = qk_{\mathrm{plasma}}\left(\omega_0\right) - k_{\mathrm{plasma}}\left(q\omega_0\right) = \frac{\omega_p^2\left(1 - q^2\right)}{2qc\omega_0}. \tag{2.58}$$

From the equation above, it is evident that the plasma's contribution to phase mismatching is negative.

Neutral Atoms Contribution ($\Delta k_{neutrals}$)

The dispersion contribution from neutral gas atoms, $\Delta k_{\text{neutrals}}$, is described as

$$\Delta k_{\text{neutrals}} = (n_0 - n_q)\,\frac{q\omega_0}{c}. \tag{2.59}$$

Here, $(n_0 - n_q)$ corresponds to the difference in refractive indices between the fundamental frequency n_0 and the q^{th} harmonic n_q. For the fundamental frequency, the refractive index n_0 exceeds 1, while for the harmonic frequencies beyond the ionization threshold, the refractive index n_q is less than 1, resulting in a positive contribution. If we include the ionization and pressure of the non-linear medium, Eq.(2.59) becomes

$$\Delta k_{\text{neutrals}} = (n_0 - n_q)\,\frac{q\omega_0}{c} p(1-\eta). \tag{2.60}$$

Here, p denotes the gas pressure and $\eta = \frac{N_e}{N_{\text{neutral}}}$ is the fraction of ionization, where N_e is the number of free electrons, and N_{neutral} is the number of neutral gas atoms.

Atomic Dipole Phase Mismatch (Δk_i)

The dipole phase results from the single-atom response to the laser electric field and relies on the electron's quantum path in the continuum, whether it is short or long trajectory. The atomic dipole phase mismatch is given by the equation [46]

$$\Delta k_{\text{i}} = \frac{\partial \Phi_{\text{i}}}{\partial I}\frac{\partial I}{\partial z}. \tag{2.61}$$

The parameter i can be s and ℓ, corresponding to the electron trajectory types, where 's' stands for short trajectories and 'ℓ' denotes long trajectories. The term $\partial\Phi_{\text{i}}/\partial I$ is calculated as

$$\frac{\partial \Phi_{\text{i}}}{\partial I} = \alpha_{\text{i}} - \gamma_{\text{i}} \left(q\omega_0 - \frac{I_{\text{p}}}{\hbar}\right)^2 \frac{1}{I^2}, \tag{2.62}$$

and $\partial I/\partial z$ can be derived from Eq.(2.22). Thus, Eq.(2.61) becomes

$$\Delta k_{\text{i}} = -\frac{2z\beta_{\text{i}}(z)}{z^2 + z_{\text{R}}^2}, \tag{2.63}$$

where

$$\beta_{\text{i}}(z) = \alpha_{\text{i}} I(z) - \frac{\gamma_{\text{i}}}{I(z)} \left(q\omega_0 - \frac{I_{\text{p}}}{\hbar}\right)^2 < 0. \tag{2.64}$$

The parameter γ_{s} is equal to $0.22\ \text{cm}_{\text{e}}/(\alpha\lambda)$, and $\gamma_\ell = -0.19\ \text{cm}_{\text{e}}/(\alpha\lambda)$, with α being the fine structure constant.

Considering all the above, the final expression for the phase matching conditions reads

$$\Delta k = \underbrace{\Delta k_{\mathrm{G}}}_{<0} + \underbrace{\Delta k_{\mathrm{plasma}}}_{<0} + \underbrace{\Delta k_{\mathrm{neutrals}}}_{>0} + \underbrace{\Delta k_{\mathrm{i}}}_{same\ sign\ as\ z} \quad . \tag{2.65}$$

For phase matching conditions, the intensity $|E_q|^2$ of the q^{th} harmonic within a non-linear medium of length L, assuming negligible absorption, is proportionally related to the squared *sin* function [48]

$$|E_q|^2 \propto \left| \frac{\sin(\Delta k L/2)}{\Delta k} \right|^2 . \tag{2.66}$$

Here, the *sin* function characterizes the interference pattern along the propagation distance. Optimizing experimental conditions to minimize the phase mismatch is crucial for enhancing the harmonic intensity in the non-linear medium.

Chapter 3

The Experimental Setup

3.1 The Laser System

The laser system employed in this study was the ZEUS, located at the Institute of Plasma Physics and Lasers (IPPL) of the Hellenic Mediterranean University [49]. ZEUS is a 45 TW laser system built upon the chirped pulse amplification (CPA) technology [2]. It has three amplification stages and delivers two beams: the first beam has a pulse energy exceeding 1 J, and the second a pulse energy of 10 mJ. The central wavelength of both beams is 807 nm, with an FTL pulse duration of 26 fs. The experiments in this thesis utilized the 10 mJ beam. As depicted in Fig. 3.1, the ZEUS laser system comprises the following components:

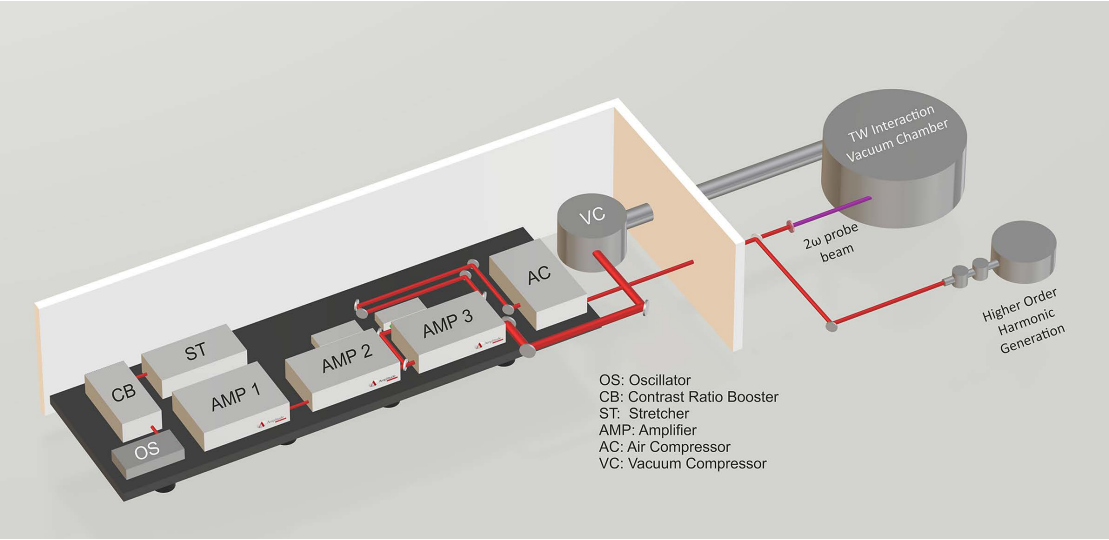

Figure 3.1
A 3D schematic layout of the ZEUS 45 TW laser system. (from Ref.[49])

Oscillator

The seed pulse in the laser system is generated by the oscillator. In this specific setup, a commercially available “Synergy Pro" oscillator manufactured by Femtolasers is employed for this purpose. Operation of the oscillator is based on self-mode-locking principles [50, 51]. The specifications of the oscillator are presented in Appendix A.

Booster

The booster module enhances the contrast ratio of the oscillator output by purifying the pulses with a saturable absorber, eliminating residual background noise, specifically amplified spontaneous emission (ASE). The primary components include a 20-pass multi-pass amplifier and a saturable absorber for ASE removal. Additionally, the booster incorporates a pulse picker, a Pockels cell that reduces the pulse train frequency from the initial 80 MHz oscillator pulse train to 10 Hz.

Stretcher

Stretcher is handling the increase in pulse duration to over 500 ps and the reduction of laser output intensity to prevent damage to the optics. The stretcher employed in this system is designed to mitigate on-axis comatic and chromatic aberration, potential causes of laser pulse distortion and reduced output quality. Comatic aberration, a type of lens distortion, and chromatic aberration, resulting from the wavelength-dependent behavior of light in an optical medium, are explained in detail in [52].

Regenerative Amplifier

The regenerative amplifier generates approximately 1 mJ stretched pulses at a rate of 10 Hz. It comprises two Pockels cells, with one seeding the stretched pulse into the resonant cavity and the other dumping the pulse at the maximum energy level. Synchronization and switching of the Pockels cells are performed by an electronic module, allowing precise control over the number of passes. Adjustment of the delay between the switch-in and switch-out times enables control over the number of passes, optimizing the conversion efficiency [53].

Multi-pass Amplifier

This thesis employs the output of the first multi-pass amplifier within the ZEUS laser system. This choice is made because intensities exceeding $10^{16}\,\mathrm{W/cm^2}$ do not result in XUV radiation generation. The multi-pass amplifier technique is widely used in laser systems to deliver high-power amplification. This method is preferred over other amplifier techniques due to its ability to produce high-intensity laser beams without affecting the beam quality. The multi-pass amplifier utilizes flat mirrors to reduce the risk of introducing optical aberrations into the beam.[54]

Compressor

The amplified pulses are directed toward the final component of the laser system, known as the compressor. Its objective is to decrease the pulse duration, approximating a duration close to the Fourier transform limit. Key components of the compressor include two flat gratings, each with a density of 1200 lines per millimeter [55]. In Fig.3.2 the principle of the operation of the compressor is illustrated.

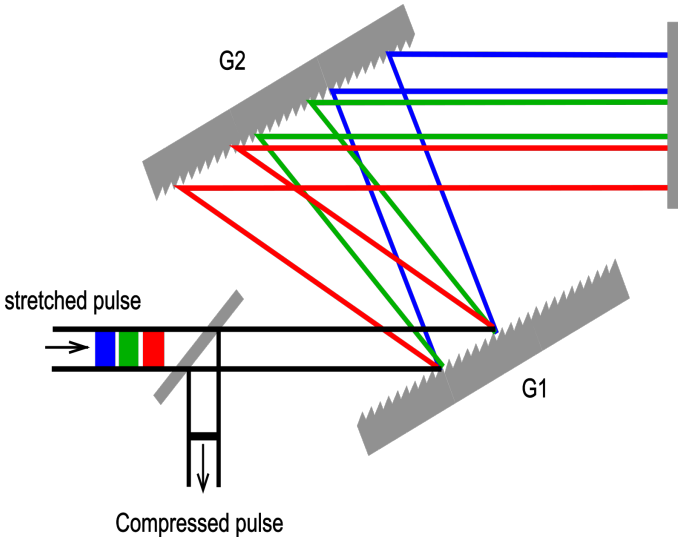

Figure 3.2
Compressor principle of operation. A pulse duration in the fs regime is achieved by introducing negative or positive chirp by adjusting the distance between the compressor gratings (from `https://commons.wikimedia.org/wiki/File:Schematic_drawing_of_a_stretcher-compressor.svg` , accessed March 2, 2024.).

In Fig.3.3 the principle of CPA operation, including all the above optical devices, is illustrated.

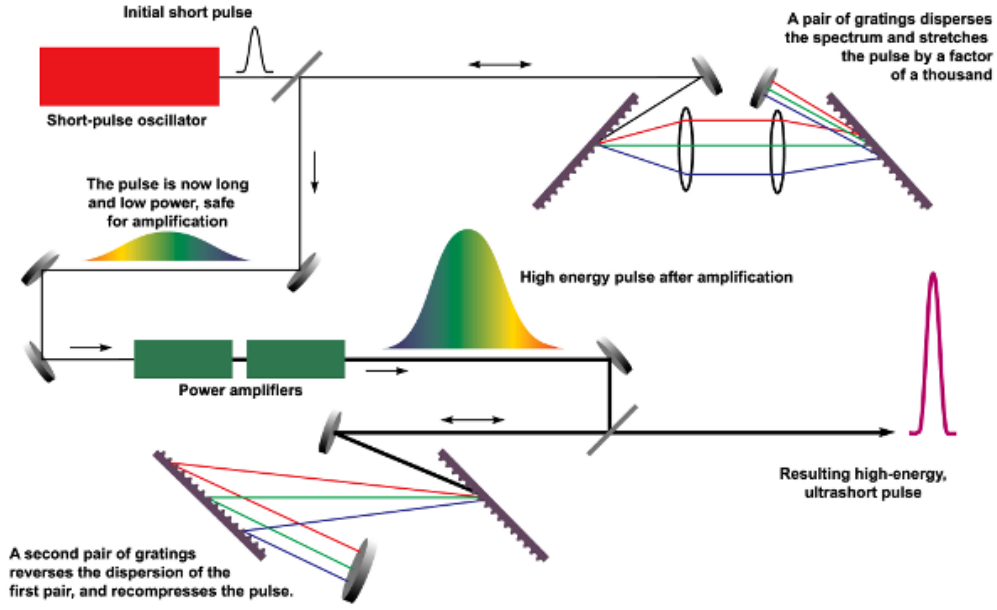

Figure 3.3
The operation principle of CPA. The chirped pulse undergoes stretching, amplification, and subsequent compression. The temporal spreading before amplification facilitates effective energy extraction without inducing damage to the amplifying medium, resulting in the creation of high-intensity, ultrashort laser pulses (from `https://commons.wikimedia.org/wiki/File:Cpa.png`, accessed March 2, 2024.).

Control and Monitoring System

The laser system's operations are primarily managed by computers and timing units, overseeing and coordinating various components throughout the system. Spectrum and beam quality monitoring occurs at multiple stages within the laser system. The principal controls include:

The Gepulse device (Fig. 3.4), tasked with:

- Regulating high voltage and triggering the 4 Pockels Cells (Pockels) at the Booster and Regenerative Amplifier (Regen).
- Managing shutters for the seed beam, the cavity of the Regen, and the shutter output of Amplifier-1 (Ampli1).
- Coordinating trigger signals for the acousto-optic modulators, Dazzler, and Mazzler.
- Overseeing the single-shot/burst-mode/frequency-divider shutter.
- Generating the 10 Hz clock signal through division of the Oscillator's pulse train (RF), used for all synchronizations.
- Supplying power to several photodiodes within the system.

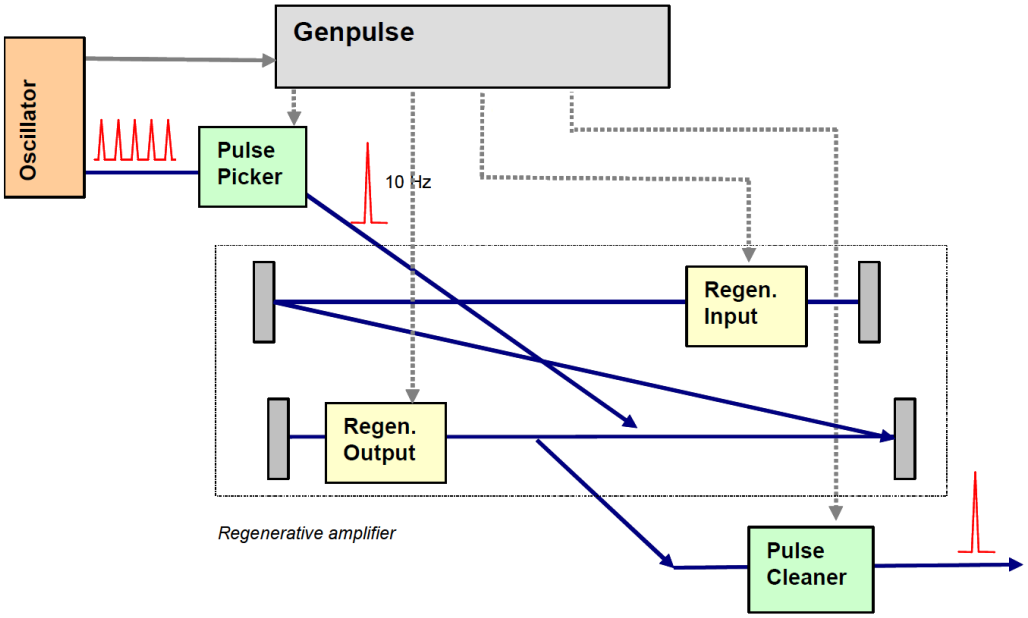

Figure 3.4
Genpulse Operation Diagram.

The MasterPulse device performs the following functions:

- Controls the trigger signals of the flashlamps and the Pockels Cells for all pump lasers, along with their associated shutters.
- Generates self-clock from the RF signal and the 10Hz trigger from GenPulse to eliminate synchronization jitter.
- Manages the trigger signals for all cameras within the system.
- Receives external interlocks from the Cryostat system and the Vacuum Compressor while verifying the consistency of the RF signal, with the ability to disable channels in case of a fault.

Spectrum and Pulse Duration Manipulation

The pulse duration after stretching is about 500 ps. At this point, an Acousto-Optic Programmable Dispersive Filter (AOPDF) device controls the spectral phase (chirp) of the infrared pulse. It is an acousto-optic programmable filter, named Dazzler, manufactured by Fastline company [56]. Its operation relies on collinear acousto-optic interaction, maximizing the interaction length. The AOPDF compensates for gain narrowing in amplifiers and phase distortions in the laser chain, resulting in compressed pulses approaching their transform limit. Additionally,

it enables arbitrary pulse shaping in both the temporal and spectral domains [57–60]. The operational principle is depicted in Fig. 3.5.

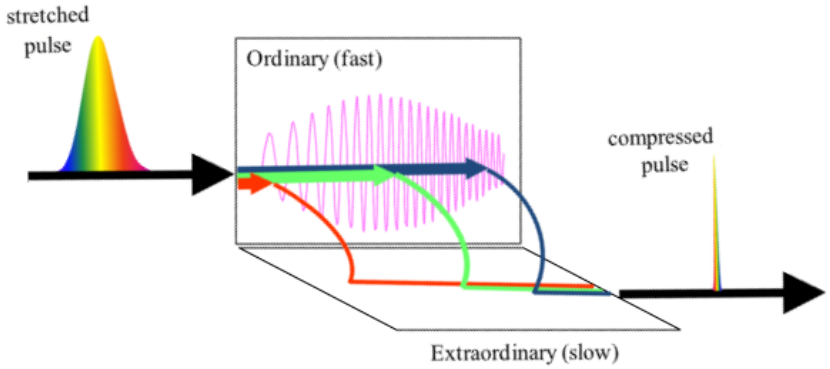

Figure 3.5
Principle of spectral phase and amplitude shaping by an acousto-optic programmable dispersive filter [61].

To manipulate the spectral amplitude, an Acousto-Optic Programmable Gain Control Filter (AOPGCF) is employed, named Mazzler, manufactured by Fastline company [56]. This device is integrated into laser systems to regulate the amplifier's gain. Positioned within the regenerative amplifier cavity, the AOPGCF serves the purpose of fine-tuning the gain of laser pulses, thereby compensating for the phenomenon of gain narrowing, which may manifest during the amplification of wide-bandwidth pulses. Facilitating programmable gain control, the AOPGCF allows for the optimization of pulse energy and stability. It operates in conjunction with other system components, including the AOPDF and measurement tools, employed for calibration and optimization objectives. By contributing to the enhancement of laser system stability and performance, the AOPGCF plays a pivotal role [61]. Figure 3.6 illustrates the spectrum shape following manipulation with the AOPGCF device.

The pulse duration measurement employs the Single Shot Autocorrelation (SSA) method with the assistance of the Bonsai device from Amplitude Technologies (see Fig.3.7(a)). The SSA method, shown in Fig.3.7(b), records the cross-distribution of second harmonic energy generated in the nonlinear crystal during the nonlinear interaction of two pulses with a defined aperture [62–64]. The duration of the laser pulses is obtained from the spatial distribution of the second harmonic (see Fig.3.7(c)).

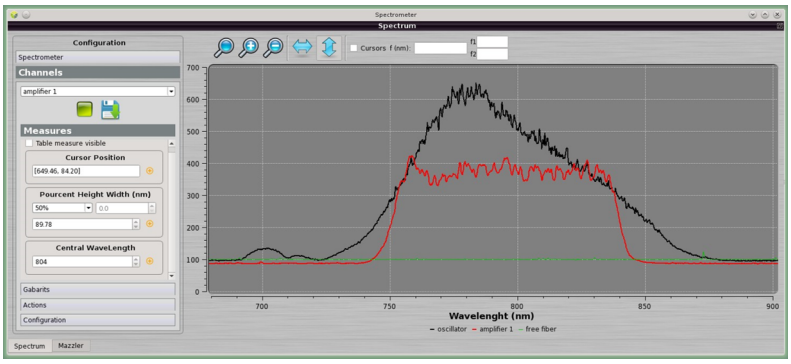

Figure 3.6
A typical spectrum measurement. The red line represents the spectrum of the beam at the output of the amplifier, while the black line corresponds to the oscillator output. In the amplifier spectrum, FWHM was measured at 89 nm with a central wavelength of 804 nm.

3.2 The Vacuum Chambers Manifold

The experimental setup consists of four stages depicted with letters A, B, C, and D as presented in Fig. 3.8.

The first stage, A, is the semi-infinite static cell filled with the gas target at pressures in the order of tens of mbar. Stage A is equipped with a tube manifold and a mechanical pump for evacuating and filling it with a variety of gases at accurately measured pressures during the experiment, as will be detailed later on. The laser IR laser beam is focused at the neighborhood of the exit of the semi-infinite cell which ends in a 100 μm thin copper foil. The foil is drilled by the laser beam creating an exit pinhole of about 100 μm in diameter. The laser IR beam along with the generated harmonic XUV radiation propagate through the drilled pinhole to the second and third stages of the setup. The plasma formation inside the semi-infinite gas cell can be imaged by a CCD camera.

The second stage, B, is a differentially pumped chamber, that separates the high-pressure first stage A from the third and fourth low-pressure stages. The entry aperture is the laser drilled pinhole at the exit of the semi-infinite cell, the small size of which minimizes the gas throughput. The exit aperture has a diameter of 3 mm that is wide enough to allow the propagation of the XUV radiation but simultaneously block a large part of the more divergent IR laser beam. Stage B is pumped by a 150 l/s turbomolecular pump reaching pressure values of $\sim 10^{-4}$ mbar in gas-cell operation conditions.

The third stage, C, is a 70 cm in diameter chamber that is pumped by a 350 l/s turbomolecular pump, thus reaching a background pressure of 1×10^{-6} mbar or of $\sim 10^{-5}$ mbar in gas-cell operation. Stage C hosts all the necessary optical and

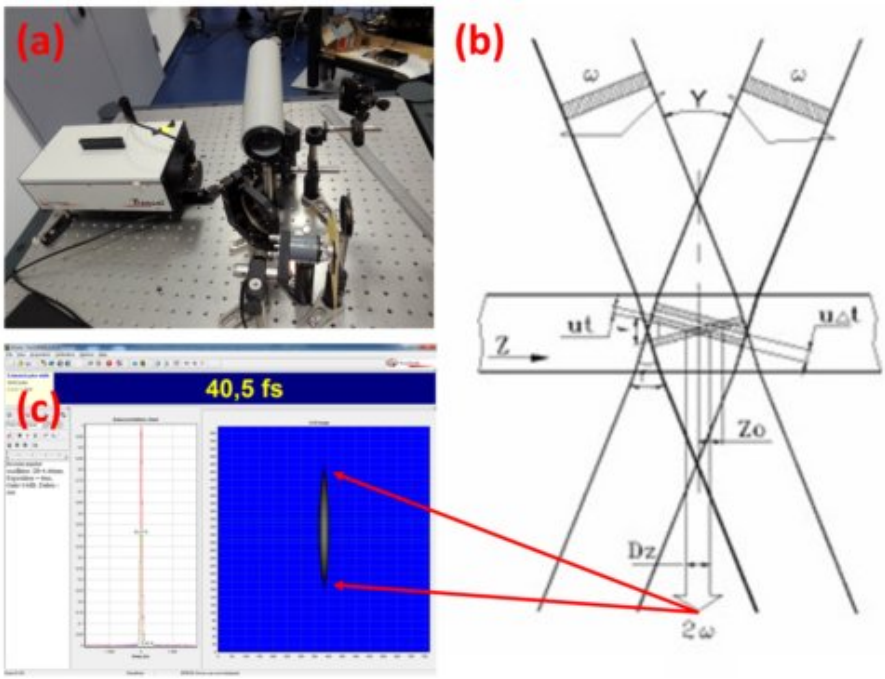

Figure 3.7
(a) The Bonsai device for measuring the duration of the laser pulse. (b) Principle of operation of the SSA method. (c) Typical measurement of a laser pulse.

optomechanical components for the automated optimization, filtering and selection of the HHG XUV wavelengths, and propagation of the resulting XUV beam to the target area at the fourth stage, as will be detailed later on.

The fourth stage, D, is an ISO 200 6-way cross attached to and pumped by the third stage. It hosts the target that is mounted on a variable in the three dimensions XYZ base as well as in the polar rotation angle Θ. The position of the target with respect to the laser focal area is accurately controlled by vacuum compatible steppers. The XUV radiation diffracted by the target is recorded at a vacuum compatible XUV CCD camera resulting in the coherent diffraction image.

3.3 High-order Harmonic Generation (HHG)

3.3.1 Laser Beam Optics

After exiting the compressor, the laser beam is directed toward the experimental setup. This stage has two primary objectives: firstly, to focus the laser beam, achieving the necessary intensity for generating XUV radiation, and secondly, to implement an initial filtration mechanism. Our study includes both solid (Gaussian) laser beams as well as annular beams. In the first case the filtering is done using a pair of Si wafers, while in the second a thin aluminum foil with a thickness of

Figure 3.8
The vacuum chambers manifold. A: The first stage hosting the semi-infinite gas cell. B: The second stage hosting the differentially pumped region. C: The third stage hosting the XUV filtering, diagnostics, and wavelength selection. D: The fourth stage hosting the target and diffraction imaging device.

400 nm is utilized, as described in Section 3.4.

To form an annular laser beam, the laser beam entering the setup at stage A, first encounters a 7 mm sphere designed to block its central part and create an annular beam. Positioned 38 cm before the focusing lens, matching the focal length of the focusing lens, this setup follows a principle where the lens focus shapes the field distribution. This process results in a clear image of the annular beam in the far-field [65–69].

Next, the laser beam passes through an iris used to control the beam radius. Although the iris's placement seems simple, its intricate effect on high harmonic generation requires investigation [70]. We conduct a detailed analysis of this parameter in Chapter 4 to fully investigate its effect on HHG. A mechanical shutter, connected to the XUV camera, is positioned prior the iris to block the laser beam during camera readout. In addition, a 300 μm thick glass plate is also placed after the shutter, driving the small fraction of the reflected laser beam at an alignment point located at about 3 m away. Thus, the daily alignment of the beam can be reproduced easily and with high accuracy.

The laser beam goes through a focusing lens with a focal length of 38 cm, set on a three-dimensional micro-metric stage, and through the entry window of the HHG production chamber into the interaction area. To prevent material damage and non-linear effects, the window is positioned 32 cm away from the laser's focus. It is also tilted to avoid any damage from focus back-reflection, as shown in Fig.3.9. Then, the laser beam enters the subsequent chamber to interact with the gaseous medium, producing XUV radiation.

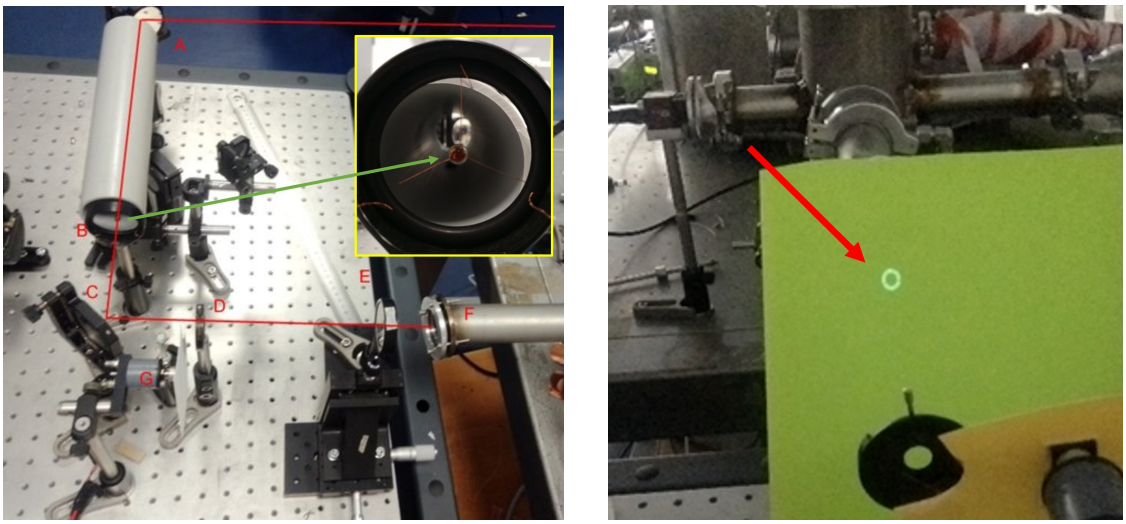

(a) (b)

Figure 3.9
(a) Annular beam formation and beam focusing. A,C: steering mirrors. B: beam block. D: iris. E: focusing lens. F: entrance window. G: shutter. (b) Annular beam indicated with the red arrow.

3.3.1.1 Mechanical Vibration Tests

The development of the coherent XUV source, studied here, has applications on diffraction imaging of micro- and nano-structures. Given the demanding nature of imaging such structures, ensuring the spatial stability of the source is crucial. Therefore, this study focuses on recording and controlling vibrations of the setup. The aim is to determine if these vibrations adversely affect the final display to an unacceptable extent, enabling necessary actions to mitigate their impact.

The experimental setup for characterizing the HHG source is depicted in Fig.3.10a. The laser beam enters stage A, the semi-static cell filled with Ar gas, to produce coherent XUV radiation. The produced XUV radiation along with the laser beam propagate through the differential pumping chamber, stage B, to stage C. There, the laser beam undergoes filtration using the system of two Si wafers. Subsequently, the transmitted 3^{rd} harmonic beam is directed using a metal mirror and a quartz lens, to focus it onto the surface of the CCD camera mounted externally. To safeguard the camera and block the residual IR radiation, a bandpass optical filter was employed.

The experimental assessment of the optical drive system's tolerance to mechanical vibrations was conducted in two parts. Firstly, to detect vibrations originating from the laboratory environment, such as building mechanical installations, measurements were taken with the electromechanical components of the setup, such as vacuum pumps, turned off. The CCD camera was synchronized with the 10

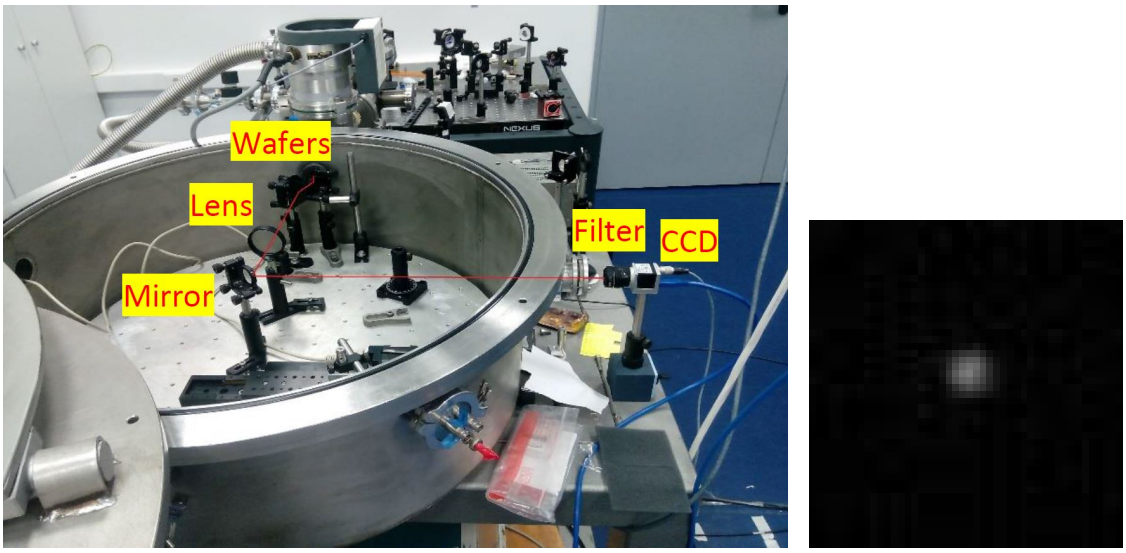

(a) (b)

Figure 3.10
(a) Experimental setup for detecting mechanical vibrations. (b) Typical CCD image showing the spatial distribution of the 3^{rd} harmonic.

Hz repetition rate of the laser. Secondly, to detect vibrations stemming from the electromechanical components, such as vacuum pumps, the latter were activated, and measurements were taken in vacuum conditions. The optical setup was the same for both measurements.

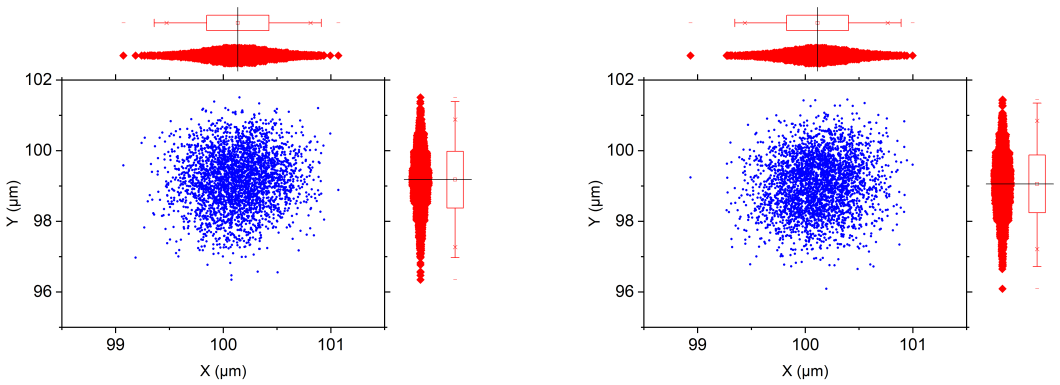

(a) (b)

Figure 3.11
Maximum intensity positions for a series of 3000 consecutive pulses with the electromechanical parts of the experimental setup: (a) disabled, (b) activated. The numbers on the axes are the mean value of multiple measurements.

A series of images was recorded, comprising 3000 consecutive frames per part, to observe the spot of the 3^{rd} harmonic. Subsequently, for each image the maximum intensity position was determined. Figure 3.11 displays the calculated positions of the centers, with the axes calibrated in pixels. For the first part, the standard deviation along the X-axis was 0.289 pixels or 0.636 µm, while for the Y-axis, it

was 0.804 pixels or 1.77 μm (refer to Fig.3.11a). In the second part, the standard deviation along the X-axis was 0.286 pixels or 0.629 μm, and along the Y-axis, it was 0.818 pixels or 1.80 μm (see Fig.3.11b). The results indicate that vibrations in both parts remain well below 1 μm and 2 μm for the X- and Y-axis, respectively, corresponding to a negligible percentage relative to the diameter of the beam.

3.3.2 The Pulsed Gas Jet

Initially, an attempt was made to use a pulsed gas jet target using an electically driven pulsed valve, shown in Fig. 3.12(a) and (b). The pulsed valve was developed in the Atomic and Molecular Physics laboratory of the Department of Physics of University of Ioaninna. This apparatus utilized a 25 mm diameter piezoelectric crystal mechanically coupled to a nozzle, regulating the 1 mm diameter gas exit orifice. Housed within a 70 mm diameter cylindrical steel chamber, the crystal and orifice mechanism also served as the reservoir for the pressurized gas intended for expansion into the production chamber [71]. The pulsed valve was electrically driven by the controller shown in 3.12(c). The valve was placed in the HHG production chamber. A glass viewing window was placed at the top of the chamber allowing for the observation of plasma generation resulting from the interaction between the laser beam and the gas.

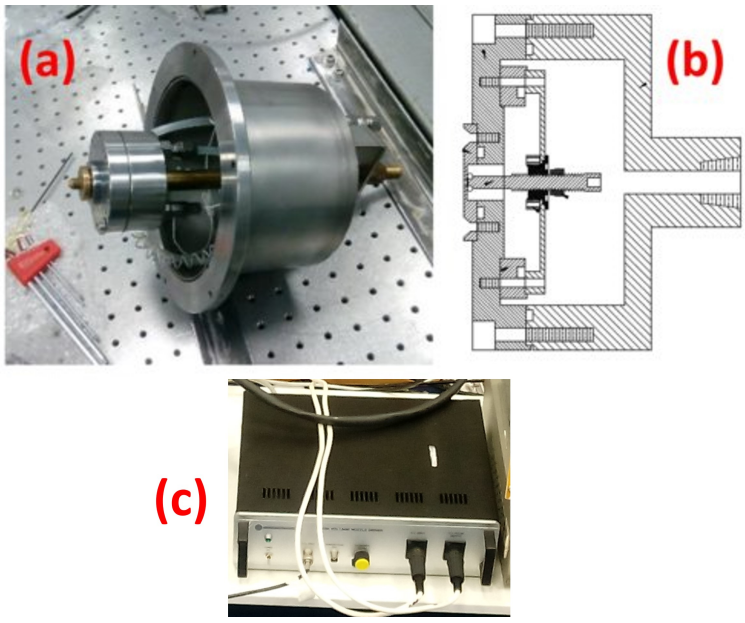

Figure 3.12
Pulsed gas jet valve (a) The pulsed gas jet valve. (b) Cross section of the valve (c) Pulsed valve driving unit.

To achieve optimal conditions for HHG, it was necessary to synchronize the laser pulse arrival at the nozzle with the gas jet expansion. This synchronization was

attained by electronically triggering the pulsed nozzle driver with the laser clock and introducing a precise time delay for the nozzle activation. Fig.3.13 illustrates the synchronized plasma generation resulting from the interaction of the laser beam with the argon gas jet.

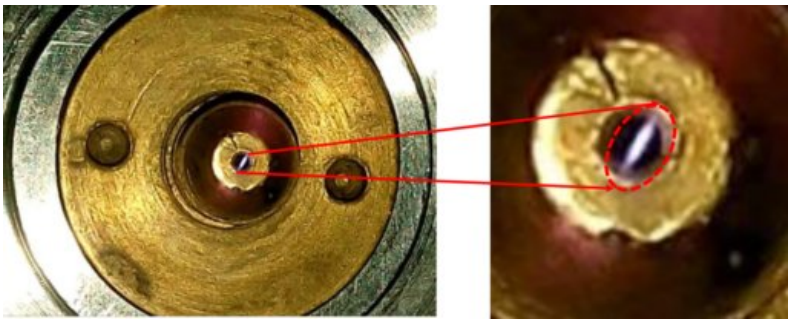

Figure 3.13
Pulsed gas jet nozzle and plasma formation from the interaction of the laser focused beam with the argon gas.

However, during the ongoing efforts to enhance high harmonics production, it became evident that the pulsed nozzle exhibited small variations in its repeatability. To address this issue, an interferrometric Mach-Zehnder optical setup was built to spatially visualize the gas jet during nozzle activation and estimate its pressure. Fig. 3.14(a) illustrates the Mach-Zehnder interferrometer while in Fig. 3.14(b) a typical interferometric image is shown, demonstrating the fringes variation around the nozzle area. From the analysis of a series of such interferometric images it became evident that the constraint of high stability conditions, necessary for HHG, was not fulfilled. Thus, the idea of using a pulsed gas jet was abandoned and instead the idea of replacing it with a semi-infinite gas cell was promoted.

3.3.3 The Semi-infinite Gas Cell

The semi-infinite gas cell was developed in the Atomic and Molecular Physics laboratory of the Department of Physics of University of Ioaninna, and it is shown in Fig.3.15. The gas cell consists of a small chamber, the one edge of which is the entry window for the laser beam and the other edge bears a 1.5″ aluminum tube that has a replaceable thin copper foil, approximately 100 μm thick. The laser beam passes through the optical window, and it is focused on the thin copper foil, thus opening an aperture of the size of its focal spot, i.e. about 100 μm. The location of the laser beam focus in the neighbor of the drilled pinhole area can be varied, by moving the lens micrometrically along the laser propagation axis. The minute size of the aperture minimizes the gas throughput, necessary for the pumping conditions of the rest of the setup as will be cleared later on. This

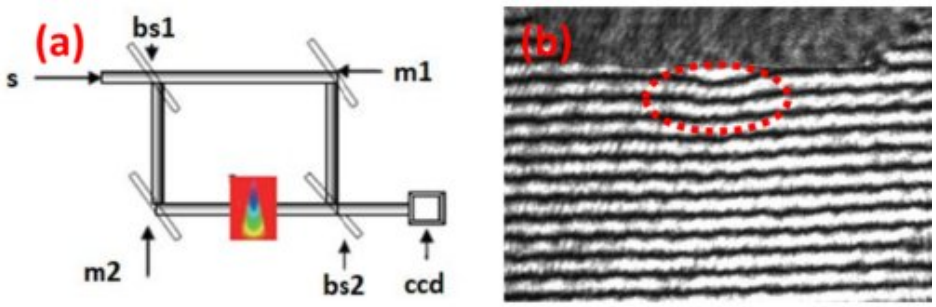

Figure 3.14
(a) A standard Mach-Zehnder configuration: The incident laser beam splits (S) into two branches using beam splitter bs1. The first branch reflects off mirror m1, with a portion directed through beam splitter bs2 to a CCD camera. The second branch reflects off mirror m2, passes through the gas jet, and a portion reaches the camera through beam splitter bs2. The camera captures the intersection image of the two branches, which changes as the optical path of the second branch is affected by variations in the refractive index caused by the presence of gas. (b) Interferometric image highlighting the observable bending of interference fringes within the region delineated by the oval shape with the dotted line.

region is the locus for radiation-matter interaction leading to the generation of the XUV radiation. Subsequently, the laser beam along with the XUV radiation, exits through this aperture and propagates to the subsequent components of the experimental setup. This configuration adheres to the principles of the semi-infinite cell [**Peatross2009**, 72].

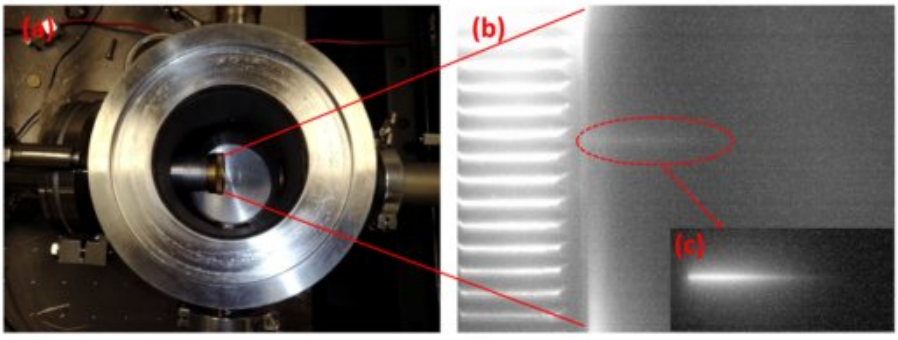

Figure 3.15
(a) Top view of the semi-infinite gas cell. (b) Plasma formation from the interaction of the laser beam with atmospheric air. (c) The plasma formation area after background subtraction.

The key feature of the semi-infinite cell is that the pressure can be controlled and kept at a certain constant value throughout the measurement. The gas target pressure control system is illustrated in Fig. 3.16. Initially, all shut valves V1, V2, V3, V4, and V5, the gate valve GV, as well as the needle valve NV, are open and the gas in the interaction chamber is pumped through tubes T1 and T4 by the mechanical pump (tube T3). Similarly, tube T1, which is connected to the supply gas tank, can be evacuated through valves V5 and V3 if necessary. Otherwise, valves

V1 and V5 remain closed. After pumping the chamber (pressure gauge indication about 10^{-2} mbar), we close valves V2, V3, V4, and V5 and leave valve V1 open. The gas flow to the chamber is regulated with the needle valve NV to a constant value no higher than 100 mTorr for the current measurements.

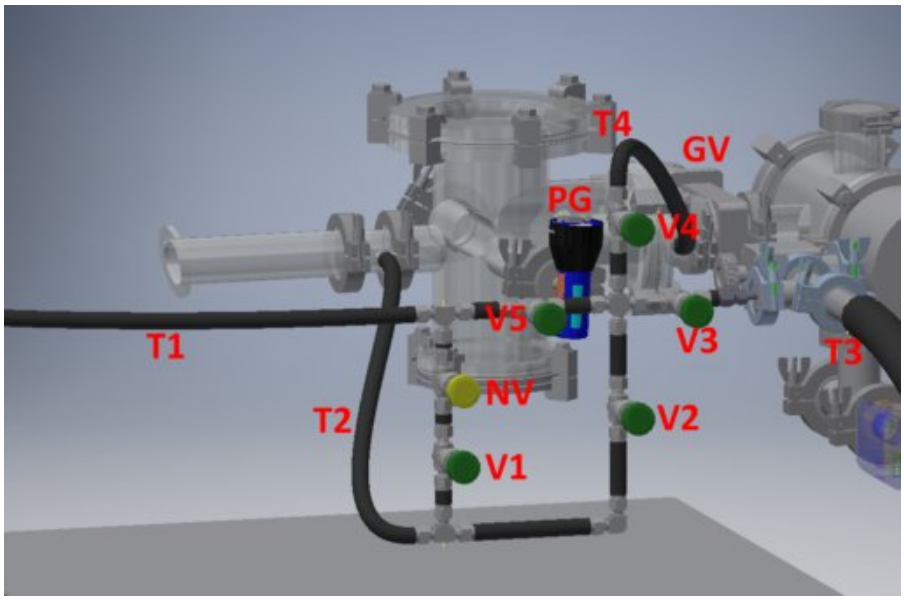

Figure 3.16
HHG production chamber manifold. T1: Gas supply to the manifold. V1-V5: Shut valves. F: Gate valve, NV needle valve. PG: Low pressure gauge.

The gas, after interacting with the laser, passes into the differential pumping chamber, stage B, where it is pumped by the 150 L/s turbomolecular pump. Stages B and C are connected with a 3 mm diameter aperture, which is wide enough to allow the propagation of the XUV radiation and at the same time support the differential pumping.

Since the propagation of XUV radiation must take place in a vacuum to avoid absorption and scattering effects, all components involved in the path of XUV radiation are located in chambers where the pressure is on the order of 10^{-6} mbar. In addition, the XUV camera should be at a temperature of about $-40\,^{\circ}$C so the vacuum is necessary to avoid condensation on the ccd sensor or to avoid the formation of oxides on optical and film surfaces, or the sensitivity and protection of the MCP sensor.

3.4 HHG Diagnostics and Wavelength Selection

The harmonic spectroscopy including filtering, optimization, and wavelength selection, takes place in stage C. The XUV harmonic beam is first filtered by

the residual IR radiation and then the appropriate wavelength is selected. Below we will describe each step of IR filtering and XUV wavelength selection.

3.4.1 IR Filtering

Following the generation of XUV radiation and an initial filtering of the infrared component by the 3 mm aperture between stages B and C, the combined IR and XUV beam is introduced into stage C. Depending whether we use an annular or solid laser beam, two different IR filtering ways were used. For solid laser beams a pair of silicon (Si) wafers were employed, while for the annular beam a thin aluminum filter was adequate. Below both approaches are detailed.

3.4.1.1 Silicon Wafers

The laser beam is p-polarized, and thus results in optimal transmission through a Si wafer when it is oriented at Brewster angle for the laser wavelength [73]. Thus, Si wafer acts as a filter that blocks the reflection of the IR laser wavelength while it reflects the XUV radiation with a reflectivity of about 60%. For minimizing the presence of the IR beam two pairs of Si wafers were used in a parallel geometry that results in a parallel displacement of the entrance beam, as shown in Fig.3.17a.

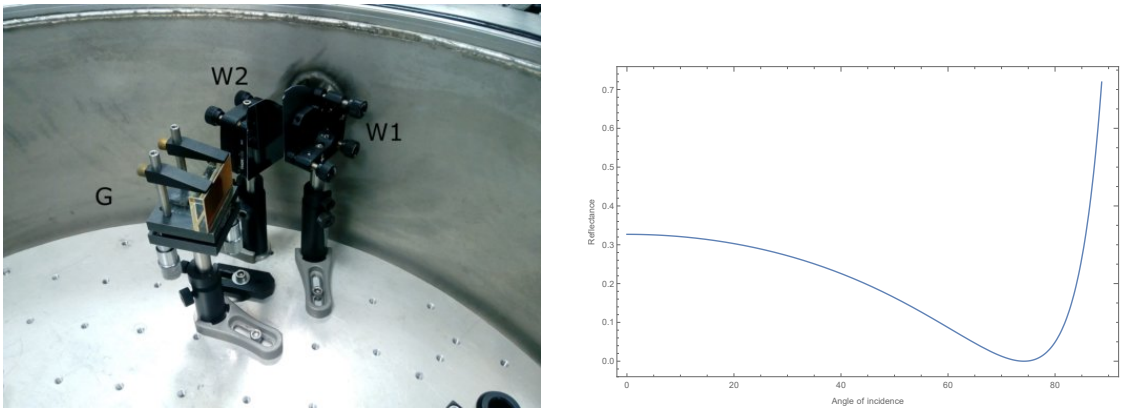

(a) **(b)**

Figure 3.17
Silicon wafer filters. (a) Two silicon wafers, W1 and W2, are positioned at Brewster angle for the IR beam to facilitate the filtering of the IR radiation. The subsequent element in the optical sequence (G) corresponds to the flat-field diffraction grating. (b) Reflectivity of a Si wafer for P-polarized radiation at 800 nm as a function of the incident angle. The minimum value corresponds to an angle of 74.8°.

The reflectivity for the pair of Si wafers can be estimated as follows. The Brewster angle θ_B is determined as

$$\theta_B = \arctan\left(\frac{n_{\mathrm{Si}}}{n_{\mathrm{V}}}\right), \tag{3.1}$$

where n_{Si} is the refractive index of silicon, and n_{V} is the refractive index of vacuum [73]. For silicon, with a refractive index of $n_{\mathrm{Si}} = 3.673$, and for a wavelength of 800 nm, Brewster angle is calculated to be 74.8°, in agreement with the literature [74]. The reflectivity of a Si wafer at Brewster angle can be calculated using the Fresnel equation for p-polarization, which describes how light is reflected and transmitted at the interface between two media with different refractive indices

$$R_p = \left| \frac{n_{Si}\cos(\theta_i) - n_V\cos(\theta_t)}{n_{Si}\ cos(\theta_i) + n_V\cos(\theta_t)} \right|^2, \tag{3.2}$$

where R_p is the reflectivity for p-polarization, $\theta_i = \theta_B$ is the angle of incidence (Brewster angle), and θ_t is the angle of transmission, which is calculated using Snell's law

$$\theta_t = \sin^{-1}\left(\frac{n_V}{n_{Si}}\sin(\theta_i)\right). \tag{3.3}$$

By combing Eqs. (3.1), (3.2), and (3.3) for the current experimental parameters, the IR reflectivity diminishes to 1.8×10^{-6} of its initial value, thereby achieving an adequate IR filtering. In Fig.3.17b, the Si wafer reflectivity for a p-polarized laser beam is presented as a function of the incident angle, depicting the minimum of reflectivity at Brewster angle of 74.8°.

3.4.1.2 Aluminum Thin Foil

For the case of the annular IR beam, due to the reduced residual IR radiation, the use of Si wafers is not necessary. Instead, a thin aluminum foil with a thickness of 400 nm was introduced in the beam after entering stage C, thus blocking the IR radiation. It should be noted here a solid IR beam would have damaged the aluminum thin foil.

As shown in Fig.3.18b, the aluminum thin foil essentially blocks the IR wavelengths, but has a transmission for the XUV wavelengths of interest here (30-50 nm) of about 40% [75]. This makes aluminum foil an ideal choice for further clearing the XUV radiation from the residual IR radiation. The noticeable drop in the transmission around 70 nm offers a valuable feature for harmonics wavelength calibration.

As illustrated in Fig. 3.18a, the aluminum filter is positioned on a motorized platform, which serves the purpose of moving the filter from its initial position to a secure nest. This relocation minimizes the risk of breakage due to air currents generated during the chamber's evacuation or venting processes.

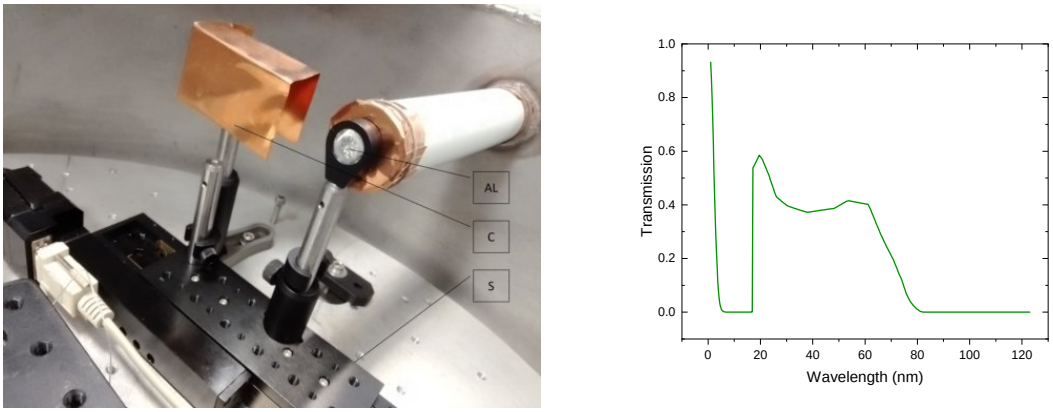

(a) (b)

Figure 3.18
Aluminum filter. (a) 400 nm-thick aluminum filter integrated into the experimental setup. AL: Aluminum foil. C: Filter nest designed to mitigate potential airflow-induced damage during chamber pumping or venting. S: Motorized Stage. (b) Transmission curve of an aluminum foil with thickness of 400 nm (Calculated using the tools provided at the The Center for X-Ray Optics, Lawrence Berkeley National Lab, `https://henke.lbl.gov/optical_constants/gastrn2.html`, accessed August 13, 2023.).

3.4.2 HHG Spectral measurements

Spectral measurements are accomplished with the use of a diffraction grating, where the XUV radiation is diffracted towards a detector for recording its spectrum. Here, two different detectors were used: (a) An MCP equipped with a slit and placed on a traveling stage to record the total XUV spectra. (b) An XUV CCD camera to obtain the image (wavelength and angular divergence) of a part of the total XUV spectra. Below we describe the principle of operation and use of the diffraction grating, as well as the two types of HHG XUV spectral measurements.

3.4.2.1 Diffraction Grating

The spatial separation of the XUV radiation spectrum was achieved using the grazing-incidence, flat-field diffraction grating (model 001-0639, Hitachi [76]). The dimensions of the grating are $50 \times 30 \times 10$ mm with the long dimension having a concave geometry with a radius of curvature of 5649 mm. The diffracted radiation is focused onto a plane without requiring additional optics, thus minimizing energy losses. The grating is gold plated and has variable distance grooves with the median being at 600 lines per mm, a feature that allows for a flat field imaging. The grating supports a wavelength dispersion efficiency ranging from 22 nm up to 124 nm.

The values of the parameters of the grating geometry in use, shown in Fig.3.19, are r, r', L equal to 350, 469 and 110.16 mm, respectively. The distance between the diffraction grating and the plane of XUV radiation foci, r', is related to the

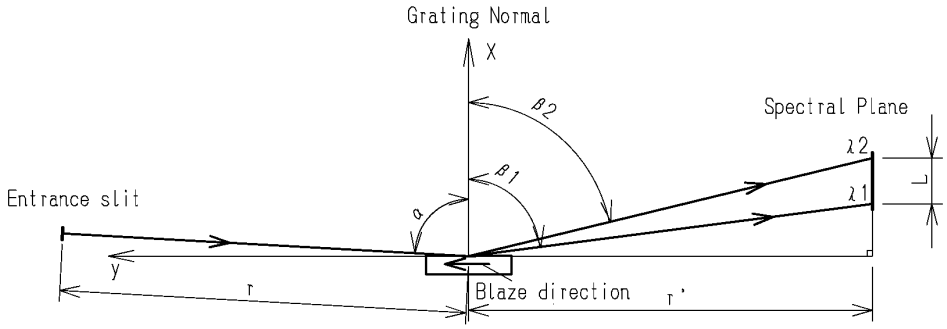

Figure 3.19
Optical geometry for the diffraction grating. r: Distance between entrance slit and diffraction grating. r': Distance between the diffraction grating and the plane of XUV radiation foci. α: Angle of incidence of radiation. β: Angle of diffraction of radiation. L: Distance corresponding to the limits of the range of the diffracted XUV radiation.

optical and geometrical parameters of a grating by Eq.(3.4) [77]

$$r' = \frac{rR\cos^2\beta}{r\left[\cos\alpha + \cos\beta - 2\left(\sin\alpha + \sin\beta\right)b_2\right] - R\cos^2\alpha}, \tag{3.4}$$

where R is the radius of curvature, and b_2 is a parameter related to the density of grooves, σ, described by Eq. (3.5)

$$\sigma = \frac{\sigma_0}{1 + \frac{2b_2}{R}\omega + \frac{3b_3}{R^2}\omega^2 + \frac{4b_4}{R^3}\omega^3 + \cdots}, \tag{3.5}$$

where b_2, b_3 and b_4 are parameters of variation of the distance between the grooves and σ_0 is the density of grooves at the middle of the grating, i.e. for $\omega = 0$ [77–79]. According to the manufacturer, the values of the above parameters are -8.9, 86.3, -1349 for b_2, b_3, b_4, while for R and σ_0 the values are 5649 mm and $1/600mm$, respectively. The manufacturer suggests for the placement the values $r = 350mm$ and $\alpha = 85.3°$. The diffraction angle β results from the basic relation of diffraction gratings

$$Gm\lambda = \sin\alpha + \sin\beta \tag{3.6}$$

as

$$\beta = \arcsin\left(Gm\lambda - \sin\alpha\right), \tag{3.7}$$

where G is the density of the grooves, which for the case varying as here, is equal to σ_0, m the order of diffraction and λ the wavelength of the incident radiation. Also, the manufacturer provided the efficiency curve as shown in Fig. 3.20 which agrees with the one calculated by the program REFLECT [80–82].

From Eqs. 3.4, 3.5, 3.6 and 3.7 the distance r' and the corresponding angle β

can be calculated, thus defining the focal point (x,y) in a XY plane at the detection area. Therefore, for each incident angle and wavelength a focal family of focal curves can be obtained. Such a study is presented in Fig. 3.21 (green lines) for a distance r of 350 mm (location of the entry slit). Additionally, in Fig. 3.21, the location of the XUV wavelengths is also presented (red lines).

According to Fig. 3.21, the grating was placed at a distance of 469 mm from the center of grating, and with an incident angle of 85.3°, in accordance with the suggestion of the manufacturer. The placement and alignment of the grating were facilitated by implementing the aforementioned grating equations as well as the setup spatial limitations into a CAD software.

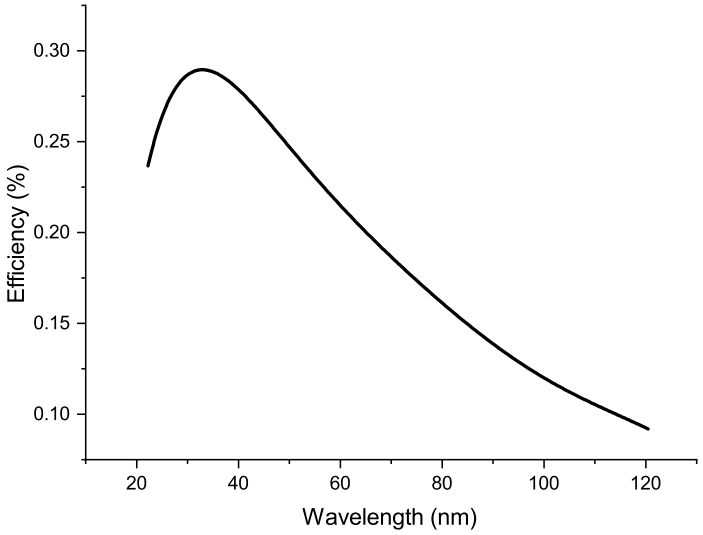

Figure 3.20
The efficiency curve of Hitachi 001-0639 diffraction grating.

3.4.2.2 HHG Spectra

Initially, the recording of the full range XUV spectra (i.e., from 22 to 124 nm.) was done using a 1″ in diameter MCP with 1 mm entry slit (see Appendix B for details), mounted on a motorized linear stage, placed at the area of grating focal plane. In Fig.3.22a, the optical setup, including the Si wafers, the diffraction grating, and the MCP, developed in stage C is presented. The spectra were recorded by stepping the MCP along the focal regions of the generated harmonics. The whole spectrum supported by the grating is recorded during one travel of the stage ($\simeq$5 min duration) with an adequate spectral resolution $\Delta\lambda \sim 0.02$ nm. It should be noted that the efficiency of the MCP for the laser wavelength of 800 nm, is below

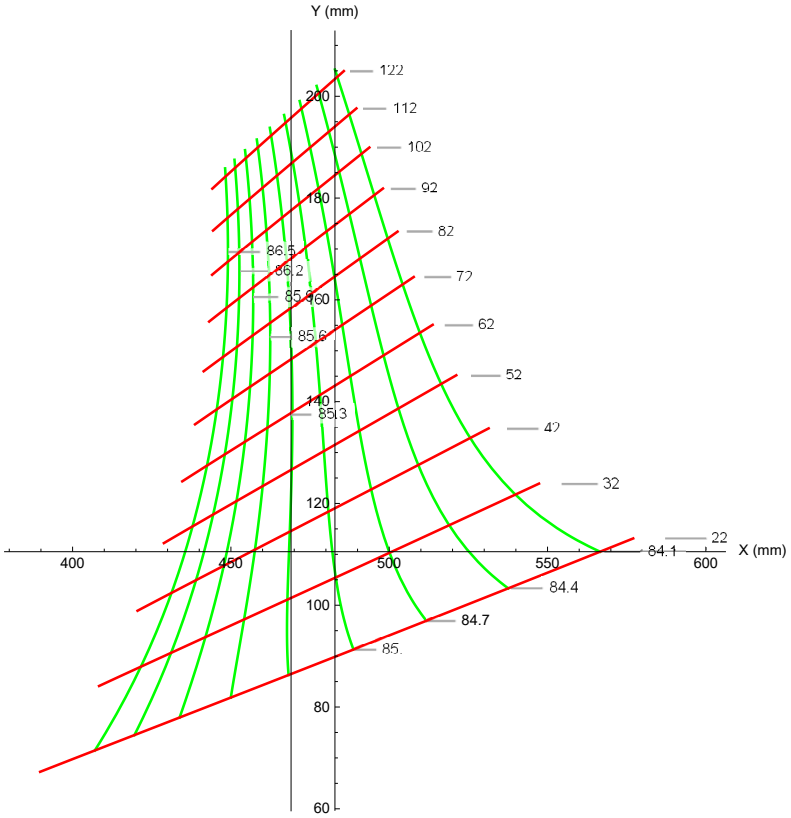

Figure 3.21
The focal curves of Hitachi 001-0639 diffraction grating. The green lines correspond to the focal curves resulted as a function of the incident angle and wavelength. The corresponding red lines show the location of certain XUV wavelengths. The vertical black line shows the suggested XUV sensor position. The coordinates (x,y) are the distances from the center of the grating on a detection plane XY.

1%, and considering the filtering of the Si wafers, the residual IR radiation does not add any noise in the measurements.

The MCP signal was sent to an oscilloscope (model DPO 7104, Tektronix) via an in vacuum RC circuit. A LabVIEW program was developed to control the measurement and record the XUV signals from the oscilloscope in an automated way. A typical measurement of a harmonic spectrum in the LabVIEW acquisition environment is shown in Fig.3.22b. Details about the LabVIEW acquisition program are given in Appendix C.

3.4.2.3 HHG Image Spectra

The setup for the measurement of the image harmonic spectra is the same as in Fig.3.22a, with the MCP replaced by the XUV CCD camera (XUV CCD1) and the necessary angular adjustments in the Si wafers and the grating to maintain the same incident angle α. The XUV CCD camera is a high quantum efficiency 16-bit XUV vacuum CCD camera (Raptor Photonics, Eagle XO) with a sensor

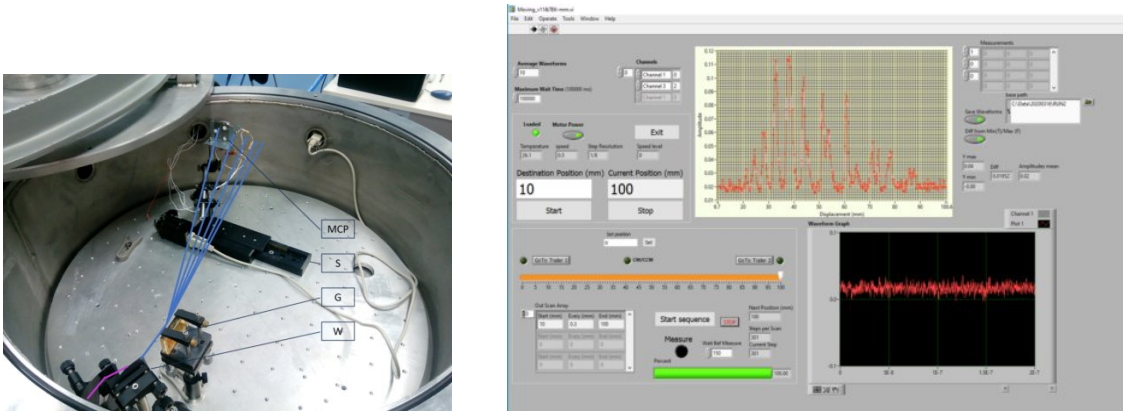

(a) **(b)**

Figure 3.22
(a) Optical experimental configuration employed to record total spectral region utilizing an MCP detector positioned on a movable stage (S), traversing the harmonic focus zone, depicted by the blue lines. G: Diffraction grating, W: Silicon wafers in Brewster angle. (b) Typical entire harmonic spectrum measurement in the LabVIEW acquisition environment.

having 2048 pixels (27.65 mm) at the grating diffraction axis and 512 pixels (6.90 mm) at the XUV divergence axis (perpendicular to the grading diffraction axis). The positioning of the grating was accomplished utilizing CAD, as illustrated in Fig. 3.23(a), where the grating equations from subsection 3.4.2.1 were employed for the geometry of the stage C. The CAD design was vital in determining the orders of the harmonics measured experimentally, as demonstrated in Fig.3.23(b). For this, the harmonic spectra were measured at low gas pressure and the lowest allowed laser intensity to avoid spectral shifting effects. The optimum overlap of the experimental imaged HHG spectra with the outcome of the CAD outcome for the harmonic order location, was the cornerstone for the optimum arrangement of the optical setup as well as the absolute wavelength calibration of the HHG spectra.

A typical measurement of the image of the HHG harmonics with the XUV camera is presented in Fig. 3.23(c). The XUV grating and XUV CCD detector allow for a relatively high spectroscopic resolution from ∼80 to ∼100 pixels per 1 nm, on the CCD, for the spectral region of interest. This resolution is a significant experimental tool for optimizing the quality and characteristics of the XUV beam.

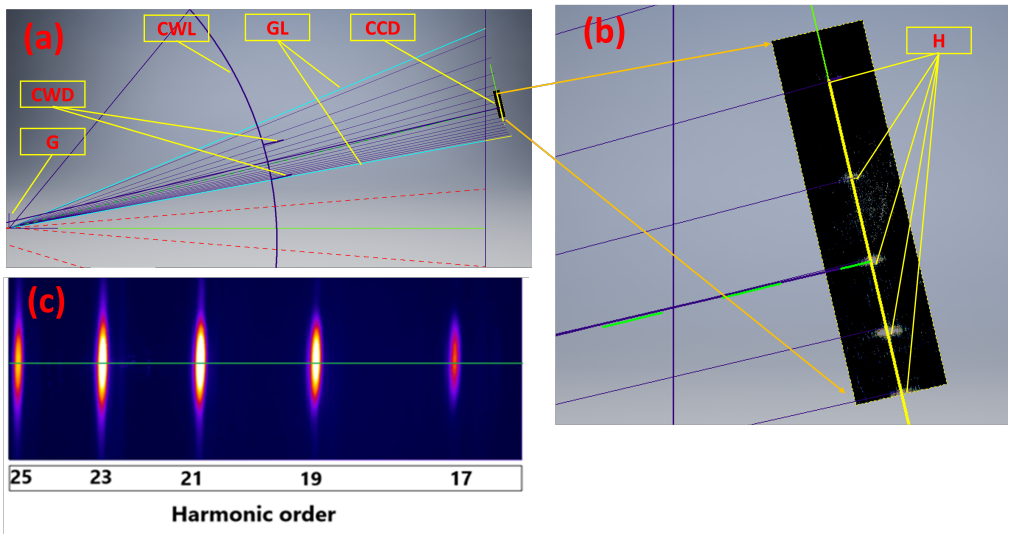

Figure 3.23
(a) CAD schematic for grating positioning. G: Grating, CWD: Chamber Window, CWL: Chamber Wall, GL: Grating diffraction limits, CCD: CCD of the XUV camera. (b) H: Harmonics recorded by the XUV camera in comparison with the CAD calculations. (d) Typical imaging measurement with XUV camera.

3.4.3 XUV Wavelength Selection

The selection of the XUV wavelengths was done via two similar pairs of multilayer mirrors. Each pair consists of a multilayer flat mirror and a multilayer spherical concave mirror, placed in opposite direction as shown in Figure 3.24. The pair of multilayer mirrors reflects only a narrow band (∼2 nm) around a central wavelength, with the spherical mirror, having a radius of curvature (ROC) 1000 mm, focusing the selected XUV beam onto the target at the fourth stage D of the setup. Both sets of multilayer mirrors were specially manufactured from SiC/Mg layers (NTT Advanced Technology Corporation) to deliver the central wavelengths of 32.2 nm and 47.6 nm, respectively, at maximum reflectivity for the geometry in use. The pairs of mirrors were fixed on a movable platform placed on a linear rod equipped with a vacuum compatible motor that is externally controlled with sub-millimeter accuracy. Thus, the two pairs of multilayer mirrors could be exchanged at will during the measurement. In addition, the fine alignment of the pairs of mirrors was also done externally by vacuum compatible piezoelectric devices attached to the mounts of the mirrors.

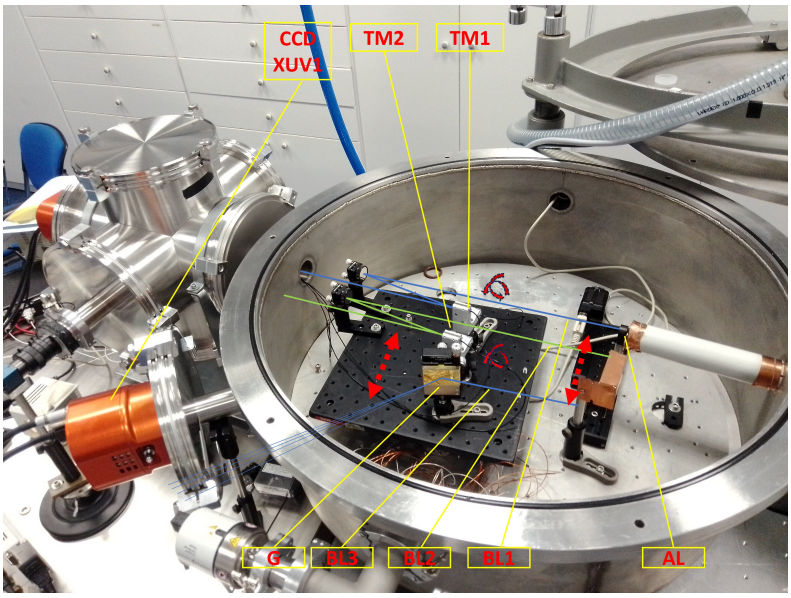

Figure 3.24
Stage C of the experimental setup. AL: aluminum filter on a movable base. The large breadboard movable base hosts thee interchangeable optical paths, i.e. BL1, BL2, and BL3. In BL1 and BL2, there are pairs of multilayer mirrors, delivering the wavelengths of 32.2 and 47.6 nm, respectively. TM1 and TM2 are remote-controlled piezoelectric mounts to fine control the optical paths. In BL3, the diffraction grating G diffracts the XUV beam toward the XUV CCD camera (XUV1) for measuring the harmonics image spectra.

As shown in Fig.3.24, the diffraction grating is also mounted on the platform. The grating can be inserted into the generated XUV beam path to monitor the XUV spectral image at the XUV CCD camera (XUV1) during the experiment, and thus perform an online optimization.

3.4.3.1 XUV Transmittance in Al Filter

The use of pairs multilayer mirrors requires the use of annular laser beam and an IR filtering by Al foil. For this, below we studied the transmittance of the HHG XUV radiation through a 400 nm Al foil, estimated in Fig.3.18b. For this the HHG from Ar, Kr, and Xe gases were measured using the optical setup shown in Fig.3.25. In particular, the Al metal filter was placed on a special micrometric precision linear displacer, which allows its movement in and out of the beam of harmonics. The HHG spectra were recorded using the solid beam and the MCP detector. In Figs. 3.26,3.27, and 3.28 the measured HHG spectra without the use of the filter (red line) and with the use of the filter (blue line) are shown for Ar, Kr and Xe, respectively, at pressure of 60 Torr. Note that in the HHG spectra second order diffracted harmonics might also appear. For this, the position of the first diffraction order is denoted by a black solid line, while for the second order by a black dashed line.

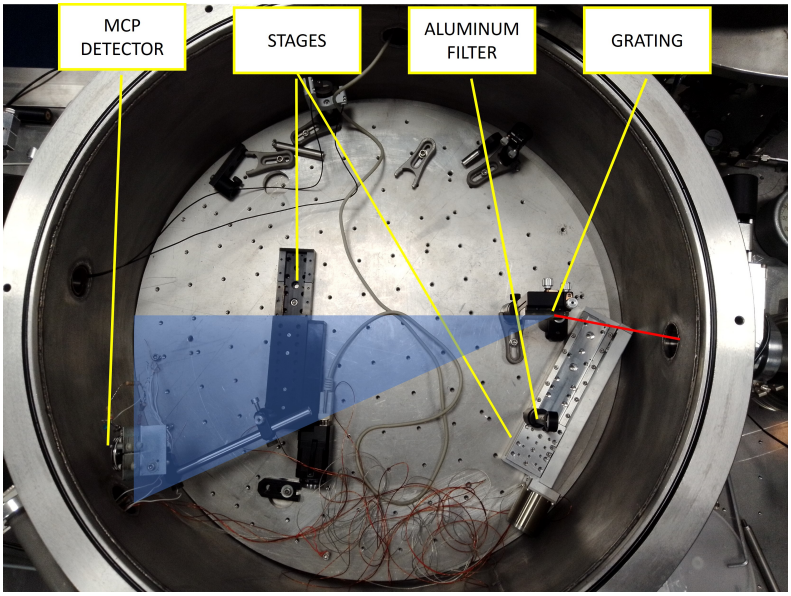

Figure 3.25
Setup for determining the XUV transmittance of the 400 nm thick Al filter.

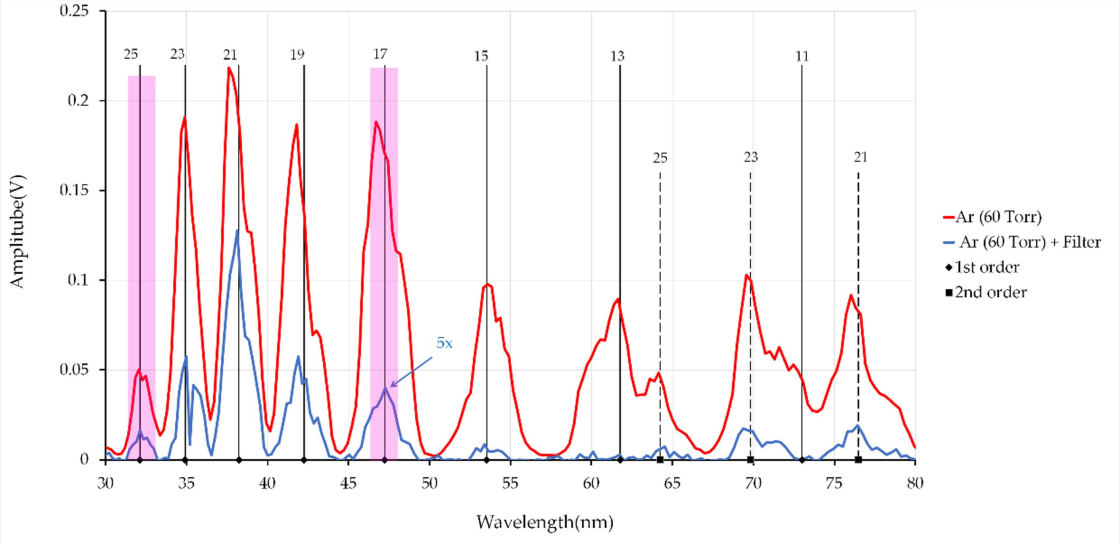

Figure 3.26
HHG spectrum resulting from Ar at 60 Torr without the use of the 400 nm thick Al filter (red line) and with the use of the filter (blue line). Pink stripes correspond to the harmonics of interest in this work.

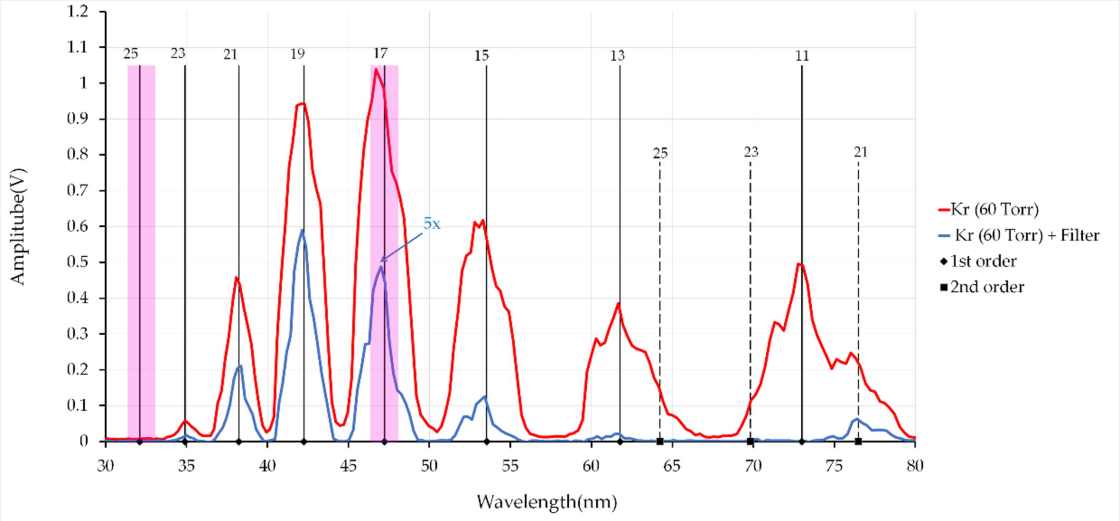

Figure 3.27
Same as in Fig.3.26 but for Kr.

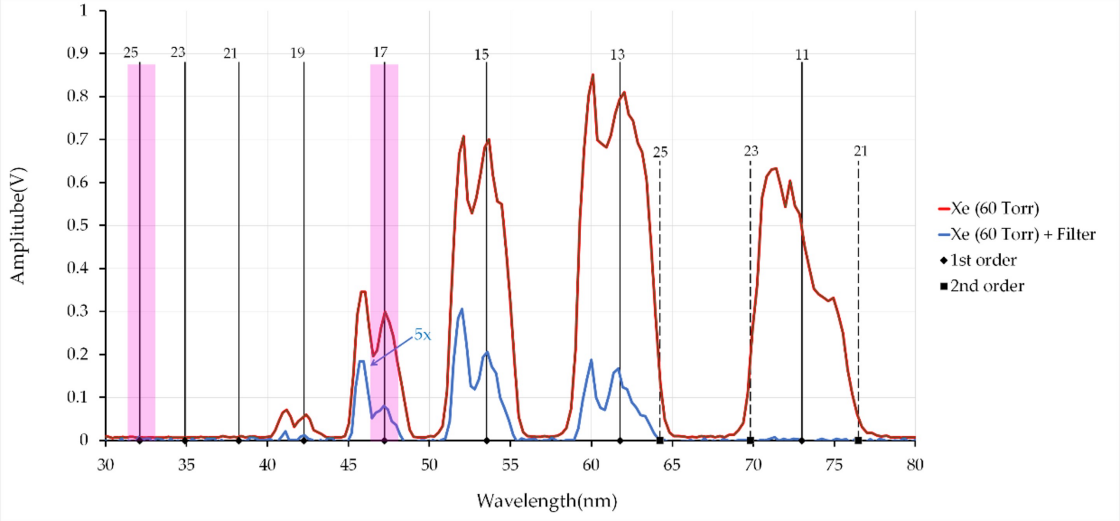

Figure 3.28
Same as in Fig.3.26 but for Xe.

A more general study employing various gas pressures for the two wavelengths of interest in this study, i.e. 32.2 nm and 47.6 nm, is presented in Fig. 3.29. From Fig. 3.29a, corresponding to 32.3 nm (25^{th} harmonic), it is evident that the preferable gas in use is Ar since the production at pressures larger than 60 Torr surpasses the production of Kr and Xe by almost an order of magnitude. Similarly, from Fig.3.29b, corresponding to 47.6 nm (17^{th} harmonic), it is evident that the preferable gas in use is Kr since the production at pressures larger than 60 Torr largely surpasses the production of Ar and Xe.

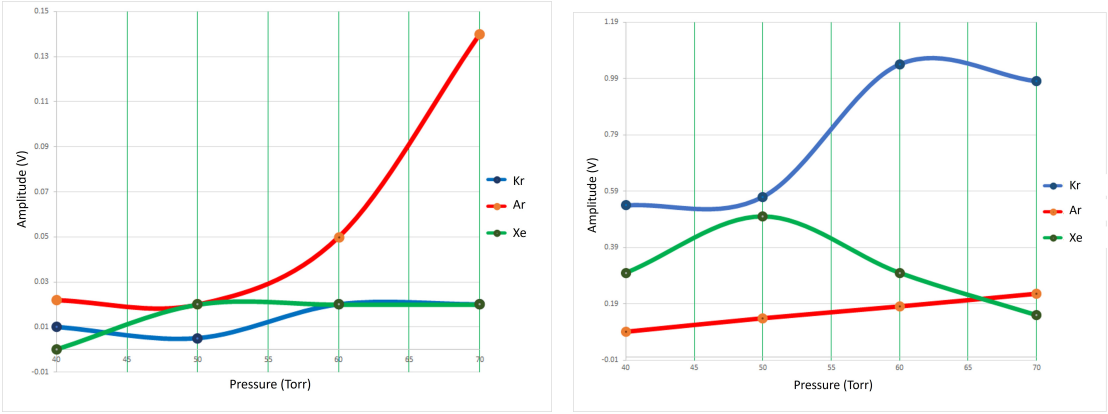

(a) (b)

Figure 3.29
(a) HHG signal for the 32.2 nm (25^{th} harmonic) using the 400 nm thick Al filter as a function of the pressure for Ar, Kr and Xe gases. (b) Same as in (a) but for the 47.6 nm (17^{th} harmonic).

3.4.3.2 Selection of the 17^{th} and 25^{th} harmonics

After generating the XUV radiation and filtering it from the IR radiation, the next step was to isolate XUV radiation at a specific wavelength from the total spectrum. This is achieved by employing multilayer mirrors operating as wavelength-selective filters. The design and ordering of the filters in use in this thesis was determined from the cutoff limit and maximum production efficiency of the HHG. Thus, we decided for the next two harmonics and corresponding wavelengths:

- 17^{th} harmonic with a wavelength of 47.6 nm is situated in the plateau region of the spectrum, dependent on the target gas used. This selection ensures high resolution and a faster response (attributed to higher XUV efficiency).
- 25^{th} harmonic with a wavelength of 32.2 nm. Despite falling within the cutoff region for Ar, this choice ensures maximum resolution.

Multilayer mirrors (multiple reflective layers) were developed to enhance the overall reflectivity of a medium. The operation principle of a reflective multilayer mirror is illustrated in Fig. 3.30. Alternating layers of specific materials create periodic structures (d), enhancing reflectivity through repeated reflections added coherently. The one material establishes the required distance, while the other, with higher molecular weight, induces reflection. Reflectivity calculations are based on the Fresnel equations [83]. Experimental data supported that the most suitable combination of materials for the wavelengths of interest is SiC/Mg on a Si substrate [84]. Based on all the above, the multilayer mirrors that were ordered

and implemented in the setup have the specifications presented in Table 3.1. In Fig.3.31, the multilayer mirror pairs reflectivities for 32.2 nm and for 47.6 nm, given by the manufacturer, are presented.

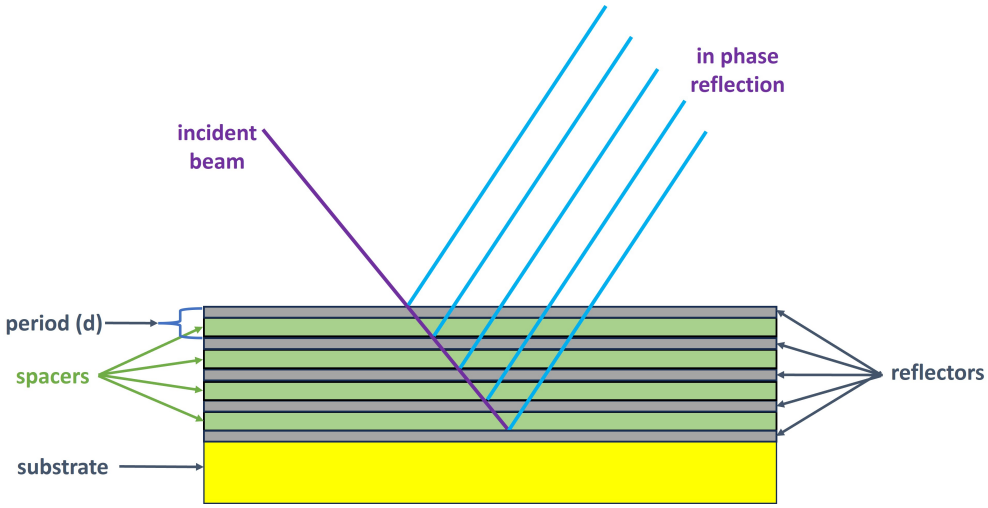

Figure 3.30
Reflective multi-layer mirror operation principle. Alternating layers of specific materials create periodic structures (d), enhancing reflectivity through repeated reflections added coherently.

Table 3.1
Specifications for the two pairs of multilayer mirrors (NTT Advanced Technology Corporation [85]).

Selection central wavelength λ (nm)	47.6	32.2
Incident angle	8°	8°
Substrate diameter (inch)	1	1
Thickness (mm)	6.35	6.35
Radius of curvature (mm)	1000	1000
Material	SiC/Mg	SiC/Mg
Period length (nm)	26.6 ($\pm$1.5%)	16.8 ($\pm$1.5%)
Calculated reflectivity	35%	46%
Guaranteed reflectivity	$>$ 28%	$>$ 38%
Spectral range (FWHM) (nm)	3.8	1.4

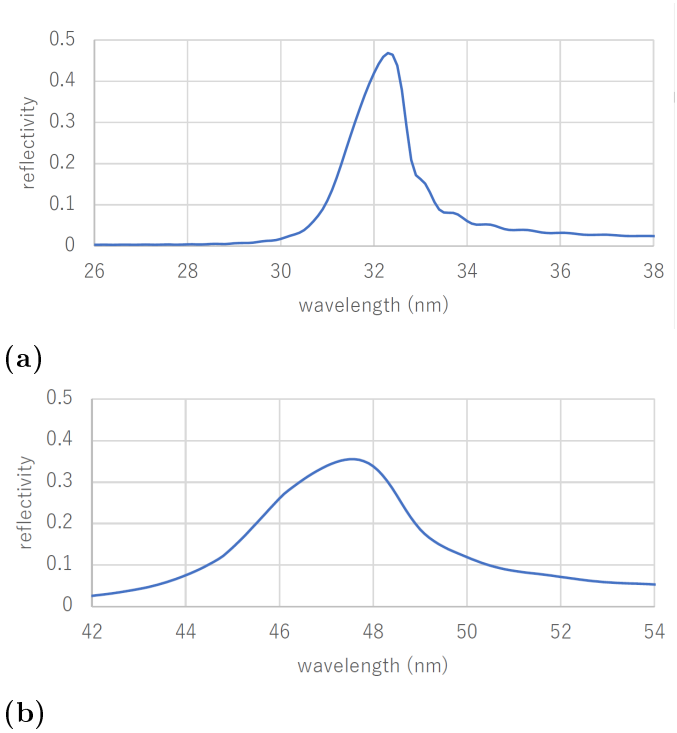

Figure 3.31
Multilayer mirror pairs reflectivities: (a) for 32.2 nm, (b) for 47.6 nm.

Although the pairs of XUV multilayer mirrors were specially designed for the geometry of our setup and for the wavelengths of 32.2 nm and 47.6 nm, their transmittance was additionally tested in realistic experimental conditions. For this, an optical setup in the chamber of stage C was developed, so that the generated XUV beam is first filtered by the 400 nm Al foil, then propagates through the pair of multilayer mirrors and finally is spectrally analyzed by the flat field grating, as shown in Fig.3.32. The recording of the XUV spectrum was done via the MCP scanning mode in order to obtain the full spectrum. The results of these measurements for both pairs of multilayer mirrors are presented in Fig. 3.33.

It can be seen that the pair of low value wavelength mirrors transmits at a central wavelength of 32.2 nm with a FWHM of 2.5 nm, while the pair of the high value wavelength mirrors transmits at a central wavelength of 47.6 nm with a FWHM of 1.5 nm. The appearance of peaks at lower value wavelengths in both spectra are due to the second order of diffraction, as can be inferred from their twice in magnitude wavelength value. Finally, it should be noted that for the 32.2 nm Ar gas was used, while for the 47.6 Kr gas was used, as resulted from the study presented in subsection 3.4.3.1.

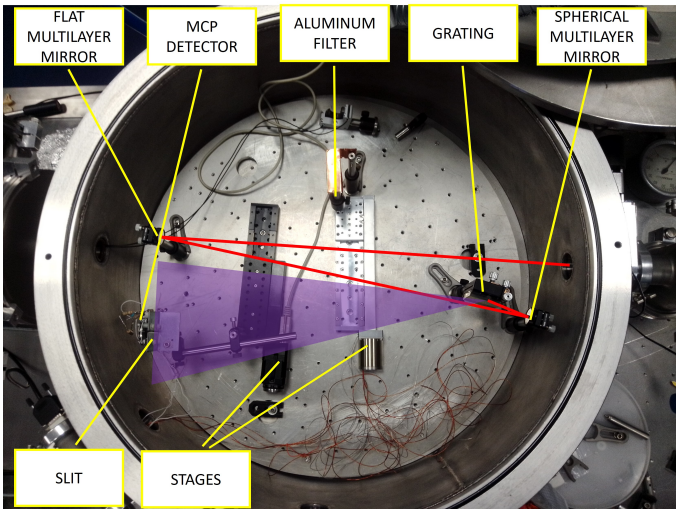

Figure 3.32
Setup for selection and characterization of harmonics using multilayer mirrors and the characterization of their spectral transmittance (reflectivity) curve. Harmonics are detected using the MCP detector.

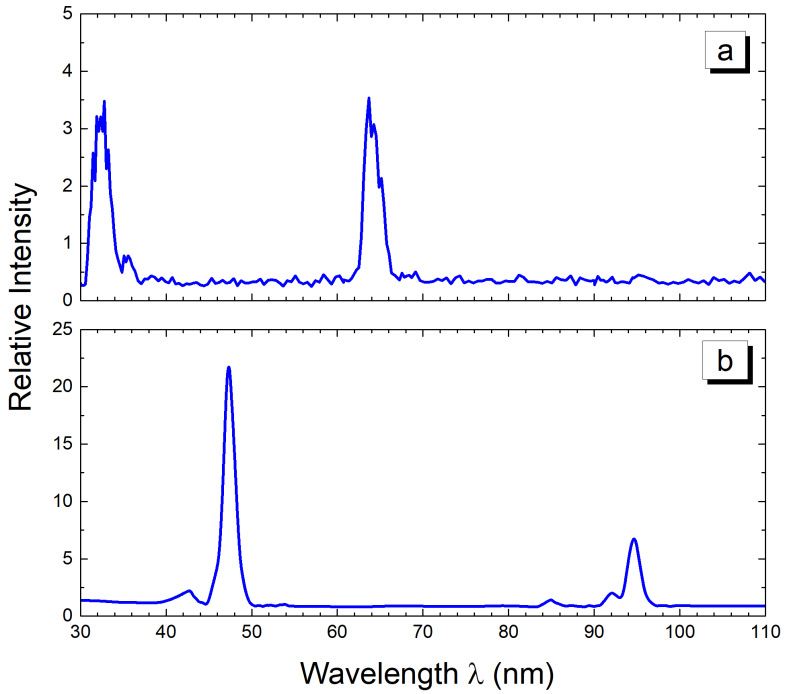

Figure 3.33
Overall transmission spectra of the generated XUV radiation obtained for both pairs of multilayer mirrors. (a) Pair for the 32.2 nm. (b) Pair for the 46.7 nm. The peaks at ∼65 nm in (a) and ∼95 nm in (b) correspond to the second order of diffraction.

3.5 Coherent Diffraction Imaging (CDI)

The coherent XUV radiation with the selected wavelength from the pairs of multilayer mirrors is directed to the next stage D of the experimental setup.

There, the target is placed between the focus of the XUV radiation and the XUV CCD camera chip. The target is mounted on an XYZθ translation/rotation stage system, for precise control of the target positioning, as shown in Fig. 3.34a. The XYZ translation stage utilizes the XLS-1 stage for the horizontal (X and Y) axes, featuring a holding and driving force of 1 N and a travel range of 40 mm. The vertical (Z) axis employs the XLS-3 stage, having a sub-micron precision and ability to support the weight of the horizontal stage components. The rotational stage atop linear stages enables precise angular adjustments for sample alignment with the incident laser beam, a critical requirement [86]. After the XUV beam is aligned and focused on the target area, the coherent diffraction image is recorded by the XUV CCD camera which is similar to the one used for measuring the image spectra (XUV CCD1) but with a square sensor of 1024 $\times$ 1024 pixels (13.8 $\times$ 13.8 mm) (see Appendix D for operation details). The CDI data are later on analyzed resulting in the reconstruction of the target pattern, as will be described in Chapter 6.

In addition to the positioning and alignment stages, a lateral camera serves as a real-time visual feedback tool, helping to ensure the accurate pre-alignment of the laser beam with the sample before XUV irradiation, adding an extra level of precision to the alignment process. Alongside the camera, a LED light source illuminate the chamber, aiding the preliminary target positioning.

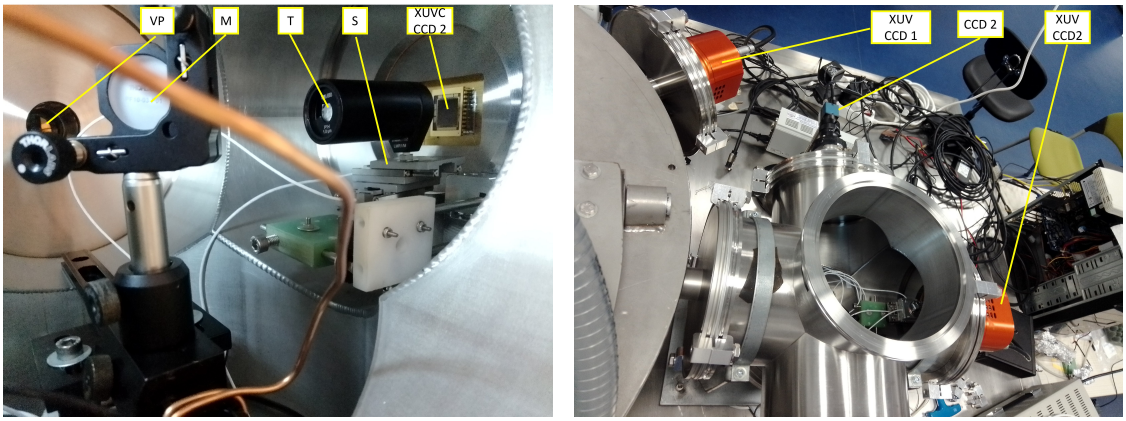

(a) **(b)**

Figure 3.34
Stage D. Setup for target positioning and coherent diffraction imaging. (a) VP: Lateral view-port, M: Mirror for lateral CCD2 camera, T: Target, S: XYZθ positioning stages, XUV CCD2 camera chip. (b) XUV CCD1 camera for measuring the XUV spectra, CCD2: Lateral camera for alignment purposes, C: XUV CCD2 camera for coherent diffraction imaging.

Chapter 4

Optimization of the HHG XUV Source

The optimization of the generated XUV radiation is a multiparameter laborious task. In this chapter, the experimental results of the optimum conditions for HHG in gases with respect primary to the conversion efficiency but also to the spectral and divergence characteristics are presented. For this, key parameters including laser beam diameter, laser beam focus position, gas pressure and species, as well as laser chirp were examined. Especially, the study includes optical layouts that use a solid laser beams as well as annular laser beams.

The experimental results presented in this chapter serve as a resource for the upcoming chapters, facilitating discussions on theoretical frameworks and practical applications. By isolating and showcasing the empirical outcomes, this chapter lays the groundwork for a comprehensive understanding of the optimization process in HHG, ensuring a seamless transition to subsequent discussions and analyses.

4.1 Solid Laser Beam

The optimization studies presented here relate to the investigations that use the solid laser beam, presented in Chapter 6. For this, the optical geometry shown in Fig. 3.22, that involves the filtering of the IR radiation with the pair of Si wafers, and the diffraction of the XUV beam by the grating towards the MCP detector, operating in stepping mode, to record the total XUV spectrum was employed.

4.1.1 Laser Beam Diameter

The laser beam diameter is a pivotal parameter in HHG experiments, exerting a multifaceted influence on key processes. Truncating the beam diameter impacts both single-atom HHG, volume effects, and phase matching. Notably, reducing the aperture diameter can significantly boost harmonic flux and conversion efficiency, with improvements by factors up to 10. Remarkably, this trend holds consistently across different experimental conditions, including gas species and harmonic orders, underscoring the laser parameters' robustness.

The adjustments in beam diameter trigger a cascade of effects. They lead to a reduction in focused intensity, affecting ionization rates and consequently altering the gas's refractive index. Simultaneously, they shape the amplitude and phase of the induced harmonic dipole. Moreover, varying the aperture diameter can encompass a larger volume for generating a specific harmonic order and change the Gouy phase shift gradient due to altered focal geometry. It's imperative to account for laser diffraction by the circular aperture and its implications for the Strehl[1] ratio when selecting the central part of the beam [70, 72].

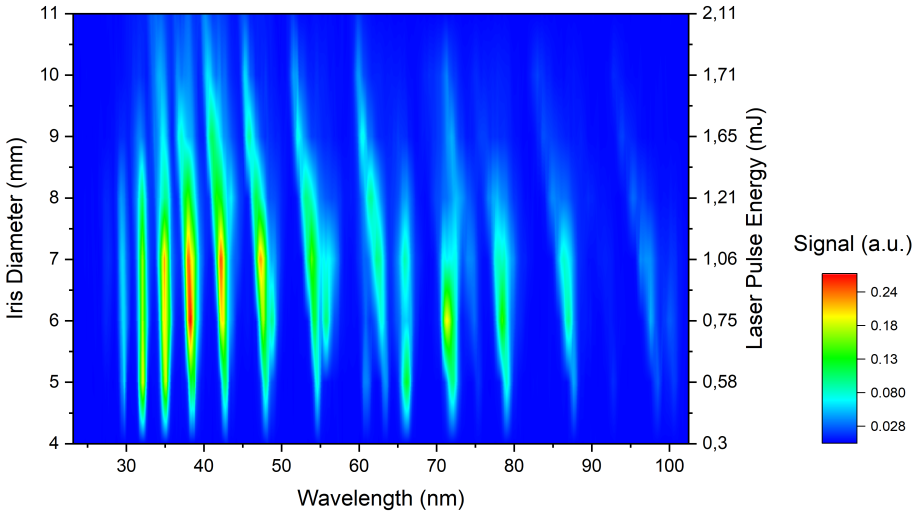

Figure 4.1
Results from a series of XUV spectra measurements obtained after varying the laser beam diameter. The laser pulse duration was 26 fs FTL, while the gas in use was argon at a pressure of 40 Torr.

The HHG measurements were done with the solid laser beam being truncated by an iris prior to its entry to the semi-infinite gas cell. The iris diameter was varied from a minimum value of 4 mm to a maximum value of 11 mm, with a step of 1 mm,

[1] The Strehl ratio, serves as a quantitative measure of optical system performance. It is defined as the ratio of the peak intensity of the actual optical system's point spread function to the peak intensity of an ideal diffraction-limited system. A Strehl ratio of 1 indicates optimal, diffraction-limited performance, while lower values signify increased aberrations and reduced imaging quality [87].

where the HHG signal was barely measurable. The laser pulse duration was kept at its FTL value, i.e. 26 fs FTL, and the laser focus was placed at the laser-drilled exit aperture of the semi-infinite cell. The gas in use was argon at a pressure of 40 Torr. The MCP stepping method (see subsection 3.4.2.2) was applied to obtain the total HHG spectra.

The results are summarized in Fig. 4.1 where the HHG spectra are presented as a function of the beam truncated diameter and the corresponding laser pulse energy. It should be noted that the laser beam diameter before the iris (untruncated) was about 1.8 cm with a pulse energy of 5 mJ. From Fig. 4.1 it is evident that the overall maximum harmonic yield is realized when the iris aperture is set between 5.5 and 7.5 mm in diameter. For higher diameter values the harmonic yield is reduced due to the ground state depletion resulting from the enhancement of the ionization competing process. These findings underscore the subtle effect of the truncated laser beam geometry, affecting the pulse energy and intensity, the depth of focus, the medium's ionization and corresponding phase matching conditions for the efficient HHG.

For the rest of the study in this Chapter the value of 7 mm for the iris diameter was adopted as the optimum for the most efficient HHG. Small variations around this value, while the other parameters were studied, showed minimum variations. In some cases, a small variation of the iris diameter around this value was implemented for fine optimizations.

4.1.2 Laser Focus Position and Pressure

The next step of the investigation was to vary the laser focus position at the exit of the semi-infinite cell along with the argon gas pressure dependence. We combined these two parameters as both affect substantially the phase matching conditions of the HHG, while the laser intensity was maintained at a constant value as previously determined by the diameter of the iris set at 7 mm. The laser focus position, i.e. focal point, was determined from the distance of the focusing lens from the copper terminal plate at the exit of the semi-infinite cell.

The results are presented in Fig. 4.2, where a discernible impact of increasing pressure on the performance of harmonics is evident. Notably, this influence varies across different harmonics, indicating a nuanced response to changing pressure conditions. Furthermore, variations in pressure induce shifts in the spectral characteristics of the harmonics. This intricate relationship between pressure adjustments and the laser focus position significantly influences the efficiency, spectral broadening, and central wavelength of specific harmonics. The non-uniform

effect on various harmonics emphasizes the complexity of the interplay between pressure variations and focus position in the HHG process. These findings hold practical significance for the imaging stage, as they serve as tools for determining optimal harmonics with respect to efficiency, spectral characteristics, and central wavelength.

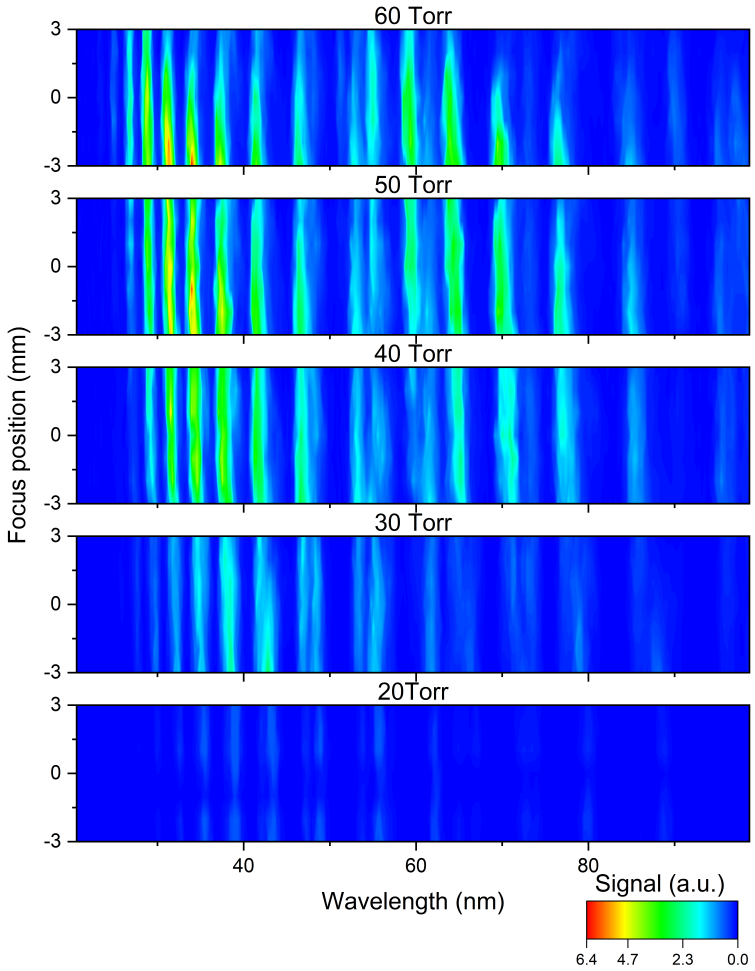

Figure 4.2
HHG measurements as a function of argon pressure. The laser pulse energy was kept at 1 mJ (7 mm iris diameter), with the focal spot corresponding to the position of the copper thin foil of the semi-infinite cell.

4.1.3 Gases and Gas-mixtures

In this section, we extend our study on the investigation of HHG production by utilizing various gas targets as well as gas mixtures of them as the non-linear medium. The part of study referring to the use of various gases has been presented

in subsection 3.4.3, and only indicative results will be included and commented here.

In Fig.4.3, the comparative HHG spectra obtained for Ar, Kr and Xe gases are presented. All spectra were obtained at pressures of 70 Torr and identical laser focusing conditions. An overall higher HHG efficiency is evident for Kr and Xe gases compared to Ar. This is due to their lower ionization potential (15.76 eV, 13.99 eV and 12.13 eV for Ar, Kr and Xe, respectively) which, however, affects their spectral cutoff. Especially, Xe is known to have a maximum cutoff at laser peak intensities close to 8×10^{13} W/cm^2 which corresponds to a cutoff of 43 nm in accordance with our measurements. For the laser pulse energy of 1 mJ in use, the Ar and Kr cutoffs result in 30 and 32 nm, respectively, in accordance with our measurements. Thus, from this comparative study it becomes evident that for the wavelengths supported from multilayer mirrors, i.e. 47.6 nm and 32.2 nm, respectively, the use of Kr and Ar gases, respectively, is mandatory.

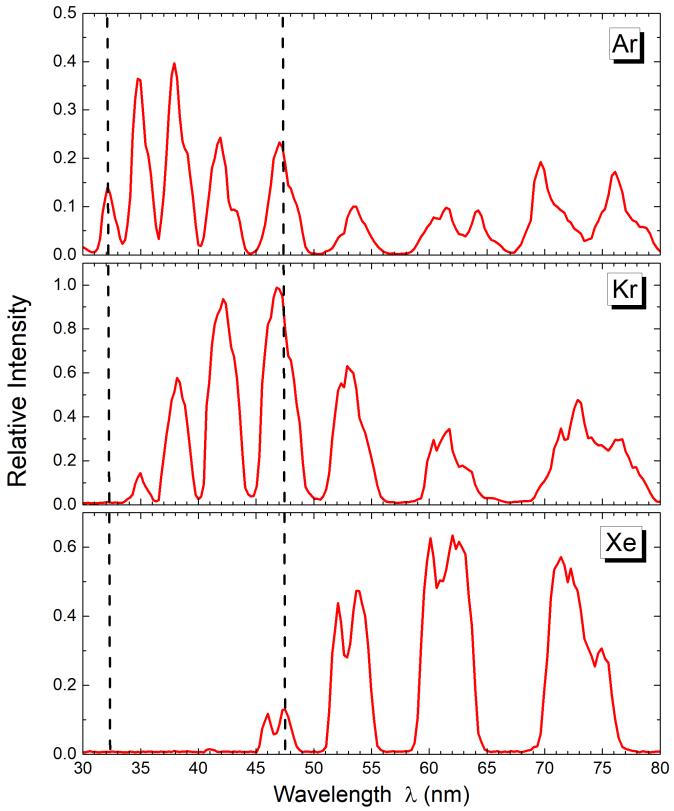

Figure 4.3
XUV HHG spectra obtained for the Ar, Kr, and Xe HHG gases. All spectra were obtained at pressures of 70 Torr and identical laser focusing conditions. Dashed lines indicate the wavelengths of interest. (from Ref.[88])

Next, we investigated the HHG production by introducing into the semi-infinite cell mixture of gases. We used mixtures of Ar gas, used as the generating medium, with small percentages of Ne or He gases in the mixture. The introduction of Ne

and He gases into the Ar medium, maintains the HHG production from the Ar medium but modifies the refractive index of the gas, leading to changes in the wave propagation characteristics. Ne and He gases do not contribute to the HHG due to their high ionization potential compared to that of Ar. Thus, the main effect is the modification of the index of refraction which is encapsulated in the phase matching term Δk in Eq.(2.50).

In Fig. 4.4, HHG spectra from gas Ar-Ne and Ar-He mixtures, and from pure Ar gas are presented. In all cases the Ar pressure in the mixture was kept at the same value as the corresponding one in the pure Ar case, so that the HHG production from Ar remains the same. Each figure showcases two spectra, one for pure Ar gas and one for the corresponding mixture. From these it is evident that the Ar-Ne mixture, with 20 % Ne, and Ar pressures up to 50 Torr resulted in noticeable efficiency enhancement for the higher harmonics compared to pure Ar as seen in Figs.4.4(a,b). However, for higher Ar pressures this enhancement is reduced as evident from Fig.4.4(c).

Similarly, for the mixture of Ar-He, with 10 % He, an HHG enhancement for the higher harmonics is evident in agreement with the Ar-Ne case (see Fig.4.4(d)). The latter was expected since Ne and He have close in value ionization potentials. However, it should be emphasized that the overall HHG production is much lower than that for Ar-Ne mixtures, since we had to operate the MCP at 1800 volts instead of 1500 for the Ar-Ne cases.

Similar results have been reported in the literature, where efforts have been made to elucidate this effect [46, 87, 89–95]. Aside from the use of He or Ne as a phase-matching agent, it has been reported in the literature that in a Xe-He mixture, with a Xe/He ratio of 0.04, the harmonics originating from Xe serve as a booster for those produced by He [96]. Moreover, in the literature it has been proposed that in a Ne-He mixture, with a ratio of Ne/He of 35%, HHG enhancement is the result of the interference between harmonics produced by each gas agent separately [97]. However, these mechanisms are not applicable in our case since the HHG intensities from Ne or He are approximately 16 times weaker than these from Ar. Finally, it should noted that approaches following the principle of refractive index compensation for HHG enhancement, using multi-jets gas targets have also been reported [95, 98, 99]

4.1.4 Chirp of Laser Pulses

In this section we examine the role of the laser chirp in the HHG. Since we will investigate these effects in detail in Chaptet 5, only an overall approach will be

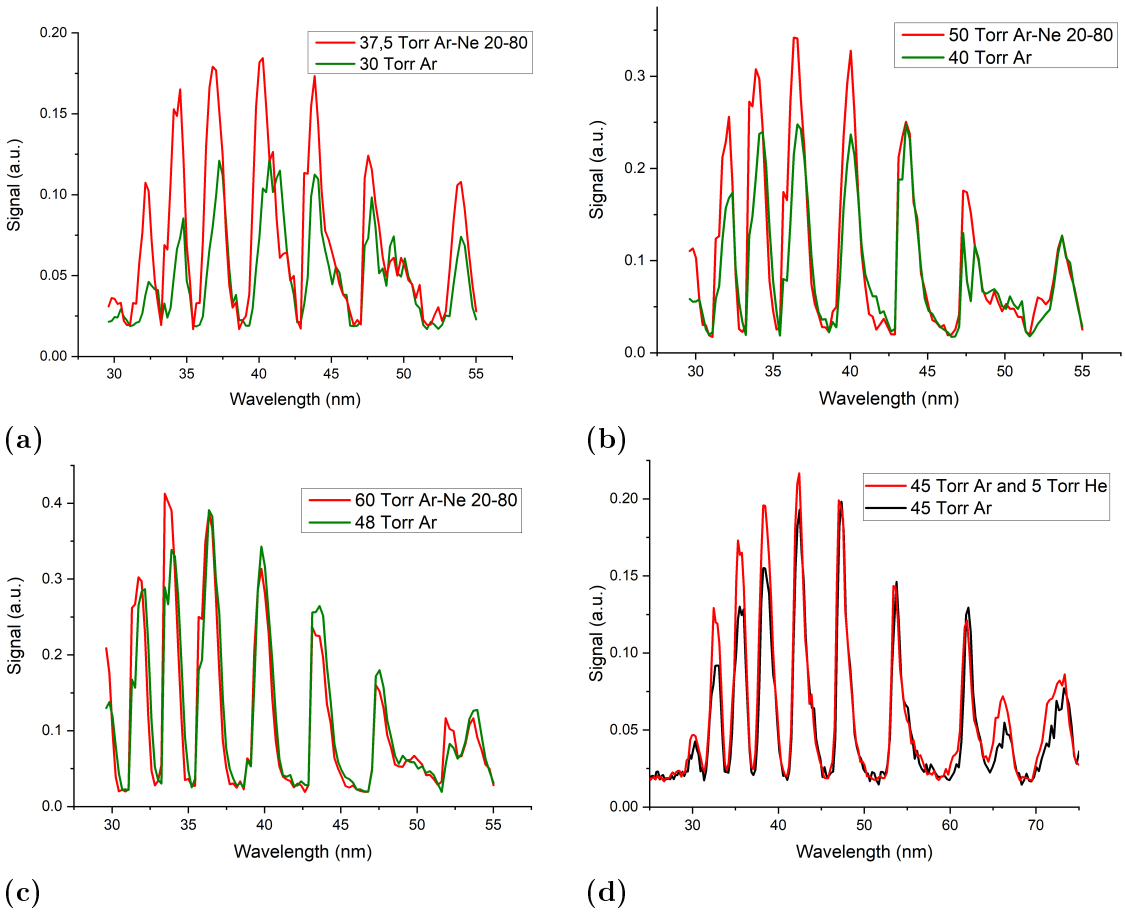

Figure 4.4
Comparison of Ar gas mixtures. All spectra originate from argon gas, with mixtures displaying enhanced radiation, especially at shorter wavelengths.

presented here. When varying the chirp of a laser pulse, the pulse's duration is increased while its intensity decreases accordingly, thus affecting the HHG and corresponding phase matching conditions. The laser chirp was varied by adjusting the spacing of the compressor diffraction gratings while the laser pulse duration was measured at the experimental setup using the Bonsai autocorrelator.

In Fig. 4.5 we present a series of HHG spectra generated in Ar gas for various pressures, while all the other experimental parameters, are kept identical. The right vertical y-axis is the duration of the pulse, while the left y-axis denotes the position of the compressors' diffraction gratings. The y-axis increases from positive to FTL and to negatively chirped pulses. It is evident that the maximum efficiency is achieved when the diffraction grating position is about 26.2 mm with a corresponding pulse duration of 60 fs, the chirp being negative. Thus, the chirp of a laser pulse seems to play an crucial role in HHG, and for this reason it is investigated in detail in Chapter 5.

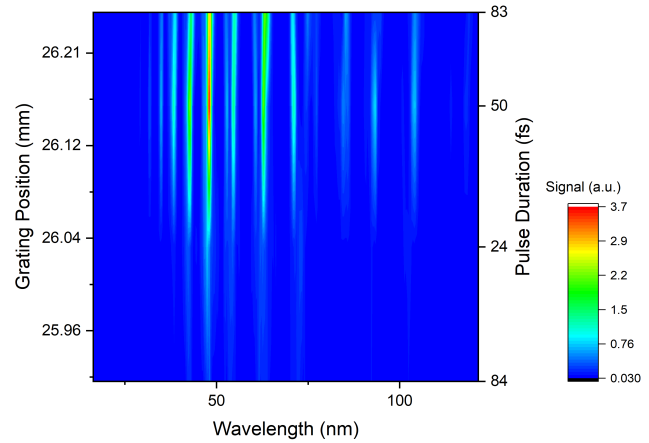

(a)

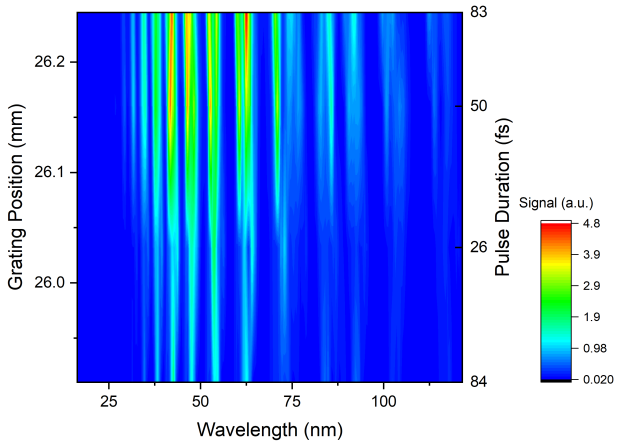

(b)

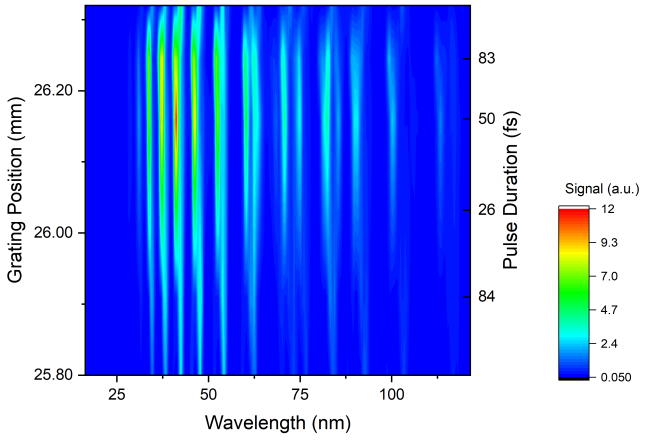

(c)

Figure 4.5
Series of HHG spectral measurements by varying the chirp of the laser pulse though the variation of the spacing of the compressor's diffraction gratings. The left y-axis increases from positive to FTL and to negatively chirped pulses. Argon gas was used as the generating medium with pressure of (a) 20 Torr, (b) 30 Torr, (c) 40 Torr, while the pulse energy was kept constant at 0.8 mJ

4.2 Annular Laser Beam

The additional optimization studies presented here relate to the investigations that use the annular laser beam, presented in Section 3.4. For this, the optical geometry shown in Fig.4.6, that involves the filtering of the IR radiation with the Al filter, and the diffraction of the XUV beam by the grating towards the XUV CCD1 camera, to simultaneously record part of the total XUV spectrum, was employed.

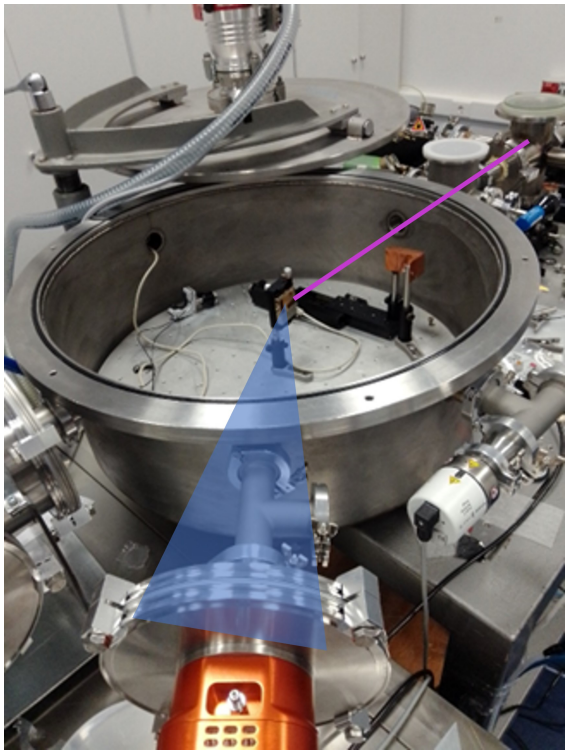

Figure 4.6
Experimental optical setup for studies with annular laser beam.

4.2.1 Laser Pulse Energy

In Fig.4.7b, the study of HHG production as a function of the energy of the IR pulse for Ar and Kr gases is presented. For all the measurements the annular beam block diameter was 7 mm while the outer beam was varied at will. Based on these, it becomes evident that for optimal overall harmonic production the most suitable energy is that of 1.0 mJ.

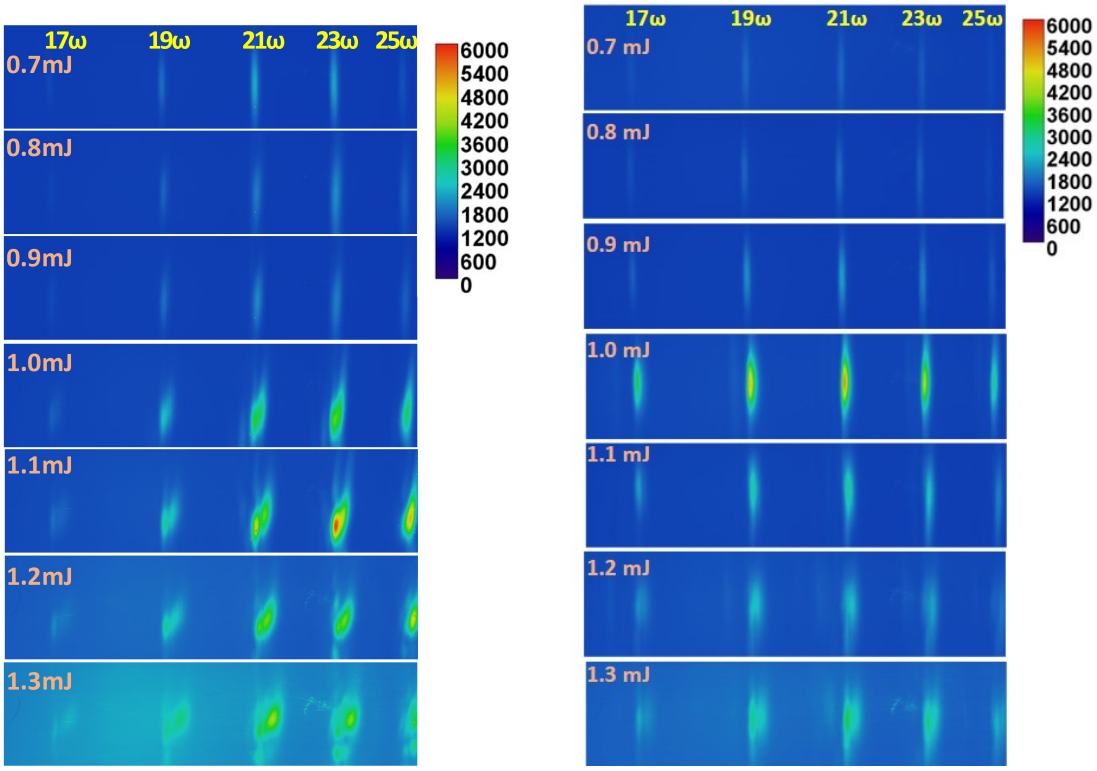

(a) (b)

Figure 4.7
Plateau harmonic production for various IR pulse energies. The block diameter of the annular laser beam was kept at 7 mm. (a) Kr gas at 90 Torr pressure (b) Ar gas at 70 Torr pressure.

4.2.2 Laser Beam Diameter

Fig. 4.8 shows the study of HHG spectra as a function of the diameter of the block ball while simultaneously varying the outer diameter of the IR beam, so that the energy remains constant at 1.0 mJ, according to the previous study. It is found that the optimum diameter of the cutoff barrier is that of 7 mm.

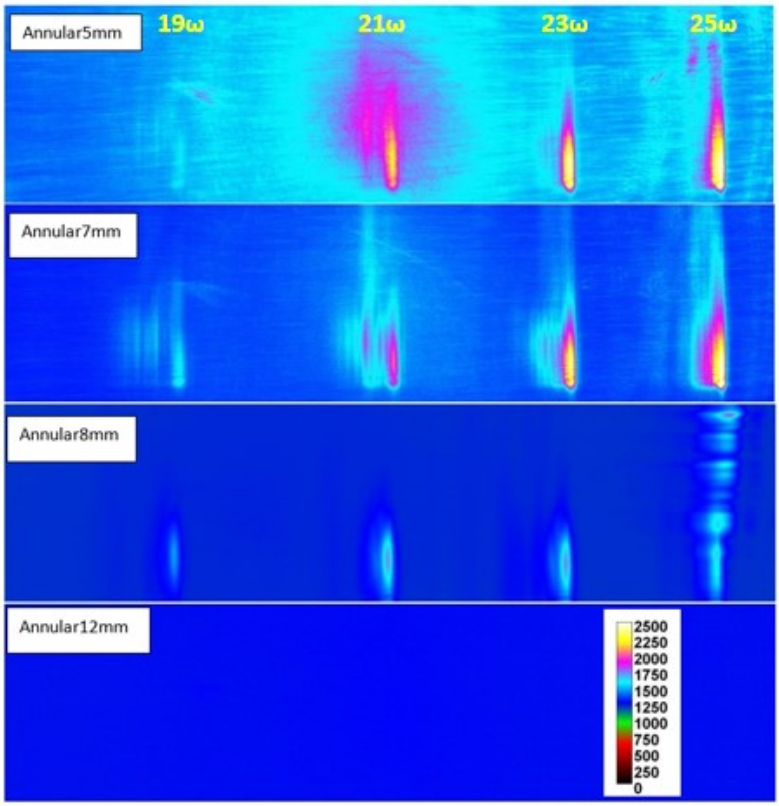

Figure 4.8
Plateau harmonics for various laser beam block diameter forming annular IR beams. The laser pulse intensity was maintained at 1.0 mJ.

4.2.3 Gases and Gas Pressure

In Fig. 4.9a, the study of the production of harmonics with respect to the gas species and gas pressure is shown. According to the above studies, the block diameter of the annular laser beam was kept at 7 mm, while the energy of the laser pulse was maintained at 1.0 mJ. In Fig.4.9a, the pressure dependence of the HHG spectra for the Ar gas are presented, while in Fig.4.9b the corresponding spectra for Kr gas are shown. Based on these results, it becomes evident that optimal harmonic production is achieved for Ar for pressures around 80 Torr, while for Kr a bit higher at 90 Torr.

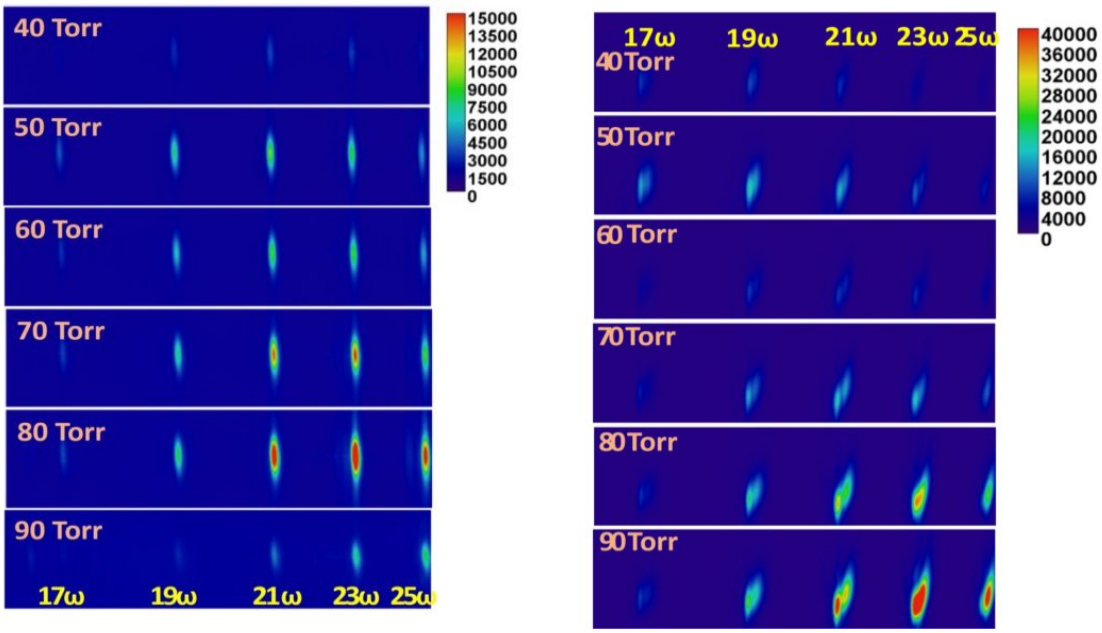

(a) **(b)**

Figure 4.9
Plateau harmonic production for various gas pressures, using an annular laser beam with block diameter of 7 mm and energy 1.0 mJ. (a) Ar. (b) Kr.

Chapter 5

Electron quantum path control in HHG via chirp variation

5.1 Introduction

As it has been explained in Section 2.2, there is an infinite number of quantum paths for the recolliding electron. However, for the same electron return energy, there are only two surviving paths that lead to a recollision with the parent ion for which ionization and recombination times are different. The path with the shortest travel time τ is termed short trajectory while the path with the longer travel time is termed long trajectory, respectively. Typically, the short trajectory duration is shorter than $0.65T$, where T is the laser pulse period, while the long trajectory duration is longer than $0.65T$. The quasi-classical action of the electron that determines the phase of the trajectory [9] depends on the travel time τ while it also depends linearly on the intensity of the driving laser pulse [100]. The total quantum phase of the q^{th}-order harmonic is $\phi(q) = a_s I(t) + a_l I(t)$, where $I(t)$ is the cycle-averaged laser pulse time-dependent intensity, while the parameters a_s and a_l, with $a_s \leq a_l$, correspond to the short and long trajectories, respectively. The q^{th}-order harmonic signal results from the coherent summation of the aforementioned quantum paths and corresponds to an energy of $E = q\hbar\omega_L$, where ω_L is the laser central frequency.

The temporal characteristics of the plateau harmonics depend on the phase difference between the long and short trajectories. As the cutoff region is approached, the duration of the two quantum paths becomes comparable, and at the cutoff the two quantum paths become degenerate with $a_s \simeq a_l$. Thus, cutoff harmonics are favorable in coherent summation applications. Indeed, the initial attempts for generation of attosecond beatings were largely oriented in the cutoff

region [101–103]. However, a significant obstacle was the inherent low efficiency of the cutoff harmonics.

From the above discussion it becomes evident that controlling the relevant contribution of long and short trajectories of the plateau harmonics is of fundamental significance. Not only it helps to the detailed understanding of the HHG process, but it also facilitates applications such as attosecond pulses generation [16, 20] and coherent diffraction imaging [28–31], where the geometrical and phase characteristics of the harmonics beam play a major role. The main geometrical distinctive footprint of the two trajectories in the harmonics imaging spectra is the difference in their divergence. The long trajectory has a larger divergence than the short, since the electron travels longer distances in the partially ionized medium during the recollision process [41]. In addition, for laser intensities causing a relatively high ionization of the medium, the central wavelength of the two trajectories is slightly different. This is attributed to the different time dependence of the two trajectory phases, which leads to coherent summation for each trajectory at different wavelengths (double-peaking) [104].

The origin of divergence of the two paths in HHG has been investigated in a number of publications [9, 14, 100, 105, 106], while attempts to separate and control the two trajectories have also been reported. Bellini *et al.* [107] used interferometric methods to demonstrate the different divergence distribution of the two trajectories (see Fig.5.1). Their results were soon adopted by the attoscience community to filter the long trajectory and achieve high quality attosecond pulse trains [20]. Willner *et al.* used a multi-jet arrangement of two gases showing a clear spectral separation of the two trajectories [98, 99]. Ishii *et al.* used phase-locked two-colour ($\omega - 2\omega$) laser fields to demonstrate the control of the electron trajectories near the cutoff region, through the relative phase between fundamental and second-harmonic fields [108]. Brugnera *et al.* varied the phase of a two-colour driving field and demonstrated near complete control over the long trajectory, which was easily separated spatially from the short [109]. Recently, Abbing *et al.* used tailored laser pulses consisting of the fundamental and its intense orthogonally polarised second harmonic in a two-colour HHG scheme [32]. They showed the suppression and enhancement of long and short electron trajectories, respectively, by controlling the relative delay between the two fields.

This chapter presents a novel method for the coherent control of the two quantum paths in plateau harmonics generated in a noble gas, based on the chirp of the laser pulse, i.e. the temporal rearrangement of the spectral content (time-dependent frequency) of the high intensity laser pulses. This control over the chirp of the high intensity laser pulses, allows for the control of the time-dependent slope of

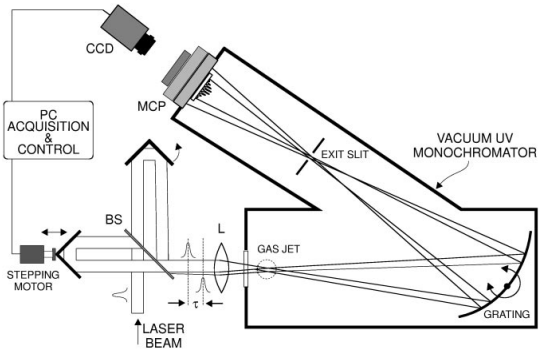

(a) Experimental setup for measuring temporal harmonic pulse coherence.

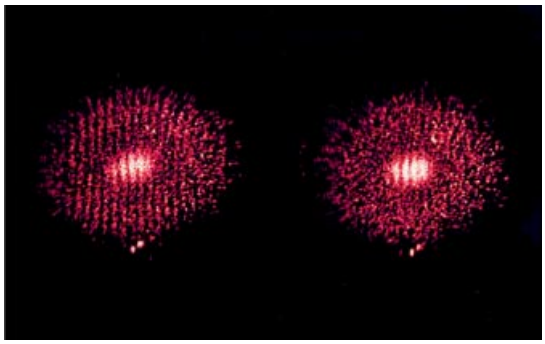

(b) Interference fringe pattern for the 15^{th} harmonic (53 nm) generated in Xe. Right: without delay, Left: with a delay of 15 fs.

Figure 5.1
Temporal coherence measurement of the 15^{th} harmonic generated in Xe, as reported by Bellini *et al.* [107]

.

the cycle-averaged laser intensity, the temporal evolution of the ionization degree of the medium within the laser pulse, and the SPM of the laser pulse inside the partially ionized medium. Since the temporal phase of each trajectory depends on all the above factors, the variation of the chirp of the laser pulse is expected to allow for an accurate control on them and the subsequent trajectories. Below the detailed study of the HHG, emphasizing on the generation efficiency and trajectories separation, from chirped high intensity laser pulses is presented. It is shown that HHG efficiency can be accurately controlled when varying the chirp, while for certain chirp values the two trajectories were clearly resolved in the HHG spectra. Moreover, experimental conditions were found under which the only surviving trajectory was the short one. Finally, a phenomenological model has been developed, which takes into account the aforementioned physical processes, that supports the experimental results.

5.1.1 Experimental Layout

The HHG experiments utilized the experimental setup presented in Chapter 3, the optical layout of which is illustrated in Fig.5.2. The laser pulses were focused at the exit pinhole of an Ar gas filled semi-infinite cell, generating high order harmonic that propagate along with the laser to stage C of the setup as described in Section 3.2. For the measurements of this chapter the pair of silicon wafers was used to filter the laser IR beam, as described in Subsection 3.4.1.1. The filtered XUV comb of high harmonics was then diffracted by the grazing-incidence flat-field diffraction grating (see Subsection 3.4.2.1) towards the XUV CCD1 camera. Detection of the XUV light occurred at the focal plane of the harmonics of interest ($15\omega - 23\omega$). The

XUV grating and detector contributed to a relatively high spectroscopic resolution of 80 to 100 pixels per 1 nm on the XUV CCD for the presented spectral region, offering adequate experimental precision.

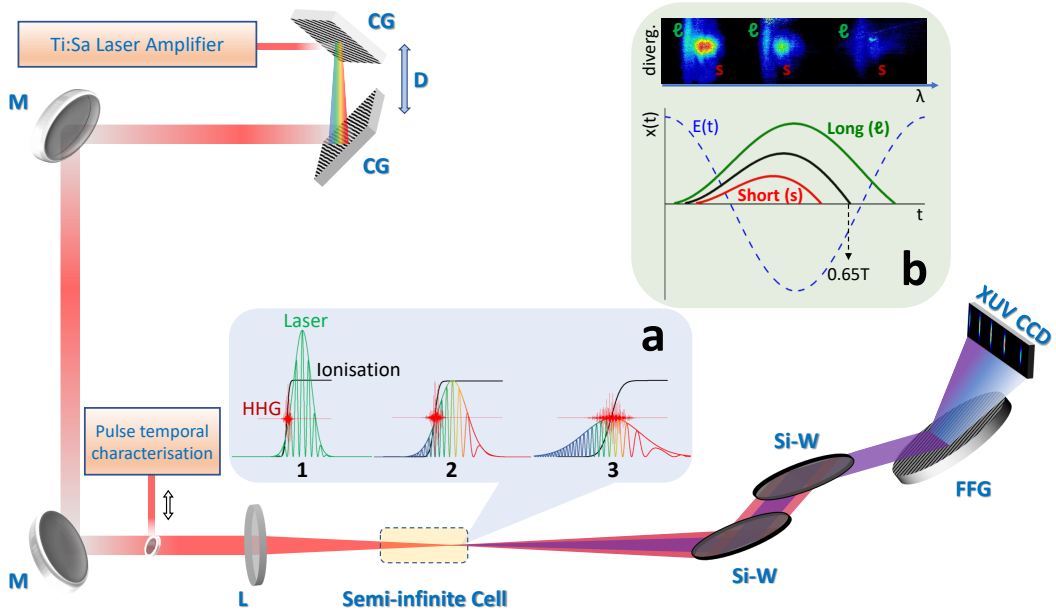

Figure 5.2
Schematic layout of HHG experiments. The laser pulses were chirped by varying the spacing between the compressor gratings (CG). Laser high harmonics were generated after focusing the chirped laser pulses on a semi-infinite Ar gas cell. High harmonic spectra were measured by an XUV CCD camera after IR filtering by silicon wafers (Si-W) and XUV dispersion by a flat-field concave grating (FFG). Inset (a): HHG E-fields for three cases of chirped laser pulses having the same energy; (a1) FTL pulses; (a2) Low negatively chirped pulses; (a3) High negatively chirped pulses. Inset (b): [Bottom] Schematic of electron trajectories within an E-field laser period leading to the recollision with the parent nucleus. [Top] HHG spectral images from long and short electron trajectories exhibiting different spectral and geometrical characteristics. D: Adjustable grating distance; M: Low dispersion fs mirror; L: Low dispersion thin focusing lens. (from Ref.[110])

Control over the chirp of the laser pulses was achieved by tuning the compressor gratings of the laser amplifier relative to the position delivering FTL laser pulses of 26 fs duration. Positive chirp values caused lower frequencies to appear at the leading edge of the laser pulse, while negative chirp values shifted them to the trailing edge (see Fig. 5.2a). The linear chirp value was experimentally measured on a shot-to-shot basis using a femtosecond single-shot intensity autocorrelator (see Section 3.1) just before the interaction cell. The distance between the gratings in the laser compressor could be adjusted according to the measured pulse durations, providing full control over the laser pulse chirp during the experiments.

5.2 Results & Discussion

5.2.1 Electron Trajectory Control

A systematic investigation of HHG has been performed by measuring the high harmonic spectrum as a function of the laser pulse chirp. Typical plateau harmonic spectra generated in 60 Torr Ar filled semi-infinite cell for various laser pulse chirp values are presented in Fig. 5.4(a). All the measurements were performed maintaining a constant laser pulse energy at 1.0 mJ as well as the same focusing conditions, i.e. focal length $f = 38$ cm, beam diameter 7 mm, and focus at the exit pinhole of the semi-infinite cell. The laser peak intensity for the FTL pulse of 26 fs was experimentally assessed to be $2.3 \pm 0.5 \times 10^{15}\, W/cm^2$. The pulse durations indicated in the spectral images in Fig. 5.4(a) were measured using the Bonsai autocorrelator, while the plus and minus signs correspond to the positive and negative chirp values, respectively.

As can be inferred from Fig. 5.4(a), the spectral locations of the harmonics are spectrally blue shifted with respect to their positions estimated according to the setup optical geometry. This is a known behavior in the literature [104, 111, 112] and it has been identified as the result of mainly two mechanisms [113].

The first mechanism is the propagation effects of the laser pulse in the ionized medium. The partial ionization of the generating medium during the laser pulse induces a variation of the refractive index $\delta n_L(\mathbf{r}, z, t)$ [114]

$$\delta n_L(\mathbf{r}, z, t) = -\frac{2\pi e^2}{m_e \omega_L^2} \mathcal{N}_e(\mathbf{r}, z, t), \tag{5.1}$$

where $N_e(r, z, t)$ describes the electron density. This leads to a blue spectral shift of the laser field [115]

$$\delta\lambda_L = -\frac{\lambda^3 e^2}{2\pi m_e c^3} \frac{d\mathcal{N}_e}{dt} L, \tag{5.2}$$

where L is the propagation length. The spectral blue shift of the harmonics results from both the change in the refractive index at the frequency $q\omega$, i.e.

$$\delta\lambda_q = \delta\lambda_L / q, \tag{5.3}$$

as well as the spectral shift of the fundamental, i.e.

$$\delta\lambda_q = -\frac{(\lambda_L/q)^3 e^2}{2\pi m_e c^3} \frac{d\mathcal{N}_e}{dt} L = \delta\lambda_L / q^3. \tag{5.4}$$

The second mechanism is the nonadiabatic response of the electronic dipole of

the generating medium to the rapid change of laser fields. Since the laser intensity is rising in the leading edge of the pulse, the recolliding electrons gain more energy with each successive laser field cycle. Therefore, the HHG at the leading edge of the laser pulse induces a positive chirp in HHG, thus leading to a blue spectral shift in HHG [116]. It should be emphasized here that blue shift is observed for high intensity laser pulses where the process of HHG occurs at the leading edge of the pulses, as in this study. When HHG occur at lower intensities, i.e. at the peak of the laser pulses, blue shift is absent in HHG spectra.

From Fig. 5.4(a) it is also evident that the 17^{th} and 15^{th} low order harmonics are seen to be strongly suppressed in the spectral images. This is due to their strong absorption by the Ar gas as can be inferred from Fig. 5.3, where the XUV transmission in Ar gas at pressure of 60 Torr and a length of 5 mm is estimated [75].

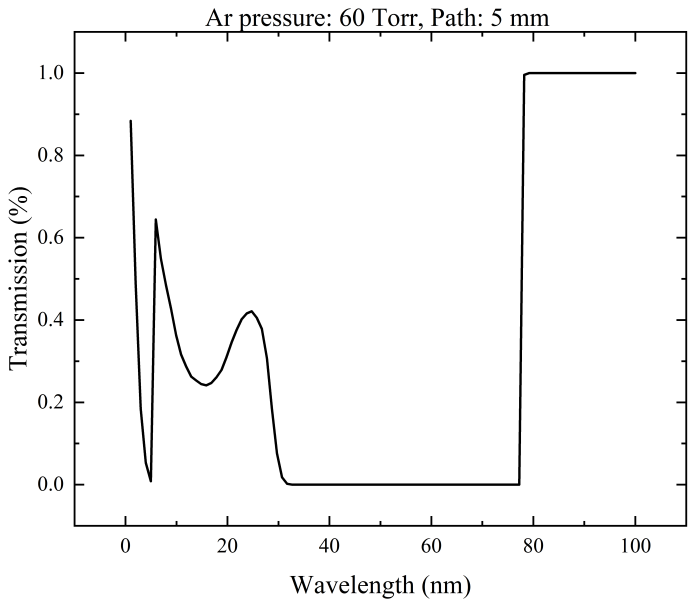

Figure 5.3
XUV transmission in Ar gas at pressure of 60 Torr and a length of 5 mm (calculated using the tools provided at the The Center for X-Ray Optics, Lawrence Berkeley National Lab, `https://henke.lbl.gov/optical_constants/gastrn2.html`, accessed August 13, 2023.).

In accordance with the above interpretations, it is seen in Fig. 5.4(a) that the harmonics generated by negatively chirped laser pulses exhibit an overall stronger blue shift that increases with increasing the negatively chirped laser pulse duration. Additionally, for certain chirp values, the blue shift is not the same for the short and long trajectories, the latter identified by their larger divergence. This is evident for the cases of laser pulse duration -43 fs and -30 fs, as well as the FTL case of 26 fs. For

these cases, the long trajectories, exhibit a stronger blue shifting, most possibly due to the fact that the long trajectory travels longer distances in the partially ionized medium. Thus, this clear separation of the long and short trajectory is realized in our method by simply varying the laser pulse chirp values in high intensity laser pulses that promote HHG at the leading edge of the pulse.

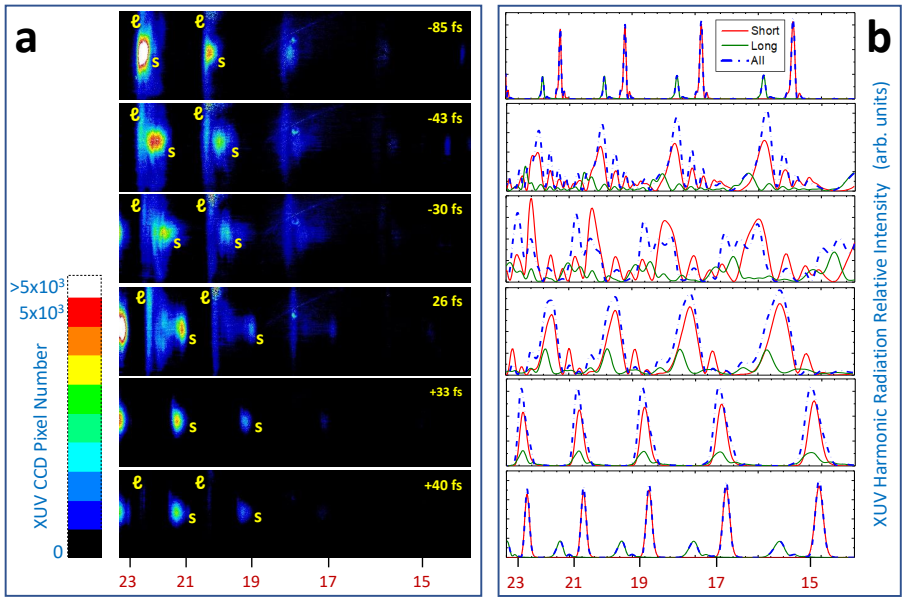

Figure 5.4
(a) Representative measurements of XUV harmonic spectral images for various laser pulse durations controlled by the imposed chirp. The harmonics spectral locations are noted at the bottom of the figure. Negative and positive signs of the laser pulses durations correspond to negatively and positively chirped laser pulses, respectively. The the short and long trajectories, indicated by the letters "ℓ" and "s", respectively, are spectrally separated for certain chirp values. (b) XUV harmonic spectra obtained with our model calculations corresponding to the experimental conditions of their counterpart XUV harmonic spectral images in (a). Both short and long trajectory contributions, as well as their coherent addition, are presented. It is seen that the calculations fairly reproduce the main qualitative characteristics of the measured spectral images. Note that the 17^{th} and 15^{th} order harmonics are seen to be strongly suppressed in the experimental spectral images due to their strong absorption by the Ar gas, a condition not included in the simulations. (from Ref.[110])

The most significant finding of this study is that at a positive chirp value corresponding to the laser pulse duration of +33 fs, the long trajectories are severely suppressed, thus leaving only the short trajectories in the spectral image. This suppression is fully within the dynamic range of our XUV CCD camera and it is not a matter of color scale choice. This behavior is of exceptional importance not only for fundamental Physics but also for applications in coherent diffraction imaging as well as in attoscience.

Indeed, for high quality imaging applications the presence of both trajectories introduces chromatic aberrations [32, 117]. For a qth-order harmonic, the different

contributions of the short and the long trajectories result in different virtual generation positions. Thus, when the harmonic is refocused, the images of the long and short trajectories will not be fully overlapped at the focal area, thus leading to an overall smearing of the image profile. In addition, larger divergent beams reduce the numerical aperture of an optical system. Similarly, in attoscience, the presence of both trajectories largely degrades the quality of the formation of attosecond pulse trains and their corresponding use. From all the above it becomes clear that the understanding of the underlying physical mechanisms is of fundamental importance for the control of this behavior. For this model calculations, presented below, have been developed in an effort to understand and interpret this phenomenon.

5.2.2 HHG Spectral Calculations

The Model

A model for HHG spectral calculations has been developed based on the phenomenological model introduced by Carlstrom *et al.* [41]. The model treats the problem as single atom response only temporally, omitting the spatial contributions like spatial phase matching, laser focusing, and SPM outside of the laser k-vector. Our model is an extension of the Carlstrom model, the extension related to the addition of the temporal dependence of the Ar gas ionization and of the laser propagation in the generating medium that induces spectral variations owed to SPM induced by the optical Kerr effect and by the plasma. This extension is indispensable for our HHG conditions since the laser peak intensity is in most of the cases higher than the intensity inducing considerable Ar gas ionization, and thus the higher order harmonics are generated at the different temporal intervals of the leading edge of the laser pulse as seen in Fig. 5.5.

The electric field of the q^{th} order XUV harmonic radiation, corresponding to the short and long trajectories, symbolized with the subscripts s and l, respectively, can be written as [41]

$$E_{s/l}(t) = C_{s/l} I^{\frac{n}{2}}(t) \exp\left[iq\omega_L(t) + i\frac{qb(\tau)}{2}t^2 + i\alpha_{s/l} I(t) + i\Phi^0_{s/l} \right], \tag{5.5}$$

where $I(t)$ is given by the Eq.(2.22), $b(\tau)$ is given by Eq.(2.26). ω_L is the instantaneous laser frequency, including SPM modifications by Kerr-effect in the atoms and by the plasma

$$\omega_L(t) = \omega_{L0} + \omega_{SPM}(t) + b(\tau)t, \tag{5.6}$$

where ω_{L0} is the central laser frequency, and ω_{SPM} is given by Eq.(2.28). $C_{s/l}$ are weights for each of the short and long trajectories while n is a non-linearity parameter for the HHG conversion. $a_{s/l}$ are the dipole phase constants [106, 118] and $\Phi^0_{s/l}$ is a phase offset depending on the atomic properties. In our extended model, the time dependent laser angular frequency ω_{SPM} accounts for the SPM effects caused by the laser propagation in the non-linear medium.

The HHG spectral intensity is calculated as the absolute square of the Fourier transform of the coherent summation of the E-fields over the participating harmonics. For each harmonic the E-field of the short and long trajectory is considered. Thus, the spectral intensity equation reads

$$I(\omega) = \left| \mathcal{F} \left\{ \sum_q [E^q_s(t) + E^q_l(t)] \right\} \right|^2 . \tag{5.7}$$

In the model, we explicitly include the ionization of the medium, since it is the primary competing process for the laser intensities used in this work. For this we use the ADK model, appropriate for tunneling ionization that prevails for the laser intensity conditions used here. The generated electric field of the qth order XUV harmonic radiation obtained in Eq. (5.7) is multiplied by the probability that the atoms of the generating medium have not been ionized by tunneling ionization, i.e.

$$E^q_{s/l}(t)_{\text{out}} = [1 - P(t)] E^q_{s/l}(t), \tag{5.8}$$

where $P(t)$ is the tunneling ionization probability up to the moment t, described by the Eq.(2.33). Calculation details can be found in Appendix E.

Calculations

Using Eq. (5.7), we simulated the experimental conditions and calculated the spectral intensity of the high harmonics in the region of interest. The aim of these model simulations was to qualitatively reproduce their main features and behavior of the experimental HHG spectra. The following values for the parameters were used in the model which result form experimental measurements or adopted from the literature:

- Laser pulse.
  - Laser wavelength $\lambda = 807$ nm.
  - FTL laser pulse duration, $\tau_{FTL} = 26$ fs.
  - Peak intensity for the FTL pulse $I_0(\tau_{FTL}) = 2.3 \times 10^{15}\,\text{W/cm}^2$.

- Argon generating medium.
  - Refractive index $n_0 = 1.0000$ for 60 Torr pressure.
  - Nonlinear index coefficient $n_2 = 1 \times 10^{-20}\,\mathrm{cm}^2/\mathrm{W}$ for 60 Torr pressure [118].
  - z_p, the distance of the laser beam propagating in the plasma, was estimated from the plasma luminescence images of the generating medium taken during measurements. Typical values are in the range of 1-2.5 mm depending on the chirped pulse duration.
  - z_g, the propagation length of the laser beam in the Ar medium before the HHG region, estimated as the Rayleigh length minus the plasma length experimentally measured for each laser chirp.
  - $\rho(t)$, the temporal function of the electron plasma density at the HHG area. The measured plasma luminescence varies along the the laser propagation axis, being strongest at the area closest to the exit pinhole of the semi-infinite cell, where HHG is efficient. By integrating the plasma luminescence along the plasma channel, a single plasma luminescence value is extracted at each laser chirp. By corresponding the maximum luminescence value to the maximum electron plasma density that can be reached for a singly ionized 60 Torr Ar gas density ($1.5 \times 10^{18}\mathrm{cm}^{-3}$), an average electron plasma density, that the laser beam experiences along its propagation inside the plasma channel, is extracted. The temporal function of the electron plasma density at the HHG area, $\rho(t)$, described by Eq. (2.28), is estimated by multiplying the previously extracted average plasma density with the temporal ADK ionization probability, described by Eq. (2.33).
- HHG phase parameters α_s and α_l for the short and long trajectories, respectively [41].
  - $\alpha_s = 0.5 \times 10^{-14}\,cm^2/W$.
  - $\alpha_l = 13 \times 10^{-14}\,cm^2/W$.
    These values were kept at the same values for the five plateau harmonics of the simulated spectral region since this is an acceptable approximation for close neighboring plateau harmonics. We emphasize that small variations in the above values did not seem to appreciably alter the final results, maintaining the constraint that $\alpha_l >> \alpha_s$, which is well established in the literature [41].

In addition to the above, the high harmonic phase offset $\Phi^0_{s/l}$ was set to zero, since it only corresponds to an offset in the harmonic E-field interference. Finally, it is a common observation in our HHG spectra, for the conditions where the high harmonics generated by the short and long trajectories are spectrally separated, that short trajectory high harmonic exhibit a higher signal than the long trajectory high harmonic. We experimentally estimate an overall acceptable ratio of $C_l/C_s \simeq 0.6$, and thus this value was adopted in our simulations.

In Fig. 5.4(b) the spectral model calculations based on Eq. (5.7) are presented for the conditions that simulate the corresponding experimental spectral images in Fig. 5.4(a), as described above. It is evident seen that the model calculations reproduce fairly well the main qualitative characteristics of the measured spectral images as they predict:

- The spectral separation of the HHG for the long and short trajectories at the corresponding experimental pulse durations.
- The coherent mixing of the two quantum paths when they are not appreciably spectrally separated (e.g. for the 26 fs case).
- An increase in the ratio between short and long trajectory contributions for the case of the optimal pulse chirp (+33 fs), as compared to the severe suppression of the long trajectory observed in the corresponding experimental data. We attribute this to the fact that our model treats the problem as single atom response.

Note that in the spectral model the self-absorption of the high harmonic in argon medium was not included in the simulations. This explains the presence of high harmonic intensity in the spectral region of the 15^{th} - 17^{th} harmonics, as opposed to the experimental spectral images.

To further investigate the above behavior, the temporal variation of the plateau harmonics E-field, corresponding to the spectra of Fig. 5.4(b), is presented in Fig. 5.5 (red line, Eq. (5.5)). In the same figure, the laser intensity (black line, Eq. (2.22)), the laser angular frequency (blue line, Eq. (2.29)) and the medium ionization probability (green line, Eq. (2.33)) are also presented as a function of time in the same temporal window for direct comparison. Calculation details can be found in Appendix E. From these it evident that HHG takes place during the leading edge of the laser pulse at an intensity interval determined by laser pulse duration the medium ionization around its half-maximum value. For higher laser pulse intensities, medium ionization prevails and HHG is diminished.

From Fig. 5.5 it is also evident that, for high laser pulse intensities, i.e. for small chirp values, the laser angular frequency is strongly modulated due to SPM effects. This strong modulation along with the temporal variation of the laser intensity within the HHG intensity interval are fundamentally responsible for the structure of the spectral images, as seen from Eq. (5.5). Thus, SPM effects play a major role in the generation of high quality harmonics corresponding essentially to short trajectories.

It should be noted that similar additional measurements were performed where the Ar gas pressure was varied. These showed that the suppression of the HHG from the long trajectory routinely appeared for small positive chirp values and corresponding laser pulse durations in the range of +30 to +40 fs. This is fully supported by our spectral model calculations since small variations in the values of the physical parameters of the model do not appreciably alter the findings.

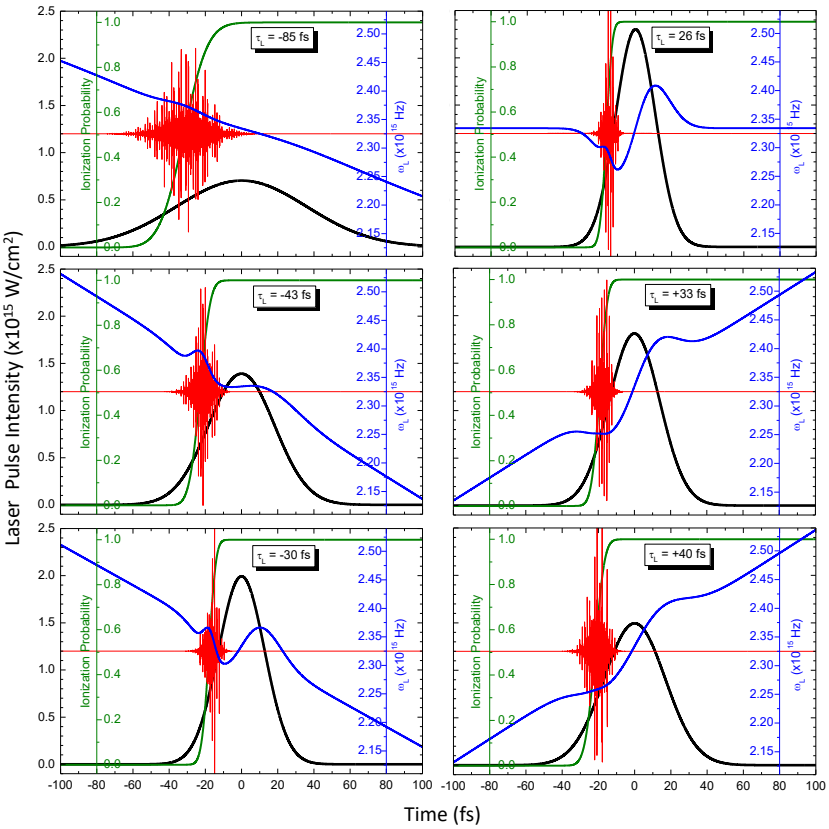

Figure 5.5
Details of our model calculations corresponding to the cases presented in Fig. 5.4. Black line: Laser intensity; Blue line: Laser angular frequency accounting for the linear laser chirp and SPM effects in the non-linear Ar medium and the plasma; Green line: ionization probability of Ar according to the ADK model; Red line: Generated XUV radiation E-field, arbitrarily scaled along the y-axis in each graph for presentation purposes. (from Ref.[110])

5.3 Conclusions

Our experimental results and model calculations clearly show that the chirp of the laser pulses is a crucial parameter for the control of the electron quantum paths in the HHG. This control affects the HHG spectra (a) by spectrally separating the short and long trajectories in the plateau harmonics, and (b) by significantly affecting their relative generation efficiency. In this work, it is demonstrated that the HHG efficiency of the long trajectory is dramatically reduced compared to that of the short trajectory, simply by adjusting the frequency chirp of the driving laser pulse to an appropriate value. This effect is attributed to the interplay of the inherent quantum phases for each quantum path, controlled by the fine adjustment of the HHG temporal window within the laser pulse envelope, the slope of the temporal intensity at this window, and the chirp of the laser pulse. The above conditions are met for laser intensities that cause a significant degree of ionization in the generating medium, that defines the temporal window for HHG.

The key feature of our method compared to the previously reported ones [14, 32, 98, 99, 107–109], is the simplicity. The only parameters that requires is the appropriate selection of (a) the intensity of a single driving laser field, (b) the atomic target, and (c) the accurately controlled laser frequency chirp. In addition, since our method utilizes a semi-infinite cell, the generating medium can be easily kept at the same conditions throughout the measurements, further supporting the experimental repeatability. Thus, our method is easily applicable with an enhanced potentiality for applications such as the new generation high average power MHz amplified fs laser systems, which is the new trend for high averaged power XUV high harmonic sources, favorable for imaging applications and for basic research in storage ring accelerators.

Finally, our finding that, under certain experimental conditions, plateau harmonics are fully attributed to the short electron trajectory is emphasized. The geometrical characteristics of such coherent harmonic radiation significantly favors coherent diffraction imaging applications in the scale of few-tenths of nanometers [32]. Furthermore, high efficiency plateau harmonics generated by only the short trajectory, could be used in the attosecond pulse formation, since the produced attosecond pulses exhibit single sign frequency chirp, and thus could be compressed to their FTL value.

Chapter 6

Spectral and Divergence Characteristics of HHG

6.1 Introduction

In Chapter 5, it was shown that the HHG spectral and divergence characteristics manifest the quality of the coherent XUV source. These depend on the dynamic response of the generation process both at the atomic level as well as at a macroscopic level.

At the atomic level, the dynamics is governed from the two surviving quantum paths that result in a recollision with the parent ion, i.e. the short and long trajectories, respectively. The temporal characteristics of the plateau harmonics depend strongly on the phase difference between the long and short trajectories. At the macroscopic level, the dynamics is governed by the coherent addition of the generated harmonics in each laser half-cycle. This coherent addition is affected by propagation effects detailed in Subsection 2.2.3.

Moreover, in conditions of strong laser pulses, the laser field may suffer variations with respect to the temporal arrangement of its spectral content (chirp), and consequently to its pulse duration and temporal intensity due to SPM effects discussed in Subsection 5.2.2. SPM effects, depending on their strength, may result in spectral lines shifting and broadening that significantly affect the HHG spectra and their divergence [110].

From the above it becomes evident that the quality of the HHG source, in terms of the geometrical and phase characteristics of the harmonics beam, depends strongly on the temporal characteristics of the long and short trajectories as well as on the SPM effects. Thus, developing methods for controlling the relevant

contribution of long and short trajectories of the plateau harmonics, and the role of the SPM effects is of fundamental significance.

This chapter presents a systematic study on the spectral and divergence characteristics of plateau harmonics within an Ar-filled semi-infinite gas cell. Various gas pressures and laser beam focal conditions are explored against the chirp imposed on the laser pulses. The evolution of plateau HHG spectra and their divergence from positive to negative chirp values with increasing gas pressures is monitored. The study clealy indicates that, under high laser intensity conditions, the maximum HHG signal occurs with negatively chirped pulses close to the FTL value of the laser pulses, even at low gas pressures. For higher pressures, additional and broader lines emerge in the HHG spectra, resembling a quasi-continuum spectrum. This feature holds significance as the secondary coherent HHG source can be easily tuned to denser spaced wavelengths. Moreover, the contribution of long and short trajectories to HHG spectra, evident in their divergence, is tracked with the smooth variation of chirp. Unlike existing literature reports such as [119, 120], this work records both HHG spectra and HH divergence simultaneously, providing a finer tool for investigating the delicate dynamics behind HHG and the role of short and long trajectories. Finally, calculations based on the phenomenological model presented in Subsection 5.2.2 accompany the experimental findings.

6.2 Results

The data were collected with the geometry of the experimental setup presented in Chapter 5, the optical layout of which is presented in Fig.5.2. The findings of our study are summarized in Figs. 6.1 and 6.2, where the spectral images of the plateau harmonics, $15\omega_{L0}$–$23\omega_{L0}$, accompanied by their corresponding plasma formation images, are systematically recorded as a function of the laser pulse chirp for Ar gas pressures ranging form 30 to 90 Torr. In Fig. 6.1 the focus of the laser beam is at the exit pinhole of the semi-infinite cell, while in Fig. 6.2 it is 3 mm before the exit pinhole. Both sets of measurements were performed maintaining a constant laser pulse energy of 1.0 mJ as well as the same focusing conditions. The laser peak intensity for the FTL pulse of 26 fs was experimentally estimated to be $2.3 \pm 0.5 \times 10^{15}\,\mathrm{W/cm^2}$, which is far above the ionization saturation intensity for Ar. The pulse durations, indicated in the spectral images in Figs. 6.1 and 6.2 with plus and minus signs, correspond to the positive and negative chirp values, respectively. The color code scale in Figs. 6.1 and 6.2 was kept identical for both XUV spectral as well as plasma images for comparison purposes. The main features that are readily observed in the images are the following:

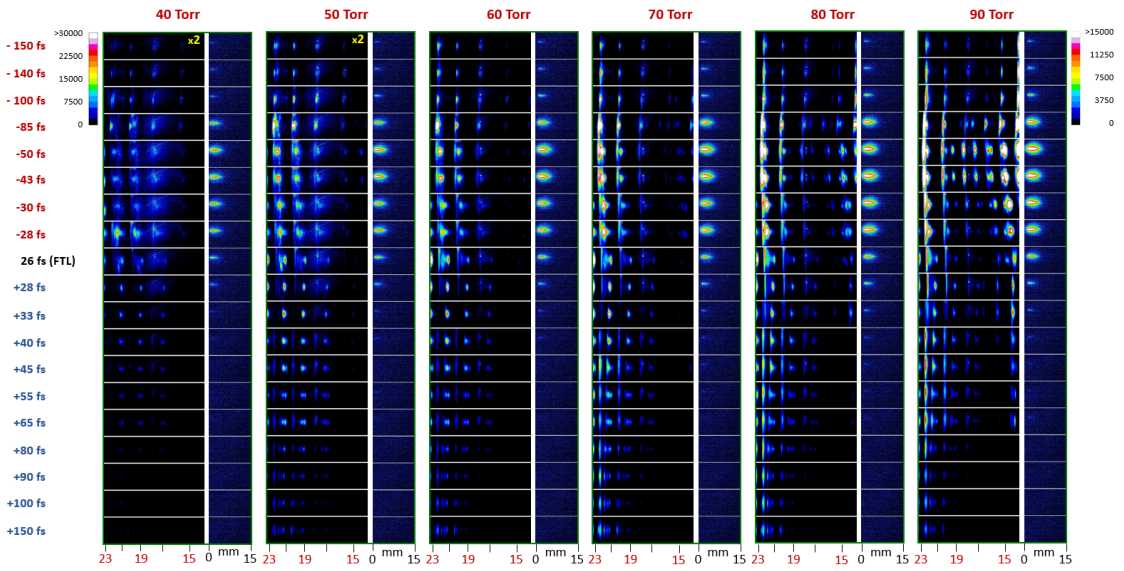

Figure 6.1
XUV harmonic spectral images (left) and corresponding plasma formation images (right) measured for various laser pulse durations and Ar gas pressures. The focus of the laser beam is at the exit pinhole of the semi-infinite cell. The negative/positive sign of the laser pulse durations correspond to the negatively/positively laser pulses, respectively. The nominal spectral locations of the harmonics order are noted at the bottom of the XUV spectral images for each gas pressure. The color intensity of the XUV spectral images corresponding to the pressures of 40 and 50 Torr was multiplied by a factor of two for better visibility. (from Ref.[121])

Line broadening and quasi-continuum spectra

For low negative chirp values ($<$ -50 fs), the plateau HHG signal experiences a remarkable enhancement, even at Ar gas pressures as low as 30 Torr. Simultaneously, the harmonic lines undergo considerable spectral broadening. At high gas pressures (90 Torr in Fig. 6.1 and above 60 Torr in Fig. 6.2), additional spectral bands emerge between the locations of the plateau harmonics, resulting in a spectrum resembling quasi-continuum. This spectral behavior is related to the increased degree of ionization in the generating medium, as indicated by corresponding plasma luminescence images. Notably, this feature is absent for lower negative chirps ($<$ -85 fs) or any positively chirped laser pulses, where the degree of ionization is significantly smaller.

To quantify this behavior, the relative enhancement of the integrated measured XUV emission in the spectral bands between harmonic locations was assessed. Specifically, attention was directed to the case of -43 fs laser pulse duration in Fig. 6.2, where the overall XUV emission is observed to be maximized. The spectral bands considered have bandwidths, $\Delta\lambda$, of (38.5-41.3), (42.4-45.4), (48.4-50.5), and (53.7-56.0) nm, as determined from the 30 Torr pressure XUV image.

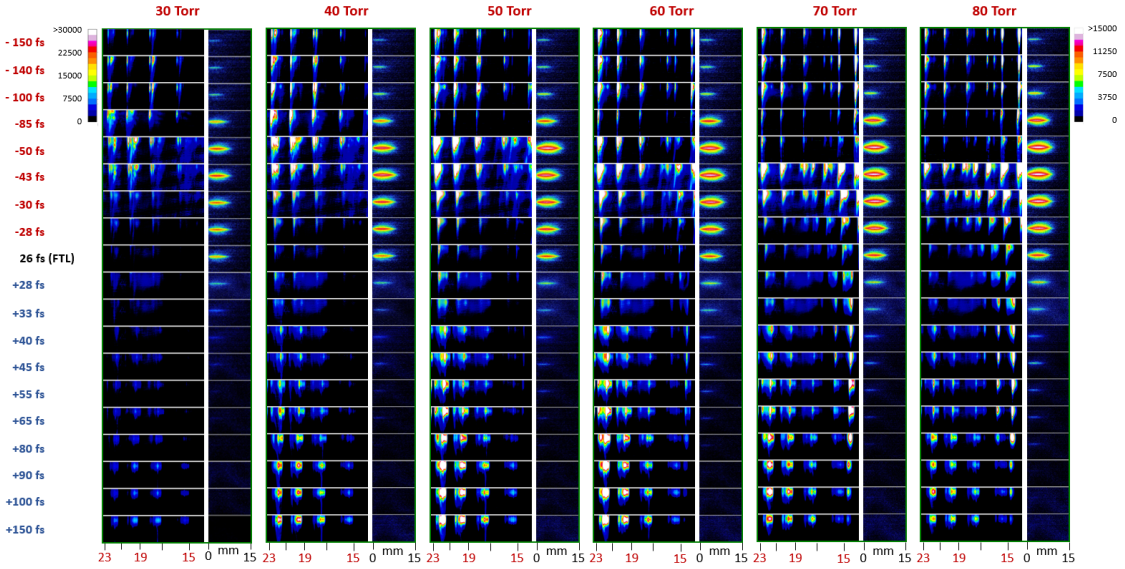

Figure 6.2
Same as in Fig. 6.1, except that the focus of the laser beam is 3 mm before the exit pinhole of the semi-infinite cell. (from Ref.[121])

The enhancement of XUV emission for each band was determined as the ratio of integrated XUV emission for each pressure to that of 30 Torr, the latter being close to the detection limits of our system. The relative enhancement of XUV band emission is presented as a function of generating gas pressure in Fig. 6.3. Results clearly indicate an overall relative enhancement factor between 5 and 6 for the bands of (38.5-41.3), (42.4-45.4), and (48.4-50.5) nm. However, the band of (53.7-56.0) nm exhibits enhancement for pressures up to 60 Torr, followed by a reduction for higher pressures. This is attributed to wavelength absorption at high Ar density values, as inferred from [75].

Harmonics divergence and quantum paths separation

A notable characteristic of the spectral images is the variation in the divergence of plateau harmonics as the laser chirp varies from positive to negative values. This feature is clearly evident in Fig. 6.1, whereas it is less pronounced in Fig. 6.2, where higher and broader XUV emission obscures the divergence characteristics. Upon closer inspection in Fig. 6.1 of the spectral area for each harmonic, two components, attributed to the long and short electron trajectories, are identified. Their identification is based on their distinct divergences, with the long trajectory exhibiting higher divergence as it was explained in Subsection 5.2.1. Moreover, their spectral splitting is due to their spectral blue shift, with the long trajectory experiencing a more pronounced shift, appearing at shorter wavelengths [41]. Specifically, the divergence of the 21^{st} harmonic's short and long trajectories, as a

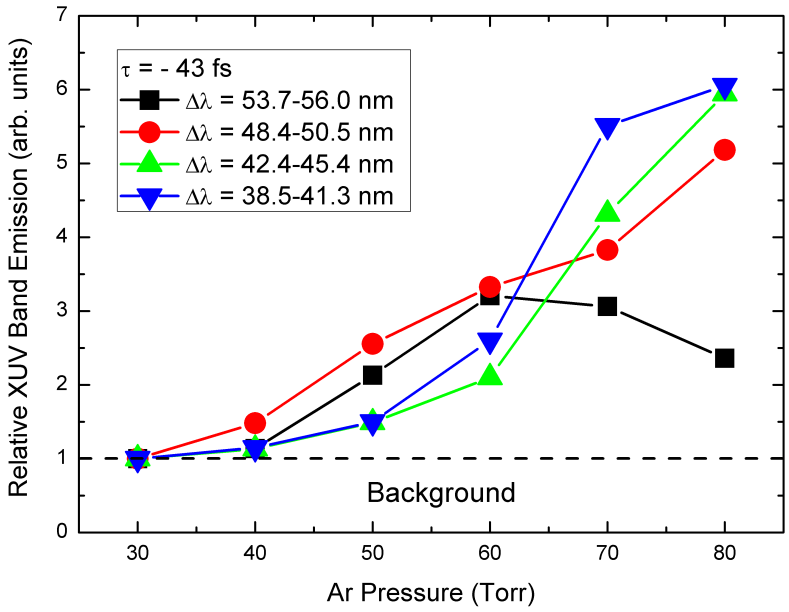

Figure 6.3
Relative enhancement of the measured XUV band emission for the spectral areas between the harmonics as a function of the generating gas pressure. The data correspond to those of Fig. 6.2 for the pulse duration of τ=-43 fs. Relative XUV band emission error bars are estimated lower than 1% and are within the data symbols. (from Ref.[121])

function of the chirped laser pulse duration for the case of 90 Torr Ar gas pressure in Fig. 6.1, is presented in Fig. 6.4.

Spectral shift

The plateau harmonics undergo an overall spectral shift as the chirp of the laser pulse varies from positive to negative values. From Fig. 6.1, where the short and long trajectories are more distinctly spectrally separated, it is evident that the long trajectory is more blue-shifted as opposed to the short trajectory. This behavior has been reported in the literature [104, 111–113], aligning with our measurements.

An intriguing characteristic, observed in both Figs. 6.1 and 6.2, is the rapid change of the spectral blue shift around the area of low-value negatively chirped laser pulses ($<$ -43 fs). This behavior is closely related to the intense plasma formation under these conditions. To quantify this effect, the overall spectral shift of the high-order harmonics 17^{th}, 19^{th}, and 21^{st} is presented in Fig. 6.5 as a function of the laser chirp for an Ar gas pressure of 80 Torr.

Wavelength tunability

Building upon the aforementioned observations, HHG can be regarded as a secondary coherent XUV source with tunable wavelength. The tunability is based

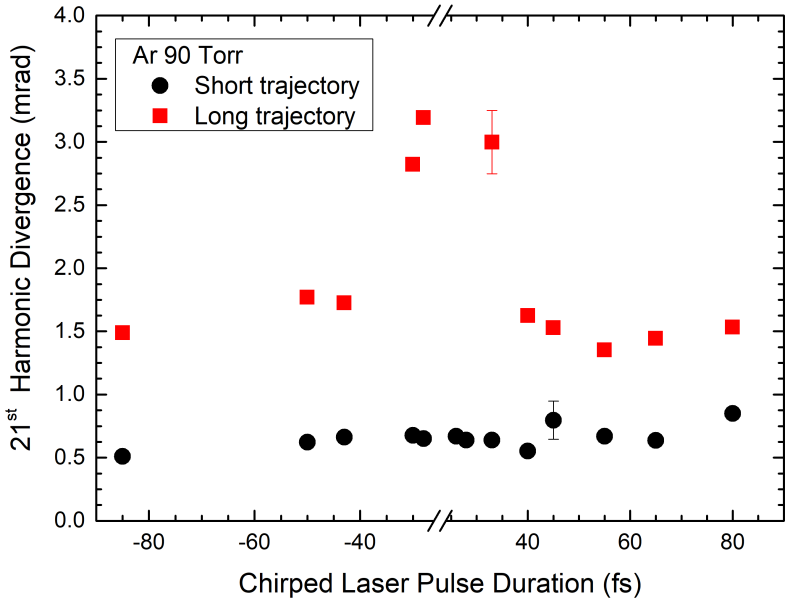

Figure 6.4
Experimentally determined divergence of the 21^{st} harmonic short (black solid circle) and long (red solid square) trajectories as a function of the chirped laser pulse duration for the case of 90 Torr Ar gas pressure of Fig. 6.1. Indicative error bars for the short and long trajectories are shown. (from Ref.[121])

upon: (a) The blue shift of a harmonic as the chirp varies from positive to negative values. (b) The broadening of HHG lines and the emergence of XUV spectral bands between harmonics, forming quasi-continuum spectra.

6.3 Discussion

The above presented qualitative features of XUV spectral images necessitate a thorough understanding and interpretation. An effort towards this goal will be given here.

For an intense laser pulse, where the HHG process is not confined at the peak of the pulse envelope, the change in its chirp corresponds to a variation in the temporal window of the laser pulse during which HHG occurs. In more detail, for negatively chirped pulses, HHG primarily occurs at the leading edge of the pulse. This is because at higher intensities, the competing process of ionization takes over, as seen in the intense plasma formation images in Figs. 6.1 and 6.2. Therefore, HHG conditions are significantly influenced by the slope of the temporal intensity and frequency of the laser pulse in this temporal window [110]. On the other hand, for positively chirped pulses, plasma formation is marginal. Hence, HHG is expected

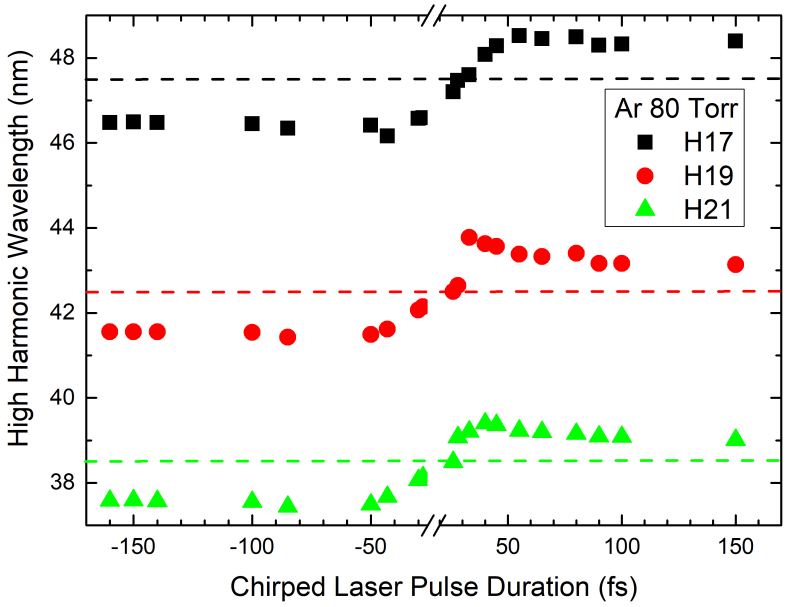

Figure 6.5
Experimentally determined spectral shifts of the high order harmonics 17^{th} (black solid square), 19^{th} (red solid cirlce), and 21^{st} (green solid triangle) as a function of the chirped laser pulse duration for the pressure of 80 Torr of Fig. 6.2. Dashed horizontal lines correspond the unshifted harmonic peak positions. Estimated error bars are within the data symbols. (from Ref.[121])

to occur over a broader temporal window of the laser pulse, which, for high positive chirp values, includes the envelope peak area.

The spectral shift of harmonic peaks, quantified in Fig. 6.5, is attributed to the nonadiabatic response of the electronic dipole to the rapid change in the laser field and the propagation effects of the laser pulse in the partially ionized medium, as described in Section 5.2.1. In more detail, laser pulses with large positive chirp values show barely measurable ionization, as seen in the plasma luminescence images in Figs. 6.1 and 6.2. Consequently, the absence of considerable plasma formation, coupled with intense laser peak values, results in an overall red shift for the generated harmonics (see Eq. (2.28)). As the positive chirp values decrease, SPM effects in the gas medium become more pronounced, causing a further red shift in the generated harmonics. This behavior changes rapidly as the laser pulse approaches positive chirp values close to the FTL duration. At this point, due to the higher laser pulse intensity, SPM effects of both the gas medium and the emerging plasma become significant, leading to the appearance of blue shifts as the chirp vary from positive to negative values. For lower negative chirp values ($<$ -85 fs), the harmonics still exhibit a blue shift, consistent with the considerable degree of ionization seen in the corresponding plasma images at these high chirp values.

It is noteworthy that higher plasma production is not observed for FTL pulses but rather for negatively chirped pulses with a duration of around -40 fs

due to the aforementioned SPM effects. Under these conditions, the medium is entirely depleted even before reaching the laser peak intensity, distorting the XUV spatiotemporal characteristics, as observed experimentally.

As discussed in Chapter 5, the spectral separation of the long and short trajectory contributions is evident from the divergence of each harmonic. Long trajectories exhibit larger divergence than the short ones, attributed to the fact that recolliding electrons travel longer paths in the generating medium [41]. This phenomenon is heightened when the generating medium is partially ionized, as is the case for negatively chirped pulses in our study. Moreover, for laser intensities inducing a relatively high degree of ionization in the generating medium, the central wavelength of the two trajectories is slightly different. This leads to coherent summation for each trajectory at different wavelengths, resulting in a double-peaking phenomenon [104]. The divergence of the two paths in HHG has been investigated in various early publications [9, 14, 100, 105, 106]. Experimental methods involving interferometric methods [107], multi-jet arrangements of two gases [98, 99], and phase-locked two-color ($\omega - 2\omega$) laser fields [32, 108, 109] have been developed to separate and selectively control the two trajectories.

Specifically, the spectral separation of the long and short trajectories is evident in Fig. 6.1 for positively chirped pulses. The long trajectory displays a narrower bandwidth and larger divergence compared to the short trajectory, which has a broader bandwidth and much lower divergence. Additionally, the long trajectory is blue-shifted to smaller wavelengths than the short one, facilitating their clear identification. For negatively chirped pulses with durations close to the FTL value ($<$ -50 fs), the spectral separation of the long and short trajectories is still noticeable, though not as pronounced as in the case of positively chirped pulses. Both trajectories undergo a considerable blue shift, leading to partial spectral overlap. At even larger negative chirp values, the blue shift of the long and short trajectories results in complete spectral overlap. However, the large divergence of the long trajectory and the higher intensity of the short trajectory are retained. Overall, it is evident that the signal of the short harmonic surpasses that of the long one. Particularly, for the +33 fs pulse duration and 60 Torr Ar gas pressure in Fig. 6.1, only the short trajectory survives in the HHG spectra. As an additional remark it is worth noting that HHG production at high positively chirped pulses is significantly increased in the case of Fig. 6.2 compared to Fig. 6.1. HHG production peaks for Ar gas pressures between 50 and 70 Torr, while it significantly drops for lower and higher pressure values, respectively.

Finally, considering the case of Fig. 6.2, where the spectral broadening effects are more pronounced, the observed blue shifts, line broadenings, and additional

spectral band appearance for small duration negatively chirped pulses ($<$ -50 fs) are primarily due to enhanced SPM effects of the generating gas and plasma formation. This is supported by the corresponding plasma images in Fig. 6.2, where the highest plasma production occurs for low-value negative chirps and high-value pressures.

For a more in-depth investigation, the HHG model presented in Chapter 5 was utilized, adjusting its parameters according to representative HHG conditions studied here, i.e. for chirped laser pulses of -150 fs, -43 fs, and 150 fs at an Ar gas pressure of 60 Torr, where the spectral and divergence characteristics are reasonably distinctive. The results of the model calculations are presented in comparison to their corresponding spectral images in Fig. 6.6. It is seen that the calculations fairly reproduce the main qualitative characteristics of the measured spectral images as they predict: (a) The marginal but evident spectral separation of the long and short trajectories for laser pulses with a duration of -150 fs. (b) The broader spectral lines and the spectral overlap between the short and long trajectories for laser pulses with a duration of +150 fs. (c) The line broadening and the appearance of additional spectral bands in between the harmonic spectral locations for laser pulses with a duration of -43 fs, thus resembling a quasi-continuum spectrum.

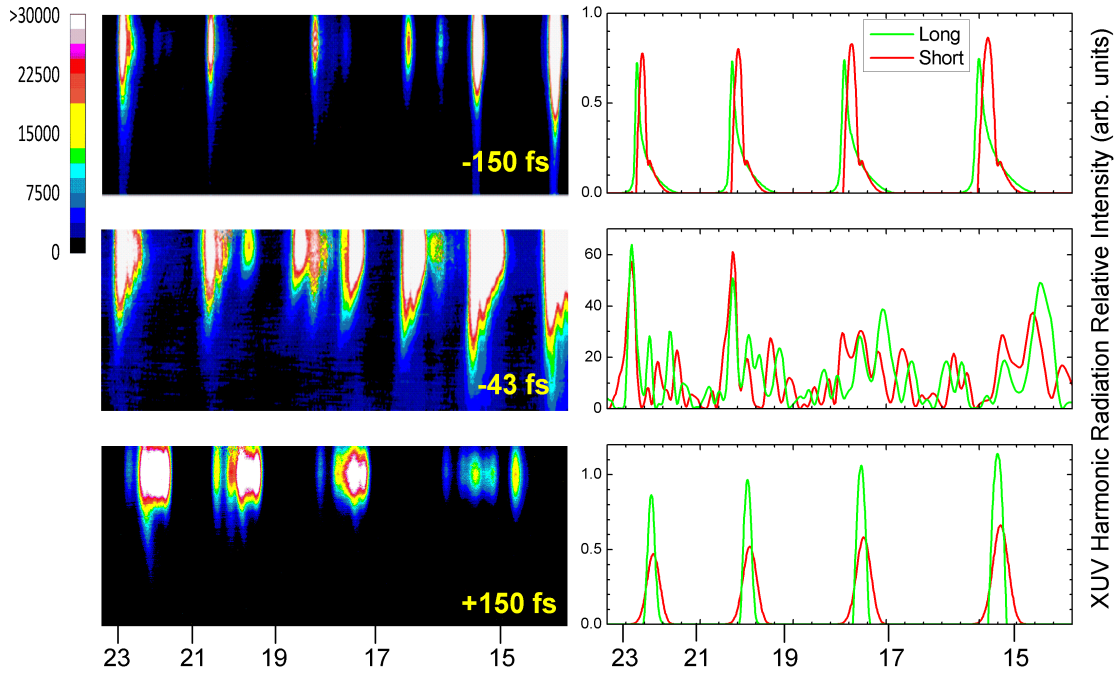

Figure 6.6
Qualitative comparison between measured XUV harmonic spectral images for chirped laser pulse durations of -150 fs, -43 fs and +150 fs, corresponding to those presented in Fig.6.2, and XUV harmonic spectra obtained with our model calculations, corresponding to the experimental conditions of their counterpart XUV harmonic spectral images. Long and short trajectory contributions are included separately. (from Ref.[121])

6.4 Conclusions

Based on the preceding analysis and discussion, it is evident that the frequency chirp of femtosecond laser pulses is a convenient and practical parameter for controlling the spatiotemporal properties of HHG spectra. This control can be easily and accurately achieved by detuning the ultrafast laser compressor gratings. Such control over HHG conditions and subsequent spatiotemporal characteristics of HHG spectra is crucial for a reliable and versatile coherent XUV source. Moreover, the utilization of a semi-infinite cell as the generating medium for the secondary HHG source aligns with the aforementioned conditions. Gas pressure is kept constant and can be adjusted at will, while the geometry of the generating gas medium can be managed according to laser beam focusing conditions, influencing plasma formation geometry and subsequent phase matching conditions. The method, initially presented in [110], contributes to previously reported methods [14, 32, 98, 99, 107–109] in the literature. It introduces novel features such as controlled wavelength tunability, based on the effects of blue shift and quasi-continuum generation, as well as the separation of short and long trajectories. Such a coherent XUV source significantly benefits coherent diffractive imaging applications [32], of interest in this dissertation.

Chapter 7

Coherent XUV Multispectral Diffraction Imaging

7.1 Introduction

This chapter presents our efforts towards the implementation of multispectral XUV CDI in transmission and reflection mode, based on the HHG setup described so far. Multispectral imaging in the visible part of the EM spectrum and longer wavelengths up to thermal infrared are well-documented in the literature, as different object details become discernible across spectral ranges [35–37, 122]. For example, the visible part of the EM spectrum is used for imaging of atmospheric pollutants, water, vegetation, soil, and biological tissues. The IR part is used for imaging of forest fires, geological features, clays, mapping terrain, and night studies. The extension of this technique in the XUV and soft x-ray wavelengths is of increased interest for the imaging community and currently under intense studies, as was emphasized by Nobel Laureate A. L'Huillier in her Nobel talk.

XUV CDI is a lensless microscopy technique, based on coherent XUV, soft x-ray or hard x-rays, first experimentally demonstrated in 1999 by Miao *et al.* [33]. Conventional XUV CDI involves an isolated sample that is simultaneously illuminated over its entire surface with spatial coherence to ensure that the intensity of the diffraction pattern from the sample is correctly captured by a camera, while the phase information is numerically recovered using iterative algorithms [123–127]. Furthermore, a scanning type of CDI method is ptychography [128–132], where the sample is scanned trough a focused beam of coherent radiation for well-overlapping multiple positions and the corresponding diffraction patterns are recorded. Although suitable XUV/soft x-ray sources were previously only available in large-scale facilities such as synchrotrons [133] and free-electron lasers [134], with

the advancement of ultrafast laser technology, XUV sources based on HHG allowed for table-top high spatial resolution CDI of fixed targets in transmission [135–140] and reflective modes [128, 129, 131], including femtosecond x-ray holography [141]. Indeed, as first demonstrated by Seaberg *et al.* [28], imaging of a sample with $\simeq$200 nm resolution was achieved using a single harmonic order at a wavelength of 29 nm. Over the past decade, rapid progress in understanding the dynamics and development of HHG sources [142] has resulted in a consequent increase of resolution at sub-wavelength values [143].

Here, our work on the development and proof-of-principe operation of a multispectral XUV CDI experimental setup is presented. The setup has been described in the previous chapters of this thesis, except for the operation of the last stage D, where the CDI measurements of solid targets in transmission and reflection mode are taken. Our system offers automated, in-vacuum selection of specific harmonics while preserving their coherence and pulse duration for CDI applications. Consequently, our system extends the multispectral paradigm to the XUV region of the EM spectrum. Detailed analyses of XUV CDI applications in transmission and reflection modes will be provided, demonstrating its efficacy in different experimental scenarios. A discussion regarding the implications of the findings and their potential for future discoveries will conclude the chapter.

7.2 HHG XUV Radiation Coherence

Laser beam coherence ensures the stability of wavefronts, a fundamental prerequisite for coherent interference phenomena. In CDI, the reliability of phase relationships among scattered waves hinges on the coherence of the laser beam. This coherence, both spatial and temporal, directly influences the clarity and precision of the interference patterns, laying the foundation for accurate structural reconstructions [144, 145].

The overall coherence of the XUV radiation produced was initially assessed by capturing diffraction images generated through the illumination of a copper grid. This grid, featuring a density of 70 lines per inch and wires with a thickness of 5 µm, was positioned at the entrance of stage C. Diffraction images were then acquired using the XUV CCD2 camera. Fig. 7.1b depicts the corresponding diffraction and reconstructed images, respectively. Due to the absence of spectral filtering during the acquisition of the diffraction image across the complete XUV spectrum, precise calculation of the characteristic lattice dimension from the reconstructed image proved challenging. However, leveraging the optical geometry arrangement and assuming an average XUV wavelength of 50 nm, the characteristic

grating dimension was approximated, closely aligning with the manufacturer's specifications. The results presented here are in agreement with what is reported in the literature [146].

Verification of the coherence of the filtered XUV radiation was subsequently undertaken, employing the pair of multilayer mirrors for the wavelength of 47.6 nm. To confirm the accuracy of the selected wavelength beam, a precision pinhole with a 50 μm diameter (Thorlabs, model P15C) was positioned in part D, as illustrated in Fig. 7.1c. There, the expected diffraction image (Airy disc) is shown, unequivocally confirming the agreement with the wavelength in use.

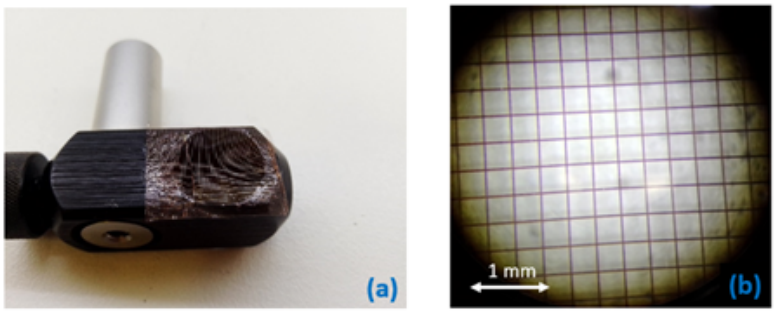

(a) The copper mesh with a density of 70 lines per inch. (a) Positioned on its base of support. (b) The copper mesh.

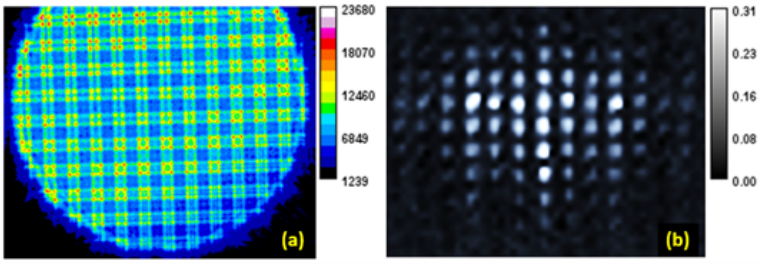

(b) Coherence measurements of the generated XUV radiation. (a) Diffraction image obtained by illuminating the copper mesh with the entire XUV spectrum. (b) Reconstructed image of the copper mesh. Axes in (a,b) are in pixel.

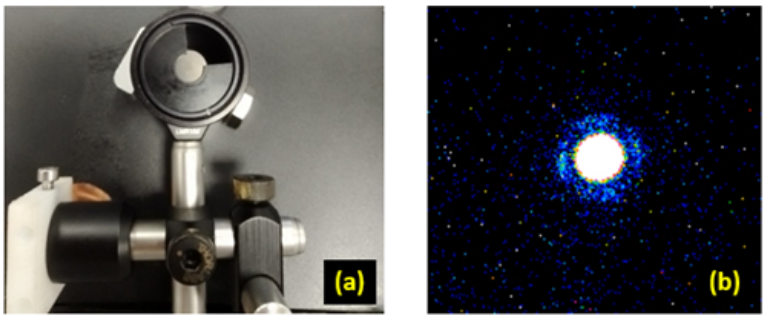

(c) (a) The 50 μm diameter precision pinhole, positioned on its base in the target section. (b) Diffraction image of the pinhole, represented as an Airy disk, captured utilizing the 47.6 nm filtered XUV beam.

Figure 7.1
XUV radiation coherence tests.

7.3 The XUV CDI Experimental Layout

The XUV experimental setup was described in detail in Section 3.5. However, the CDI layout of the entire setup, shown Fig. 7.2, will be presented here, including some more necessary details. The setup consists of four stages depicted with letters A, B, C, and D. Stage A is the semi-infinite cell filled with the gas target, where the XUV radiation is produced. Stage B is the differentially pumped chamber, that separates the high-pressure stage A from the low-pressure stages C and D. Stage C hosts all the necessary optical and optomechanical components for the optimization, filtering and selection of the XUV wavelengths, and propagation of the resulting XUV beam to the target area at stage D.

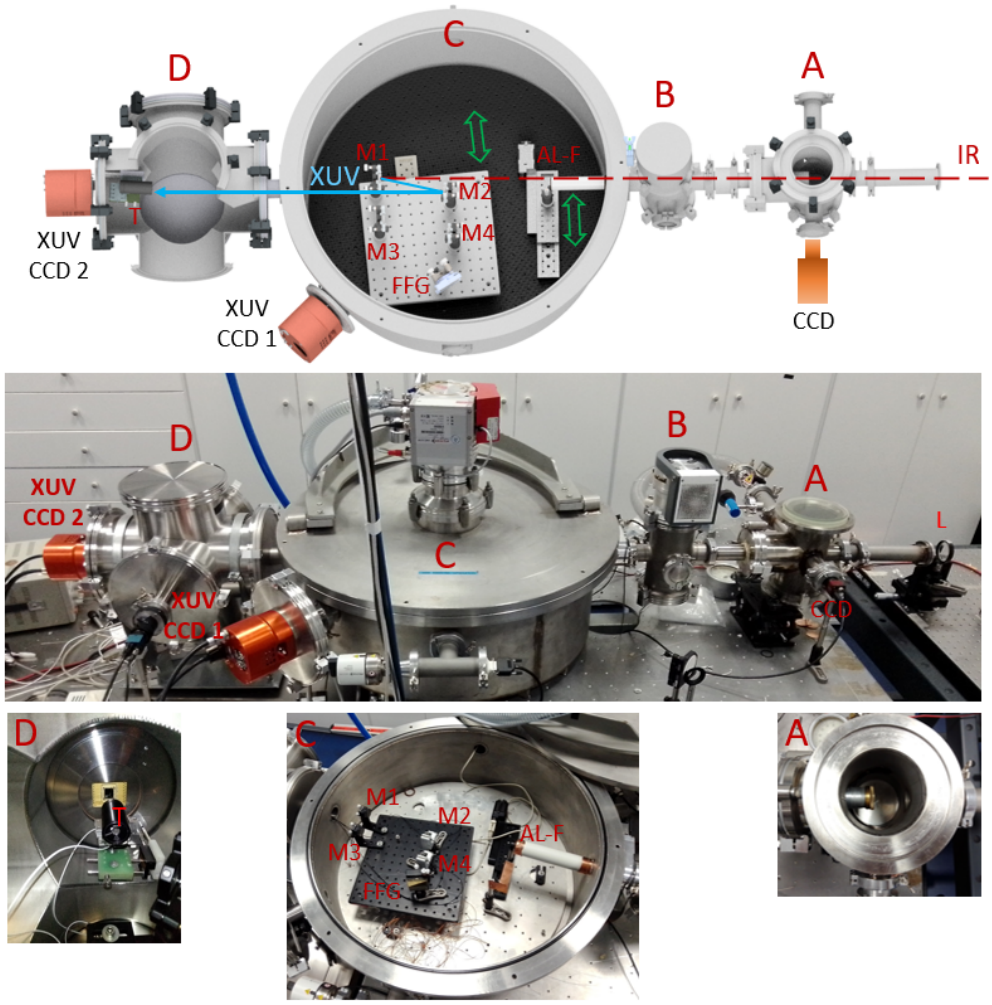

Figure 7.2
The XUV CDI experimental setup shown in a CAD design (top) and in the IPPL laboratory with zoom pictures for the stages of A, C and D (middle and bottom). A: The first stage hosting the semi-infinite gas cell. B: The second stage hosting differentially pumped region. C: The third stage hosting the XUV filtering, diagnostics and wavelength selection. D: The fourth stage hosting the target and the recording of the CDI result. L: Lens. AL-F: aluminum filter. M1, M3: Multilayer mirrors. M2, M4: Concave mirrors. FFG: Flat field Grating. T: Target. (from Ref.[88])

The mixed XUV and IR beam, upon entering stage C, is filtered from the IR laser residual beam using the 400 nm thick Al filter (see Subsection 3.4.1.2, while at the same time the XUV radiation spectrum of interest (i.e. 30 nm to 50 nm) suffers only an overall reduction in intensity. The selection of the wavelengths is done via two pairs of multilayer mirrors (See Subsection 3.5) that can be interchanged during the measurements. An optical layout of this feature is shown in Fig. 7.3. Each pair consists of a flat mirror and a spherical concave mirror, placed in opposite direction as shown in Fig. 7.2. The pair of multilayer mirrors reflects only a narrow band (∼2 nm) around a central wavelength, while the spherical mirror focuses the selected XUV beam onto the target at the fourth stage of the setup. Both sets of multilayer mirrors were specially manufactured to deliver the central wavelengths of 32.2 nm and 47.6 nm, respectively, at maximum reflectivity for the geometry in use.

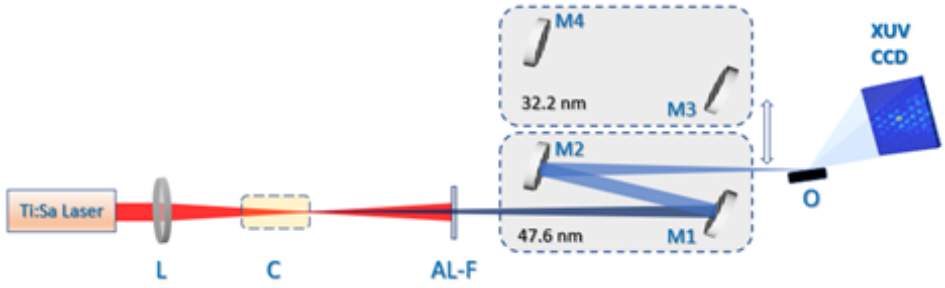

Figure 7.3
The optical layout of the XUV CDI experimental setup operating in reflection mode. L: Lens. C: Semi-infinite gas cell. AL-F: Aluminum filter. M1, M3: Flat multilayer mirrors. M2, M4: Concave spherical multilayer mirrors. O: Object. Two pairs of multilayer mirrors (M1, M2) and (M3, M4) can be interchanged allowing for the selection of the XUV wavelengths of 47.6 nm and 32.2 nm, respectively.

The fourth stage D hosts the target (object) that is mounted on a variable in the three dimensions XYZ base as well as in the polar rotation angle Θ (See Section 3.5). Vacuum compatible steppers for the four degrees of freedom are externally controlled and set with micrometer accuracy. Thus, the position of the target with respect to the laser focal area is accurately controlled. The monochromatic coherent XUV radiation diffracted by the target is recorded at the second vacuum compatible XUV CCD2 camera.

The software interface for controlling the initial XUV filtering, the selection of recording the XUV spectrum, the selection of the pair of mirrors for selecting the wavelength and the XYZΘ position control of the target is presented in Appendix F. The positions of the optomechanical devices can be calibrated independently and stored for future use or self-calibrated during the experiments.

7.4 Image Reconstruction

7.4.1 Fourier Theory

If a coherent plane wave light illuminates an object of density $f(r)$, the diffraction pattern in the far field is the Fourier transform of the function $f(r)$ [147]

$$\mathcal{F}(f(r)) \equiv F(k) = |F(k)| \exp(i\psi(k)), \tag{7.1}$$

where r and k are spatial and frequency coordinates in real and inverse space, respectively, and $\mathcal{F}$ is the Fourier transform operator. Thus, the Fourier transform of $F(k)$ can be written as amplitude and phase factors. In the experiment, only the intensity distribution of $F(k)$, i.e. $|F(k)|^2$, can be recorded by the detector while losing phase information due to the high frequency (9.4×10^{15} Hz for 32.2 nm and 6.4×10^{15} Hz for 47 nm). Therefore, in order to fully recover the density of the object, the phase of the function $F(k)$ given by $\psi(k)$ must be determined. Then, using the inverse Fourier transform we obtain [123]

$$f(r) = \mathcal{F}^{-1}\left(|F(k)|\, exp\left(i\psi\left(k\right)\right)\right), \tag{7.2}$$

where $\mathcal{F}^{-1}$ denotes the inverse Fourier transform operator.

The problem of phase retrieval from the diffraction pattern has been extensively studied in x-ray crystallography and can be solved using the oversampling method [123]. [1] Since the experiments use cameras with a certain number of pixels, Eq.(7.1) takes the following form

$$|F(k)| = \left| \sum_{x=0}^{N-1} f(r) \exp(-ik \cdot r) \right|, \tag{7.3}$$

where N is the number of pixels on the sensor side. In Eq. (7.3) the factor $f(r)$ contains the number of unknown equations. The degree of oversampling σ is given by the relation [123]

$$\sigma_o = \frac{\text{total pixel number}}{\text{unknown-valued pixel number}}, \tag{7.4}$$

where pixels refer to the object space. Eq.(7.3) is solvable for a 2D object if $\sigma_o > 2$ [123].

In CDI there is no reference wave and phase retrieval is not straightforward.

[1] Oversampling refers to the process of padding the density distribution function of an object with known values to increase the sampling rate of the signal spectrum in the Fourier domain.

Instead, the object distribution is obtained from the diffraction pattern through a process of iterations based on the Gerchberg-Saxton (GS) algorithm [148]. The main variants of the GS algorithm are the Error Reduction (ER) algorithm, the Hybridic Input - Output (HIO), and the reduced support algorithm Shrink - Wrap (SW) [125]. Algorithms have also been developed which try to deal with the problem of noisy and incomplete data. This category includes relaxed averaged alternating reflection (RAAR) [149, 150] with its variations and combinations with other algorithms [151]. It is worth noting that in recent years with the rapid increase in computing power and progress in the field of artificial intelligence, methods are being developed where the recovery of the phase, after the corresponding "training" of the respective model, is done almost in real time [152–155].

A work flow diagram for the above algorithms is presented in Fig. 7.4. Initially, the magnitude $|F|$ is obtained from the experimental CDI picture as the square root of the signal intensity for each pixel. Additionally, a starting guess for the phase of each pixel is given, along with $|F|$, as an input to the algorithm, thus forming the diffraction function $G' = |F|e^{-i\varphi}$ in inverse space at the detector plane. Then, by applying an inverse Fourier transformation, $\mathcal{F}^{-1}$, the object density distribution function, g', is obtained in real space at the object plane. In the next step, certain geometrical and methodological constraints, which depend on the algorithm in use, are applied, thus resulting in a new object density distribution function, g, at the object plane. The latter is then subject to a Fourier transformation, $\mathcal{F}$, resulting in a new diffraction function, $G = |G|e^{-i\varphi}$, in inverse space at the detector plane. The retrieved phase, φ, from this function, G, is inserted into the initial diffraction function $G' = |F|e^{-i\varphi}$, which has the experimentally measured magnitude $|F|$ as the input, thus initiating the next iteration step. The calculation is repeated for a predetermined iteration number of steps, which result in the final reconstructed image of the object.

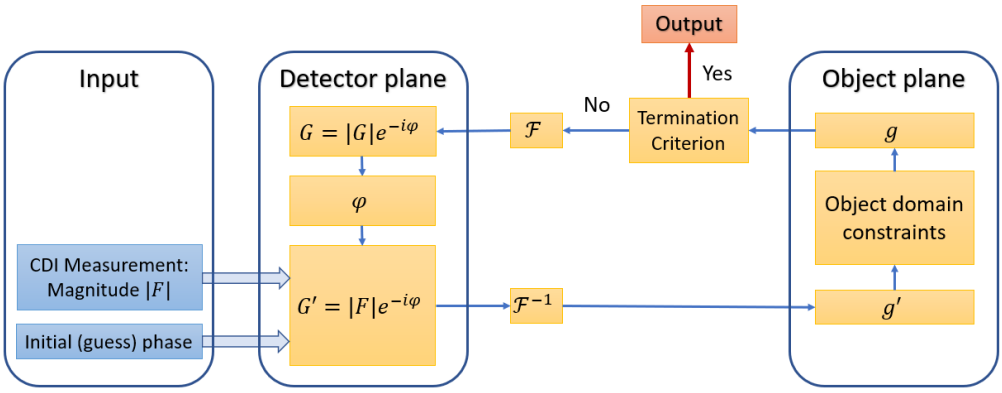

Figure 7.4
CDI reconstruction algorithm flow diagram. (from Ref.[88])

As a first step, a support area at the object domain, $S(x, y)$, usually is defined as follows: Initially, a Gaussian filter with a unity amplitude and standard deviation σ is applied to g'. Then, by defining a threshold value θ, the value at the (x, y) point of the support area $S(x, y)$ is set to zero or one for the g' filtered values below or above the threshold value of θ, respectively, i.e.,

$$S(x,y) = \begin{cases} 1 & g'(x,y) \geq \theta \\ 0 & g'(x,y) < \theta \end{cases} . \tag{7.5}$$

The object domain constraint for ER is [125]

$$g_{k+1}(x,y) = \begin{cases} g'_k(x,y) & (x,y) \in S \quad \& \quad g'_k(x,y) \geq 0 \\ 0 & (x,y) \notin S \quad \text{or} \quad g'_k(x,y) < 0 \end{cases} , \tag{7.6}$$

which for HIO, it is [125]

$$g_{k+1}(x,y) = \begin{cases} g'_k(x,y) & (x,y) \in S \quad \& \quad g'_k(x,y) \geq 0 \\ g_k(x,y) - \beta g'_k(x,y) & (x,y) \notin S \quad \text{or} \quad g'_k(x,y) < 0 \end{cases} , \tag{7.7}$$

while for RAAR, it is [149]

$$g_{k+1}(x,y) = \begin{cases} g'_k(x,y) & (x,y) \in S \ \& \ g'_k(x,y) \geq 0 \\ \beta g_k(x,y) + (1-2\beta) g'_k(x,y) & (x,y) \notin S \text{ or } g'_k(x,y) < 0. \end{cases} \tag{7.8}$$

where k is the k^{th} iteration.

Regarding the spatial constraints of the object, the density function within the support region is equivalent to the Fourier transformation outcome. However, outside the support region, the resultant value depends on the specific algorithm employed as it is expressed with above equations. In the case of the ER algorithm, it is zero. For the HIO algorithm, it corresponds to the disparity between the results obtained in the current and preceding iterations, which has been scaled by the β factor. As for the RAAR algorithm, it also involves the disparity between the previous and current iterations, but in this case, the derivative is additionally weighted by the β factor, while the current iteration is weighted by a factor of $1 - 2\beta$. In the HIO algorithm, $\beta \in [0, 1]$. A smaller β value enhances the stability of the convergence process, whereas a larger β value prevents the occurrence of error entrapment within local minima (see Fig. 7.5). For RAAR algorithm $\beta \in [0.5, 1]$. RAAR is noise-resistant if the $\beta \ll 1$ and stable against stagnation when $\beta \approx 1$. Determining a beta value is an trial-and-error process that relies on the experimental data and striking a balance between resistance to noise and

avoidance of stagnation [156]. In the implementation of phase retrieval, a common approach is to employ a combination of algorithms. Typically, the initial algorithms chosen are robust against noise and resistant to getting trapped in local minima. Subsequently, algorithms like EP are utilized to enhance resolution[149].

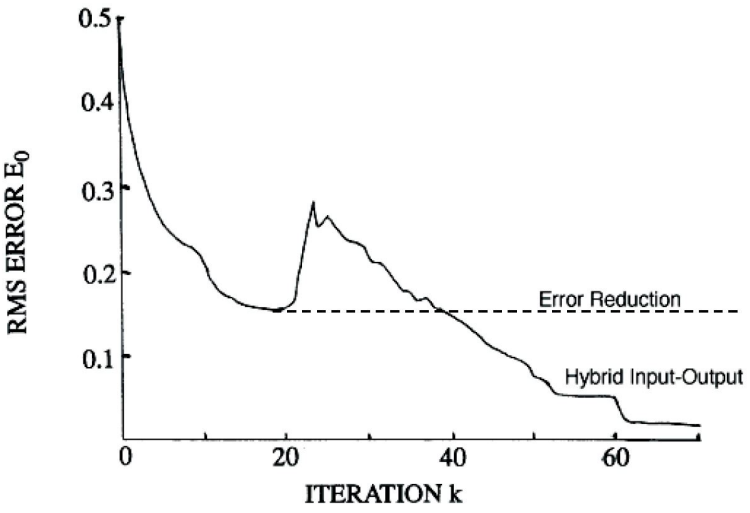

Figure 7.5
RMS error versus the number of iterations. The ER algorithm appears to be trapped in a local minimum. Adapted from Ref.[125].

The updating of the support area S can occur after a sa certain number of iterations, a method known as the shrink-wrap algorithm (technique). This is performed by applying a Gaussian filter with smaller σ, so that the object support S approaches the shape of the object distribution [127, 157].

The convergence of the retrieval process is monitored through error calculation. In the case of the ER algorithm, this error denotes the disparity between the computed diffraction pattern and the measured as [125]

$$Error_{F_k} = \left\{ \frac{N^{-2} \sum_k \left[|G_k(k)| - |\ F(k)| \right]^2}{\sum_k |F(k)|^2} \right\}^{1/2}. \tag{7.9}$$

For HIO, RAAR, and SW the error concerns whether the constraints are satisfied in real space and is given by [33, 123, 126]

$$Error_{f_x} = \left\{ \frac{\sum_{x \in \gamma} |g'_k(x)|^2}{\sum_{x \notin \gamma} |g'_k(x)|^2} \right\}^{1/2}. \tag{7.10}$$

7.4.2 Implementation

The ratio $\Delta\lambda/\lambda$ should be below 10% [158, 159]. According to the manufacturer's specifications (Table 3.1), $\Delta\lambda/\lambda$ is 4.3% and 8.0% for 32.2 nm and 47.35 nm respectively, so this condition is fulfilled. In Addition, the Fraunhofer criterion should be satisfied which corresponds to plane wave imaging, i.e. the target object should be at a distance z from the camera sensor such that

$$z \gg \frac{D^2}{\lambda}, \tag{7.11}$$

where D is the diameter of the object and λ is the wavelength of the radiation. The oversample value can be calculated from the experimental data by the relation [160]

$$\sigma_o = \frac{z\lambda}{Dp}, \tag{7.12}$$

where p the pixel size of the camera which according to the manufacturer was $13\,\mu\text{m} \times 13\,\mu\text{m}$. So we see from Eq.(7.4) and Eq.(7.12) that z should satisfy the inequality

$$z > \frac{\sqrt{2}Dp}{\lambda}. \tag{7.13}$$

The camera pixel size in a reconstructed image is

$$r = \alpha\frac{z\lambda}{pN}, \tag{7.14}$$

where $\alpha = 1.22$ according to the Rayleigh criterion and N the number of pixels in a camera with a $N \times N$ sensor [158]. Therefore according to (7.14) the pixel size of the reconstructed image is proportional to the distance z between object and sensor. Thus, in order to increase the resolution, the distance z of the object from the camera should be decreased.

In order to enable the operation of the recovery algorithms, the necessary pre-processing had to be done on the obtained diffraction images of the XUV radiation. The basic processings were (a) denoising, (b) replacing saturated pixels with pixels of images with shorter exposure time by modifying the values appropriately, and (c) moving the center of symmetry of the diffraction pattern to the center of the image.

Denoising removed clusters of bright or dark pixels with a diameter much smaller than the diffraction pattern structures, in practice about two to three pixels. Also, background images had been captured and subtracted from raw data images. The images were taken with different exposure times with a minimum of five minutes and a maximum of thirty. The saturated pixels of the long times which are located

in the center of the pattern, i.e. the low frequencies, were replaced with the corresponding unsaturated ones of shorter times, proportionally increasing their values so that the transition is smooth. This replacement, in addition to recovering the low frequency information, also increased the dynamic range of the reception. A typical example of the above process is depicted in Fig.7.6.

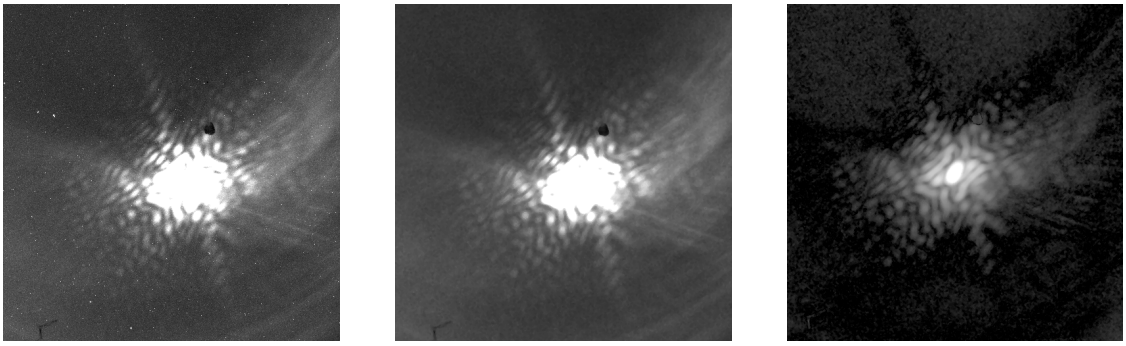

(a) Raw image. **(b)** Denoised. **(c)** After background subtraction, in a logarithmic scale.

Figure 7.6
Typical diffraction pattern processing.

7.5 XUV CDI in Transmission Mode

The object used for the CDI studies was a hole drilled by our tightly focused laser beam on a 13 μm thin aluminum foil. It was selected among a series of objects, imaged by scanning electron microscope, based on (i) the sharpness of its edges and (ii) its contour details to be less than 1 μm. In Fig. 7.7 a SEM image of the object is shown. The maximum dimension of the hole was 45 μm, thus, from Eq. (7.11), the minimum distance z should be 6.1 cm and 4.3 cm for radiation with 32.2 nm and 47.6 nm, respectively.

From Eq. (7.13) results that the minimum Z for 32.2 nm has to be 25.7 mm while for 47.6 nm has to be 17.5 mm.

Considering the above, the object was placed at a distance of 9 cm from the sensor. Thus, according to Eq.(7.14) each pixel corresponds to an object dimension of 531 nm and 781 nm for radiation 32.2 nm and 47.35 nm, respectively. In this position σ_o takes the values $\sigma_o\,[47.35\,\text{nm}] = 7.2$ and $\sigma_o\,[32.2\,\text{nm}] = 4.9$ which satisfy the requirement of $\sigma_o > 2$.

The object was illuminated by the XUV beam just before its focus in order to cover as large area as possible of the object. Since the ROC of the spherical multilayer mirror is 1000 mm this choice is not expected to affect the XUV phase

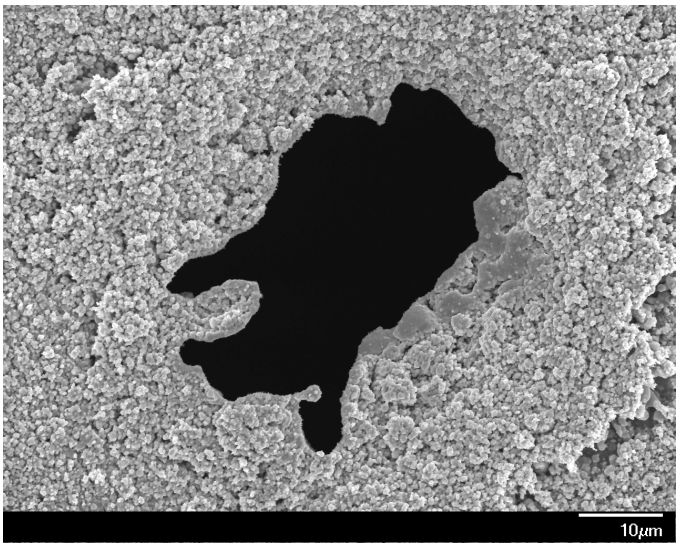

Figure 7.7
SEM image of the object, i.e. a whole drilled by our tightly focused laser beam on a 13 μm thin aluminum foil.

front. Our automated system allowed the acquisition of a series of CDI images by moving the object in the plane perpendicular to the k-vector of the XUV beam.

In Figs.7.8c and 7.8e the CDI images for the wavelengths of 47.6 nm and 32.2 nm, respectively, are shown. These CDI images were selected in order to demonstrate the imaging capabilities of sub-micrometer details. In Fig.7.8b, the ideal calculated CDI image of the object is shown. Comparing the experimental CDI images for these two wavelengths it is clearly shown that the smaller the wavelength the finer the details of interference modulation in the k-space of the CDI image, as expected.

In Figs.7.8d and 7.8f, the reconstructed images in real space are shown, for the wavelengths of 47.6 nm and 32.2 nm, respectively, as calculated using the reconstruction algorithm presented in Appendix II. In brief, the reconstruction process initiates using the SW algorithm with a starting value of $\sigma = 7.5$, reduced to $\sigma = 0.8$ during 120,000 iterations, while changing the support S every 20 iterations. The values of θ and β were empirically set to 0.15 and 0.9 , respectively, in accordance with the values from the literature [26]. Finally, using the ER algorithm, 200 additional iterations were applied to obtain the final result [156].

From the reconstructed images it is evident that using the shorter wavelength, the reconstructed image has higher resolution, resolving the details with a higher number of pixels. Moreover, the reconstructed image size of the object is $\simeq 1.5$ times larger for the wavelength of 32.2 nm as compared to 47.6 nm, reflecting the inverse ratio of the wavelengths.

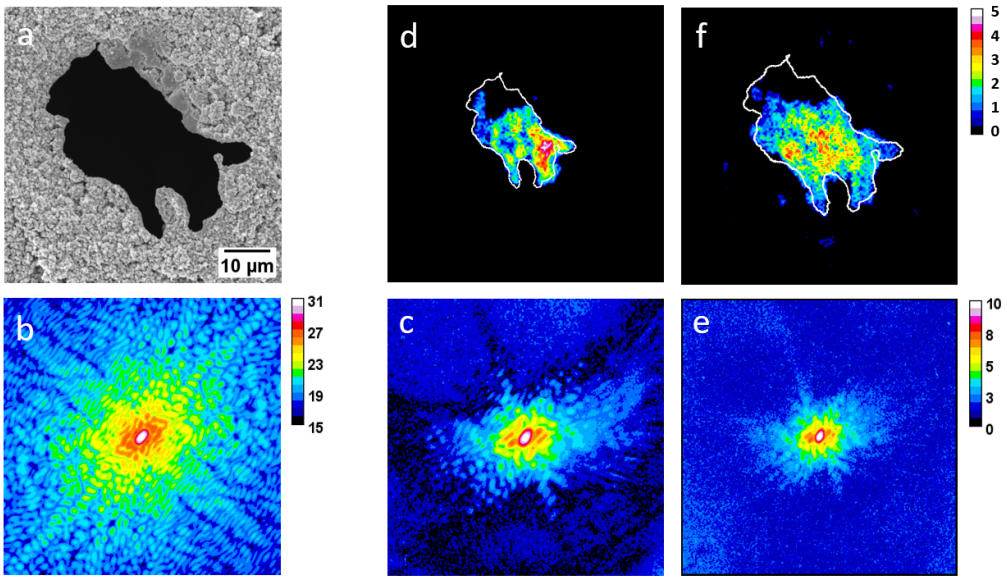

Figure 7.8
(a) The object under ultrafast CDI study. (b) The ideal CDI result corresponding to the object shown in (a). (c) CDI result for the object shown in (a) using the central wavelength of 47 nm. (d) Reconstruction of the object shown in (a) using the CDI result of (c). (f) CDI result for the object shown in (a) using the central wavelength of 32 nm. (f) Reconstruction of the object shown in (a) using the CDI result of (e). The white contour shown in (d) and (f) corresponds to the shape of the object shown in (a) and were placed to guide the eye. The image size of (b)-(f) is 512×512 pixels. (from Ref.[88])

7.6 XUV CDI in Reflection Mode

Since XUV wavelengths possess a minimal penetration depth, CDI in reflection mode becomes imperative for characterizing micro- and nano-structures developed on surfaces as well as for dense plasma diagnostics, not previously applied. Apart from offering high spatiotemporal resolution, XUV CDI systems provide a spectrum of wavelengths suitable for multispectral imaging. CDI in reflection mode introduces additional complexity as the XUV radiation must be incident onto the sample at grazing angles to ensure sufficient reflected diffraction energy.

Here, multispectral XUV CDI in reflection mode of the honeycomb structure of a commercially available MCP is presented, showcasing the ability to resolve features on the order of a few hundred nanometers. Imaging results for three different wavelengths, i.e. 807 nm, 46.7 nm, and 32.2 nm, are compared. While the 807 nm wavelength fails to accurately resolve the honeycomb structure features, the 32.2 nm wavelength exhibits higher resolution compared to the 46.7 nm wavelength.

Initially, simulations were employed to derive the expected diffraction pattern based on the optical geometry of our XUV CDI in reflection mode setup, illustrated in Fig.7.3. Thus, an artificial honeycomb structure, similar to that of the MCP

in use, was utilized and rotated by 76.1° with respect to the honeycomb surface normal. The rotation of the object resulted in geometrical shortening along the illumination direction, as depicted in Fig. 7.9a. The simulated diffraction pattern is presented in Fig. 7.9b. Fig. 7.9c shows the reconstructed object, taking into account the 76.1° rotation. Additionally, in the same figure, the honeycomb structure is overlapped with the reconstructed object for comparison. This analysis clearly indicates that the reconstructed object comprises bright spots located at the center of the honeycomb MCP channels. Therefore, the reconstruction of the real object in our experiments using the two XUV wavelengths is expected to follow a similar pattern.

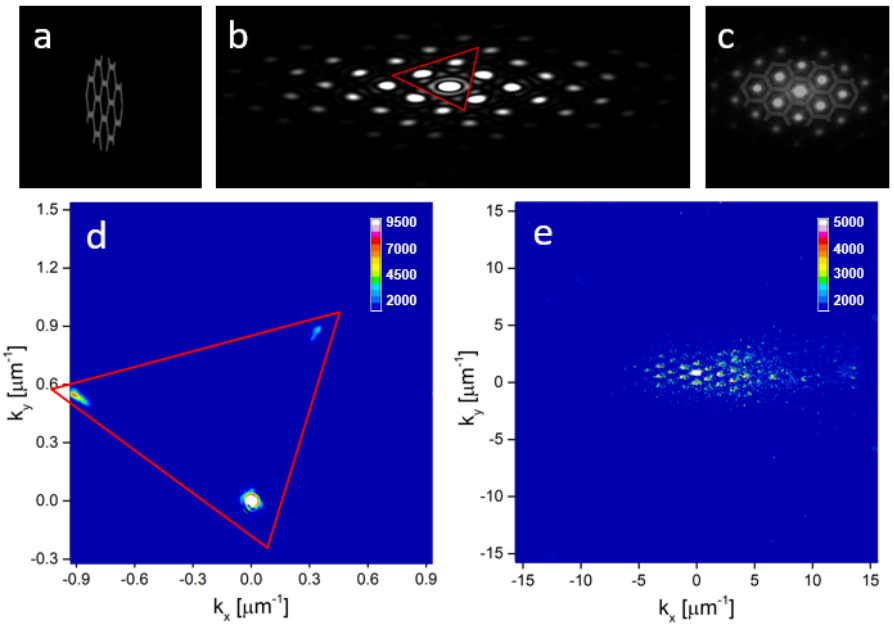

Figure 7.9
(a) Schematic of a MCP honeycomb object rotated by 76.1° to match the experimental viewing angle by the illuminating XUV beam. (b) The simulated diffraction pattern of (a). (c) The geometry-corrected reconstruction overlapped with the original MCP honeycomb object. (d) Experimentally recorded CDI image from the real MCP honeycomb object for a wavelength of 807 nm. (e) Same as in (d) but for a wavelength of 47.6 nm.

In Fig. 7.9d the measured diffraction image obtained using the fundamental laser beam with a wavelength of 807 nm is shown. Only three diffraction spots are recorded on the 1024 × 1024 pixel CCD camera sensor, contained inside a red triangle that corresponds to the red triangle of the diffraction pattern of Fig. 7.9b. This clearly shows that the use of the fundamental laser beam has additional intrinsic problems, other than the long wavelength that limits the resolution, related to the size of the diffraction image that way exceeds the limits of a typical CCD camera sensor. In Fig. 7.9e, a typical XUV diffraction pattern using the 47.6 nm wavelength is shown. Within the XUV CCD sensor, a high order diffraction pattern is recorded similar to that of the simulation in Fig. 7.9b. For the current optical

layout and for the wavelength of 47.6 nm, the 1024×1024 pixels can cover a k-vector range up to approximately $\pm 15\,\mu m^{-1}$. In contrast, with a wavelength of 807 nm, the corresponding k-vector range reaches only about $\pm 0.9\,\mu m^{-1}$. The diffracted orders extend up to approximately $10\,\mu m^{-1}$ for the 47.6 nm wavelength.

In Figs.7.10a and 7.10b, the geometry-corrected reconstruction of the real MCP honeycomb object is displayed for 47.6 nm and 32.2 nm, respectively. The reconstructions were generated using the RAAR algorithm. A honeycomb pattern with equivalent area to the object, scaled to the actual MCP channel dimensions, is overlaid onto the reconstructed images for visualization. It should be noted that in Figs.7.10a and 7.10b,, each pixel corresponds to 200 nm and 140 nm, respectively, based on the analysis outlined in Refs. [158, 161]. Similar to the artificial honeycomb structure, the reconstruction of the real MCP object exhibits bright spots positioned at the centers of the MCP channels. A comparison of the reconstructions in Figs.7.10a and 7.10b indicates that the object appears 1.5 times larger for 32.2 nm compared to 47.6 nm, reflecting the inverse ratio of the wavelengths. Moreover, employing the shorter wavelength of 32.2 nm enables the resolution of object features with finer detail since a higher pixel count corresponds to the same bright spot areas.

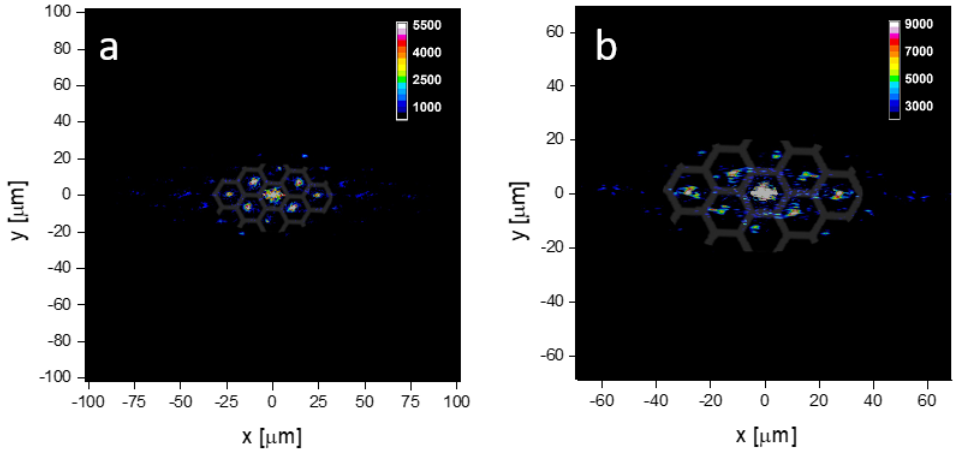

Figure 7.10
(a) Geometry-corrected reconstruction of the honeycomb MCP object using the XUV beam with a wavelength of 47.6 nm. (b) Same as in (a) but for a wavelength of 32.2 nm. The overlapped honeycomb pattern is a guide to the eye and corresponds to the actual MCP channel dimensions. Image size of (a) and (b) is 1024 × 1024 pixels.

7.7 Discussion and Conclusions

The current advances in nanotechnology require the development of multispectral imaging systems, using wavelengths in the XUV and soft x-ray region. Towards

this, the approach in this work offers a comb of coherent XUV wavelengths which can be preferentially filtered in an automated way, without altering their optical spatiotemporal characteristics. Specifically, an automated system for ultrafast multispectral CDI has been presented, demonstrating its capabilities at two different XUV wavelengths, namely 32.2 nm and 47.6 nm. Results clearly show that the imaging capabilities and the structural details that can be resolved depend on the wavelength in use.

While in this work the shortest wavelength in use was 32.2 nm, future prospects of coherent multispectral XUV CDI will be its extension in the soft x-ray spectral region utilizing appropriate phase-matching conditions [98, 99]. Using such small wavelengths will allow to assess unexplored areas of science, such as imaging of chemicals at their absorption edges, combined with fs time-resolved measurements. In accordance to the above goal, our XUV CDI setup can support a larger number of XUV wavelengths by adding more pairs of multilayer XUV mirrors. These pairs can be placed in the same platform, automatically set to the different pair positions, thus selecting the desired wavelength without altering the XUV beam path towards the object. Moreover, the use of semi-infinite gas cell for the high harmonic XUV generation, aside from the stability of HHG conditions that it offers, it can support laser systems with MHz repetition rates, which are commercially available, providing laser pulse intensities appropriate for HHG. Such high repetition rates are highly desirable in, for example, 3D tomographic imaging due to the large number of the images required.

Especially, XUV and soft x-ray CDI devices operating in reflection mode is critical for nanoscale microscopy in many areas, such as material science, biology, and medical sciences. Due to the physical principles of XUV and soft x-ray optics, reflection CDI at grazing incidence is the only efficient way for nanoscale imaging of such systems. Moreover, it could be useful for cell surface engineering or molecule development on surfaces, since it offers both high spatiotemporal resolution and the necessary wavelength selection due to different absorption edges in the XUV. This could allow for spatial identification of different chemical substances on the diffractive surface.

Going one step further, multispectral reflection XUV CDI combined with the ultrafast duration of high harmonic XUV pulses, could be proven a powerful method to investigate the real time dynamic behavior of chemical systems on surfaces after photoexcitation. This is due to the absorption spectra of numerous chemicals lie in the XUV and soft x-ray spectral regions, that cover the entire water window from carbon K-edge up to oxygen K-edge absorption edges [162–164]. The approach is highly suitable for dynamic imaging of photoexcited chemicals on surfaces, in

integration with pump-probe techniques, where the XUV probe beam is used for the ultrafast multispectral selective nanoimaging, thus opening unexplored areas of the nanoscience.

Finally, multispectral XUV CDI in reflection mode could also be proven a powerful tool for spatiotemporal imaging of the evolution of the critical plasma density front, especially for the case where a high power laser illuminates a solid surface. Oscillating high critical density plasma surfaces are the mechanism for the relativistic high harmonic generation [165]. In this framework, ultrafast and high spatial resolution imaging of the critical plasma density evolution could be a unique tool for understanding the underlying physical mechanisms.

Chapter 8

Summary & Conclusions

This thesis explores the dynamics of HHG using ultra-short intense laser pulses by systematically studying the effects of the experimental parameters, such as gas species, gas pressure, focusing conditions and chirp of the laser pulse, in the HHG process. The purpose of the study is to investigate the deeper quantum mechanical behavior of the generating mechanisms in conditions that depart from the typical HHG conditions reported in the literature. For this, intense laser pulses were employed forcing the generation process to take place at the leading edge of the laser pulse giving rise to highly non-linear phenomena, such as SPM, that largely affect the HHG process. The final goal of this part of the study is to control the HHG characteristics through these conditions. Furthermore, this thesis focuses on exploiting the HHG source in a setup that can select multiple wavelengths and perform XUV CDI measurements for reconstructing objects in the nanoscale. The results of the study are presenting below, listed by the corresponding chapters.

In Chapter 4, the optimization of the HHG XUV source by exploring the effects of parameters such as laser beam diameter, focus position, gas pressure, and laser pulses chirp is conducted. Specifically, it was found that for a Gaussian (solid) beam, the optimum laser beam diameter for generating an overall good quality plateau harmonics was 7 mm. In addition, the HHG production was studied as a function of the laser beam focus position and generating Ar gas pressure, showing that the optimum conditions were for focusing at the neighbor of the laser-drilled exit opening of the semi-infinite cell for relatively high gas pressures (50-70 Torr). Furthermore, an investigation of HHG production utilizing various gas targets and gas mixtures showed that Ar had higher efficiency for 32.2 nm, while Kr was optimal for 47.6 nm, i.e. the wavelengths of interest here. Finally, an annular beam was implemented and the HHG production was optimized for this case. The study showed that the optimum HHG conditions were achieved for a central block of

7 mm diameter and energy of 1 mJ. With these conditions, optimal harmonic production was obtained for Ar at pressures around 80 Torr, while for Kr it was slightly higher at 90 Torr.

In Chapter 5 the investigation of the control of the electron trajectories (quantum paths) through the variation of the chirp of the ultrafast, high-intensity laser pulses is presented. It was shown that for low positive chirp values and relatively high Ar gas pressure, the suppression of the long trajectory, is evident in the HHG image spectra. This was justified by model calculations as well, and it was attributed to the intense laser pulses causing HHG dynamics to happen at a temporal window in the leading edge of the laser pulse. Thus, effects such as the enhanced ionization and self-phase modulation largely affect the phase matching conditions for the two quantum paths of the HHG.

In Chapter 6, a more detailed study of the spectral and divergence characteristics of plateau high-order harmonics is conducted. The systematic variations of the Ar gas pressure in combination with the chirp of the laser pulses were employed in the investigation. Specifically, the main features observed in the image spectra were: (a) Line broadening at low negative chirp values (< -50 fs) and quasi-continuum spectra at high pressure (90 Torr). (b) Harmonics divergence and quantum path separation as the laser chirp is varied from positive to negative values. (c) Spectral shift for the plateau harmonics as the chirp of the laser pulse varies. (d) Wavelength tunability based on the blue shift of a harmonic as the chirp varies from positive to negative values, as well as the broadening of the HHG lines and the appearance of XUV spectral bands between the harmonics.

In Chapter 7 the proof-of-principle of a novel approach for extending the technique of coherent XUV CDI to coherent multispectral XUV CDI is presented. The experimental implementation includes both transmission and reflection CDI modes. In transmission mode a laser-drilled hole in a thin aluminum foil with submicrometric details was reconstructed. In the reflection mode, the honeycomb structure of an MCP was also reconstructed in its fine details. Two different XUV wavelengths, namely 32.2 nm and 47.6 nm, were used, demonstrating that the imaging capabilities and the structural details that can be resolved depend on the wavelength in use. Our multispectral XUV CDI approach has potential applications in nanoscale microscopy in many areas, such as material science, biology, medical sciences as well as in real time dynamic behavior of chemical systems on surfaces and in spatiotemporal imaging of the evolution of the critical plasma density front.

Future Perspectives

Our XUV CDI method and experimental setup would largely be benefited from the following advancements:

- Transfer of the setup to the 1 kHz repetition fs laser installation, currently operating in IPPL.
- Include another pair of multilayer mirrors in the platform to reach the soft x-ray region.
- Include a second laser beam in Mach-Zehnder optical layout, where the HHG beam will be the one arm and the IR beam will be the other arm, to initiate XUV CDI dynamic imaging through the pump-probe technique.

Bibliography

[1]"The Nobel Prize in Physics 2023", NobelPrize.org, 10.1051/epn/2023501.

[2]D. Strickland and G. Mourou, "Compression of amplified chirped optical pulses", Optics Communications **56**, 219–221 (1985).

[3]"The Nobel Prize in Physics 2018", Nobel Lectures In Physics (2011-2015), 3–6 (2022).

[4]P. Agostini, F. Fabre, G. Mainfray, G. Petite, and N. K. Rahman, "Free-free transitions following six-photon ionization of xenon atoms", Physical Review Letters **42**, 1127–1130 (1979).

[5]J. Eberly, J. Javanainen, and K. Rzażewski, "Above-threshold ionization", Physics Reports **204**, 331–383 (1991).

[6]M. V. Ammosov, N. B. Delone, and V. P. Krainov, "Tunnel Ionization Of Complex Atoms And Atomic Ions In Electromagnetic Field", High Intensity Laser Processes **0664**, edited by J. A. Alcock, 138 (1986).

[7]E. E. Fill, "Focusing limits of ultrashort laser pulses: analytical theory", Journal of the Optical Society of America B **11**, 2241 (1994).

[8]M. Protopapas, C. H. Keitel, and P. L. Knight, "Atomic physics with super-high intensity lasers", Reports on Progress in Physics **60**, 389–486 (1997).

[9]M. Lewenstein, P. Balcou, M. Y. Ivanov, A. L'Huillier, and P. B. Corkum, "Theory of high-harmonic generation by low-frequency laser fields", Physical Review A **49**, 2117–2132 (1994).

[10]T. W. Hänsch, "A proposed sub-femtosecond pulse synthesizer using separate phase-locked laser oscillators", Optics Communications **80**, 71–75 (1990).

[11]G. Farkas and C. Tóth, "Proposal for attosecond light pulse generation using laser induced multiple-harmonic conversion processes in rare gases", Physics Letters A **168**, 447–450 (1992).

[12]S. E. Harris, J. J. Macklin, and T. W. Hänsch, "Atomic scale temporal structure inherent to high-order harmonic generation", Optics Communications **100**, 487–490 (1993).

[13]P. B. Corkum, "Plasma perspective on strong field multiphoton ionization", Physical Review Letters **71**, 1994–1997 (1993).

[14]P. Salières, A. L'Huillier, and M. Lewenstein, "Coherence control of high-order harmonics", Physical Review Letters **74**, 3776–3779 (1995).

[15]A. L. Huillier, K. J. Schafer, and K. C. Kulander, "Theoretical aspects of intense field harmonic generation", Journal of Physics B: Atomic, Molecular and Optical Physics **24**, 3315–3341 (1991).

[16]N. A. Papadogiannis, B. Witzel, C. Kalpouzos, and D. Charalambidis, "Observation of attosecond light localization in higher order harmonic generation", Physical Review Letters **83**, 4289–4292 (1999).

[17]P. Corkum, "Attosecond pulses at last", Nature **403**, 845–846 (2000).

[18]M. Hentschel, R. Kienberger, C. Spielmann, G. A. Reider, N. Milosevic, T. Brabec, P. Corkum, U. Heinzmann, M. Drescher, and F. Krausz, "Attosecond metrology", Nature **414**, 509–513 (2001).

[19]P. M. Paul, E. S. Toma, P. Breger, G. Mullot, F. Augé, P. Balcou, H. G. Muller, and P. Agostini, "Observation of a train of attosecond pulses from high harmonic generation", Science **292**, 1689–1692 (2001).

[20]P. Tzallas, D. Charalambidis, N. A. Papadogiannis, K. Witte, and G. D. Tsakiris, "Direct observation of attosecond light bunching", Nature **426**, 267–271 (2003).

[21]N. A. Papadogiannis, L. A. Nikolopoulos, D. Charalambidis, G. D. Tsakiris, P. Tzallas, and K. Witte, "On the feasibility of performing non-linear autocorrelation with attosecond pulse trains", Applied Physics B: Lasers and Optics **76**, 721–727 (2003).

[22]N. A. Papadogiannis, L. A. Nikolopoulos, D. Charalambidis, G. D. Tsakiris, P. Tzallas, and K. Witte, "Two-Photon Ionization of He through a Superposition of Higher Harmonics", Physical Review Letters **90**, 4 (2003).

[23]D. Charalambidis, N. A. Papadogiannis, E. Goulielmakis, G. Nersysian, G. D. Tsakiris, and K. Witte, "A transmission grating interferometer for the temporal characterization of harmonics", Journal of Modern Optics **50-3**, 387–400 (2003).

[24]N. A. Papadogiannis, G. Nersisyan, E. Goulielmakis, T. P. Rakitzis, E. Hertz, D. Charalambidis, G. D. Tsakiris, and K. Witte, "Temporal characterization of short-pulse third-harmonic generation in an atomic gas by a transmission-grating Michelson interferometer", Optics Letters **27**, 1561 (2002).

[25]E. Goulielmakis, G. Nersisyan, N. A. Papadogiannis, D. Charalambidis, G. D. Tsakiris, and K. Witte, "A dispersionless Michelson interferometer for the characterization of attosecond pulses", Applied Physics B: Lasers and Optics **74**, 197–206 (2002).

[26]E. Goulielmakis, V. S. Yakovlev, A. L. Cavalieri, M. Uiberacker, V. Pervak, A. Apolonski, R. Kienberger, U. Kleineberg, and F. Krausz, "Attosecond control and measurement: Lightwave electronics", Science **317**, 769–775 (2007).

[27]J. Gagnon, E. Goulielmakis, and V. S. Yakovlev, "The accurate FROG characterization of attosecond pulses from streaking measurements", Applied Physics B: Lasers and Optics **92**, 25–32 (2008).

[28]R. L. Sandberg, A. Paul, D. A. Raymondson, S. Hädrich, D. M. Gaudiosi, J. Holtsnider, R. I. Tobey, O. Cohen, M. M. Murnane, H. C. Kapteyn, C. Song, J. Miao, Y. Liu, and F. Salmassi, "Lensless diffractive imaging using tabletop coherent high-harmonic soft-X-ray beams", Physical Review Letters **99**, 098103 (2007).

[29]M. Zürch, J. Rothhardt, S. Hädrich, S. Demmler, M. Krebs, J. Limpert, A. Tünnermann, A. Guggenmos, U. Kleineberg, and C. Spielmann, "Real-time and sub-wavelength ultrafast coherent diffraction imaging in the extreme ultraviolet", Scientific Reports **4**, 1–5 (2014).

[30]J. Miao, T. Ishikawa, I. K. Robinson, and M. M. Murnane, "Beyond crystallography: Diffractive imaging using coherent X-ray light sources", Science **348**, 530–535 (2015).

[31]D. F. Gardner, M. Tanksalvala, E. R. Shanblatt, X. Zhang, B. R. Galloway, C. L. Porter, R. Karl, C. Bevis, D. E. Adams, H. C. Kapteyn, M. M. Murnane, and G. F. Mancini, "Subwavelength coherent imaging of periodic samples using a 13.5 nm tabletop high-harmonic light source", Nature Photonics **11**, 259–263 (2017).

[32]S. Roscam Abbing, F. Campi, F. S. Sajjadian, N. Lin, P. Smorenburg, and P. M. Kraus, "Divergence Control of High-Harmonic Generation", Physical Review Applied **13**, 054029 (2020).

[33]J. Miao, P. Charalambous, J. Kirz, and D. Sayre, "Extending the methodology of X-ray crystallography to allow imaging of micrometre-sized non-crystalline specimens", Nature **400**, 342–344 (1999).

[34]H. N. Chapman and K. A. Nugent, "Coherent lensless X-ray imaging", Nature Photonics **4**, 833–839 (2010).

[35]C. Balas, G. Epitropou, and C. Pappas, *"Multi Hyper-Spectral Imaging"* (in Handbook of Biomedical Optics, Taylor & Francis Book, Inc, USA, 2011).

[36]C. Balas, G. Epitropou, A. Tsapras, and N. Hadjinicolaou, *"Hyperspectral Imaging and Spectral Classification for Pigment Identification and Mapping in Paintings by El Greco and his Workshop"* (in Multimedia Tools and Applications, pp 1-17, Springer, 2018).

[37]B. Boldrini, W. Kessler, K. Rebner, and R. W. Kessler, "Hyperspectral Imaging: A Review of Best Practice, Performance and Pitfalls for in-line and on-line Applications", Journal of Near Infrared Spectroscopy **20**, 483–508 (2012).

[38]X. Dong, M. Jakobi, S. Wang, M. H. Köhler, X. Zhang, and A. W. Koch, "A review of hyperspectral imaging for nanoscale materials research", Applied Spectroscopy Reviews **54**, 285–305 (2019).

[39]J. T. Verdeyen, *Laser Electronics. 1995*, Laser electronics (Prentice Hall, 1995).

[40]A. Siegman, "Lasers", in *University science books* (Oxford University Press, California, 1986) Chap. 17.

[41]S. Carlström, J. Preclíková, E. Lorek, E. W. Larsen, C. M. Heyl, D. Paleček, D. Zigmantas, K. J. Schafer, M. B. Gaarde, and J. Mauritsson, "Spatially and spectrally resolved quantum path interference with chirped driving pulses", New Journal of Physics **18**, 123032 (2016).

[42]E. Neyra, F. Videla, J. A. Pérez-Hernández, M. F. Ciappina, L. Roso, and G. A. Torchia, "Extending the high-order harmonic generation cutoff by means of self-phase-modulated chirped pulses", Laser Physics Letters **13**, 115303 (2016).

[43]A. Couairon and A. Mysyrowicz, "Femtosecond filamentation in transparent media", Physics Reports **441**, 47–189 (2007).

[44]X. M. Tong and C. D. Lin, "Empirical formula for static field ionization rates of atoms and molecules by lasers in the barrier-suppression regime", Journal of Physics B: Atomic, Molecular and Optical Physics **38**, 2593–2600 (2005).

[45]A. LHuillier, P. Balcou, S. Candel, K. J. Schafer, and K. C. Kulander, "Calculations of high-order harmonic-generation processes in xenon at 1064 nm", Physical Review A **46**, 2778–2790 (1992).

[46]R. Weissenbilder, S. Carlström, L. Rego, C. Guo, C. M. Heyl, P. Smorenburg, E. Constant, C. L. Arnold, and A. L'Huillier, "How to optimize high-order harmonic generation in gases", Nature Reviews Physics **4**, 713–722 (2022).

[47]T. Pfeifer, C. Spielmann, and G. Gerber, "Femtosecond x-ray science", Reports on Progress in Physics **69**, 443–505 (2006).

[48]W. Boyd Robert, *Nonlinear optics*, Fourth Edition (Academic Press, London, UK, 2020).

[49]E. L. Clark, A. Grigoriadis, S. Petrakis, I. Tazes, G. Andrianaki, A. Skoulakis, Y. Orphanos, E. Kaselouris, I. Fitilis, J. Chatzakis, E. Bakarezos, V. Dimitriou, E. P. Benis, N. A. Papadogiannis, and M. Tatarakis, "High-intensity laser-driven secondary radiation sources using the ZEUS 45 TW laser system at the Institute of Plasma Physics and Lasers of the Hellenic Mediterranean University Research Centre", High Power Laser Science and Engineering **9**, 53 (2021).

[50]A. Stingl, R. Szipöcs, M. Lenzner, C. Spielmann, and F. Krausz, "Sub-10-fs mirror-dispersion-controlled Ti:sapphire laser", Optics Letters **20**, 602 (1995).

[51]C. Spielmann, P. F. Curley, T. Brabec, and F. Krausz, "Ultrabroadband Femtosecond Lasers", IEEE Journal of Quantum Electronics **30**, 1100–1114 (1994).

[52]G. Cheriaux, B. Walker, L. F. Dimauro, P. Rousseau, F. Salin, and J. P. Chambaret, "Aberration-free stretcher design for ultrashort-pulse amplification", Optics Letters **21**, 414 (1996).

[53]J. E. Murray and W. H. Lowdermilk, "ND : YAG regenerative amplifier", Journal of Applied Physics **51**, 3548–3556 (1980).

[54]W. H. Lowdermilk and J. E. Murray, "The multipass amplifier: Theory and numerical analysis", Journal of Applied Physics **51**, 2436–2444 (1980).

[55]D. Strickland and G. Mourou, "Compression of amplified chirped optical pulses", Optics Communications **56**, 219–221 (1985).

[56]Fastlite, *Dazzler Ultrafast pulse shaper*, (2018) `http://www.fastlite.com/en/ar824665-823529-Dazzler.html?Cookie=set` (visited on 10/10/2023).

[57]F. Verluise, V. Laude, J.-P. Huignard, P. Tournois, and A. Migus, "Arbitrary dispersion control of ultrashort optical pulses with acoustic waves", J. Opt. Soc. Am. B **17**, 138–145 (2000).

[58]F. Verluise, V. Laude, Z. Cheng, C. Spielmann, and P. Tournois, "Amplitude and phase control of ultrashort pulses by use of an acousto-optic programmable dispersive filter: pulse compression and shaping", Optics Letters **25**, 575 (2000).

[59]P. Tournois, "Acousto-optic programmable dispersive filter for adaptive compensation of group delay time dispersion in laser systems", Optics Communications **140**, 245–249 (1997).

[60]D. Kaplan and P. Tournois, "A simple theory of the acousto-optic programmable dispersive filter used for femtosecond laser pulse shaping", Optics InfoBase Conference Papers **12**, 56–57 (2002).

[61]T. Oksenhendler, D. Kaplan, P. Tournois, G. M. Greetham, and F. Estable, "Ultrawideband regenerative amplifiers via intracavity acousto-optic programmable gain control", Springer Series in Optical Sciences **132**, 421–426 (2007).

[62]Y. Ishida, T. Yajima, and A. Watanabe, "A simple monitoring system for single subpicosecond laser pulses using an SH spatial autocorrelation method and a CCD image sensor", Optics Communications **56**, 57–60 (1985).

[63]A. Brun, P. Georges, G. L. Saux, and F. Satin, "Single-shot characterization of ultrashort light pulses", Journal of Physics D: Applied Physics **24**, 1225–1233 (1991).

[64]M. Raghuramaiah, A. K. Sharma, P. A. Naik, P. D. Gupta, and R. A. Ganeev, "A second-order autocorrelator for single-shot measurement of femtosecond laser pulse durations", Sadhana - Academy Proceedings in Engineering Sciences **26**, 603–611 (2001).

[65]J. Peatross, J. L. Chaloupka, and D. D. Meyerhofer, "High-order harmonic generation with an annular laser beam", Optics Letters **19**, 942 (1994).

[66]R. Klas, A. Kirsche, M. Tschernajew, J. Rothhardt, and J. Limpert, "Annular beam driven high harmonic generation for high flux coherent XUV and soft X-ray radiation", Optics Express **26**, 19318 (2018).

[67]J. Pu, "Focusing Gaussian beams by an annular lens with spherical aberration", Journal of Modern Optics **45**, 239–247 (1998).

[68]T. Gaumnitz, A. Jain, and H. J. Wörner, "Extreme-ultraviolet high-order harmonic generation from few-cycle annular beams", Optics Letters **43**, 4506 (2018).

[69]C. Jin, X. Tang, B. Li, K. Wang, and C. D. Lin, "Optimal Spatial Separation of High-Order Harmonics from Infrared Driving Lasers with an Annular Beam in the Overdriven Regime", Physical Review Applied **14**, 1 (2020).

[70]S. Kazamias, F. Weihe, D. Douillet, C. Valentin, T. Planchon, S. Sebban, G. Grillon, F. Augé, D. Hulin, and P. Balcou, "High order harmonic generation optimization with an apertured laser beam", European Physical Journal D **21**, 353–359 (2002).

[71]D. Proch and T. Trickl, "A high-intensity multi-purpose piezoelectric pulsed molecular beam source", Review of Scientific Instruments **60**, 713–716 (1989).

[72]J. R. Sutherland, E. L. Christensen, N. D. Powers, S. E. Rhynard, J. C. Painter, and J. Peatross, "High harmonic generation in a semi-infinite gas cell", Optics Express **12**, 4430 (2004).

[73]E. Hecht, *Optics (Fifth Edition)* (Pearson Education, Incorporated, 2015), p. 704.

[74]D. E. Aspnes and A. A. Studna, *Dielectric functions and optical parameters of Si, Ge, GaP, GaAs, GaSb, InP, InAs, and InSb from 1.5 to 6.0 eV*, Vol. 27, 2 (American Physical Society, Jan. 1983), pp. 985–1009.

[75]The Center for X-ray Optics, *Filter Transmission*, `http://henke.lbl.gov/optical%7B%5C_%7Dconstants/filter2.html` (visited on 08/13/2023).

[76]*Hitachi Aberration-Corrected Concave Gratings for Flat-Field Spectrographs*, `https://www.hitachi-hightech.com/products/images/9797/ana-grating%7B%5C_%7D05.pdf` (visited on 10/10/2022).

[77]N. Nakano, H. Kuroda, T. Kita, and T. Harada, "Development of a flat-field grazing-incidence XUV spectrometer and its application in picosecond XUV spectroscopy", Applied Optics **23**, 2386 (1984).

[78]T. Harada, K. Takahashi, H. Sakuma, and A. Osyczka, "Optimum design of a grazing-incidence flat-field spectrograph with a spherical varied-line-space grating", Applied Optics **38**, 2743 (1999).

[79]T. Harada and T. Kita, "Mechanically ruled aberration-corrected concave gratings", Applied Optics **19**, 3987 (1980).

[80]F. Schäfers, "The BESSY Raytrace Program RAY", Springer Series in Optical Sciences **137**, 9–41 (2008).

[81]M. Neviere and J. Flamand, "Electromagnetic theory as it applies to X-ray and XUV gratings", Nuclear Instruments and Methods **172**, 273–279 (1980).

[82]M. Neviere, J. Flamand, and J. M. Lerner, "Optimization of gratings for soft x-ray monochromators", Nuclear Instruments and Methods **195**, 183–189 (1982).

[83]V. G. Kohn, "On the Theory of Reflectivity by an X-Ray Multilayer Mirror", Physica Status Solidi (B) **187**, 61–70 (1995).

[84]H. Takenaka, S. Ichimaru, T. Ohchi, and E. M. Gullikson, "Soft-X-ray reflectivity and heat resistance of SiC/Mg multilayer", Journal of Electron Spectroscopy and Related Phenomena **144-147**, 1047–1049 (2005).

[85]*Ntt advanced technology corporation*, `https://www.ntt-at.com/` (visited on 01/29/2023).

[86]*XLS Ultrasonic linear piezo stage - Xeryon*, `https://xeryon.com/products/precision-linear-stages/xls-ultrasonic-linear-piezo-stage/` (visited on 10/30/2023).

[87]K. Strehl, "Aplanatische und fehlerhafte Abbildung im Fernrohr", Zeitschrift fur Instrumentenkunde **15**, 362–370 (1895).

[88]S. Petrakis, A. Skoulakis, Y. Orphanos, A. Grigoriadis, G. Andrianaki, D. Louloudakis, N. Kortsalioudakis, A. Tsapras, C. Balas, D. Zouridis, E. Pachos, M. Bakarezos, V. Dimitriou, M. Tatarakis, E. P. Benis, and N. A. Papadogiannis, "Coherent xuv multispectral diffraction imaging in the microscale", Applied Sciences **12** (2022).

[89]F. Brizuela, C. M. Heyl, P. Rudawski, D. Kroon, L. Rading, J. M. Dahlström, J. Mauritsson, P. Johnsson, C. L. Arnold, and A. L'Huillier, "Efficient high-order harmonic generation boosted by below-threshold harmonics", Scientific Reports **3** (2013).

[90]M. Sayrac, A. A. Kolomenskii, J. Strohaber, and H. A. Schuessler, "High harmonic generation in Ne and H2 gas mixtures", Journal of the Optical Society of America B **32**, 2400 (2015).

[91]R. Weissenbilder, S. Carlström, L. Rego, C. Guo, C. M. Heyl, P. Smorenburg, E. Constant, C. L. Arnold, and A. L'Huillier, *Efficient generation of high-order harmonics in gases*, tech. rep. (2022).

[92]G. Porat, C. M. Heyl, S. B. Schoun, C. Benko, N. Dörre, K. L. Corwin, and J. Ye, "Phase-matched extreme-ultraviolet frequency-comb generation", Nature Photonics **12**, 387–391 (2018).

[93]F. M. Lu, Y. Q. Xia, S. Zhang, and D. Y. Chen, "High harmonic generation in a Xe-He gas mixture driven by kHz tightly focused laser pulses", Laser Physics **23**, 115302 (2013).

[94]H. O. Seo, T. Arion, F. Roth, D. Ramm, C. Lupulescu, and W. Eberhardt, "Improving the efficiency of high harmonic generation (HHG) by Ne-admixing into a pure Ar gas medium", Applied Physics B: Lasers and Optics **122**, 1–6 (2016).

[95]J. Seres, V. S. Yakovlev, E. Seres, C. Streli, P. Wobrauschek, C. Spielmann, and F. Krausz, "Coherent superposition of laser-driven soft-X-ray harmonics from successive sources", Nature Physics **3**, 878–883 (2007).

[96]E. J. Takahashi, T. Kanai, K. L. Ishikawa, Y. Nabekawa, and K. Midorikawa, "Dramatic enhancement of high-order harmonic generation", Physical Review Letters **99** (2007).

[97]T. Kanai, E. J. Takahashi, Y. Nabekawa, and K. Midorikawa, "Destructive interference during high harmonic generation in mixed gases", Physical Review Letters **98** (2007).

[98] A. Willner, F. Tavella, M. Yeung, T. Dzelzainis, C. Kamperidis, M. Bakarezos, D. Adams, M. Schulz, R. Riedel, M. C. Hoffmann, W. Hu, J. Rossbach, M. Drescher, N. A. Papadogiannis, M. Tatarakis, B. Dromey, and M. Zepf, "Coherent control of high harmonic generation via dual-gas multijet arrays", Physical Review Letters **107**, 175002 (2011).

[99] A. Willner, F. Tavella, M. Yeung, T. Dzelzainis, C. Kamperidis, M. Bakarezos, D. Adams, R. Riedel, M. Schulz, M. C. Hoffmann, W. Hu, J. Rossbach, M Drescher, V. S. Yakovlev, N. A. Papadogiannis, M. Tatarakis, B. Dromey, and M. Zepf, "Efficient control of quantum paths via dual-gas high harmonic generation", New Journal of Physics **13**, 113001 (2011).

[100] P. Salières, B. Carré, L. Le Déroff, F. Grasbon, G. G. Paulus, H. Walther, R. Kopold, W. Becker, D. B. Milošević, A. Sanpera, and M. Lewenstein, "Feynman's path-integral approach for intense-laser-atom interactions", Science **292**, 902–905 (2001).

[101] M. Drescher, M. Hentschel, R. Kienberger, G. Tempea, C. Spielmann, G. A. Reider, P. B. Corkum, and F. Krausz, "X-ray pulses approaching the attosecond frontier", Science **291**, 1923–1927 (2001).

[102] M. Hentschel, R. Kienberger, C. Spielmann, G. A. Reider, N. Milosevic, T. Brabec, P. Corkum, U. Heinzmann, M. Drescher, and F. Krausz, "Attosecond metrology", Nature **414**, 509–513 (2001).

[103] M. Drescher, M. Hentschel, R. Kienberger, M. Uiberacker, V. Yakovlev, A. Scrinzi, T. Westerwalbesloh, U. Kleineberg, U. Heinzmann, and F. Krausz, "Time-resolved atomic inner-shell spectroscopy", Nature **419**, 803–807 (2002).

[104] N. A. Papadogiannis, C. Kalpouzos, E. Goulielmakis, G. Nersisyan, D. C̃haralambidis, F. Augé, F. Weihe, and P. Balcou, "Kilohertz extreme-ultraviolet light source based on femtosecond high-order harmonic generation from noble gases", Applied Physics B: Lasers and Optics **73**, 687–692 (2001).

[105] M. Lewenstein, P. Salières, and A. Lhuillier, "Phase of the atomic polarization in high-order harmonic generation", Physical Review A **52**, 4747–4754 (1995).

[106] M. B. Gaarde, "Spatiotemporal separation of high harmonic radiation into two quantum path components", Phys. Rev. A **59** (1999).

[107] M. Bellini, C. Lyngå, A. Tozzi, M. B. Gaarde, T. W. Hänsch, A. L'Huillier, and C. G. Wahlström, "Temporal coherence of ultrashort high-order harmonic pulses", Physical Review Letters **81**, 297–300 (1998).

[108] N. Ishii, A. Kosuge, T. Hayashi, T. Kanai, J. Itatani, S. Adachi, and S. Watanabe, "Quantum path selection in high-harmonic generation by a phase-locked two-color field", Optics Express **16**, 20876 (2008).

[109]L. Brugnera, D. J. Hoffmann, T. Siegel, F. Frank, A. Zaïr, J. W. Tisch, and J. P. Marangos, "Trajectory selection in high harmonic generation by controlling the phase between orthogonal two-color fields", Physical Review Letters **107**, 153902 (2011).

[110]S. Petrakis, M. Bakarezos, M. Tatarakis, E. P. Benis, and N. A. Papadogiannis, "Electron quantum path control in high harmonic generation via chirp variation of strong laser pulses", Scientific Reports **11**, 23882 (2021).

[111]H. J. Shin, D. G. Lee, Y. H. Cha, K. H. Hong, and C. H. Nam, "Generation of Nonadiabatic Blueshift of High Harmonics in an Intense Femtosecond Laser Field", Physical Review Letters **83**, 2544 (1999).

[112]D. G. Lee, J. H. Kim, K. H. Hong, and C. H. Nam, "Coherent Control of High-Order Harmonics with Chirped Femtosecond Laser Pulses", Physical Review Letters **87**, 243902 (2001).

[113]X. B. Bian and A. D. Bandrauk, "Spectral shifts of nonadiabatic high-order harmonic generation", Applied Sciences **3**, 267–277 (2013).

[114]C. G. Wahlström, J. Larsson, A. Persson, T. Starczewski, S. Svanberg, P. Salières, P. Balcou, and A. L'Huillier, "High-order harmonic generation in rare gases with an intense short-pulse laser", Physical Review A **48**, 4709 (1993).

[115]S. C. Rae and K. Burnett, "Detailed simulations of plasma-induced spectral blueshifting", Physical Review A **46**, 1084 (1992).

[116]J. B. Watson, A. Sanpera, and K. Burnett, "Pulse-shape effects and blueshifting in the single-atom harmonic generation from neutral species and ions", Physical Review A **51**, 1458 (1995).

[117]H. Wikmark, C. Guo, J. Vogelsang, P. W. Smorenburg, H. Coudert-Alteirac, J. Lahl, J. Peschel, P. Rudawski, H. Dacasa, S. Carlström, S. MacLot, M. B. Gaarde, P. Johnsson, C. L. Arnold, and A. L'Huillier, "Spatiotemporal coupling of attosecond pulses", Proceedings of the National Academy of Sciences of the United States of America **116**, 4779–4787 (2019).

[118]A. Mysyrowicz, A. Couairon, and U. Keller, "Self-compression of optical laser pulses by filamentation", New Journal of Physics **10**, 025023 (2008).

[119]J. H. Kim and C. H. Nam, "Plasma-induced frequency chirp of intense femtosecond lasers and its role in shaping high-order harmonic spectral lines", Physical Review A - Atomic, Molecular, and Optical Physics **65**, 5 (2002).

[120]W. Cao, G. Laurent, C. Jin, H. Li, Z. Wang, C. D. Lin, I. Ben-Itzhak, and C. L. Cocke, "Spectral splitting and quantum path study of high-harmonic generation from a semi-infinite gas cell", Journal of Physics B: Atomic, Molecular and Optical Physics **45**, 074013 (2012).

[121]S. Petrakis, M. Bakarezos, M. Tatarakis, E. P. Benis, and N. A. Papadogiannis, "Spectral and Divergence Characteristics of Plateau High-Order Harmonics Generated by Femtosecond Chirped Laser Pulses in a Semi-Infinite Gas Cell", Atoms **10** (2022).

[122]X. Dong, M. Jakobi, S. Wang, M. H. Köhler, X. Zhang, and A. W. Koch, "A review of hyperspectral imaging for nanoscale materials research", Applied Spectroscopy Reviews **54**, 285–305 (2019).

[123]J. Miao, D. Sayre, and H. N. Chapman, "Phase retrieval from the magnitude of the Fourier transforms of nonperiodic objects", Journal of the Optical Society of America A **15**, 1662 (1998).

[124]J. R. Fienup, "Reconstruction of an object from the modulus of its Fourier transform", Optics Letters **3**, 27 (1978).

[125]J. R. Fienup, "Phase retrieval algorithms: a comparison", Applied Optics **21**, 2758 (1982).

[126]S. Marchesini, H. He, N. Chapman, P. Hau-Riege, A. Noy, R. Howells, U. Weierstall, and H. Spence, "X-ray image reconstruction from a diffraction pattern alone", Physical Review B - Condensed Matter and Materials Physics **68** (2003).

[127]J. R. Fienup, "Phase retrieval algorithms: A personal tour [Invited]", Applied Optics **52**, 45–56 (2013).

[128]M. D. Seaberg, B. Zhang, D. F. Gardner, E. R. Shanblatt, M. M. Murnane, H. C. Kapteyn, and D. E. Adams, "Tabletop nanometer extreme ultraviolet imaging in an extended reflection mode using coherent Fresnel ptychography", Optica **1**, 39 (2014).

[129]B. Zhang, D. F. Gardner, M. D. Seaberg, E. R. Shanblatt, H. C. Kapteyn, M. M. Murnane, and D. E. Adams, "High contrast 3D imaging of surfaces near the wavelength limit using tabletop EUV ptychography", Ultramicroscopy **158**, 98–104 (2015).

[130]G. K. Tadesse, W. Eschen, R. Klas, M. Tschernajew, F. Tuitje, M. Steinert, M. Zilk, V. Schuster, M. Zürch, T. Pertsch, et al., "Wavelength-scale ptychographic coherent diffractive imaging using a high-order harmonic source", Scientific Reports **9**, 1–7 (2019).

[131]M. Tanksalvala, C. L. Porter, Y. Esashi, B. Wang, N. W. Jenkins, Z. Zhang, G. P. Miley, J. L. Knobloch, B. McBennett, N. Horiguchi, et al., "Nondestructive, high-resolution, chemically specific 3D nanostructure characterization using phase-sensitive EUV imaging reflectometry", Science Advances **7**, eabd9667 (2021).

[132]L. Loetgering, S. Witte, and J. Rothhardt, "Advances in laboratory-scale ptychography using high harmonic sources", Optics Express **30**, 4133–4164 (2022).

[133]S. Kneip, C. McGuffey, J. L. Martins, S. F. Martins, C. Bellei, V. Chvykov, F. Dollar, R. Fonseca, C. Huntington, G. Kalintchenko, A. Maksimchuk, S. P. Mangles, T. Matsuoka, S. R. Nagel, C. A. Palmer, J. Schreiber, K. T. Phuoc, A. G. Thomas, V. Yanovsky, L. O. Silva, K. Krushelnick, and Z. Najmudin, "Bright spatially coherent synchrotron X-rays from a table-top source", Nature Physics **6**, 980–983 (2010).

[134]G. Geloni, E. Saldin, L. Samoylova, E. Schneidmiller, H. Sinn, T. Tschentscher, and M. Yurkov, "Coherence properties of the European XFEL", New Journal of Physics **12**, 035021 (2010).

[135]R. L. Sandberg, C. Song, P. W. Wachulak, D. A. Raymondson, A. Paul, B. Amirbekian, E. Lee, A. E. Sakdinawat, C. La-O-Vorakiat, M. C. Marconi, et al., "High numerical aperture tabletop soft x-ray diffraction microscopy with 70-nm resolution", Proceedings of the National Academy of Sciences **105**, 24–27 (2008).

[136]D. A. Raymondson, R. L. Sandberg, W. F. Schlotter, K. S. Raines, C. La-o-Vorakiat, E. Townsend, A. Sakdinawat, A. Paul, J. Miao, M. M. Murnane, and H. C. Kapteyn, "Tabletop coherent diffractive microscopy with extreme ultraviolet light from high harmonic generation", Metrology, Inspection, and Process Control for Microlithography XXIII **7272**, 72720F (2009).

[137]A. Ravasio, D. Gauthier, F. R. Maia, M. Billon, J. P. Caumes, D. Garzella, M. Géléoc, O. Gobert, J. F. Hergott, A. M. Pena, H. Perez, B. Carré, E. Bourhis, J. Gierak, A. Madouri, D. Mailly, B. Schiedt, M. Fajardo, J. Gautier, P. Zeitoun, P. H. Bucksbaum, J. Hajdu, and H. Merdji, "Single-shot diffractive imaging with a table-top femtosecond soft X-ray laser-harmonics source", Physical Review Letters **103**, 028104 (2009).

[138]K. B. Dinh, A. X. Ong, H. V. Le, C. A. Henderson, C. Van Vuong, P. Hannaford, T. A. Smith, and L. Van Dao, "Coherent diffractive imaging of single layer microspheres", Journal of Applied Physics **117** (2015).

[139]N. X. Truong, I. Strashnov, E. Whittaker, X. L. Zhong, and M. A. Denecke, "Coherent diffractive imaging of graphite nanoparticles using a tabletop EUV source", Physical Chemistry Chemical Physics **19**, 29660–29668 (2017).

[140]W. Eschen, L. Loetgering, V. Schuster, R. Klas, A. Kirsche, L. Berthold, M. Steinert, T. Pertsch, H. Gross, M. Krause, J. Limpert, and J. Rothhardt, "Material-specific high-resolution table-top extreme ultraviolet microscopy", Light: Science and Applications **11**, 1–10 (2022).

[141]D. Gauthier, M. Guizar-Sicairos, X. Ge, W. Boutu, B. Carré, J. R. Fienup, and H. Merdji, "Single-shot femtosecond x-ray holography using extended references", Physical Review Letters **105**, 093901 (2010).

[142]J. Rothhardt, G. K. Tadesse, W. Eschen, and J. Limpert, "Table-top nanoscale coherent imaging with XUV light", Journal of Optics **20** (2018).

[143]G. K. Tadesse, R. Klas, S. Demmler, S. Hädrich, I. Wahyutama, M. Steinert, C. Spielmann, M. Zürch, T. Pertsch, A. Tünnermann, J. Limpert, and J. Rothhardt, "High speed and high resolution table-top nanoscale imaging", Optics Letters **41**, 5170 (2016).

[144]X. Ge, W. Boutu, D. Gauthier, F. Wang, A. Borta, B. Barbrel, M. Ducousso, A. I. Gonzalez, B. Carré, D. Guillaumet, M. Perdrix, O. Gobert, J. Gautier, G. Lambert, F. R. N. C. Maia, J. Hajdu, P. Zeitoun, and H. Merdji, "Impact of wave front and coherence optimization in coherent diffractive imaging", Optics Express **21**, 11441 (2013).

[145]W. Xu, S. Ning, and F. Zhang, "Numerical and experimental study of partial coherence for near-field and far-field ptychography", Optics Express **29**, 40652 (2021).

[146]R. A. Bartels, A. Paul, H. Green, H. C. Kapteyn, M. M. Murnane, S. Backus, I. P. Christov, Y. Liu, D. Attwood, and C. Jacobsen, "Generation of spatially coherent light at extreme ultraviolet wavelengths", Science **297**, 376–378 (2002).

[147]J. Miao and D. Sayre, "On possible extensions of X-ray crystallography through diffraction-pattern oversampling", Acta Crystallographica Section A: Foundations of Crystallography **56**, 596–605 (2000).

[148]R. W. Gerchberg and W. O. Saxton, "Practical Algorithm for the Determination of Phase From Image and Diffraction Plane Pictures.", Optik **35**, 237–250 (1972).

[149]D. R. Luke, "Relaxed averaged alternating reflections for diffraction imaging", Inverse Problems **21**, 37–50 (2005).

[150]A. V. Martin, F. Wang, N. D. Loh, T. Ekeberg, F. R. N. C. Maia, M. Hantke, G. van der Schot, C. Y. Hampton, R. G. Sierra, A. Aquila, S. Bajt, M. Barthelmess, C. Bostedt, J. D. Bozek, N. Coppola, S. W. Epp, B. Erk, H. Fleckenstein, L. Foucar, M. Frank, H. Graafsma, L. Gumprecht, A. Hartmann, R. Hartmann, G. Hauser, H. Hirsemann, P. Holl, S. Kassemeyer, N. Kimmel, M. Liang, L. Lomb, S. Marchesini, K. Nass, E. Pedersoli, C. Reich, D. Rolles, B. Rudek, A. Rudenko, J. Schulz, R. L. Shoeman, H. Soltau, D. Starodub, J. Steinbrener, F. Stellato, L. Strüder, J. Ullrich, G. Weidenspointner, T. A. White, C. B. Wunderer, A. Barty, I. Schlichting, M. J. Bogan, and H. N. Chapman, "Noise-robust coherent diffractive imaging with a single diffraction pattern", Optics Express **20**, 16650 (2012).

[151]J. Li and T. Zhou, "On relaxed averaged alternating reflections (RAAR) algorithm for phase retrieval with structured illumination", Inverse Problems **33** (2017).

[152]M. J. Cherukara, Y. S. Nashed, and R. J. Harder, "Real-time coherent diffraction inversion using deep generative networks", Scientific Reports **8** (2018).

[153]M. J. Cherukara, T. Zhou, Y. Nashed, P. Enfedaque, A. Hexemer, R. J. Harder, and M. V. Holt, "AI-enabled high-resolution scanning coherent diffraction imaging", Applied Physics Letters **117**, 44103 (2020).

[154]H. Chan, Y. S. Nashed, S. Kandel, S. O. Hruszkewycz, S. K. Sankaranarayanan, R. J. Harder, and M. J. Cherukara, "Rapid 3D nanoscale coherent imaging via physics-aware deep learning", Applied Physics Reviews **8**, 021407 (2021).

[155]D. J. Chang, C. M. O'Leary, C. Su, S. Kahn, A. Zettl, J. Ciston, P. Ercius, and J. Miao, *Deep learning coherent diffractive imaging*, 2022.

[156]J. R. Fienup and C. C. Wackerman, "Phase-retrieval stagnation problems and solutions", Journal of the Optical Society of America A **3**, 1897 (1986).

[157]H. N. Chapman, A. Barty, S. Marchesini, A. Noy, S. P. Hau-Riege, C. Cui, M. R. Howells, R. Rosen, H. He, J. C. H. Spence, U. Weierstall, T. Beetz, C. Jacobsen, and D. Shapiro, "High-resolution ab initio three-dimensional x-ray diffraction microscopy", Journal of the Optical Society of America A **23**, 1179 (2006).

[158]R. A. Dilanian, B. Chen, G. J. Williams, H. M. Quiney, K. A. Nugent, S. Teichmann, P. Hannaford, L. V. Dao, and A. G. Peele, "Diffractive imaging using a polychromatic high-harmonic generation soft-x-ray source", Journal of Applied Physics **106** (2009).

[159]B. Chen, R. A. Dilanian, S. Teichmann, B. Abbey, A. G. Peele, G. J. Williams, P. Hannaford, L. Van Dao, H. M. Quiney, and K. A. Nugent, "Multiple wavelength diffractive imaging", Physical Review A - Atomic, Molecular, and Optical Physics **79** (2009).

[160]J. Miao, T. Ishikawa, E. H. Anderson, and K. O. Hodgson, "Phase retrieval of diffraction patterns from noncrystalline samples using the oversampling method", Physical Review B - Condensed Matter and Materials Physics **67** (2003).

[161]P. A. Prosekov, V. L. Nosik, and A. E. Blagov, "Methods of Coherent X-Ray Diffraction Imaging", Crystallography Reports **66**, 867–882 (2021).

[162]A. D. Smith, T. Balčiu Nas, Y. P. Chang, C. Schmidt, K. Zinchenko, F. B. Nunes, E. Rossi, V. Svoboda, Z. Yin, J. P. Wolf, and H. J. Wörner, "Femtosecond Soft-X-ray Absorption Spectroscopy of Liquids with a Water-Window High-Harmonic Source", Journal of Physical Chemistry Letters **11**, 1981–1988 (2020).

[163]J. Thieme, S.-C. Gleber, P. Guttmann, J. Prietzel, I. McNulty, and J. Coates, "Microscopy and spectroscopy with X-rays for studies in the environmental sciences", Mineralogical Magazine **72**, 211–216 (2008).

[164]Y. Pertot, C. Schmidt, M. Matthews, A. Chauvet, M. Huppert, V. Svoboda, A. Von Conta, A. Tehlar, D. Baykusheva, J. P. Wolf, and H. J. Wörner, "Time-resolved x-ray absorption spectroscopy with a water window high-harmonic source", Science **355**, 264–267 (2017).

[165]Y. Nomura, R. Hörlein, P. Tzallas, B. Dromey, S. Rykovanov, Z. Major, J. Osterhoff, S. Karsch, L. Veisz, M. Zepf, D. Charalambidis, F. Krausz, and G. D. Tsakiris, "Attosecond phase locking of harmonics emitted from laser-produced plasmas", Nature Physics **5**, 124–128 (2009).

[166]Hamamatsu, *MCP (Microchannel Plate) Assembly*, (2021) `https://www.hamamatsu.com/content/dam/hamamatsu-photonics/sites/documents/99_SALES_LIBRARY/etd/MCP_assembly_TMCP0003E.pdf` (visited on 01/19/2023).

[167]*Eagle XO Open Front • Direct Detection CCD • High Resolution Soft X-ray Scientific*, `https://www.raptorphotonics.com/products/eagle-xo/` (visited on 01/06/2022).

[168]T. Latychevskaia, "Iterative phase retrieval in coherent diffractive imaging: practical issues", Applied Optics **57**, 7187 (2018).

Appendices

Appendix A

45 TW Laser System Oscillator's Specifications

Table A.1
SYNERGY^{TM} PRO oscillator specifications

Description	value
Pulse duration	$<$ 10 fs
Spectral width (FWHM) @ 800 nm	$>$ 100 nm
Mode-locked output power (average)	150 - 500 mW
Output energy @ 75 MHz	2 - 6.5 nJ
Peak power @ 75 MHz	200 - 650 kW
Beam divergence	$<$ 2 mrad
Spatial mode	TEM00 ($M^2 < 1.3$)
Polarization	$>$ 100:1 (horiz.)
Noise	$<$ 0.05% rms
Power stability	$\pm$ 1%

Appendix B

Microchannel Plates

As illustrated in Figure B.1, the fundamental structure of an MCP comprises a series of closely spaced channels, akin to microscopic tubes, aligned in a two-dimensional array. Each channel's inner walls are coated with the electron-emissive material, forming the active surface responsible for signal amplification. When an incident photon or particle enters one of the channels, it strikes the channel wall with sufficient energy to dislodge secondary electrons from the material. These liberated electrons undergo a cascading process due to the strong electric fields maintained within the channels. Consequently, a single incident particle can trigger the release of a multitude of electrons, resulting in an exponential amplification of the original signal. The cascading process is contingent upon maintaining a high electric field along the channel walls. This is accomplished by applying a voltage potential across the MCP.

The two-stage MCP F1552-11 of company HAMAMATSU PHOTONICS was used, which is a sensor consisting of a glass plates 0.48 mm thick in which there are holes with a diameter of 12 µm every 15 µm [166].

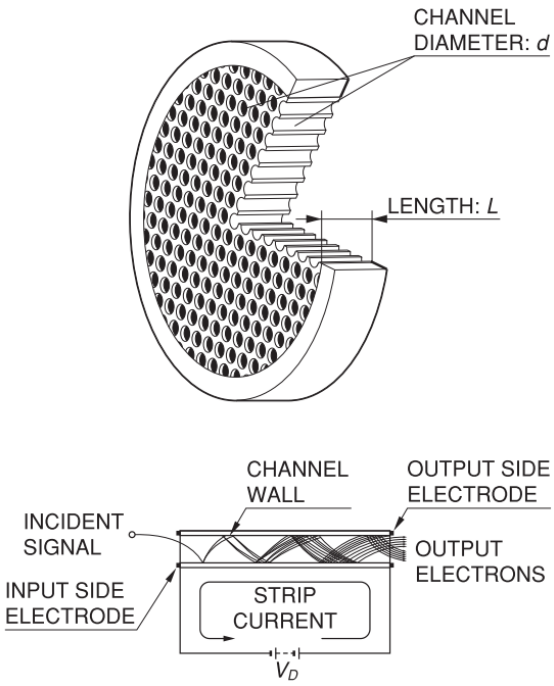

Figure B.1
Schematic structure of MCP. Reprinted from [166]

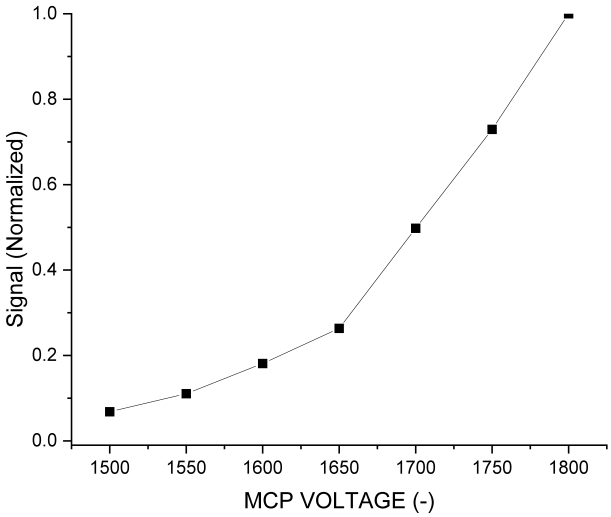

Figure B.2
Voltage-Dependent Signal Characteristics in Multichannel Plates: A graphical representation showcasing the correlation between signal intensity and applied voltage across the multichannel plates utilized in the experimental setup.

Appendix C

Data Acquisition for HHG Spectra with MCP

The data acquisition for the HHG spectra with MCP was done in the environment of the commercial software LabVIEW of the company National Instruments, in a fully automated way. Part of the program developed by our colleague Dr. Ioannis Orphanos, is shown below.

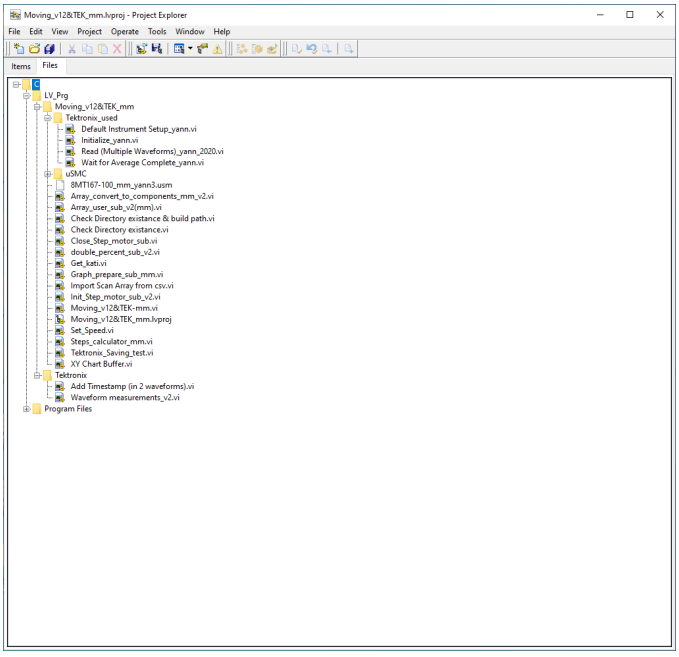

Figure C.1
Virtual tools (VI) of the LabVIEW software used to automate the HHG measurement.

Front Panel

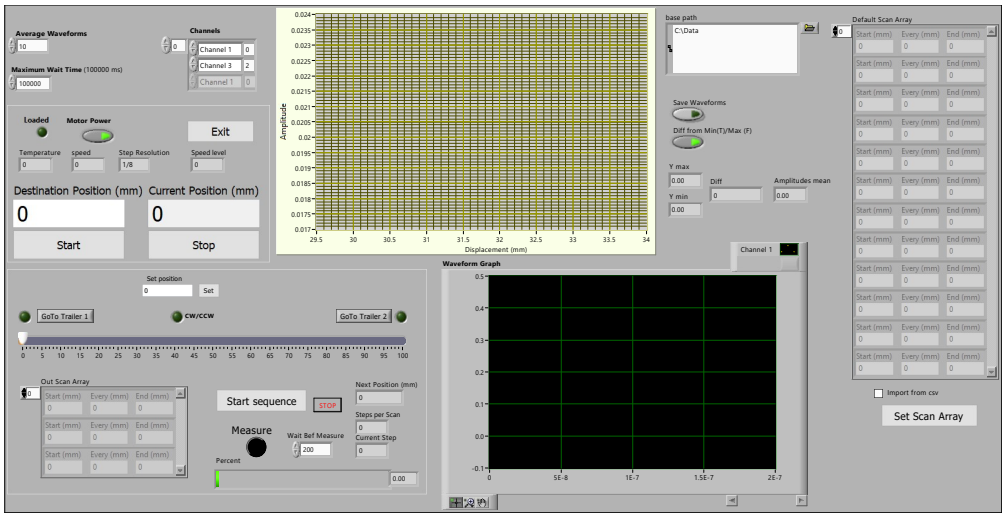

Block Diagram

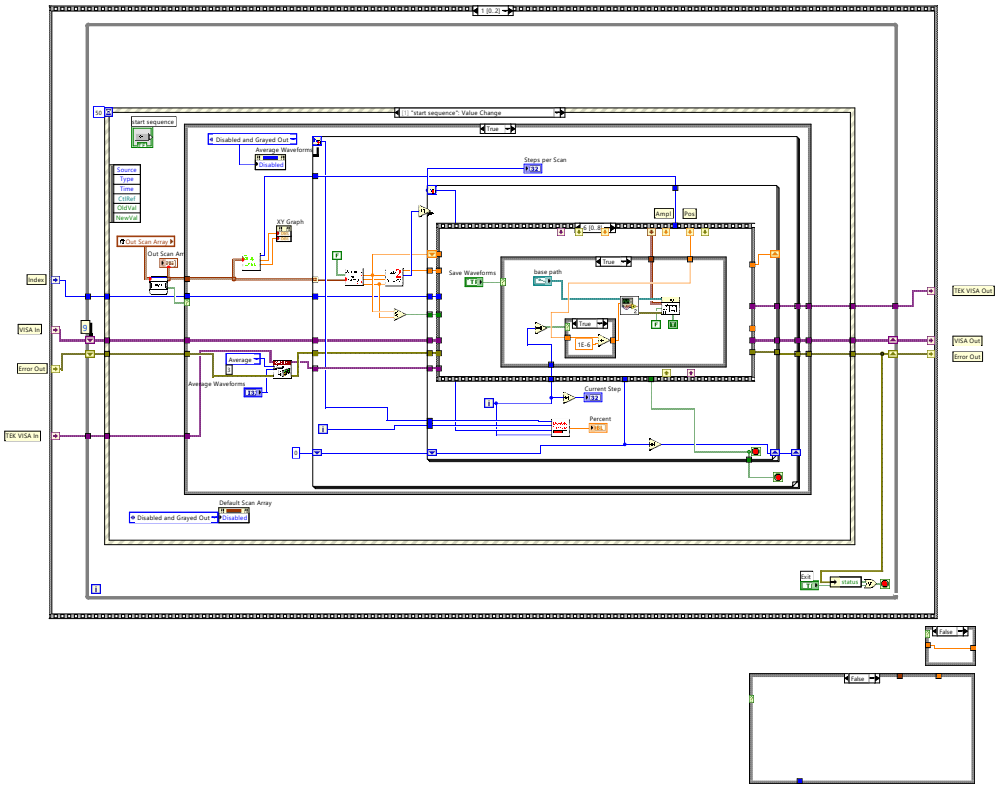

Figure C.2
LabVIEW environment (top) and main block diagram (bottom).

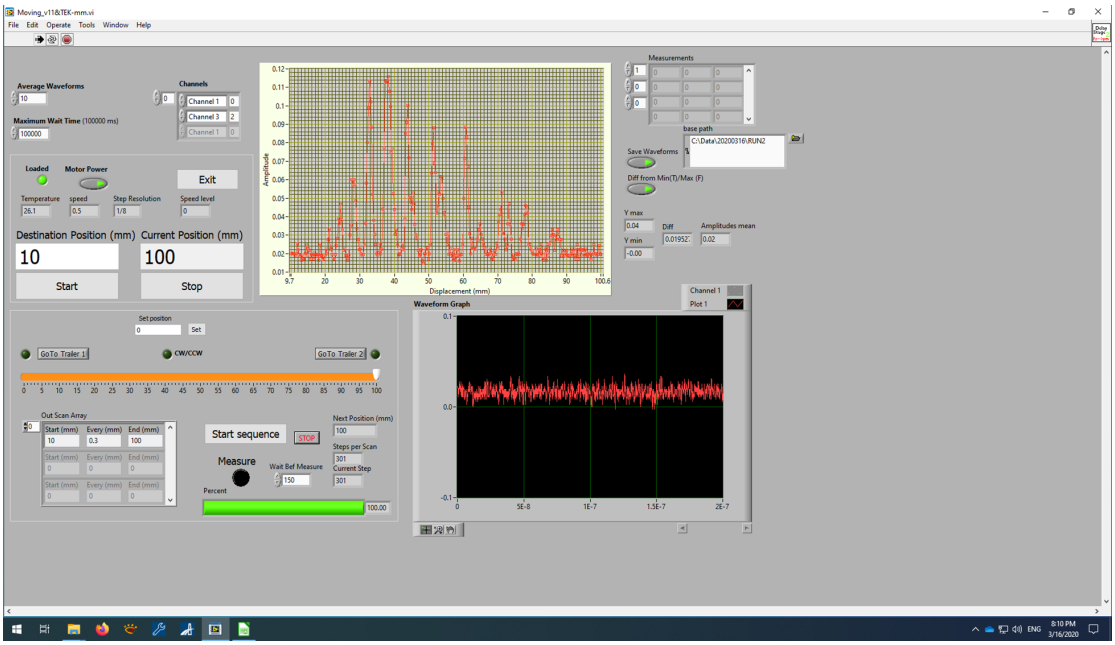

Figure C.3
Typical entire HHG spectrum (raw data) seen in the LabVIEW data acquisition environment.

Appendix D

XUV CCD cameras

Two Raptor Photonics XUV CCD cameras were used for the experiments. The model was Eagle V 4240 with the one had a square chip with dimensions 1024×1024 pixels which was used for diffraction imaging, while the other had a rectangle chip with dimensions 2048×512 pixels which was used for XUV image spectra. The pixel size was 13.5×13.5 μm for both chips. The camera has an open front-end - flange CF152 ((6″)) for direct interface with vacuum chambers, and simultaneously uses a TEC-type thermoelectric heatsink for a constant temperature at 20 °C while also having a liquid cooling system to minimize dark current. Its optimal operation is in a vacuum state, specifically in conditions below 5×10^{-5} mbar ($< 3.75 \times 10^{-5}$ Torr) [167]. The specifications of the XUV CCD camera are given in Table D.1, while its quantum efficiency is given in Fig.D.1.

Table D.1
XUV CCD camera specifications (model Eagle V 4240, Raptor Photonics).

Sensor	E2V 4240 Back Illuminated, AIMO[1]	E2V 4210 Back Illuminated, AIMO[1]
Active Pixel Array Size	2048 × 2048 pixels	2048 × 512 pixels
Pixel Size	13.5μm × 13.5μm	
Active Area	27.65mm × 6.9mm (28.45mm diagonal)	27.65mm x 27.65mm (39.10mm diagonal)
Binning	Programmable, up to 64×64 pixels	
Full Well Capacity	100,000 e/p	
Non-Linearity	$< 1\%$	
Readout Noise	@ 75kHz pixel readout rate, 2.3 e/p @ 2MHz pixel readout rate, 9.0 e- rms	
Binned Read Noise	@75kHz pixel readout rate, 16×16 binning $<$ 5.0 e- rms	
Peak Quantum Effi (QE)	$> 90\%$	
Spectral Response	1.2eV to 20KeV	
Dark Current @ -75°C (typical)	0.0004 e-/pixel/second	
Cooling Active	$\Delta T > 100$°C, -75°C air cooled / -80°C water cooler	
Cooling Method	Air / Liquid	
Flange	CF152 (6″) 2	
Synchronization	Trigger IN and OUT – TTL compatible	
Digital Output	16-bit	
Data Interface	Cameralink (base)	
Power Supply	12V DC ±10%	
Total Power Consumption	TEC OFF $<$ 9W TEC ON $<$ 100W	
Operating Temperature Range	-20°C to +55°C	
Storage Temperature Range	-40°C to +70°C	
Dimensions	141mm x 133mm x 110mm	
Weight (excluding lens)	5.0kg [11lb]	

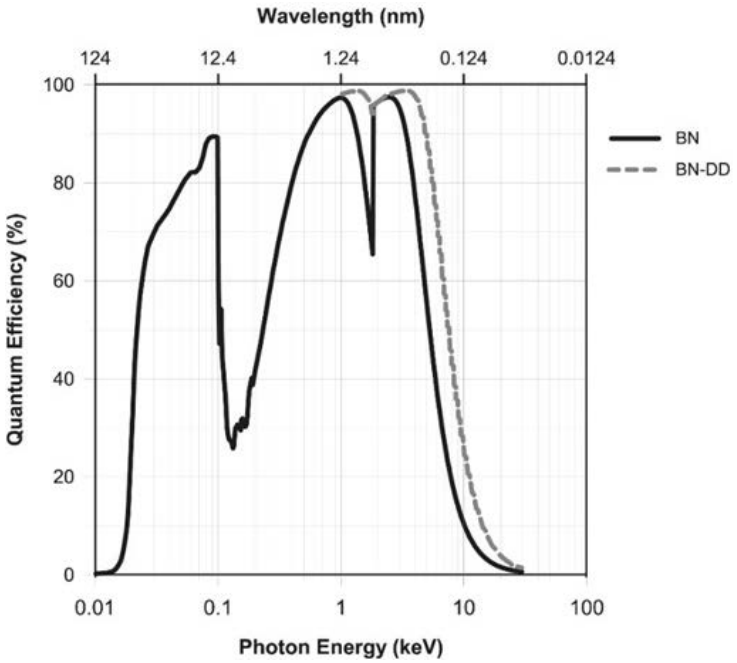

Figure D.1
Eagle V 4240 Scientific CCD Camera quantum efficiency. (Reprinted from [167])

Appendix E

Code Calculations for Chapter 5

```
ClearAll["Global`*"]
```
διαγραφή ιδιοτήτων συμβόλων
```
ClearAll["`*"];
```
διαγραφή ιδιοτήτων συμβόλων
```
Clear["Global`*"]
```
διαγραφή ορισμών και τιμών συμβόλων
```
(*Remove["Global`*"]*)
```
αφαίρεση
```
(*Quit[]*)
```
τερματισμός
```
SetDirectory[NotebookDirectory[]];
```
ορισμός τρέχον··· κατάλογος σημειωματάριου
```
(*<<RootSearch.m
  Needs["CUDALink`"];*)
```
υποχρεωτικά
```
Needs["NumericalCalculus`"]
```
υποχρεωτικά

```
Quit[]
```
τερματισμ

```
(*Experimantal parameters and constants*)
```

```
I0FL = Quantity[23 × 10^14, "Watts" / ("Centimeters")^2];
       ποσότητα
fs = Quantity[10^-15, "Seconds"];
     ποσότητα
tauFL = 26 ;

e0 = Quantity["ElectricConstant"];
     ποσότητα

ElectronCharge = Quantity["ElementaryCharge"];
                 ποσότητα
ElectronRadius = Quantity[2.82 * 10^-15, "Meters"];
                 ποσότητα
me = Quantity["ElectronMass"];
     ποσότητα
L[x_] := Quantity[x / 1000, "Meters"];
         ποσότητα
P[x_] := Quantity[x, "Torr"];
         ποσότητα
lamda[x_] := Quantity[x * 10^-9, "Meters"] (*nm*)
             ποσότητα
LaserWavlength = 807;
omega1 = 2 π Quantity["SpeedOfLight"] / lamda[LaserWavlength];
omegaq[order_] := 2 π Quantity["SpeedOfLight"] / lamda[LaserWavlength / order] ;
ℏ = Quantity["ReducedPlanckConstant"];
    ποσότητα
P0[PulseEnergyInmJ_, FWHMinfs_] :=
  N[Sqrt[4 Log[2] / π]  * Quantity[PulseEnergyInmJ / 1000, "Joules"] / Quantity[FWHMinfs 10^-15, "Seconds"]];
  αριθμητική τιμή

LaserIntensity[rinmm_, t_, PulseEnergyInmJ_, FWHMinfs_, winμm_] :=
  UnitConvert[2 P0[PulseEnergyInmJ, FWHMinfs] / (π Quantity[winμm, "Micrometers"]^2) e^(-2 (rinmm / winμm/1000)^2) e^(-4 Log[2] (t / FWHMinfs)^2), "W/cm^2"];
  μετατροπή μονάδων μέτρησης
```

```
(*ADK model*)
```

```
F0Ar = 1.24665;
nStarAr = 0.92915;
CnlAr = 4.11564;
GlmAr = 3;
IpAr = 15.759 / 27.21;
F0Ne = 1.99547;
nStarNe = 0.7943;
CnlNe = 4.24355;
GlmNe = 3;
IpNe = 21.564 / 27.21;

F[intensity_] := Sqrt[intensity / (3.55 × 10^16)];

wADKAr[intensity_] := CnlAr GlmAr IpAr (2 F0Ar / F[intensity])^(2 nStarAr - 1) Exp[-2 F0Ar / (3 F[intensity])];

wADKNe[intensity_] := CnlNe GlmNe IpNe (2 F0Ne / F[intensity])^(2 nStarNe - 1) Exp[-2 F0Ne / (3 F[intensity])];

(*FWHM=40000/24.2; (*in atomic units time*)*)
PLAr[intensity_, tau_] :=
  1 - Exp[-1.14 tau 1000 / 24.2 3^(2 nStarAr - 1) (3 F[intensity] / (2 F0Ar))^2.41 wADKAr[intensity]];

PLNe[intensity_, tau_] :=
  1 - Exp[-1.14 tau 1000 / 24.2 3^(2 nStarNe - 1) (3 F[intensity] / (2 F0Ne))^2.41 wADKNe[intensity]];

(*Fa field amplitude*)
```

```
I0[tau_] := I0FL tauFL fs / Abs[tau] fs; (*Laser peak intensity*)
```

```
Idrive[t_, tau_] := I0[tau] Exp[-4 Log[2] / tau^2 t^2]; (*Driving field intensity*)
```

```
b[tau_] := Piecewise[{{N[-4 Log[2] / (tau fs)^2 Sqrt[tau^2 / tauFL^2 - 1]], tau < 0},
    {N[4 Log[2] / (tau fs)^2 Sqrt[tau^2 / tauFL^2 - 1]], tau > 0}}]; (*Chirp*)
```

```
omega[t_, tau_] := omega1 + b[tau] t fs; (*t, tau in fs, omega chirped pulse*)
```

```
n[q_] = Piecewise[{{6, q == 13}, {6, q == 15}, {6, q == 17},
        τμηματική συνάρτηση
    {6, q == 19}, {7, q == 21}, {10, q == 23}, {10, q == 25}, {13, q == 27}}];
```

```
Cs = 1;
Cl = 1;
```

```
Phi0s = 0;
Phi0l = 0;
```

```
plasmaLuminesanceData =
  {{150, 1.51652 × 10^8}, {100, 1.55677 × 10^8}, {90 , 1.5624 × 10^8}, {80, 1.58293 × 10^8},
   {65, 1.60398 × 10^8}, {55, 1.62324 × 10^8}, {45, 1.71434 × 10^8}, {40, 1.75582 × 10^8},
   {33, 1.90378 × 10^8}, {28, 2.6165 × 10^8}, {26, 4.60131 × 10^8}, {-28, 6.78022 × 10^8},
   {-30, 6.85161 × 10^8}, {-43, 8.35979 × 10^8}, {-50, 8.4103 × 10^8}, {-85, 5.71103 × 10^8},
   {-100, 2.85818 × 10^8}, {-140, 2.2162 × 10^8}, {-150, 2.01814 × 10^8}};
(*Plasma luminesance (data from plasma images)*)
```

```
interpolatedPlasmaLuminesance =
  Interpolation[plasmaLuminesanceData, Method → "Spline" , InterpolationOrder → 1];
  παρεμβολή                          μέθοδος              βαθμός παρεμβολής
```

```
ListLinePlot[Labeled[#, #] & /@ plasmaLuminesanceData]
γραμμικό διάγρ··· με ετικέτα
```

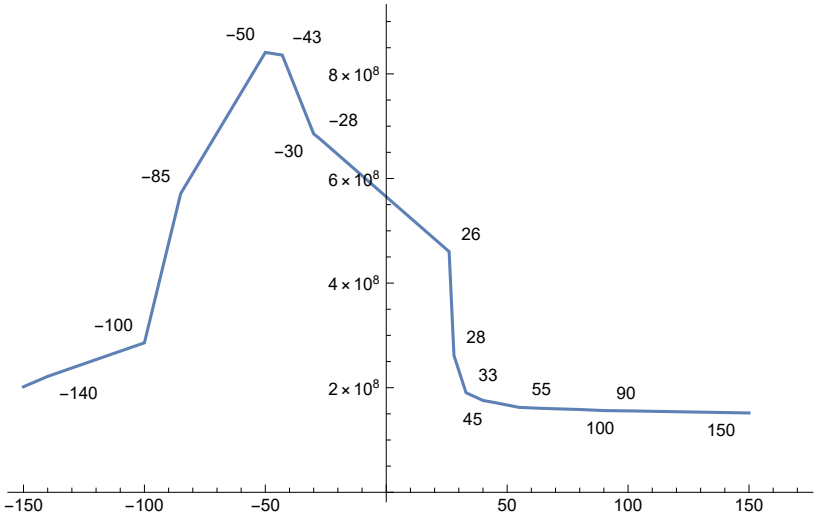


```
plasmaLuminesance[tau_] = interpolatedPlasmaLuminesance[tau];
```

```
plasmaAbsorption = NonlinearModelFit[
                   μη γραμμικό μοντέλο προσαρμογής
    {{1.62324 × 10^8, 1}, {4.60131 × 10^8, 8 / 12}, {8.35979 × 10^8, 0.4}}, a + c √x , {a, c}, x];
```

```
plasmaAbsorption["ParameterTable"]
```

	Estimate	Standard Error	t-Statistic	P-Value
a	1.46996	0.016017	91.775	0.00693647
c	−0.000037132	7.26436×10^{-7}	−51.1153	0.012453

```
FindFormula[{{1, 57.95}, {2048, 35.14}}, x]
```
εύρεση φόρμουλας

```
57.9611 - 0.0111431 x
```

```
plasmaAbsorption[interpolatedPlasmaLuminesance[-43]]
```

```
0.245983
```

```
ionizPropAr[t_, tau_] = Piecewise[{{0., -3 Abs[tau] > t},
                                   τμηματική συνάρτηση   απόλυτη τιμή
    {Quiet[1 - e^-NIntegrate[wADKAr[QuantityMagnitude[Idrive[x,tau]]],{x,-3 Abs[tau],t},AccuracyGoal→50]],
     ήσυχη αξιολόγηση έκφρασης
     t ≥ -3 Abs[tau]}}];
           απόλυτη τιμή
```

```
Plot[ionizPropAr[t, -43], {t, -100, 100}, PlotPoints → 20,
διάγραμμα                                  αριθμός σημείων διαγράμματος
 PlotRange → All, Frame → True, FrameLabel → {"fs", "Ionization Propability"}]
 εύρος διαγρ··· όλα  κορνίζα  αληθής ετικέτα κορνίζας
```

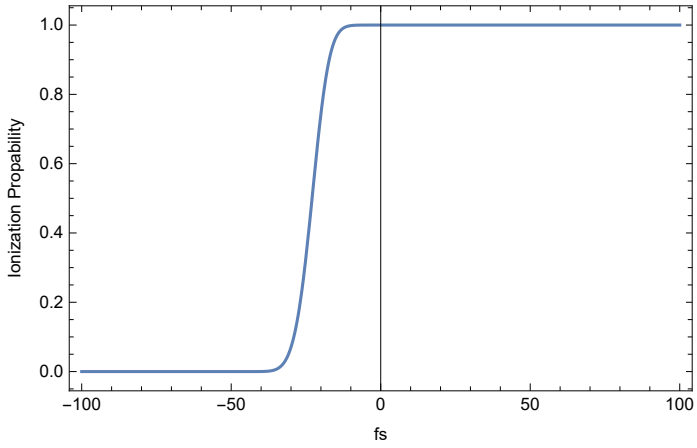


```
ClearAll[Envelope];
```
διαγραφή ιδιοτήτων συμβόλων

```
Envelope[t_, tau_] :=
  N[Re[ (1 - ionizPropAr[t, tau]) Quantity[QuantityMagnitude[UnitConvert[
  ···πραγματικό μέρος                 ποσότητα

                √(2 Idrive[t, tau] / (e0 Quantity["SpeedOfLight"])), "Volts"/"Meters"]]^8, "Volts"/"Meters" ]];
```

```
ClearAll[InterpolatedEnvelope];
InterpolatedEnvelope =
  Interpolation[Flatten[ParallelTable[{{t, tau}, QuantityMagnitude[Envelope[t, tau]]},
    {t, Flatten[{Table[k, {k, -375, -70, 10}], Table[k, {k, -60, 60, 1}],
       Table[k, {k, 70, 375, 10}]}], {tau, {26, -30, -43, -85, 33, 40, -40}}],
   1], Method → "Spline", InterpolationOrder → 2];
```

```
Plot[Table[InterpolatedEnvelope[t, tau], {tau, {26, -30, -43, -85, 33, 40}}],
 {t, -70, 20}, PlotRange → All,
 AxesLabel → {HoldForm[fs], RawBoxes[RowBox[{"Effective", " ", "Laser", " ", "Intensity",
      " ", RowBox[{"(", RowBox[{"a", ".", "u", "."}], ")"}]}]]}, PlotLabel → None]
```

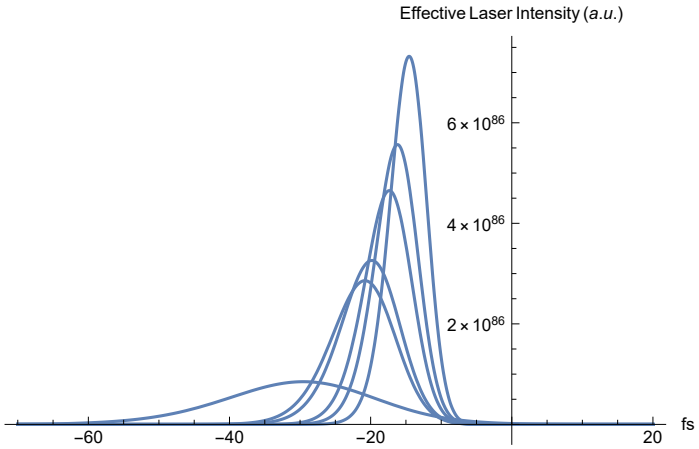


```
(*Self-face modulation  calculations *)
```

```
n0Ar = 1.00027977;
n2Ar = Quantity[3 × 10^-19 × 60/760, ("Centimeters")^2 / "Watts"]; (* 1.2/12 10^-19 *)

k0 = 2 π / Quantity[LaserWavlength, "Nanometers"];
z[tau_] = Quantity[1, "Millimeters"] ×
   Piecewise[{{3.6, tau == 26}, {4.1, tau == -28}, {4, tau == -30}, {4.1, tau == -43},
     {4, tau == -40}, {4.2, tau == -50}, {3.7, tau == -85}, {2.9, tau == -100},
     {2.6, tau == -140}, {2.6, tau == -150}, {2.8, tau == 28}, {2.5, tau == 33},
     {2.3, tau == 40}, {2.1, tau == 45}, {2.3, tau == 55}, {0, tau == 65},
     {0, tau == 80}, {0, tau == 90}, {0, tau == 100}, {0, tau == 150}}];
```

```
LNL[tau_] := n0Ar / (n2Ar k0 I0[tau]);
```

```
Rayleigh = 5;
```

```
spmGas[t_, tau_] :=
 -N[((omega1 (*z[tau]*)) (Quantity[Rayleigh, "Millimeters"] - z[tau]/2)) / Quantity[
        "SpeedOfLight"]] n2Ar ND[Idrive[x, tau], x, t]/fs]; (*Neutral gas induced SPM*)
```

```
no = 1;
Pc = Quantity[1.7 × 10^21, "Centimeters"^-3];
Po = Quantity[N[0.25 × 2 × 10^19 × 60/760], "Centimeters"^-3];
(*for ionization propability =  1 times 1,33 for mbar*)
```

```
ionizPropabilityInterpolated =
  Interpolation[Flatten[ParallelTable[{{t, tau}, ionizPropAr[t, tau]},
     {t, -200, 200, 2}, {tau, {26, -30, -43, -85, 33, 40, -40}}], 1],
   Method → "Spline", InterpolationOrder → 3];
```

```
spmPlasma[t_, tau_] :=
 N[(omega1 z[tau]/2)/Quantity["SpeedOfLight"] * 1/(2 × 1 Pc) ND[ionizPropabilityInterpolated[x, tau], x, t]/fs Po];

(*Plasma induced SPM*)
```

```
PlasmaFactorFromLuminesance[tau_] :=
 (1/((*25*) 100) Piecewise[{{15, tau == -85}, {25, tau == -43}, {22, tau == -40},
    {19, tau == -30}, {11, tau == 26}, {3, tau == 33}, {2.7, tau == 40}}]);
(*from plasma images*)
```

```
spm[t_, tau_] := PlasmaFactorFromLuminesance[tau] × spmPlasma[t, tau] + spmGas[t, tau];
```

```
Clear[InterpolatedSPMmagnitude];
```
διαγραφή ορισμών και τιμών συμβόλων
```
InterpolatedSPMmagnitude =
  Interpolation[Flatten[ParallelTable[{{t, tau}, QuantityMagnitude[spm[t, tau]]},
```
παρεμβολή ισοπέδ··· παράλληλος πίνακας μέγεθος ποσότητας
```
    {t, -200, 200, 2}, {tau, {26, -30, -43, -85, 33, 40, -40}}], 1],
   Method → "Spline" , InterpolationOrder → 2];
```
μέθοδος βαθμός παρεμβολής
```
Show[Plot[{InterpolatedSPMmagnitude[t, 26], InterpolatedSPMmagnitude[t, -30],
```
πρ··· διάγραμμα
```
   InterpolatedSPMmagnitude[t, -43], InterpolatedSPMmagnitude[t, -85],
   InterpolatedSPMmagnitude[t, 33], InterpolatedSPMmagnitude[t, 40]
   (*,-spmGas[t,26]*)}, {t, -150, 150}, PlotRange → All,
```
εύρος διαγρ··· όλα
```
  PlotLegends → {"26", "-30", "-43", "-85", "33", "40"(*,"spmGas[t,26]"*)},
```
υπομνήματα διαγράμματος
```
  PlotStyle → {Thick}, PlotLabel → {"Po ", Po / (2 × 10^19 × 60 / 760), "Rayleigh ", Rayleigh}]]
```
στυλ διαγράμμ··· παχύ ετικέτα διαγράμματος

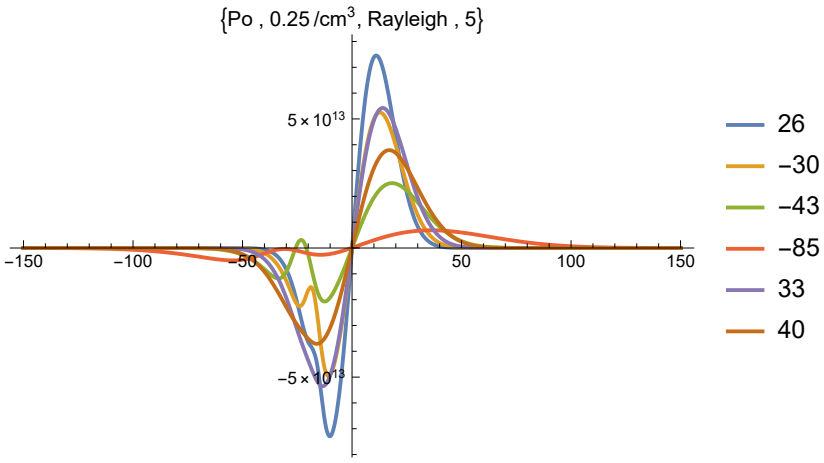


```
al[q_] =
  Piecewise[{{1, q == 7}, {1, q == 9}, {1, q == 11}, {1, q == 13}, {1, q == 15}, {1, q == 17},
```
τμηματική συνάρτηση
```
    {1, q == 19}, {1, q == 21}, {1, q == 23}}] × Quantity[10^-14, "Centimeters"^2 / "Watts"];
```
ποσότητα

```
as[q_] = Piecewise[{{1, q == 7}, {1, q == 9}, {1, q == 11}, {1, q == 13}, {1, q == 15},
```
τμηματική συνάρτηση
```
    {1, q == 17}, {1, q == 19}, {1, q == 21}, {1, q == 23}(*,{2,q==25},{2,q==27}*)}] ×
   Quantity[10^-14, "Centimeters"^2 / "Watts"];
```
ποσότητα

```
Phi0Long[q_] = Piecewise[{{2 * 2, q == 13}, {2 * 2, q == 15}, {2 * 2, q == 17},
```
τμηματική συνάρτηση
```
    {2 * 2.4, q == 19}, {2 * 4, q == 21}, {2 * 4, q == 23}, {2 * 4, q == 25}, {2 * 4, q == 27}}] ;
```

```
omegaLaser[t_, tau_] := QuantityMagnitude[
                        μέγεθος ποσότητας
   UnitConvert[((omega1 + Quantity[InterpolatedSPMmagnitude[t, tau], 1 / "Seconds"])
   μετατροπή μονάδων μέτρησης  ποσότητα
        t fs +  b[tau] (t fs)^2) / (t fs), "Hertz"]];
```

```
(*Short trajectory E-field*)
 σύντομη μορφή έκφρ···  σταθερά e
```

```
Clear[Es];
διαγραφή ορισμών και τιμών συμβόλων
Es[t_, tau_, q_, alphaPreFactor_, phiSort_] =
  N[Cs InterpolatedEnvelope[t, tau] Re[ Exp[i (q (omega1 + Quantity[
  αριθμητική τιμή                    π···  εκθετική συνάρτηση     ποσότητα
                InterpolatedSPMmagnitude[t, tau], 1 / "Seconds"]) t fs + q b[tau] / 2 (t fs)^2 +
          alphaPreFactor as[q] × Idrive[t, tau] + phiSort(*+  Phi0s*))]]];
```

```
(*Long trajectory E-field*)
                  σταθερά e
```

```
Clear[El];
διαγραφή ορισμών και τιμών συμβόλων
El[t_, tau_, q_, alphaPreFactor_, cLong_, alphaPreFactorLong_, phiLong_] =
  N[cLong InterpolatedEnvelope[t, tau]
  αριθμητική τιμή
    Re[ Exp[i (q (omega1 + Quantity[InterpolatedSPMmagnitude[t, tau], 1 / "Seconds"])
    π···  εκθετική συνάρτηση     ποσότητα
          t fs + q b[tau] / 2 (t fs)^2 +  (*το 0.5 για να έχουν
          τα alpha συγκρίσιμες τιμές με τα προιγούμενα run*)
         alphaPreFactorLong al[q] × Idrive[t, tau] + phiLong(*-π/4 +3-π/2*))]]];
```

```
(*Grating correction*)
```

```
nmSpectrumTommChip = {{34.6, 0.016}, {35, 0.561}, {36, 1.914}, {37, 3.25}, {38, 4.57},
    {39, 5.878}, {40, 7.17}, {41, 8.448}, {42, 9.712}, {43, 10.964}, {44, 12.203},
    {45, 13.431}, {46, 14.646}, {47, 15.85}, {48, 17.042}, {49, 18.225}, {50, 19.396},
    {51, 20.558}, {52, 21.709}, {53, 22.851}, {54, 23.984}, {55, 25.107},
    {56, 26.222}, {57, 27.328}, {57.3, 27.658}};(*ήταν αυτό στο αρχικό file*)
```

```
interpolatednmSpectrumTommChip =
  Interpolation[nmSpectrumTommChip, Method → "Spline" , InterpolationOrder → 1];
  παρεμβολή                       μέθοδος                βαθμός παρεμβολής
```

```
AbsoluteTiming[
απόλυτος χρόνος αξιολόγησης
 Block[
 τοπικοποίηση συμβόλων
```

```
{
 from,
 to ,
 segments ,
 calculationArea,
 calculationAreaLength,
 xAxis
},
{

 Table[{
   from := -1.5 Abs[tau];,
   to := 1.5 Abs[tau];,
   segments := Round[2^13/100 (to - from), 2];,

   calculationArea := to - from;,
   calculationAreaLength := Length[
      Abs[Fourier[ParallelTable[Total[Table[Es[t, 26, 15, 0, 0], {q, {(*7,*)9, 11, 13,
            15, 17, 19, 21, 23, 25}}]], {t, from, to, calculationArea / segments}]]];,
   xAxis := Table[interpolatednmSpectrumTommChip[299.79 / frequenscy], {frequenscy, 0,
       (segments / calculationArea) - (segments / calculationArea) / calculationAreaLength,
       (segments / calculationArea) / calculationAreaLength}];,

   all =
     ListLinePlot[Transpose[{xAxis,  Abs[Fourier[ParallelTable[Total[Table[El[t, tau, q,
                 alphaPreFactor, cLong, alphaPreFactorLong, phiLong] + Es[t, tau,
                 q, alphaPreFactor, phiSort], {q, {(*7,*)9, 11, 13, 15, 17, 19,
                 21, 23, 25}}]], {t, from, to, calculationArea / segments}]]]^2}],
     PlotRange → {{interpolatednmSpectrumTommChip[34.7],
         interpolatednmSpectrumTommChip[57.03]}, {0, All}},
     PlotLabel → {"El+Es[t", tau, " as= ", alphaPreFactor, " al= ", alphaPreFactorLong,
       "] ", N[I0FL] , plasmaAbsorption[interpolatedPlasmaLuminesance[tau]] × N[I0FL] ,
       "Cl=", cLong,  " phiLong ", phiLong , "phiSort ", phiSort,
       "Po ", Po / (2 × 10^19 × 60 / 760), "Rayleigh ", Rayleigh},
     AxesLabel → {"mm on chip", "a.u."}, ImageSize → {800, 500},
     Epilog → {(*add vertical lines*)
       InfiniteLine[{interpolatednmSpectrumTommChip[LaserWavlength / 11], 0}, {0, 1}],
```

```
    InfiniteLine[{interpolatednmSpectrumTommChip[LaserWavlength / 13], 0}, {0, 1}],
    InfiniteLine[{interpolatednmSpectrumTommChip[LaserWavlength / 15], 0}, {0, 1}],
    InfiniteLine[{interpolatednmSpectrumTommChip[LaserWavlength / 17], 0}, {0, 1}],
    InfiniteLine[{interpolatednmSpectrumTommChip[LaserWavlength / 19], 0}, {0, 1}],
    InfiniteLine[{interpolatednmSpectrumTommChip[LaserWavlength / 21], 0}, {0, 1}],
    InfiniteLine[{interpolatednmSpectrumTommChip[LaserWavlength / 23], 0}, {0, 1}],
    InfiniteLine[{interpolatednmSpectrumTommChip[LaserWavlength / 25], 0}, {0, 1}],
    InfiniteLine[
     {interpolatednmSpectrumTommChip[LaserWavlength / 27], 0}, {0, 1}]};
sort = ListLinePlot[Transpose[{xAxis, Abs[Fourier[ParallelTable[Total[
          Table[Es[t, tau, q, alphaPreFactor, phiSort], {q, {(*7,*)9, 11, 13, 15,
             17, 19, 21, 23, 25}}]], {t, from, to, calculationArea / segments}]]]^2}],
  PlotRange → {{interpolatednmSpectrumTommChip[34.7],
     interpolatednmSpectrumTommChip[57.03]}, {0, All}},
  PlotLabel → {"Total q Es[t", tau, alphaPreFactor, "] ", N[I0FL] ,
    plasmaAbsorption[interpolatedPlasmaLuminesance[tau]] × N[I0FL] , "Cl=", cLong},
  AxesLabel → {"mm on chip", "a.u."}, ImageSize → {800, 500},
  PlotStyle → Red, Epilog → {(*add vertical lines*)
    InfiniteLine[{interpolatednmSpectrumTommChip[LaserWavlength / 11], 0}, {0, 1}],
    InfiniteLine[{interpolatednmSpectrumTommChip[LaserWavlength / 13], 0}, {0, 1}],
    InfiniteLine[{interpolatednmSpectrumTommChip[LaserWavlength / 15], 0}, {0, 1}],
    InfiniteLine[{interpolatednmSpectrumTommChip[LaserWavlength / 17], 0}, {0, 1}],
    InfiniteLine[{interpolatednmSpectrumTommChip[LaserWavlength / 19], 0}, {0, 1}],
    InfiniteLine[{interpolatednmSpectrumTommChip[LaserWavlength / 21], 0}, {0, 1}],
    InfiniteLine[{interpolatednmSpectrumTommChip[LaserWavlength / 23], 0}, {0, 1}],
    InfiniteLine[{interpolatednmSpectrumTommChip[LaserWavlength / 25], 0}, {0, 1}],
    InfiniteLine[{interpolatednmSpectrumTommChip[LaserWavlength / 27], 0},
```

```
                                                                    άπειρη γραμμή
    {0, 1}]}];, long = ListLinePlot[Transpose[
                                    γραμμικό διάγρ··· αναστροφή
   {xAxis, Abs[Fourier[ParallelTable[Total[Table[El[t, tau, q, alphaPreFactor,
           cLong, alphaPreFactorLong, phiLong], {q, {(*7,*)9, 11, 13, 15, 17,
            19, 21, 23, 25}}]], {t, from, to, calculationArea / segments}]]]^2}],
  PlotRange → {{interpolatednmSpectrumTommChip[34.7],
                εύρος διαγράμματος
     interpolatednmSpectrumTommChip[57.03]}, {0, All}},
                                              όλα
  PlotLabel → {"Total q El[t", tau, alphaPreFactor, " ", alphaPreFactorLong,
                ετικέτα διαγράμ··· άθροισμα στοιχείων
    "] ", N[I0FL] , plasmaAbsorption[interpolatedPlasmaLuminesance[tau]] × N[I0FL] ,
          αριθμητική τιμή                                                αριθμητική τιμή
    "Cl=", cLong,  " phiLong ", phiLong (*," ALL alpha factor ",
    alphaPreFactor alphaPreFactorLong  al[19]Idrive[-tau/2,tau] +  Phi0l,"al",
    al[19]/Quantity[10^-14, "Centimeters" /"Watts"],"al[19]Idrive[-tau/2,tau]",
                 ποσότητα
    N[al[19]Idrive[-tau/2,tau]] ,*)}, AxesLabel → {"mm on chip", "a.u."},
    αριθμητική τιμή                              ετικέτες αξόνων
  ImageSize → {800, 500}, PlotStyle → Green, Epilog → {(*add vertical lines*)
  μέγεθος εικόνας          στυλ διαγρά··· πράσινο επίλογα γραφικά
    InfiniteLine[{interpolatednmSpectrumTommChip[LaserWavlength / 11], 0}, {0, 1}],
    άπειρη γραμμή
    InfiniteLine[{interpolatednmSpectrumTommChip[LaserWavlength / 13], 0}, {0, 1}],
    άπειρη γραμμή
    InfiniteLine[{interpolatednmSpectrumTommChip[LaserWavlength / 15], 0}, {0, 1}],
    άπειρη γραμμή
    InfiniteLine[{interpolatednmSpectrumTommChip[LaserWavlength / 17], 0}, {0, 1}],
    άπειρη γραμμή
    InfiniteLine[{interpolatednmSpectrumTommChip[LaserWavlength / 19], 0}, {0, 1}],
    άπειρη γραμμή
    InfiniteLine[{interpolatednmSpectrumTommChip[LaserWavlength / 21], 0}, {0, 1}],
    άπειρη γραμμή
    InfiniteLine[{interpolatednmSpectrumTommChip[LaserWavlength / 23], 0}, {0, 1}],
    άπειρη γραμμή
    InfiniteLine[{interpolatednmSpectrumTommChip[LaserWavlength / 25], 0}, {0, 1}],
    άπειρη γραμμή
    InfiniteLine[{interpolatednmSpectrumTommChip[LaserWavlength / 27], 0},
    άπειρη γραμμή
     {0, 1}]}];, Show[all, sort, long], Now}
                 προβολή γραφικών      τώρα
 , {tau, {-40, 40(*26,-28,-30,-43,-50,-85,-100,-140,-150,28,33,40,45,55,65,80,
   90,100,150*)}}, {alphaPreFactor, {0.5}}, {cLong, {0.6}}, {alphaPreFactorLong, {13}},
  {phiLong, {0}}, {phiSort, {0}}] (*,calculationArea,calculationAreaLength,
 N[calculationAreaLength/calculationArea]*), EmitSound[Sound[SoundNote[]]]}
 αριθμητική τιμή                              αναπαραγ··· ήχος μουσική νότα
]

]
```

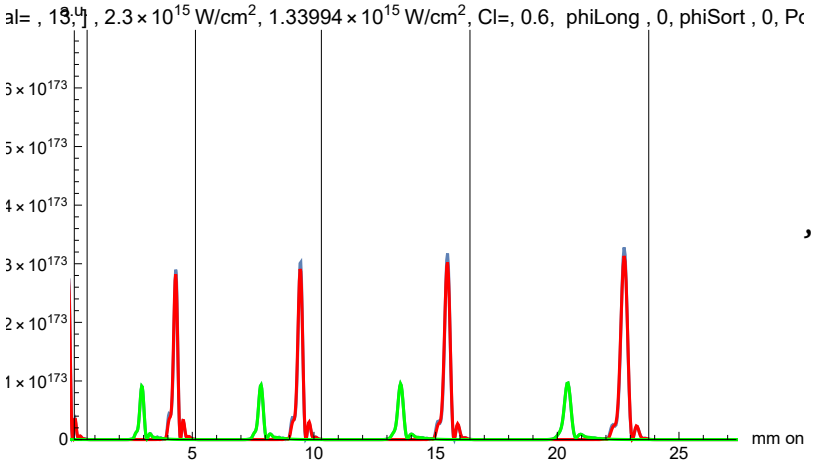
a.u.
al= , 13,] , 2.3 × 10^15 W/cm^2, 1.33994 × 10^15 W/cm^2, Cl=, 0.6, phiLong , 0, phiSort , 0, Pc
3 × 10^173
2 × 10^173
1 × 10^173
0
5
10
15
20
25
mm on

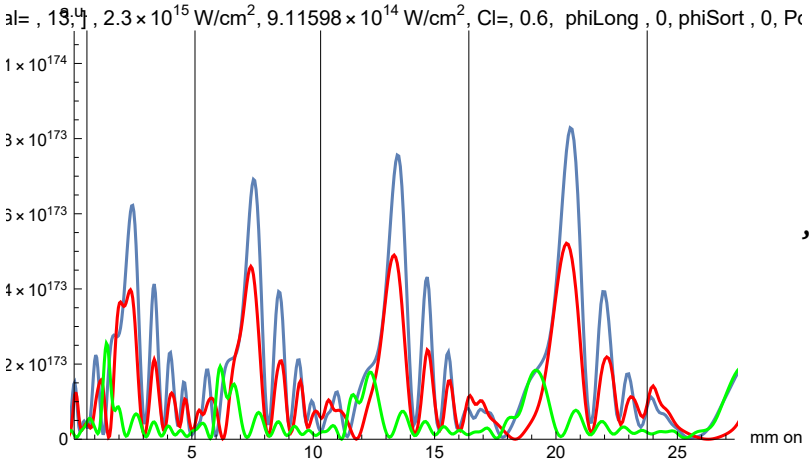
a.u.
al= , 13,] , 2.3 × 10^15 W/cm^2, 9.11598 × 10^14 W/cm^2, Cl=, 0.6, phiLong , 0, phiSort , 0, Pc
1 × 10^174
3 × 10^173
2 × 10^173
0
5
10
15
20
25
mm on

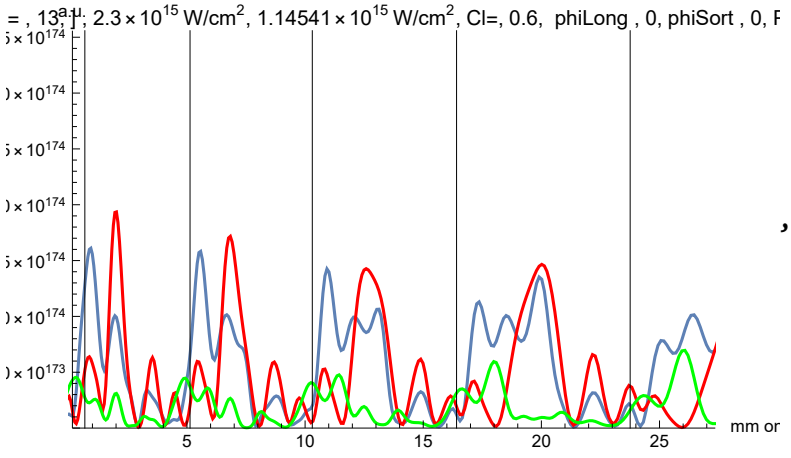
a.u.
= , 13,]; 2.3 × 10^15 W/cm^2, 1.14541 × 10^15 W/cm^2, Cl=, 0.6, phiLong , 0, phiSort , 0, F
5 × 10^174
) × 10^174
5 × 10^174
) × 10^174
5 × 10^174
) × 10^174
) × 10^173
5
10
15
20
25
mm or

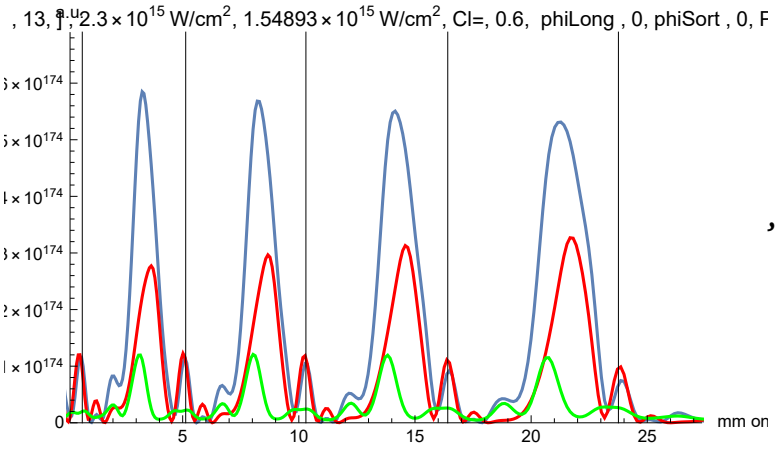
, 13,], 2.3 × 10^15 W/cm^2, 1.54893 × 10^15 W/cm^2, Cl=, 0.6, phiLong , 0, phiSort , 0, F
a.u.
5 × 10^174
4 × 10^174
3 × 10^174
2 × 10^174
1 × 10^174
0
5
10
15
20
25
mm on

,

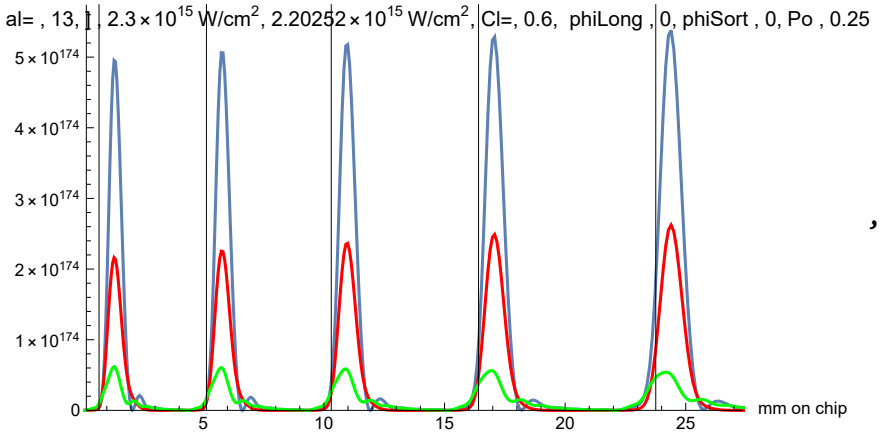
al= , 13,], 2.3 × 10^15 W/cm^2, 2.20252 × 10^15 W/cm^2, Cl=, 0.6, phiLong , 0, phiSort , 0, Po , 0.25
5 × 10^174
4 × 10^174
3 × 10^174
2 × 10^174
1 × 10^174
0
5
10
15
20
25
mm on chip

,

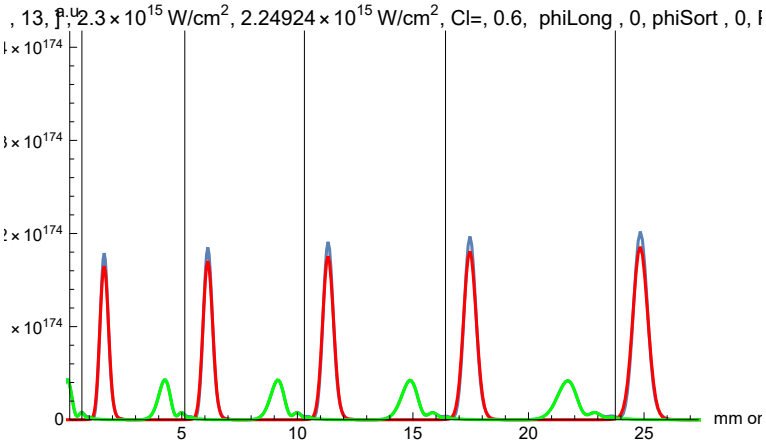
, 13,], 2.3 × 10^15 W/cm^2, 2.24924 × 10^15 W/cm^2, Cl=, 0.6, phiLong , 0, phiSort , 0, I
a.u.
× 10^174
3 × 10^174
2 × 10^174
× 10^174
0
5
10
15
20
25
mm or

Appendix F

XUV CDI Control Interface

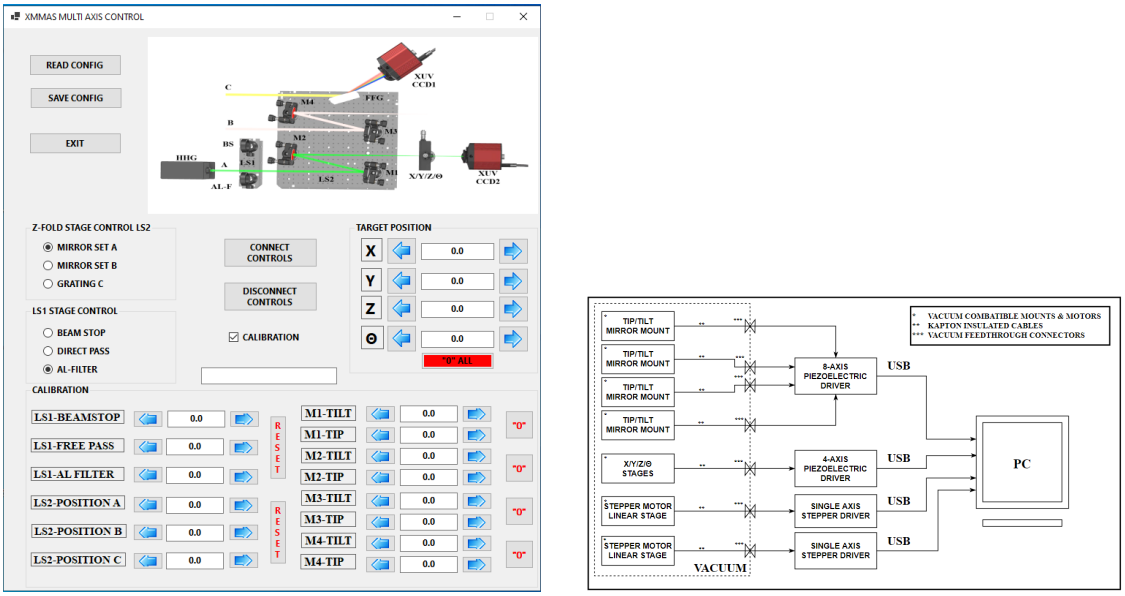

(a) **(b)**

Figure F.1
(a) The software interface for controlling all the optomechanical components installed inside the vacuum stages C and D of the setup. (b) Schematic of the multi-axis control electronic block diagram.

Appendix G

XUV CDI Reconstruction Code

Matlab code for reconstruction. It is a modified version of [168] extended to include the RAAR algorithm.

```
1
2         %ER, HIO and RAAR algorithms, with
3         %support shrinkwrap
4         % "X-ray image reconstruction from a diffraction
5         %pattern alone"
6         % Phys. Rev. B 68(14), pages 140101 (2003)
7         % The error function: J. Miao "Phase retrieval
8         % from the magnitude of the Fourier transforms
9         %of nonperiodic objects", J. Opt. Soc. Am.
10        % A 15(6), 1662 - 1669 (1998)
11        %D. R. Luke, Relaxed averaged alternating
12        %reffections for diffraction imaging, Inverse
13        %Problems, vol. 21, no. 1, pp. 37 50, 2005.
14        % This code is a modified and extented version
15        %of: Tatiana Latychevskaia, "Iterative phase
16        %retrieval in coherent diffractive imaging:
17        %practical issues", Applied Optics 57(25),
18        T7187 - 7197 (2018)
19        close all
20        clear all
21
22        % Pixel values has to be between 0,00001
23        %and 1000000
24        % parameters
25        algorithm = 1;          %  0  for ER,
```

```
%1 for RAAR, everthing else for HIO
beta = 0.8;
Iterations = 2000;        %
Reconstructions = 1;
p = 0.01;
Nm = 20;              % Every Nm changes sigma
a = 1;                % gausse
sigma_start = 8.00;
sigma_end =2.50;
if (Iterations <= Nm)
delta_sigma = 0;
else
delta_sigma = (sigma_start - sigma_end)/...
(Iterations/Nm - 1);
end

treshold = 0.09;          %  support treshold

% reading diffraction pattern

[file, fpath] = uigetfile('*.tif');
image  = imread(file);
image0=rescale(image,0,100);
tic
diffractionPattern = double(rot90(rot90...
(rot90(image0(:,:,1)))));

N = size(diffractionPattern,1) ;
amplitude_experimental = ...
sqrt(diffractionPattern);

% creating initial object support
support = double(zeros(N,N));
support0= abs(fftshift(fft2(amplitude_...
experimental)));
support0=rescale(support0);
support(support0> treshold)=1;


```

```
65          % reconstruction
66          for rr = 1:Reconstructions
67
68          % creating initial complex-valued field
69          %distribution at detector plane
70          phase =  (2*rand(N,N) - 1)*pi;
71          field_detector_0 = amplitude_experimental...
72           .* exp(1i*phase);
73          % getting initial object distribution
74          object_0 = fftshift(ifft2(ifftshift(field_...
75          detector_0)));
76          realObject_0 = real(object_0);
77
78          % iterative loop
79          tic
80
81          % iterative loop
82          qq = 0;
83          field_detector_updated = complex(zeros(N, N));
84          error = 0;
85          gk1 = zeros(N, N);
86
87          for ii = 1:Iterations
88          %parfor (ii = 1:Iterations)
89          fprintf('Reconstruction: %d\n', rr)
90          fprintf('Iteration: %d\n', ii)
91
92          field_detector_updated = fftshift(fft2(...
93          ifftshift(realObject_0)));
94
95          % replacing updated amplitude for measured
96          % amplitude
97          field_detector_updated = amplitude_experimental...
98           .* exp(1i*angle(field_detector_updated));
99
100         % getting updated object distribution
101
102         updatedObjectDistribution = real(fftshift(...
103         ifft2(ifftshift(field_detector_updated))));
```

```
104
105
106         %error Miao
107
108         positives =support > 0;
109         negatives=support <= 0;
110         error = sqrt(( sum(sum(negatives.*...
111         updatedObjectDistribution.^2),2)   )/...
112         (   sum(sum(positives.*updatedObject...
113         Distribution.^2),2)));
114
115
116         % updating support
117         q = ii - Nm*floor(ii/Nm);
118         if (q == 0)
119         sigma = sigma_start - qq*delta_sigma;
120         Gau = zeros(N, N);
121
122         [Gx, Gy]=ndgrid(((1:N)-N/2 -1).^2, ...
123         ((1:N)-N/2 -1).^2);
124         rG= Gx+Gy;
125         Gau = a.*exp(-(rG)/(2.*sigma.^2));
126
127         support1 = abs(fftshift(ifft2(ifftshift...
128         (fftshift(fft2(ifftshift(Gau))) .*  ...
129         fftshift(fft2(ifftshift(realObject_0)))))));
130         support1=rescale(support1);
131         support= zeros(N, N);
132         support(support1>treshold)=1;
133         qq = qq + 1;
134         end
135         % constraints in the object plane
136         logicalupdatedObjectDistribution= ...
137         updatedObjectDistribution > 0;
138         logicalsupport= support > 0;
139         logicalBetter=logicalupdatedObjectDistribution...
140          .* logicalsupport;
141         LogicalWorse=zeros(N, N);
142         LogicalWorse(logicalBetter~=1)=1;
```

```
143
144
145         switch algorithm
146         case 0
147         gk1= (logicalBetter.*updatedObjectDistribution)...
148         %+(LogicalWorse.*0);%ER
149         case 1
150         gk1= (logicalBetter.*updatedObjectDistribution)...
151         +(LogicalWorse.*(beta*realObject_0 - (1-2*beta)...
152         *updatedObjectDistribution));%RAAR
153         otherwise
154         gk1= (logicalBetter.*updatedObjectDistribution)...
155         +(LogicalWorse.*(realObject_0 - beta*...
156         updatedObjectDistribution));%HIO
157         end
158
159
160         realObject_0 = gk1;
161         end % iterations
162
163
164
165         toc
166         [pathstr,name,ext] = fileparts(file);
167         imshow(flipud(rot90(imresize(realObject_0,0.5)))...
168         , []);
169         title(strcat('reconstruction from  ', name,...
170          ' beta ',num2str(beta), ' iter ',...
171          num2str(Iterations), ' Nm ',num2str(Nm),...
172           ' sigma start ',num2str(sigma_start),'...
173            sigma end ',num2str(sigma_end), ' t1 ...
174             ',num2str(t1),' treshold  ',num2str...
175              (treshold)))
176         xlabel({'x / px'})
177         ylabel({'y / px'})
178         axis on
179         set(gca,'YDir','normal')
180         colormap('gray')
181         colorbar;
```

```
182
183         phase = angle(field_detector_updated);
184         field_detector = sqrt(diffractionPattern)...
185         .*exp(1i*phase);
186         object=   real(fftshift(ifft2(ifftshift...
187         (field_detector))));
188
189         error = error*10^8 + 10^10;
190         % saving reconstruction as JPG and txt file
191
192         object = rot90(object);
193
194         filename1 = char(strcat('D:\PHD\CDI\...
195         object_rec_', int2str(error),name, '.jpg'));
196         imwrite(object, filename1);
197         filename2 = char(strcat('D:\PHD\CDI\...
198         obj_rec_', int2str(error),name, int2str(...
199         Iterations),'.txt'));
200         dlmwrite(filename2 ,object);
201         filename3 = char(strcat('D:\PHD\CDI\...
202         gk1object_rec', int2str(error),name, '.jpg'));
203         imwrite(flipud(rot90(imresize(...
204         realObject_0,0.5))), filename3);
205         filename4 = char(strcat('D:\PHD\CDI...
206         \gk1obj_rec', int2str(error),name, ...
207         int2str(Iterations),'.txt'));
208         dlmwrite(filename4 ,flipud(rot90...
209         (imresize(realObject_0,0.5))));
210
211
212         end
213         toc
```

Εκτεταμένη Σύνοψη της Διατριβής

Το αντικείμενο της παρούσας έρευνας είναι η δυναμική της παραγωγής των αρμονικών υψηλής τάξης (high harmonic generation - HHG) κατά την αλληλεπίδραση ισχυρών παλμών λέιζερ με αέριους στόχους, ο έλεγχος των χαρακτηριστικών των αρμονικών, και η χρήση τους σε εφαρμογές περιθλαστικής μικροσκοπίας. Η έρευνα της διδακτορικής διατριβής πραγματοποιήθηκε στις εργαστηριακές εγκαταστάσεις του Ινστιτούτου Φυσικής Πλάσματος και Λέιζερ (IPPL) του Ελληνικού Μεσογειακού Πανεπιστημίου (ΕΛ.ΜΕ.ΠΑ.) χρησιμοποιώντας το σύστημα λέιζερ γνωστό ως "ZEUS", ισχύος 45 TW, συχνότητας επανάληψης 10 Hz και ελάχιστης διάρκειας παλμού 26 fs.

Παραγωγή Υψηλής Τάξης Αρμονικών (HHG)

Υπό κατάλληλες συνθήκες εστίασης της δέσμης οι εντάσεις που μπορούν να επιτευχθούν είναι της τάξης του $1\times10^{15}\,\mathrm{W/cm^2}$ οπότε το ηλεκτρικό πεδίο του παλμού λέιζερ γίνεται συγκρίσιμο με αυτό του ατόμου. Εάν η εστίαση γίνει σε ένα κατάλληλο μέσο, μπορούν να συμβούν φαινόμενα όπως ιονισμός, επιτάχυνση ηλεκτρονίων, επανασυνδέσεις ηλεκτρονίων στα τα γονικά τους ιόντα, και αυτόδιαμόρφωση φάσης. Μέσω αυτών των φαινομένων εντέλει παράγεται ακτινοβολία στην περιοχή του ακραίου υπεριώδους (XUV) με χαρακτηριστικά χρήσιμα για εφαρμογές όπως της παρούσας έρευνας. Τα χαρακτηριστικά αυτά περιλαμβάνουν κυρίως την συμφωνία και το φάσμα της παραγόμενης ακτινοβολίας. Η διαδικασία παραγωγής αρμονικών περιγράφεται από το μοντέλο των τριών βημάτων. Στο πρώτο βήμα γίνεται ο ιονισμός του ηλεκτρονίου, στο δεύτερο το ηλεκτρόνιο άγεται από το ηλεκτρικό πεδίο του laser αρχικά μακριά από το ιόν του και επιστρέφοντας τελικά σε αυτό, και στο τρίτο το ηλεκτρόνιο επανασυνδέεται με το ιόν του εκπέμποντας ακτινοβολία στο XUV. Η διαδικασία αυτή συμβαίνει δύο φορές ανά περίοδο του πεδίου του λέιζερ έχοντας ως αποτέλεσμα το φάσμα της παραγόμενης ακτινοβολίας να αποτελείται από περιττά πολλαπλάσια της συχνότητας του λέιζερ. Επιπλέον το φάσμα παρουσιάζει τρεις χαρακτηριστικές

περιοχές: την περιοχή των χαμηλών αρμονικών η οποία χαρακτηρίζεται από την απότομη πτώση της απόδοσης, την περιοχή όπου η απόδοση παραμένει σταθερή (plateau) και τέλος, την περιοχή όπου η απόδοση πέφτει απότομα έως ότου μηδενιστεί (cutoff).

Υπάρχει ένας άπειρος αριθμός κβαντικών τροχιών (κβαντικά μονοπάτια) που μπορεί να ακολουθήσει το ηλεκτρόνιο πριν επανασυνδεθεί με το γονικό ιόν σε κάθε ημιπερίοδο του ηλεκτρικού πεδίου του λέιζερ, ωστόσο, για την ίδια ενέργεια επιστροφής ηλεκτρονίων, υπάρχουν μόνο δύο τέτοιες τροχιές. Για αυτές τις δύο τροχιές, τόσο οι χρονικές στιγμές ιονισμού όσο και επανασύνδεσης είναι διαφορετικές με την μία να διαρκεί λιγότερο από την άλλη, κατά συνέπεια έχουμε τις ***μικρές*** και ***μεγάλες*** τροχιές, αντίστοιχα. Το κύριο διακριτικό αυτών των δύο τροχιών είναι η διαφορά στην γωνιακή απόκλιση καθώς διαδίδονται.

Καθώς η δέσμη λέιζερ διαδίδεται στο μη γραμμικό μέσο και παράγεται η ακτινοβολία XUV από κάθε επανασύνδεση ηλεκτρονίου με το γονικό ιόν, το επόμενο ζητούμενο είναι η σύμφωνη υπέρθεση αυτής της ακτινοβολίας (phase matching). Υπάρχουν διάφοροι παράγοντες που επηρεάζουν το phase matching με βασικούς την γεωμετρία (φάση Gouy), την πυκνότητα πλάσματος, ουδέτερων ατόμων καθώς και του ατομικού δίπολου.

Υπερ-βραχείς παλμοί λέιζερ

Όπως αναφέρθηκε, για την διαδικασία HHG χρησιμοποιήθηκαν υπερβραχείς παλμοί λέιζερ υψηλών εντάσεων. Ένα σημαντικό χαρακτηριστικό αυτών των παλμών για την παρούσα έρευνα είναι η χρονική κατανομή του φασματικού περιεχομένου τους (chirp) μέσω του οποίου έγινε δυνατός ο έλεγχος – χειρισμός της απόδοσης των HHG. Η εξίσωση (1) περιγράφει το ηλεκτρικό πεδίου $E(t)$ ενός γκαουσιανού παλμού

$$E(t) = E_0 e^{-2\ln 2\left(\frac{t}{\tau_e}\right)^2} e^{i(\omega_0 t + bt^2)}, \tag{1}$$

όπου E_0 η τιμή του ηλεκτρικού πεδίου για $t = 0$, τ_e είναι το χρονικό εύρος του στο μισό του μεγίστου (FWHM), ω_0 η γωνιακή συχνότητα, και b είναι η παράμετρος του chirp.

Επιπλέον, η υψηλή ένταση του παλμού λέιζερ προκαλεί μη γραμμικά φαινόμενα όπως το φαινόμενο Kerr όπου ο δείκτης διάθλασης του μέσου αλλάζει ως απόκριση στη στιγμιαία ένταση του πεδίου που διέρχεται από αυτό. Καθώς η ένταση αυξάνεται, ο μη γραμμικός όρος του δείκτης διάθλασης αλλάζει, οδηγώντας σε τροποποίηση της φάσης και, κατά συνέπεια, της συχνότητας του διαδόμενου παλμού (self-phase modulation - SPM). Αυτά τα φαινόμενα, όπως θα δούμε παρακάτω, έχουν επίδραση

στην HHG.

Η Πειραματική Διάταξη

Η πειραματική διάταξη αποτελείται από τέσσερα στάδια που απεικονίζονται με τα γράμματα A, B, C και D όπως παρουσιάζεται στην Εικόνα 1. Το στάδιο A είναι το ημι-άπειρο κελί το οποίο περιέχει τον αέριο στόχο, όπου παράγεται η ακτινοβολία XUV. Το στάδιο B είναι ο θάλαμος διαφορικής άντλησης, που διαχωρίζει το στάδιο A υψηλής πίεσης από τα στάδια C και D χαμηλής πίεσης. Το στάδιο C φιλοξενεί όλα τα απαραίτητα οπτικά και οπτομηχανικά στοιχεία για τη βελτιστοποίηση, το φιλτράρισμα και την επιλογή των μηκών κύματος XUV και την διάδοση της δέσμης XUV που προκύπτει στην περιοχή στόχου στο στάδιο D. Η μικτή δέσμη XUV και IR, κατά την είσοδό της στο στάδιο C, φιλτράρεται από την δέσμη laser IR χρησιμοποιώντας το φίλτρο Al πάχους 400 nm. Η επιλογή των μηκών κύματος γίνεται μέσω δύο ζευγών πολυστρωματικών κατόπτρων που μπορούν να εναλλάσσονται κατά τη διάρκεια των μετρήσεων. Κάθε ζεύγος αποτελείται από ένα επίπεδο κάτοπτρο και ένα σφαιρικό κοίλο κάτοπτρο, τοποθετημένα σε αντίθετη κατεύθυνση. Το ζεύγος των πολυστρωματικών κατόπτρων ανακλά μόνο μια στενή ζώνη ($\sim$2 nm) γύρω από ένα κεντρικό μήκος κύματος, ενώ ο σφαιρικός καθρέφτης εστιάζει στον στόχο, στο τέταρτο στάδιο της διάταξης. Και τα δύο σετ πολυστρωματικών κατόπτρων κατασκευάστηκαν ειδικά για να αποδώσουν τα κεντρικά μήκη κύματος 32,2 nm και 47,6 nm, αντίστοιχα, στη μέγιστη ανακλαστικότητα για τη χρησιμοποιούμενη γεωμετρία. Το τέταρτο στάδιο D αφορά στο υπό μελέτη αντικείμενο που είναι τοποθετημένο σε μια εξωτερικά ελεγχόμενη βάση τεσσάρων διαστάσεων (XYZ και περιστροφής Θ). Η μονοχρωματική σύμφωνη ακτινοβολία XUV περιθλώμενη από τον στόχο καταγράφεται σε κάμερα XUV.

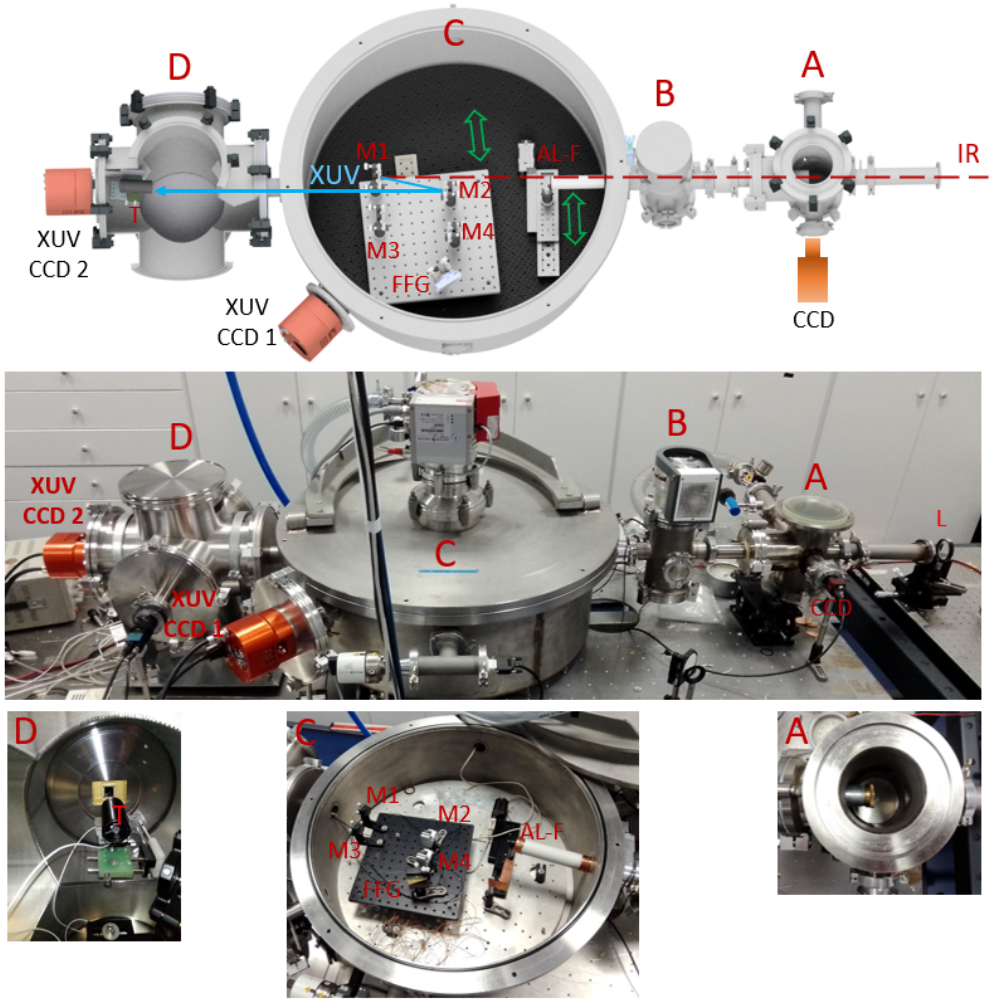

Σχήμα 1
Πειραματική διάταξη XUV CDI με τα στάδια λειτουργίας. Πάνω: σχέδιο CAD. Μέση: Φωτογραφία, Κάτω: Λεπτομέρειες για τα στάδια A, C και D. A: Το πρώτο στάδιο που αποτελεί το ημι-άπειρο κελί αερίου. B: Το δεύτερο στάδιο είναι περιοχή διαφορικής άντλησης. C: Το τρίτο στάδιο περιλαμβάνει διατάξεις φιλτραρίσματος XUV από το IR, διαγνωστική διάταξη φάσματος και επιλογή μήκους κύματος. D: Το τέταρτο στάδιο αφορά τον στόχο και την καταγραφή του αποτελέσματος CDI. L: Φακός εστίασης. AL-F: Φίλτρο αλουμινίου. M1, M3: Επίπεδοι πολυστρωματικοί καθρέφτες. M2, M4: Σφαιρικοί κοίλοι πολυστρωματικοί καθρέφτες. FFG: Φράγμα περίθλασης επίπεδου πεδίου. T: Στόχος. (από την αναφορά [88])

Η βελτιστοποίηση της παραγόμενης ακτινοβολίας XUV είναι μια πολυπαραμετρική εργασία. Εδώ παρουσιάζονται ενδεικτικά πειραματικά αποτελέσματα των βέλτιστων συνθηκών για HHG σε σχέση κυρίως με την απόδοση μετατροπής αλλά και με τα φασματικά χαρακτηριστικά. Για το σκοπό αυτό εξετάστηκαν βασικές παράμετροι όπως η διάμετρος της δέσμης λέιζερ, η θέση εστίασης της δέσμης λέιζερ, η πίεση και το είδος του αερίου, καθώς και το chirp του παλμού λέιζερ. Ενδεικτικά αποτελέσματα παρουσιάζονται στα Σχήματα 2 και 3. Ιδιαίτερα, η μελέτη περιλαμβάνει οπτικές διατάξεις που χρησιμοποιούν γκαουσιανές αλλά και δακτυλιοειδείς δέσμες λέιζερ. Οι δακτυλιοειδείς δέσμες παρέχουν την δυνατότητα μερικής αποκοπής της κεντρικής δέσμης του λέιζερ, προστατεύοντας έτσι τα επόμενα οπτικά μέρη μέρη της διάταξης

από πιθανή καταστροφή.

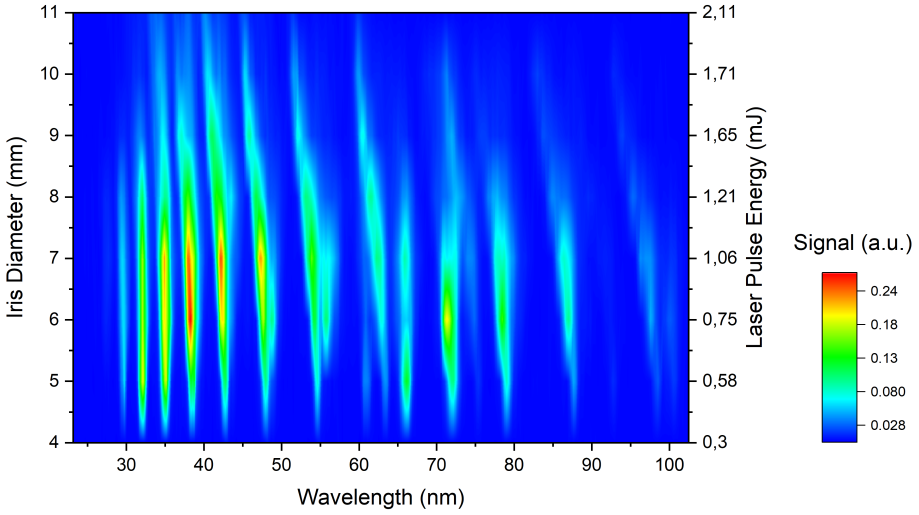

Σχήμα 2
Αποτελέσματα από μια σειρά μετρήσεων φασμάτων XUV που λήφθηκαν μεταβάλοντας την διαμέτρο της δέσμης λέιζερ. Η διάρκεια του παλμού λέιζερ ήταν 26 fs, ενώ το αέριο που χρησιμοποιήθηκε ήταν Αργό σε πίεση 40 Torr.

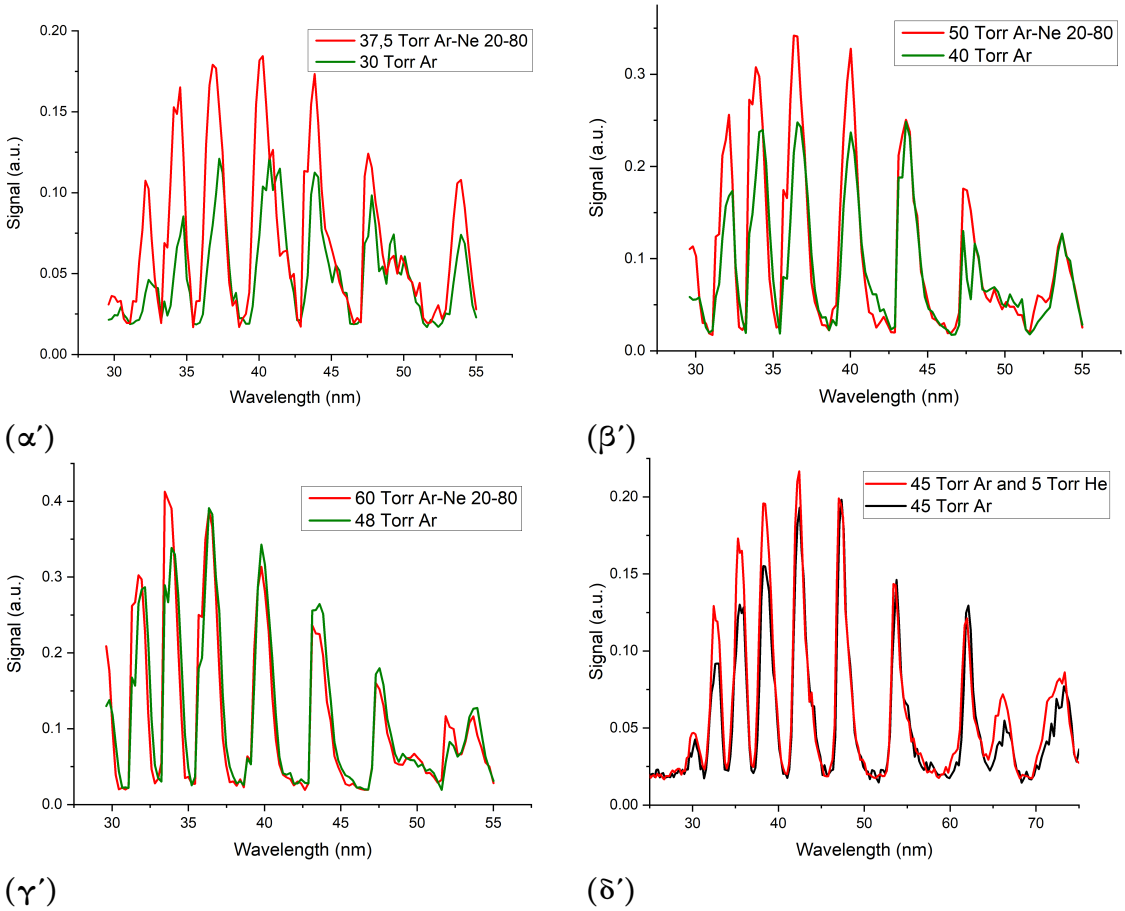

Σχήμα 3
Σύγκριση παραγωγής με Αργό και με μείγμα Αργού και άλλων αερίων. Όλα τα φάσματα προέρχονται από μείγματα εμφανίζουν ενισχυμένη απόδοση, ειδικά σε μικρότερα μήκη κύματος.

Αποτελέσματα της Έρευνας

Έλεγχος των Κβαντικών Τροχιών Ηλεκτρονίων στην Παραγωγή Υψηλών Αρμονικών Μέσω Αλλαγών στο Chirp

Η καινοτομία σε αυτή την εργασία είναι ότι οι πειραματικές συνθήκες ήταν έτσι καθορισμένες ώστε η HHG να λαμβάνει χώρα στο προπορευόμενο χρονικά άκρο του παλμού λέιζερ. Αυτό είναι εμφανές στο Σχήμα 4 όπου λόγω της υψηλής έντασης (μαύρη γραμμή), το μέσο παραγωγής ξεκινάει να ιονίζεται (πράσινη γραμμή) και να πραγματοποιείται HHG (κόκκινη γραμμή) στο προπορευόμενο άκρο του παλμού λέιζερ φτάνοντας στον πλήρη ιονισμό πριν το μέγιστο του. Στο ίδιο σχήμα είναι επίσης εμφανές (μπλε γραμμή) ότι μη γραμμικά φαινόμενα, όπως η αυτοδιαμόρφωση φάσης,

μαζί με το chirp επηρεάζουν την γωνιακή συχνότητα του λέιζερ και κατά συνέπεια την διαδικασία HHG. Επειδή αυτά αποτελούν ελέγξιμες πειραματικές συνθήκες, αυτό σημαίνει ότι τα ποιοτικά χαρακτηριστικά HHG μπορούν επίσης δευτερογενώς να ελεγχθούν.

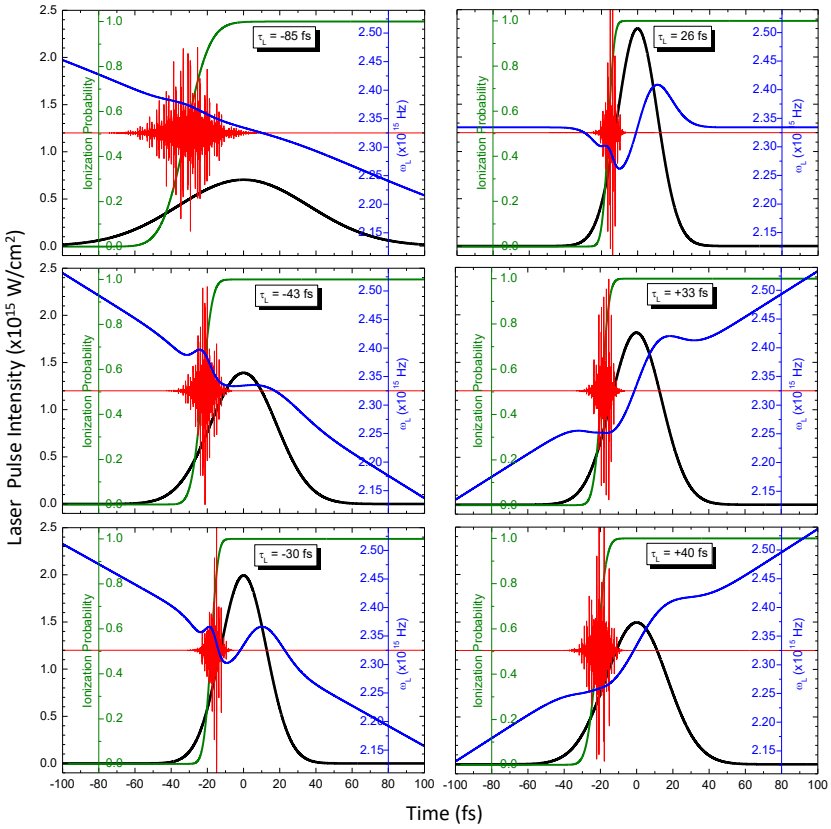

Σχήμα 4
Λεπτομέρειες των υπολογισμών του μοντέλου που αντιστοιχούν στις περιπτώσεις που παρουσιάζονται στο Σχ. 5. Μαύρη γραμμή: Ένταση λέιζερ. Μπλε γραμμή: Γωνιακή συχνότητα λέιζερ που λαμβάνει υπόψη το chirp του παλμού λέιζερ και το SPM στο μη γραμμικό μέσο (Αργό) και στο πλάσμα. Πράσινη γραμμή: πιθανότητα ιονισμού του αερίου Αργού σύμφωνα με το μοντέλο ADK. Κόκκινη γραμμή: Παραγόμενο πεδίο E ακτινοβολίας XUV, σε αυθαίρετη κλίμακα σε κάθε γράφημα για σκοπούς παρουσίασης.

Επίσης μελετήθηκαν τα φασματικά και χωρικά χαρακτηριστικών των αρμονικών (φασματικές μετατοπίσεις και διαπλανύνσεις, και γωνιακή απόκλιση) ως συνάρτηση των πειραματικών παραμέτρων του είδους του αερίου, της πίεσης του αερίου και του chirp του παλμού λέιζερ, αναδεικνύοντας τις βέλτιστες συνθήκες για το HHG σε συνθήκες ισχυρών παλμών λέιζερ. Από τα πειραματικά αποτελέσματα και τους κβαντομηχανικούς υπολογισμούς όπως απεικονίζονται στο Σχήμα 5 φαίνεται ότι το chirp των παλμών λέιζερ είναι μια κρίσιμη παράμετρος για τον έλεγχο των κβαντικών διαδρομών ηλεκτρονίων στην HHG. Αυτός ο έλεγχος επηρεάζει τα φάσματα HHG διαχωρίζοντας φασματικά τις μικρές και μεγλαλες τροχιές στις αρμονικές του plateau και επηρεάζοντας σημαντικά τη σχετική απόδοση παραγωγής τους. Σε αυτή την

εργασία, αποδεικνύεται ότι η απόδοση HHG της μεγάλης τροχιάς μειώνεται δραματικά σε σύγκριση με εκείνη της μικρής τροχιάς, απλά ρυθμίζοντας το chirp του παλμού λέιζερ.

Πιο συγκεκριμένα, ένα σημαντικό εύρημα αυτής της μελέτης είναι ότι σε μια θετική τιμή chirp που αντιστοιχεί στη διάρκεια παλμού λέιζερ +33 fs, οι μεγάλες τροχιές καταστέλλονται ισχυρά, αφήνοντας έτσι μόνο τις μικρές τροχιές στη φασματική εικόνα. Αυτή η συμπεριφορά είναι εξαιρετικής σημασίας όχι μόνο για τη θεμελιώδη Φυσική αλλά και για εφαρμογές στην σύμφωνη περιθλαστική μικροσκοπία διότι, σύμφωνα με την βιβλιογραφία το μήκος συμφωνίας των μικρών κβαντικών τροχιών είναι μεγαλύτερο από αυτό των μεγάλων.

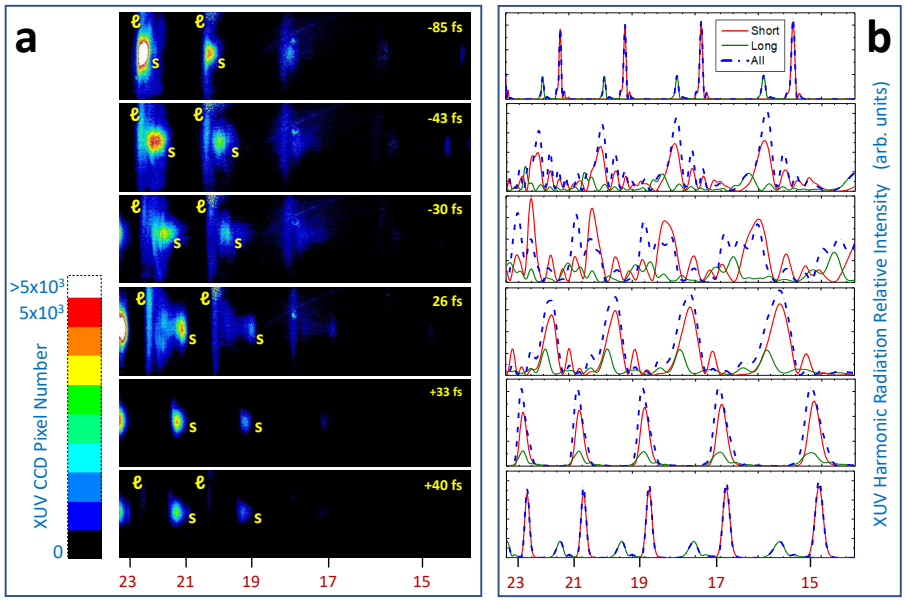

Σχήμα 5
(a) Αντιπροσωπευτικές εικόνες μετρήσεων φασματών αρμονικών για διάφορες διάρκειες παλμού λέιζερ που ελέγχονται από το επιβαλλόμενο chirp. Οι φασματικές θέσεις των αρμονικών σημειώνονται στο κάτω μέρος του σχήματος. Το πρόσημο της διάρκειας του εκάστοτε παλμού λέιζερ αντιστοιχεί στο πρόσημο του chirp. Η μικρή και η μεγάλη τροχιά, που υποδεικνύονται με τα γράμματα 'ℓ' και 's', αντίστοιχα, διαχωρίζονται φασματικά για ορισμένες τιμές chirp. (b) Τα φάσματα XUV των αρμονικών που λαμβάνονται με τους υπολογισμούς του μοντέλου που αντιστοιχούν στις πειραματικές συνθήκες των αντίστοιχων αρμονικών φασματικών εικόνων XUV στο (a). Παρουσιάζονται τόσο οι συνεισφορές μικρής όσο και μεγάλης τροχιάς, καθώς και το άθροισμά τους. Είναι φανερό ότι οι υπολογισμοί αναπαράγουν αρκετά καλά τα κύρια ποιοτικά χαρακτηριστικά των εικόνων των φασματικών μετρήσεων. Σημειωτέον ότι οι τάξεις αρμονικών 15 και 17 φαίνεται να καταστέλλονται έντονα στις πειραματικές φασματικές εικόνες λόγω της ισχυρής απορρόφησής τους από το αέριο Αργό, μια συνθήκη που δεν περιλαμβάνεται στις προσομοιώσεις.

Στο Σχήμα 6 παρουσιάζεται η συστηματική διερεύνηση των φασμάτων των αρμονικών στην περιοχή του plateau, ανιχνεύοντας με την XUV κάμερα τις αρμονικές από την 15η τάξη έως την 23η. Παρατηρήθηκε στις χαμηλές αρνητικές τιμές chirp

αξιοσημείωτη ενίσχυση στην περιοχή του plateau ακόμη και σε χαμηλές πιέσεις. Επιπλέον, υπήρξε σημαντική διαπλάτυνση τους. Για υψηλές πιέσεις αερίων και αρνητικό chirp, νέες φασματικές ζώνες αναδύονται μεταξύ αρμονικών, δημιουργώντας ένα οιονεί συνεχές φάσμα. Αυτή η συμπεριφορά συνδέεται με αυξημένο ιονισμό στο μέσο παραγωγής, επιβεβαιωμένο από εικόνες φωταύγειας πλάσματος.

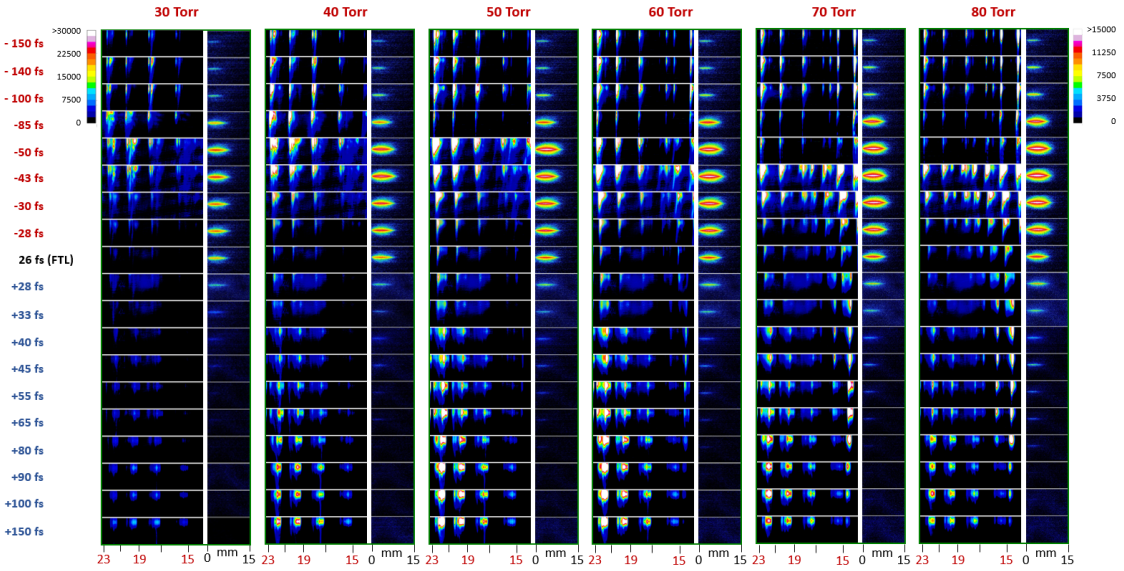

Σχήμα 6
Εικόνες φασμάτων αρμονικών (αριστερά) και αντίστοιχες εικόνες σχηματισμού πλάσματος (δεξιά) μετρημένες για διάφορες διάρκειες παλμών λέιζερ και πιέσεις αερίου Αργού. Η εστίαση της δέσμης λέιζερ είναι 3 mm πριν από την οπή εξόδου του ημι-άπειρου κελιού. Το πρόσημο της διάρκειας του εκάστοτε παλμού λέιζερ αντιστοιχεί στο πρόσημο του chirp. Οι φασματικές θέσεις των αρμονικών σημειώνονται στο κάτω μέρος του σχήματος για κάθε πίεση αερίου. Η χρωματική ένταση των φασματικών εικόνων XUV που αντιστοιχούν στις πιέσεις 40 και 50 Torr πολλαπλασιάστηκε επί δύο για καλύτερη απεικόνιση.

Η εκπομπή XUV εντός των νέων φασματικών ζωνών ποσοτικοποιείται για διαφορετικές πιέσεις στο Σχήμα 7, καταδεικνύοντας βελτιώσεις μεταξύ έως και 6 φορές για τις περισσότερες ζώνες. Τα ευρήματα αυτά δείχνουν ότι ο κατάλληλος έλεγχος του chirp μπορεί να επηρεάσει τα χαρακτηριστικά εκπομπής XUV.

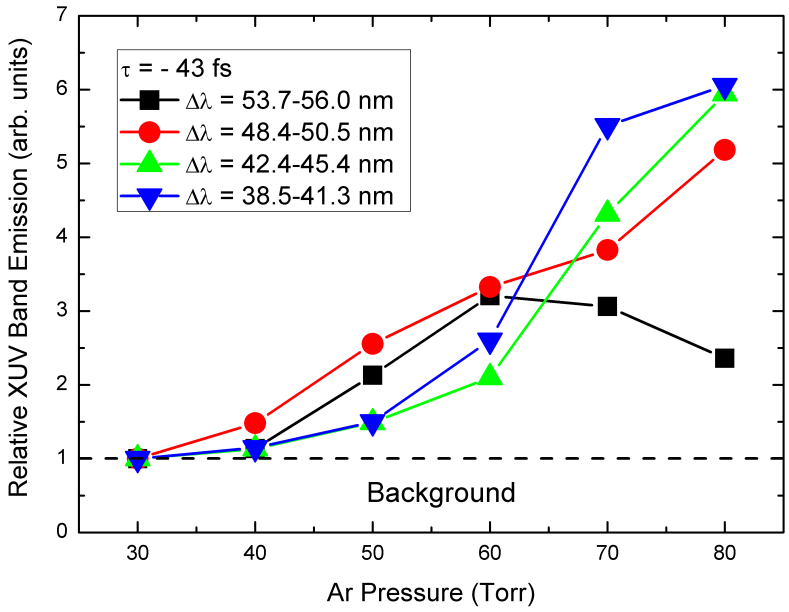

Σχήμα 7
Σχετική ενίσχυση της μετρηθείσας εκπομπής ακτινοβολίας XUV για τις φασματικές περιοχές μεταξύ των αρμονικών ως συνάρτηση της πίεσης του παραγωγού αερίου. Τα δεδομένα αντιστοιχούν σε εκείνα του Σχήματος 6 για τη διάρκεια παλμού τ = -43 fs. Τα σφάλματα της σχετικής εκπομπής ζώνης XUV εκτιμώνται χαμηλότερα από 1%.

Παρατηρήθηκε διακύμανση της γωνιακής απόκλισης των αρμονικών του plataeu καθώς μεταβαλλόταν το chirp του παλμού λέιζερ. Αναγνωρίστηκαν δύο συνιστώσες γωνιακής απόκλισης, που αποδίδονται στις μικρές και μεγάλες τροχιές ηλεκτρονίων. Η αναγνώρισή τους βασίζεται στις διακριτές γωνιακές αποκλίσεις τους, με τη μεγάλη τροχιά να παρουσιάζει την μεγαλύτερη. Επιπλέον, η φασματική απομάκρυνση των μεγάλων από τις μικρές τροχιές οφείλεται στη φασματική μετατόπισή τους προς τα μικρότερα μήκη κύματος, με τη μεγάλη τροχιά να υφίσταται την μεγαλύτερη μετατόπιση, η οποία εμφανίζεται σε μικρότερα μήκη κύματος. Συγκεκριμένα, η γωνιακή απόκλιση των μικρών και μεγάλων τροχιών της αρμονικής 21, παρουσιάζεται στο Σχήμα 8, ως συνάρτηση της διάρκειας παλμού λέιζερ για την περίπτωση πίεσης αερίου 90 Torr Ar.

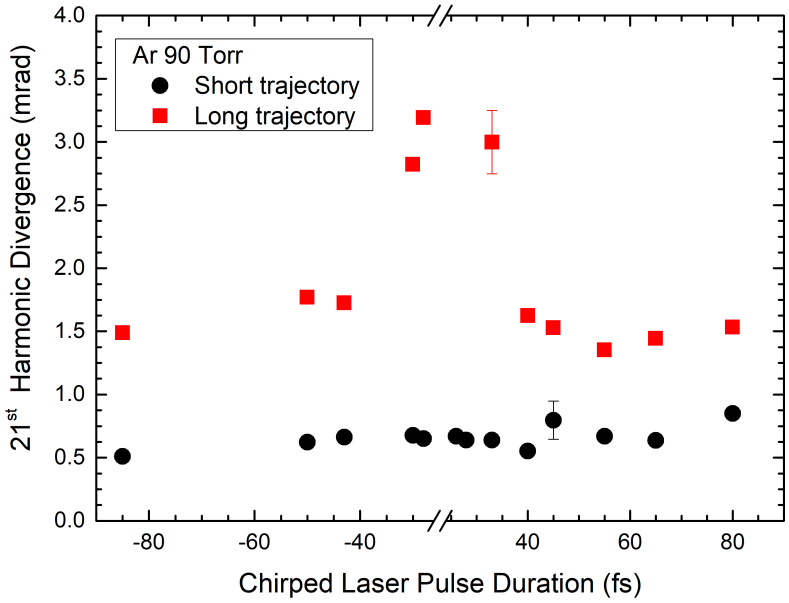

Σχήμα 8
Πειραματικά προσδιορισμένη γωνιακή απόκλιση των τροχιών της 21ης αρμονικής, της μικρής τροχιάς (μαύροι κύκλοι) και της μεγάλης τροχιάς (κόκκινα τετράγωνα), ως συνάρτηση της διάρκειας του παλμού του λέιζερ με chirp φάσμα, για την περίπτωση αερίου Αργού πιέσης 90 Torr. Απεικονίζονται ενδεικτικά σφάλματα μετρήσεων.

Παρατηρήθηκε ότι οι αρμονικές του plateau υφίστανται μια συνολική φασματική μετατόπιση καθώς μεταβαλλόταν το chirp του παλμού λέιζερ. Μια ποσοτικοποίηση του φαινομένου, παρουσιάζεται στο Σχήμα 9 όπου φαίνονται οι συνολικές φασματικές μετατόπισεις των αρμονικών 17^{η}, 19^{η}, και 21^{η} συναρτήσει του chirp του παλμού λέιζερ για πίεση αερίου Ar 80 Torr.

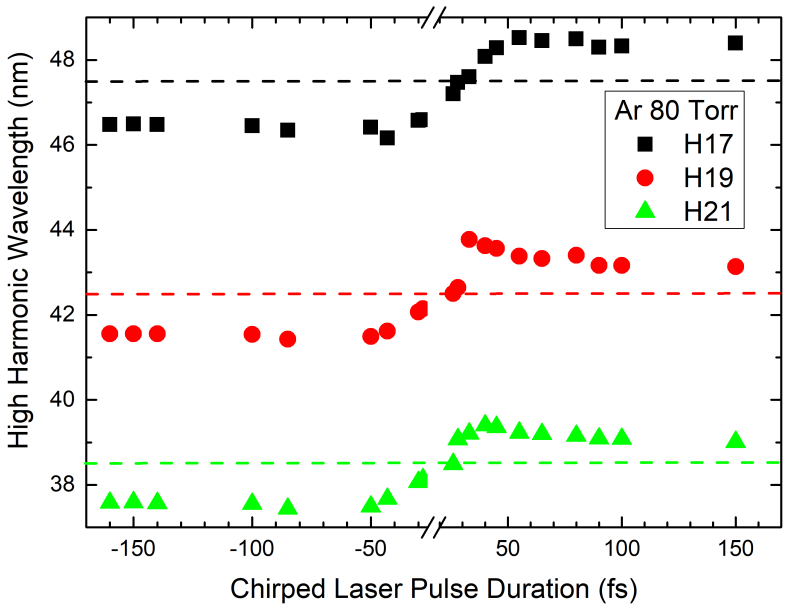

Figure 9
Φασματικές μετατοπίσεις όπως προκύπτουν από τα πειραματικά αποτελέσματα των αρμονικών υψηλής τάξης 17^{η} (μαύρο τετράγωνο), 19^{η} (κόκκινος κύκλος) και 21^{η} (πράσινο τρίγωνο) ως συνάρτηση της διάρκειας παλμού λέιζερ για την πίεση 80 Torr του Σχήματος 6. Οι διακεκομμένες οριζόντιες γραμμές αντιστοιχούν στις μη μετατοπισμένες θέσεις αρμονικών.

Σύμφωνη Πολυφασματική Περιθλαστική Μικροσκοπία

Η παρούσα διατριβή διερευνά και την ικανότητα επέκτασης της τεχνικής της σύμφωνης περιθλαστικής απεικόνισης στο ακραίο υπεριώδες (XUV CDI) σε πολυφασματική XUV CDI μέσω της πειραματικής της πραγματοποίησης και της απόδειξης αρχής λειτουργίας.

Η υλοποίηση έγινε σε λειτουργία διάδοσης ακτινοβολίας μέσα από το δείγμα και ανάκλασης, με βάση τα προαναφερθέντα ευρήματα της παρούσας εργασίας. Το XUV CDI είναι μια τεχνική μικροσκοπίας χωρίς παρεμβολή οπτικών εξαρτημάτων στον οπτικό δρόμο μεταξύ του υπό εξέταση αντικειμένου και αισθητήρα της κάμερας και βασίζεται στην συμφωνία της ακτινοβολίας XUV. Στην κάμερα καταγράφεται η εικόνα περίθλασης, η οποία αναπαριστά το φάσμα ισχύος του μετασχηματισμού Fourier του αντικειμένου, αλλά απουσιάζουν οι πληροφορίες φάσης οι οποίες είναι αναγκαίες για την ανακατασκευή της αρχικής εικόνας του αντικειμένου. Προκειμένου να γίνει η ανάκτηση της φάσης χρησιμοποιήθηκαν επαναληπτικοί αλγόριθμοι.

Στις εικόνες 10c και 10e απεικονίζονται λήψεις CDI για τα μήκη κύματος 47.6 nm και 32.2 nm, αντίστοιχα. Οι συγκεκριμένες εικόνες CDI επιλέχθηκαν για να επιδείξουν τις δυνατότητες απεικόνισης λεπτομερειών κάτω του μικρομέτρου. Στην εικόνα 10b παρουσιάζεται το προσομοιωμένο μοτίβο περίθλασης του αντικειμένου. Συγκρίνοντας τις πειραματικές εικόνες CDI για αυτά τα δύο μήκη κύματος, είναι

εμφανές ότι όσο μικρότερο είναι το μήκος κύματος, τόσο περισσότερες λεπτομέρειες μπορούν να περιλαμβάνονται. Στις Εικόνες 10d και 10f απεικονίζονται οι ανακατασκευασμένες εικόνες, για τα μήκη κύματος 47.6 nm και 32.2 nm αντίστοιχα. Από τις ανακατασκευασμένες εικόνες είναι εμφανές ότι χρησιμοποιώντας το μικρότερο μήκος κύματος, η ανακατασκευασμένη εικόνα έχει υψηλότερη ανάλυση, αναλύοντας τις λεπτομέρειες με μεγαλύτερο αριθμό pixels. Επιπλέον, το μέγεθος της ανακατασκευασμένης εικόνας του αντικειμένου είναι $\simeq 1.5$ φορές μεγαλύτερο για το μήκος κύματος 32.2 nm σε σύγκριση με τα 47.6 nm, υποδηλώνοντας την αντίστροφη αναλογία των μηκών κύματος.

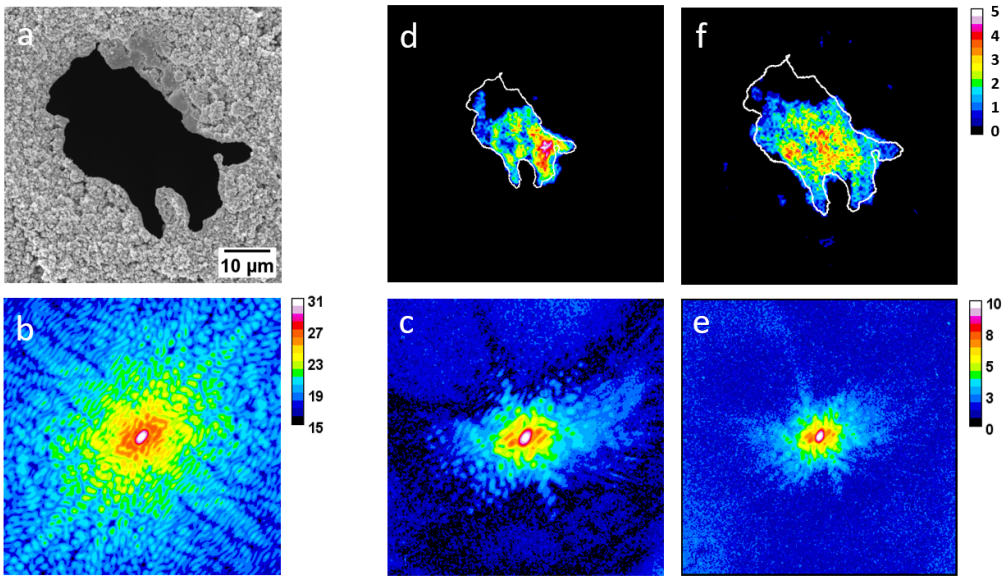

Σχήμα 10
(a) Το υπό μελέτη αντικείμενο. (b)Το προσομοιωμένο μοτίβο περίθλασης του αντικειμένου. (c) Πειραματικό αποτέλεσμα CDI αντικειμένου χρησιμοποιώντας κεντρικό μήκος κύματος των 47.6 nm. (d) Ανακατασκευή του αντικειμένου χρησιμοποιώντας το (c). (f) Ανακατασκευή του αντικειμένου χρησιμοποιώντας το (e). Το λευκό περίγραμμα που εμφανίζεται στο (d) και το (f) αντιστοιχεί στο σχήμα του αντικειμένου που εμφανίζεται στο (a) και προστέθηκε για να βοηθήσει στην οπτικοποίηση. Το μέγεθος εικόνας των (b)-(d) είναι 512×512 pixels.

Τέλος, στην παρούσα εργασία υλοποιήθηκε XUV CDI σε λειτουργία ανάκλασης, ζωτικής σημασίας για τον χαρακτηρισμό μικρο- και νανο- δομών και διαγνωστικής υπέρπυκνου πλάσματος. Έγινε πολυφασματική απεικόνιση της κυψελοειδούς δομής ενός MCP, επισημαίνοντας τις διαφορές ανάλυσης μεταξύ των μηκών κύματος (σχήματα 11 και 12). Οι προσομοιώσεις και τα πειραματικά αποτελέσματα καταδεικνύουν δυνατότητες απεικόνισης και αναλύσεις σε διαφορετικά μήκη κύματος, με επιπτώσεις στη νανοτεχνολογία, τη μικροσκοπία νανοκλίμακας και τη δυναμική χημική απεικόνιση σε επιφάνειες. Επιπλέον, διερευνήθηκε η δυνατότητα του XUV CDI για τη μελέτη της δυναμικής του πλάσματος, τονίζοντας τη σημασία του στην κατανόηση σχετικιστικών μηχανισμών παραγωγής υψηλών αρμονικών.

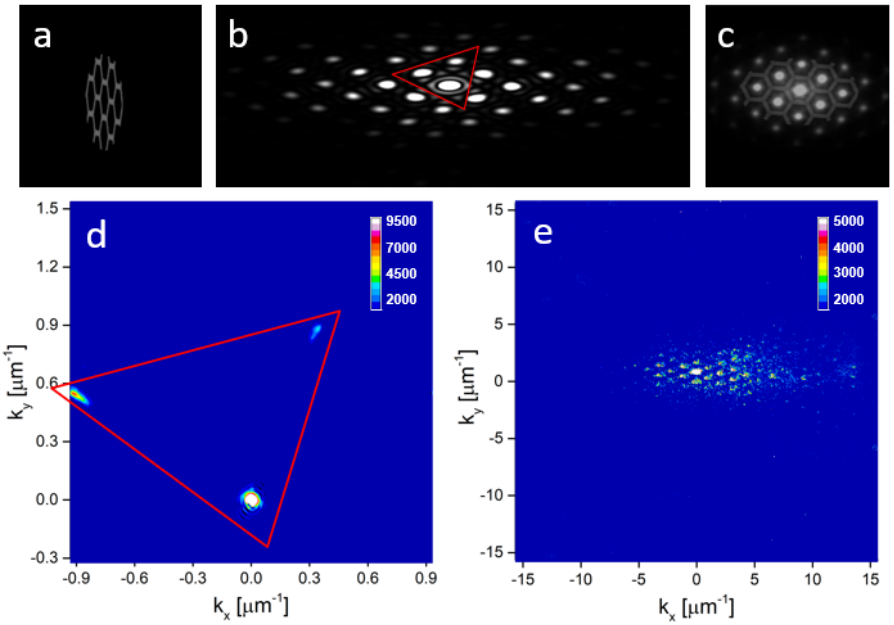

Σχήμα 11
(a) Σχηματική απεικόνιση αντικειμένου κυψέλης (MCP) περιστρεφόμενο κατά 76.1° για να ταιριάξει με τη γωνία θέασης του πειράματος από την ακτινοβολία (XUV) που το φωτίζει. (b) Το προσομοιωμένο μοτίβο περίθλασης του (a). (c) Η διορθωμένη ως προς τη γεωμετρία ανακατασκευή επικαλύπτεται με το αρχικό αντικείμενο κυψέλης MCP. (d) Πειραματικά καταγεγραμμένη εικόνα CDI από το πραγματικό αντικείμενο κυψέλης MCP για μήκος κύματος 807 (nm). (e) Ίδιο με το (d) αλλά για μήκος κύματος 47.6 mn.

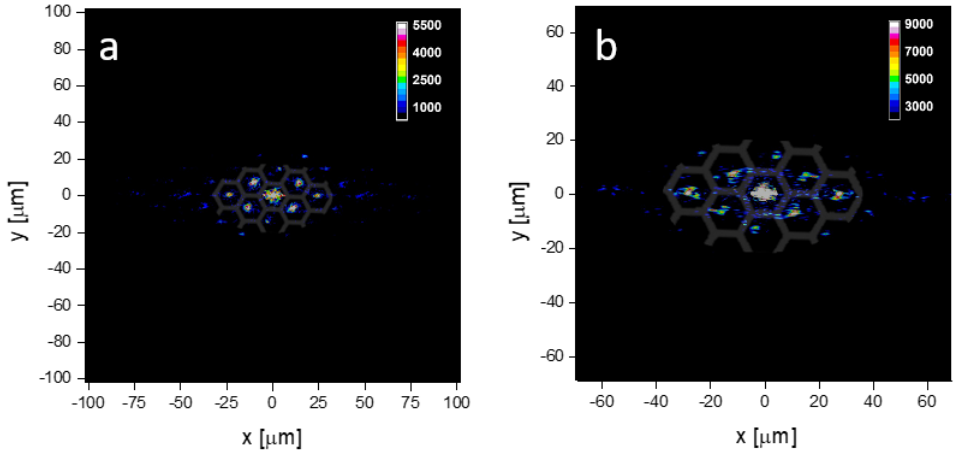

Σχήμα 12
(a) Γεωμετρικά διορθωμένη ανακατασκευή της κυψέλης MCP χρησιμοποιώντας την ακτινοβολία μήκους κύματος 47.6 nm. (b) Ίδιο με το (a) αλλά για ακτινοβολία μήκους κύματος 32.2 nm. Το επικαλυπτόμενο μοτίβο κυψέλης προστέθηκε για να βοηθήσει στην οπτικοποίηση και αντιστοιχεί στις πραγματικές διαστάσεις του καναλιού MCP. Μέγεθος εικόνας των (a) και (b) είναι 1024×1024 pixels.